Chemical Engineering Science 123 (2015) 191–196

Contents lists available at ScienceDirect

Chemical Engineering Science

journal homepage: www.elsevier.com/locate/ces

Short Communication

Evaluation of procedures for estimation of the isosteric heat of adsorption in microporous materials

Rajamani Krishna

Van't Hoff Institute for Molecular Sciences, University of Amsterdam, Science Park 904, 1098 XH Amsterdam, The Netherlands

HIGHLIGHTS

- The T-dependency of adsorption isotherms determines the isosteric heat of adsorption, Q_{st}.
- The isosteric heat of adsorption reflects both molecule–molecule and molecule–wall interactions.
- The enthalpy associated with molecule–molecule interactions is the latent heat of vaporization, ΔH_{vap}.
- The assumption $Q_{st} \approx \Delta H_{vap}$ has limited applicability.
- Generally, $Q_{st} > \Delta H_{vap}$ and can be estimated by adding the Tóth potential to ΔH_{vap}.

GRAPHICAL ABSTRACT

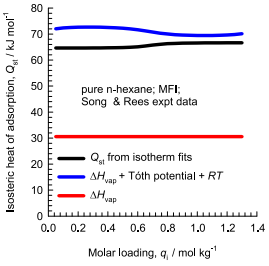

ARTICLE INFO

Article history:
Received 4 August 2014
Received in revised form
22 September 2014
Accepted 2 November 2014
Available online 11 November 2014

Keywords:
Zeolites
Metal organic frameworks
Saturated vapor pressure
Pure component isotherms
Latent heat of vaporization
Isosteric heats of adsorption

ABSTRACT

The major objective of this communication is to evaluate procedures for estimation of the isosteric heat of adsorption, Q_{st}, in microporous materials such as zeolites, metal organic frameworks (MOFs), and zeolitic imidazolate frameworks (ZIFs). For this purpose we have carefully analyzed published experimental data on adsorption isotherms at different temperatures, T, for a variety of guest molecules (water, methanol, ethanol, dimethylether, cyclohexane, benzene, toluene, xylene, ethylbenzene, ethyne, propene, propane, iso-butane, 1-butene, n-hexane) in several zeolites, MOFs, and ZIFs.

Our analysis shows that when the binding energy with the structural framework is dominated by molecule–molecule interaction forces, $Q_{st} \approx \Delta H_{vap}$, the molar enthalpy of vaporization. In such cases, the molar loading q_i at any temperature T and pressure p_i, is a unique function of (p_i/P_i^{sat}) where P_i^{sat} is the saturated vapor pressure at T.

For most guest/host combinations, however, the Q_{st} values are significantly higher than ΔH_{vap} because of strong interactions of guest molecules with the material framework. For several guest/host combinations, a reasonable estimation of Q_{st} values is obtained by addition of the Tóth potential to ΔH_{vap}.

Experimental data on the adsorption isotherms of polar compounds, such as water and alcohols, in microporous materials are commonly presented as plots of the component molar loading, q_i, as a function of (p_i/P_i^{sat}), where p_i is the bulk pressure, and P_i^{sat} is the saturation vapor pressure at the temperature, T, at which the isotherm data are measured; see, for example, Zhang et al. (2013). As illustration, Fig. 1a presents a plot of molar loadings, q_i, for adsorption of water in all-silica DDR zeolite as a function of (p_i/P_i^{sat}). We note that the experimental data at various T overlap to yield a near-unique dependence of q_i on (p_i/P_i^{sat}).

The temperature (T)-dependency of pure component adsorption isotherms in microporous materials such as zeolites, metal organic frameworks (MOFs), and zeolitic imidazolate frameworks (ZIFs) is a reflection of the binding energy between the guest molecules and the structural framework. The binding energy is

E-mail address: r.krishna@contact.uva.nl

http://dx.doi.org/10.1016/j.ces.2014.11.007
0009-2509/

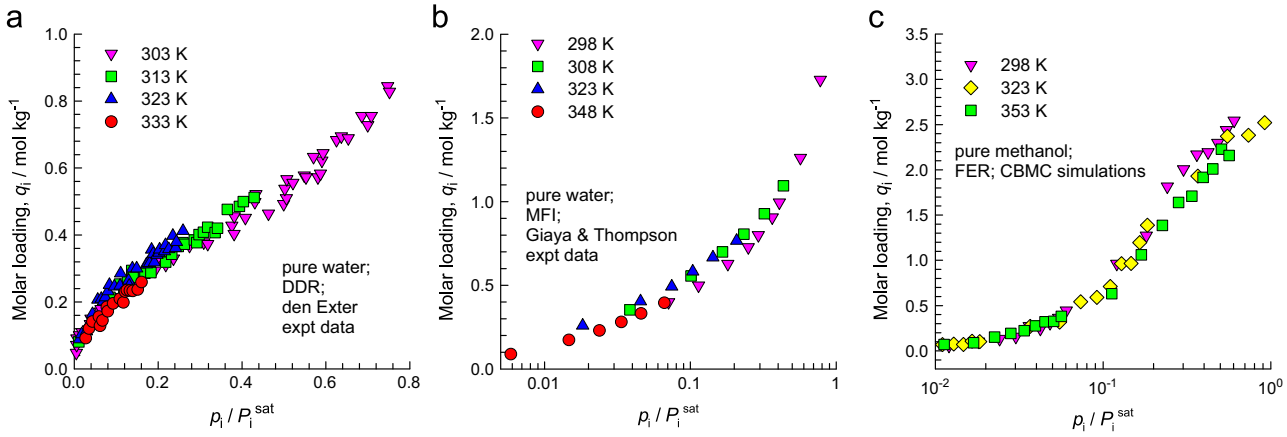

Fig. 1. Plot of component loadings vs. (p_i/P_i^{sat}) at a variety of temperatures. (a) Data of den Exter et al. (1997) for adsorption of water in DDR zeolite. (b) Data of Giaya and Thompson (2002) for adsorption of methanol in MFI zeolite. (c) Data of Hibbe et al. (2011) for adsorption of methanol in all-silica FER zeolite. Details of the calculations of the Q_{st} are available in the Supplementary material.

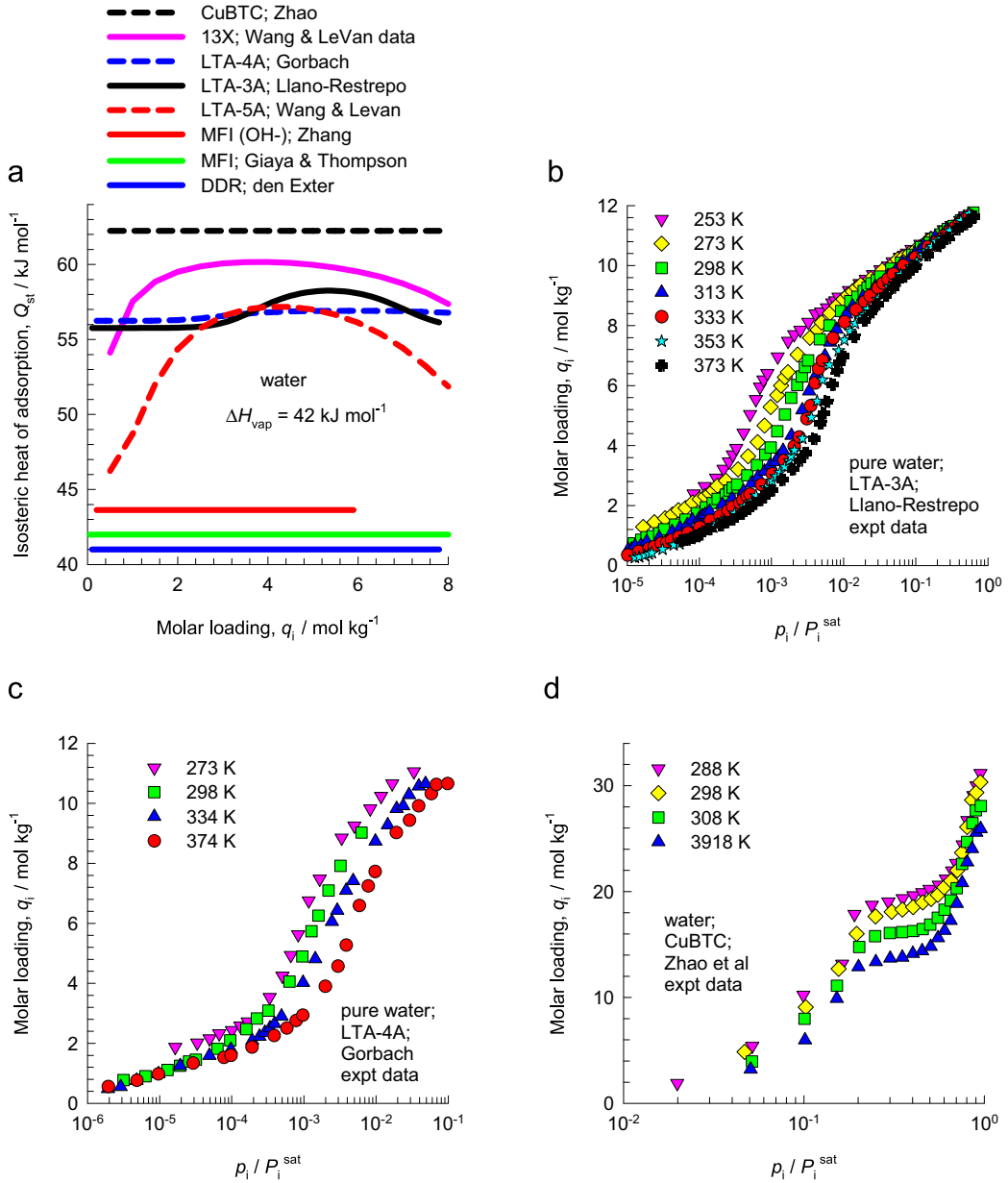

Fig. 2. (a) Comparison of the isosteric heats of adsorption, Q_{st}, of water in a variety of host materials. (b)–(d) Plot of component loadings vs. (p_i/P_i^{sat}) at a variety of temperatures. (b) Data of Llano-Restrepo and Mosquera (2009) for adsorption of water in LTA-3A. (c) Data of Gorbach et al. (2004) for adsorption of water in LTA-4A zeolite. (d) Data of Zhao et al. (2015) for adsorption of water in CuBTC. Details of the calculations of the Q_{st} are available in the Supplementary material.

quantified by the isosteric heat of adsorption, Q_{st}, that is calculated using the Clausius–Clapeyron equation:

$$\left(\frac{\partial \ln p_i}{\partial(1/T)}\right)_q = -\frac{Q_{st}}{R}; \quad Q_{st} = RT^2\left(\frac{\partial \ln p_i}{\partial T}\right)_q \tag{1}$$

For adsorption of water in all-silica DDR zeolite, the Q_{st}= 41 kJ mol^{-1}.

The T-dependency of P_i^{sat} is related to the enthalpy of vaporization ΔH_{vap}

$$\left(\frac{\partial \ln P_i^{sat}}{\partial(1/T)}\right) = -\frac{\Delta H_{vap}}{R} \tag{2}$$

The enthalpy of vaporization ΔH_{vap} is a reflection of the intermolecular forces between guest molecules; for water, ΔH_{vap}= 42 kJ mol^{-1}. The closeness between the values of Q_{st} and ΔH_{vap} implies that the molecule-molecule interactions are predominant for water/DDR system. As a direct consequence of $Q_{st} \approx \Delta H_{vap}$, the molar loadings, q_i, are primarily a function of (p_i/P_i^{sat}), irrespective of the temperature, as witnessed in Fig. 1a.

Data for water in MFI (cf. Fig. 1b), and methanol in FER zeolite (cf. Fig. 1c) also show similar overlaps of q_i vs. (p_i/P_i^{sat}) data at different T. In both these cases also, the values of Q_{st} calculated from Eq. (1) are very close to the corresponding values of ΔH_{vap} for water, and methanol, respectively.

The important advantage of the overlaps in the q_i vs. (p_i/P_i^{sat}) data is that the isotherm data measured at any specific T can be extrapolated to other temperatures. Leppäjärvi et al. (2013, 2012) present data to demonstrate similar overlaps for other guest/host combinations.

The first major objective of this communication is to examine the wider applicability of $Q_{st} \approx \Delta H_{vap}$ assumption. For this purpose, we have carried out a detailed analysis of published experimental data of pure component isotherms for a variety of guest molecules (water, methanol, ethanol, dimethylether, cyclohexane, benzene, toluene, xylene, ethylbenzene, ethyne, propene, propane, iso-butane, 1-butene, n-hexane, R12, R22) in several zeolites (MFI, LTA-3A, LTA-4A, LTA-5A, 13X, DDR, DAY-55, AFI, FER), MOFs (Zn(bdc)dabco, FeMOF-74, CoMOF-74, MgMOF-74, CuBTC, $Fe_2(BDP)_3$, MIL-101(Cr)), and ZIFs (ZIF-8). The detailed analysis of each guest/host combination is given in the Supplementary material. For each guest–host combination, we

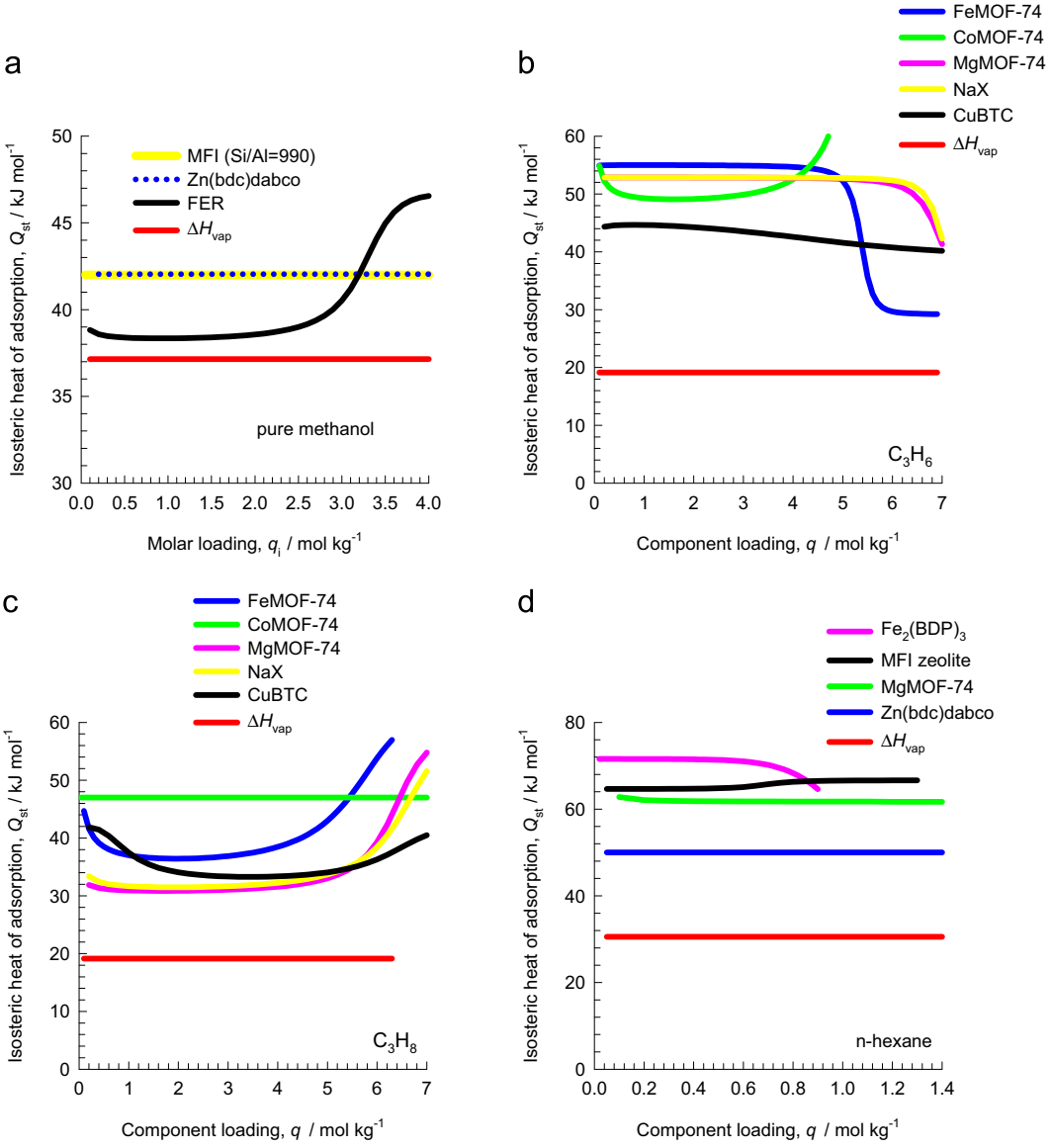

Fig. 3. Comparison of the isosteric heats of adsorption, Q_{st}, of (a) methanol, (b) C_3H_6, (c) C_3H_8, and (d) n-hexane in a variety of host materials. Details of the calculations of the Q_{st} are available in the Supplementary material.

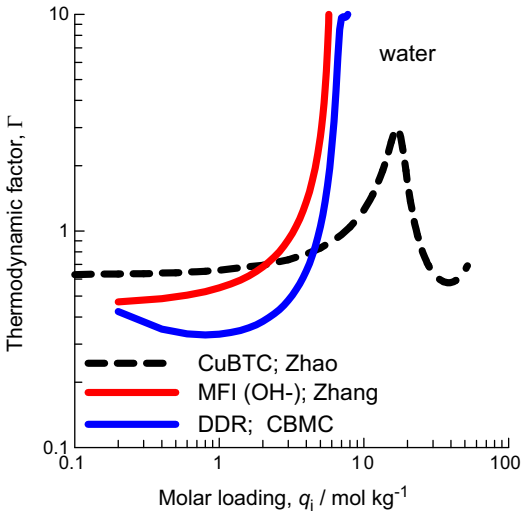

Fig. 4. Calculations of the thermodynamic factor by analytic differentiation of the dual-Langmuir–Freundlich fits for water/CuBTC (isotherm data of Zhao et al. (2015)), water/MFI(OH-) (experimental data of Zhang et al. (2012)), water/DDR (isotherm data of Krishna and van Baten (2010c)).

have fitted the pure component isotherm data using the dual-Langmuir–Freundlich isotherm model

$$q = q_{A,\mathrm{sat}}\frac{b_A p_i^{\nu_A}}{1+b_A p_i^{\nu_A}} + q_{B,\mathrm{sat}}\frac{b_B p_i^{\nu_B}}{1+b_B p_i^{\nu_B}} \tag{3}$$

with T-dependent parameters b_A, and b_B

$$b_A = b_{A0}\exp\left(\frac{E_A}{RT}\right); \quad b_B = b_{B0}\exp\left(\frac{E_B}{RT}\right) \tag{4}$$

The isosteric heat of adsorption, Q_{st}, were determined using the Clausius–Clapeyron equation (Eq. (1)). On the basis of our analysis we aim to demonstrate that the assumption $Q_{st} \approx \Delta H_{vap}$ has limited applicability and the overlaps, such as that observed in Fig. 1, do not occur for most guest/host combinations.

A further objective of this article to examine procedures for estimation of Q_{st}; for this purpose we seek guidelines from the recent work of Whittaker et al. (2013).

Fig. 2a presents a comparison of the values of Q_{st} for adsorption of water in eight different materials. For all-silica zeolites such as DDR and MFI, the values of Q_{st} fall in the narrow range of 41–43 kJ mol^{-1}; consequently, the assumption $Q_{st} \approx \Delta H_{vap}$ holds. However, for cation-exchanged zeolites such as LTA-3A, LTA-4A, LTA-

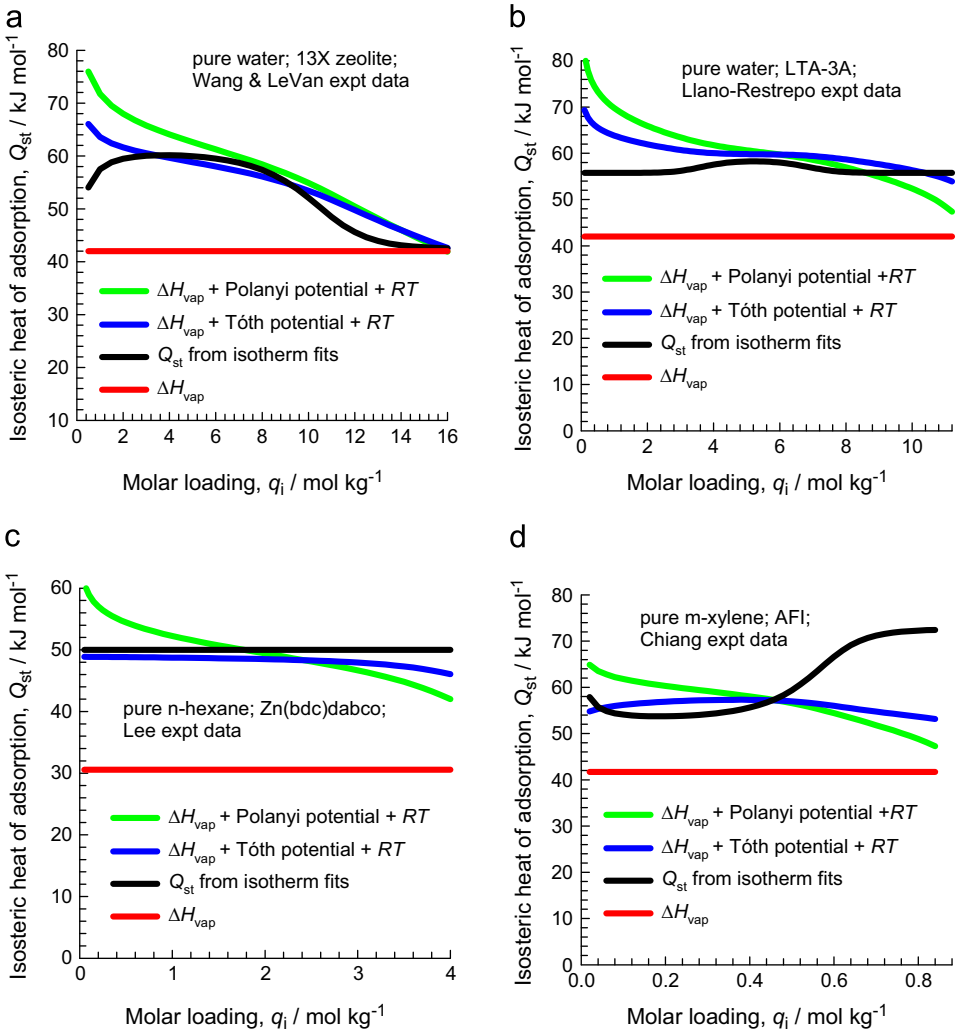

Fig. 5. Comparison of Q_s from isotherm fits with estimations using Eqs. (5) and (7) for (a) water/13X (isotherm data of Wang and LeVan (2009)), (b) water/LTA-3A (isotherm data of Llano-Restrepo and Mosquera (2009)), (c) n-hexane/Zn(bdc)dabco (isotherm data of Lee et al. (2007)), and (d) m-xylene/AFI (isotherm data of Chiang et al. (1991)). Similar comparisons for all other guest/host combinations are provided in the Supplementary material.

5A, and 13X zeolites, the binding energies are substantially higher and fall in the range 50–60 kJ mol^{-1} because water molecules experience strong Coulombic interactions with the extra-framework cations. The highest value of Q_{st} is realized with CuBTC due to strong interactions of water molecules with the unsaturated Cu(II) atoms. In such cases, the component loadings q_i in the adsorbed phase at different temperatures are not uniquely determined by (p_i/P_i^{sat}); see data for water/LTA-3A, water/LTA-4A, and water/CuBTC plotted in Fig. 2b–d.

Fig. 3 compares the isosteric heats of adsorption, Q_{st}, of (a) methanol, (b) C_3H_6, (c) C_3H_8, and (d) n-hexane in a variety of host materials. As anticipated, strong binding of the guest molecules with unsaturated metal atoms of MOFs, lead to significant departures between the values of Q_{st}, and ΔH_{vap}.

From a practical chemical process design viewpoint, it is necessary to have reliable estimation procedures for Q_{st}. This would then allow us to estimate the adsorption isotherms at temperatures that are different to those used in experiments. Furthermore, the estimation of Q_{st} is also important in the context of determination of intra-crystalline diffusivities; the stronger the binding, the lower is the value of the diffusivity (Krishna and van Baten, 2012, 2013).

The recent paper of Whittaker et al. (2013) suggests a simple procedure for the estimation of Q_{st}. Their estimation procedure consists of adding the Tóth potential (Tóth, 1962) to ΔH_{vap}

$$Q_{st} = \Delta H_{vap} + RT \ln\left((\Gamma_i - 1)\frac{p_i}{P_i^{sat}}\right) + RT \tag{5}$$

wherein the thermodynamic factor Γ_i in the Tóth potential (Tóth, 1962) is defined as

$$\Gamma_i \equiv \left.\frac{q_i \partial p_i}{p_i \partial q_i}\right|_T \tag{6}$$

The factor $(\Gamma_i - 1)$ in Eq. (7) accounts for the adsorbent heterogeneity. In the Supporting information accompanying their publication, Whittaker et al. (2013) also present an analytic expression for determination of the thermodynamic factor Γ_i using the Tóth isotherm model. As explained by Whittaker et al. (2013), the addition of RT is required for accounting for the difference between Q_{st} and the differential heat of adsorption. The contribution of RT is about 2.7 kJ mol^{-1}; this represents a relatively minor contribution to Q_{st}.

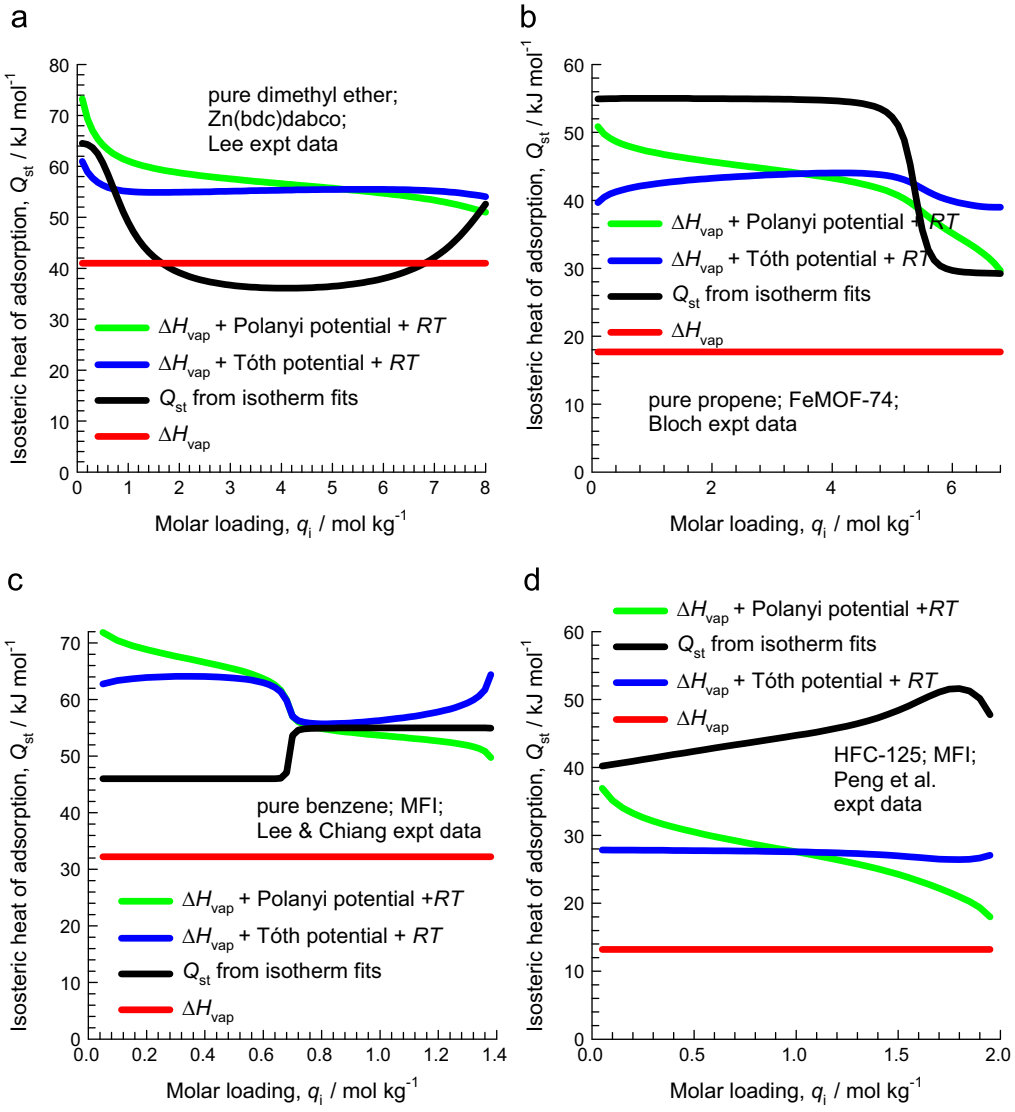

Fig. 6. Comparison of Q_s from isotherm fits with estimations using Eqs. (5) and (7) for (a) dimethylether/Zn(bdc)dabco (isotherm data of Lee et al. (2007)), (b) propene/FeMOF-74 (isotherm data of Bloch et al. (2012)), (c) benzene/MFI (isotherm data of Lee and Chiang (1996)), and (d) CFC-115/MFI (isotherm data of Peng et al. (2010)).

For homogeneous adsorbents, we obtain a simplified formula by replacing the Tóth potential by the Polanyi potential

$$Q_{st} = \Delta H_{vap} + RT \ln\left(\frac{p_i}{P_i^{sat}}\right) + RT \tag{7}$$

For adsorption of polar molecules, such as water, alcohols and aromatics, steep isotherms are often obtained for a range of pressures due to molecular clustering phenomena (Krishna and van Baten, 2010a, 2010b, 2010c, 2012, 2013). For the range of loadings for which molecular clustering occurs, the thermodynamic factor $\Gamma_i < 1$; the Tóth potential becomes indeterminate for $\Gamma_i < 1$. To illustrate this, Fig. 4 presents calculations of the thermodynamic factor for water/CuBTC, water/MFI(OH-), and water/DDR. We note that the thermodynamic factor Γ_i is less than unity for a range of loadings. For several other guest/host combinations, the Tóth potential become numerically indeterminate for a range of loadings. The paper by Whittaker et al. (2013) also alludes to the problem of indeterminacy of Γ_i, but does not offer a solution. For this reason we have used a simpler, pragmatic, procedure for calculating the thermodynamic factor Γ_i that is based on the classic Langmuir isotherm fit:

$$\Gamma_i = \frac{1}{1-(q_i/q_{i,sat})} \tag{8}$$

where $q_{i,sat} = q_{i,sat,A} + q_{i,satB}$ is the sum of the saturation capacities of sites A and B in Eq. (3). In our calculations reported below, we determined the q_i by using the dual-Langmuir–Freundlich isotherm fits (Eq. (3)). Eq. (8) can also be calculated from the measured isotherm q_i vs. p_i data at any specified temperature T. In applying Eqs. (5) and (7), we have used the values of ΔH_{vap}, P_i^{sat}, and RT in the right member of Eq. (7) at some the reference temperature, often chosen as 298 K. The T-dependence of ΔH_{vap} and P_i^{sat} does not need to be accounted for.

As illustration, Fig. 5 compares the value of Q_{st} from the isotherm fits with the estimations using Eqs. (5) and (7) and for water/13X, water/LTA-3A, n-hexane/Zn(bdc)dabco, and m-xylene/AFI; the Supplementary material contains similar comparisons for all other guest/host combinations. Both estimation procedures afford significantly improved estimations as compared to the $Q_{st} \approx \Delta H_{vap}$ assumption. Generally speaking, the predictions of Eq. (5) are slightly better than that of Eq. (7), and closer to the values determined from isotherm fits.

Fig. 6 compares the value of Q_{st} from the isotherm fits with the estimations for dimethylether/Zn(bdc)dabco, propene/FeMOF-74, benzene/MFI, and CFC-115/MFI. For these four examples, both estimations using Eqs. (5) and (7) are not in good agreement with the values determined from experimental isotherm fits.

We conclude that estimations using Eqs. (5) and (7), though significantly better than the assumption $Q_{st} \approx \Delta H_{vap}$, do not predict Q_{st} values of adequate accuracy for all guest/host combinations. The development of improved estimation procedures for Q_{st} remains a fruitful area for further research.

Appendix A. Supplementary information

Supplementary data associated with this article can be found in the online version at http://dx.doi.org/10.1016/j.ces.2014.11.007.

References

Bloch, E.D., Queen, W.L., Krishna, R., Zadrozny, J.M., Brown, C.M., Long, J.R., 2012. Hydrocarbon separations in a metal organic framework with open iron(II) coordination sites. Science 335, 1606–1610.

Chiang, A.S.T., Lee, C.-K., Chang, Z.-H., 1991. Adsorption and diffusion of aromatics in AlPO4-5. Zeolites 11, 380–386.

den Exter, M.J., Jansen, J.C., van Bekkum, H., 1997. Synthesis and characterization of the all-silica 8-ring Clathrasil DD3R comparison of adsorption properties with the hydrophilic zeolite A. Zeolites 19, 353–358.

Giaya, A., Thompson, R.W., 2002. Single-component gas phase adsorption and desorption studies using a tapered element oscillating microbalance. Microporous Mesoporous Mater. 55, 265–274.

Gorbach, A., Stegmaier, M., Eigenberger, G., 2004. Measurement and modeling of water vapor adsorption on zeolite 4A – equilibria and kinetics. Adsorption 10, 29–46.

Hibbe, F., Van Baten, J.M., Krishna, R., Chmelik, C., Weitkamp, J., Kärger, J., 2011. In-depth study of mass transfer in nanoporous materials by micro-imaging. Chem. Ing. Tech. 83, 2211–2218.

Krishna, R., van Baten, J.M., 2010a. Investigating cluster formation in adsorption of CO_2, CH_4, and Ar in zeolites and metal organic frameworks at sub-critical temperatures. Langmuir 26, 3981–3992.

Krishna, R., van Baten, J.M., 2010b. Highlighting a variety of unusual characteristics of adsorption and diffusion in microporous materials induced by clustering of guest molecules. Langmuir 26, 8450–8463.

Krishna, R., van Baten, J.M., 2010c. Hydrogen bonding effects in adsorption of water-alcohol mixtures in zeolites and the consequences for the characteristics of the Maxwell–Stefan diffusivities. Langmuir 26, 10854–10867.

Krishna, R., van Baten, J.M., 2012. Investigating the relative influences of molecular dimensions and binding energies on diffusivities of guest species inside nanoporous crystalline materials. J. Phys. Chem. C 116, 23556–23568.

Krishna, R., van Baten, J.M., 2013. Influence of adsorption thermodynamics on guest diffusivities in nanoporous crystalline materials. Phys. Chem. Chem. Phys. 15, 7994–8016.

Lee, C.K., Chiang, A.S.T., 1996. Adsorption of aromatic compounds in large MFI zeolite crystals. J. Chem. Soc. – Faraday Trans. 92, 3445–3451.

Lee, J.Y., Olson, D.H., Pan, L., Emge, T.J., Li, J., 2007. Microporous metal organic frameworks with high gas sorption and separation capacity. Adv. Funct. Mater. 17, 1255–1262.

Leppäjärvi, T., Kangas, J., Malinen, I., Tanskanen, J., 2013. Mixture adsorption on zeolites applying the Pisat temperature-dependency approach. Chem. Eng. Sci. 89, 89–101.

Leppäjärvi, T., Malinen, I., Kangas, J., Tanskanen, J., 2012. Utilization of Pisat temperature-dependency in modelling adsorption on zeolites. Chem. Eng. Sci. 69, 503–513.

Llano-Restrepo, M., Mosquera, M.A., 2009. Accurate correlation, thermochemistry, and structural interpretation of equilibrium adsorption isotherms of water vapor in zeolite 3A by means of a generalized statistical thermodynamic adsorption model. Fluid Phase Equilib. 283, 73–88.

Peng, Y., Zhang, Z., Zheng, X., Wang, H., Xu, C., Xiao, Q., Zhong, Y., Zhu, W., 2010. Comparison study on the adsorption of CFC-115 and HFC-125 on activated carbon and silicalite-1. Ind. Eng. Chem. Res. 49, 10009–10015.

Tóth, J., 1962. Gas-(Dampf-) adsorption an Festen Oberfläschen Inhomogener Aktivität, I. Acta Chim. Acad. Sci. Hung 30, 415–430.

Wang, Y., LeVan, M.D., 2009. Adsorption equilibrium of carbon dioxide and water vapor on zeolites 5A and 13X and silica gel: pure components. J. Chem. Eng. Data 54, 2839–2844.

Whittaker, P.B., Wang, X., Regenauer-Lieb, K., Chua, H.T., 2013. Predicting isosteric heats for gas adsorption. Phys. Chem. Chem. Phys. 15, 473–482.

Zhang, K., Lively, R.P., Dose, M.E., Brown, A.J., Zhang, C., Chung, J., Nair, S., Koros, W.J., Chance, R.R., 2013. Alcohol and water adsorption in zeolitic imidazolate frameworks. Chem. Commun. 49, 3245–3247.

Zhang, K., Lively, R.P., Noel, J.D., Dose, M.E., McCool, B.A., Chance, R.R., Koros, W.J., 2012. Adsorption of water and ethanol in MFI-type zeolites. Langmuir 28, 8664–8673.

Zhao, Z., Wang, S., Yang, Y., Li, X., Li, J., Li, Z., 2015. Competitive adsorption and selectivity of benzene and water vapor on the microporous metal organic frameworks (HKUST-1). Chem. Eng. J. 259, 79–89.

Supplementary Material to accompany

Evaluation of Procedures for Estimation of the Isosteric Heat of Adsorption in Microporous Materials

Rajamani Krishna

Van 't Hoff Institute for Molecular Sciences, University of Amsterdam, Science Park 904,

1098 XH Amsterdam, The Netherlands

E-mail: r.krishna@contact.uva.nl

ABSTRACT

The major objective of this communication is to evaluate procedures for estimation of the isosteric heat of adsorption, Q_{st}, in microporous materials such as zeolites, metal-organic frameworks (MOFs), and zeolitic imidazolate frameworks (ZIFs). For this purpose we have carefully analyzed published experimental data on adsorption isotherms at different temperatures, T, for a variety of guest molecules (water, methanol, ethanol, dimethylether, cyclohexane, benzene, toluene, xylene, ethylbenzene, ethyne, propene, propane, iso-butane, 1-butene, n-hexane) in several zeolites, MOFs, and ZIFs.

Our analysis shows that when the binding energy with the structural framework is dominated by molecule-molecule interaction forces, $Q_{st} \approx \Delta H_{vap}$, the molar enthalpy of vaporization. In such cases, the molar loading q_i at any temperature T and pressure p_i, is a unique function of (p_i/P_i^{sat}) where P_i^{sat} is the saturated vapor pressure at T.

For most guest/host combinations, however, the Q_{st} values are significantly higher than ΔH_{vap} because of strong interactions of guest molecules with the material framework. For several guest/host combinations, a reasonable estimation of Q_{st} values is obtained by addition of the Tóth potential to ΔH_{vap}.

Keywords: zeolites; metal-organic frameworks; saturated vapor pressure; pure component isotherms; latent heat of vaporization; isosteric heats of adsorption;

Table of Contents

1. Introduction

The temperature (T) -dependency of pure component adsorption isotherms in microporous materials such as zeolites, metal-organic frameworks (MOFs), and zeolitic imidazolate frameworks (ZIFs) is a reflection of the binding energy between the guest molecules and the structural framework. The binding energy is quantified by the isosteric heat of adsorption, Q_{st}, that is calculated using the Clausius-Clapeyron equation

$$\left(\frac{\partial \ln p_i}{\partial(1/T)}\right)_q = -\frac{Q_{st}}{R}; \quad Q_{st} = RT^2\left(\frac{\partial \ln p_i}{\partial T}\right)_q \tag{1}$$

The Clausius-Clapeyron equation shows that the enthalpy of vaporization ΔH_{vap} prescribes the T-dependency of P_i^{sat}

$$\left(\frac{\partial \ln P_i^{sat}}{\partial(1/T)}\right) = -\frac{\Delta H_{vap}}{R} \tag{2}$$

The enthalpy of vaporization ΔH_{vap} is a reflection of the intermolecular forces between guest molecules. We have carried out a detailed analysis of published experimental data of pure component isotherms for a variety of guest molecules (listed in Table 1) in a variety of zeolites (MFI, LTA-3A, LTA-4A, LTA-5A, 13X, DDR, DAY-55, AFI, FER), MOFs (Zn(bdc)dabco, FeMOF-74, CoMOF-74, MgMOF-74, CuBTC, $Fe_2(BDP)_3$, MIL-101(Cr)), and ZIFs (ZIF-8). For each guest-host combination, we have fitted the pure component isotherm data using the dual-Langmuir-Freundlich isotherm model

$$q = q_{A,sat}\frac{b_A p_i^{\nu_A}}{1+b_A p_i^{\nu_A}} + q_{B,sat}\frac{b_B p_i^{\nu_B}}{1+b_B p_i^{\nu_B}} \tag{3}$$

with T-dependent parameters b_A, and b_B

$$b_A = b_{A0}\exp\left(\frac{E_A}{RT}\right); \quad b_B = b_{B0}\exp\left(\frac{E_B}{RT}\right) \tag{4}$$

For each guest-host combination, we have determined the isosteric heat of adsorption, Q_{st}, using the Clausius-Clapeyron equation (1), and compare this with the corresponding values of the latent heats of vaporization, ΔH_{vap}, that are listed in Table 1. Furthermore, we compare the values of Q_{st} calculated as a sum of three different contributions

$$Q_{st} = \Delta H_{vap} + RT \ln\left(\frac{p_i}{P_i^{sat}}\right) + RT \tag{5}$$

where $RT \ln\left(\frac{p_i}{P_i^{sat}}\right)$ is the Polanyi potential. The contribution of RT is about 2.7 kJ mol^{-1}; this represents a relatively minor contribution to Q_{st}. The calculation of the Polanyi potential $RT \ln\left(\frac{p_i}{P_i^{sat}}\right)$ requires isotherm q_i vs p_i data at temperature T. In our calculations reported below, we determined this by applying the dual-Langmuir-Freundlich fits, equations (3), and (4) . Alternatively, the Polanyi potential can be calculated from the measured isotherm q_i vs p_i data.

Equation (5) is the simplified form of the predictive model for Q_{st} that has been suggested by Whittaker et al.[1]. In the Whittaker procedure, the Polanyi potential is replaced by the Tóth potential $RT \ln\left((\Gamma_i - 1)\frac{p_i}{P_i^{sat}}\right)$, following the classic 1962 paper: [2].

$$Q_{st} = \Delta H_{vap} + RT \ln\left((\Gamma_i - 1)\frac{p_i}{P_i^{sat}}\right) + RT \tag{6}$$

wherein the thermodynamic factor Γ_i is defined as

$$\Gamma_i \equiv \frac{q_i}{p_i}\frac{\partial p_i}{\partial q_i}\bigg|_T \tag{7}$$

The thermodynamic factor Γ_i can be calculated by analytic differentiation of the dual-Langmuir-Freundlich fits. For adsorption of polar molecules, such as water, alcohols and aromatics, steep isotherms are often obtained for a range of pressures due to molecular clustering phenomena.[3-7] For the

range of loadings for which molecular clustering occurs, the thermodynamic factor $\Gamma_i < 1$; the Tóth potential becomes indeterminate for $\Gamma_i < 1$. To illustrate this, Figure 1 presents calculations of the thermodynamic factor for water/CuBTC, water/MFI(OH-), and water/DDR. We note that the thermodynamic factor Γ_i is less than unity for a range of loadings. For several other guest/host combinations, the Tóth potential become numerically indeterminate for a range of loadings. For this reason we have used a much simpler procedure for calculating the thermodynamic factor Γ_i that is based on the classic Langmuir isotherm fit.

$$\Gamma_i = \frac{1}{1 - \frac{q_i}{q_{i,sat}}} \tag{8}$$

where $q_{i,sat} = q_{i,sat,A} + q_{i,satB}$ is the sum of the saturation capacities of sites A, and B. In our calculations reported below, we determined the thermodynamic correction factor by applying the dual-Langmuir-Freundlich fits, equations (3), and (4) in reverse. Equation (8) can also be calculated from the measured isotherm q_i vs p_i data.

In the following sections, we have compared the calculated values of Q_{st}, with the predictions of Equations (5) and (6). The analysis of each guest-host combination is provided in the subsequent sections.

2. Data of Zhao for adsorption of water in CuBTC

Figure 2a shows the experimental data of Zhao et al.[8] for pure isotherm data for water, measured at temperatures of 288 K, 298 K, 308 K, and 318 K. The isotherms show perceptible inflections at loadings corresponding to 18 mol kg^{-1}. The initial steep adsorption at low pressures is associated with strong adsorption at unsaturated Cu atom sites, as well as with the oxygen-containing groups in the ligand.[8] Further increase in the loading occurs due to filling of the large cavities. Figure 2b show a plot of component loadings q_i vs. (p_i/P_i^{sat}) at a variety of temperatures. We note that the data at all temperatures do *not* overlap and we must therefore conclude that there is no unique relationship

between the loadings q_i and (p_i/P_i^{sat}). The calculations of the isosteric heats of adsorption, Q_{st}, for water are shown in Figure 2c,d. The isotherm inflections get reflected in a corresponding inflection in the data for Q_{st} vs loading. For loadings lower than about 18 mol kg^{-1}, the Q_{st} are significantly higher than the corresponding latent heat of vaporization, ΔH_{vap} = 42 kJ mol^{-1}. This departure from the values of Q_{st} and ΔH_{vap} provides the rationale that there is no unique relationship between the loadings q_i and (p_i/P_i^{sat}) for various temperatures, witnessed in Figure 2b. Figure 2c shows that Equation (5) provides a reasonably good estimate of the value of Q_{st}. The use of equation (6) provides better estimates of Q_{st} as a function of the loading.

3. Data of Gorbach for adsorption of water in LTA-4A zeolite

Figure 3a shows the experimental data of Gorbach et al. [9] for pure component isotherms for water in LTA-4A zeolite at a variety of temperatures. Figure 3b shows a plot of component loadings q_i vs. (p_i/P_i^{sat}) at a variety of temperatures. We note that the data at all temperatures do *not* overlap and we must therefore conclude that there is no unique relationship between the loadings q_i and (p_i/P_i^{sat}). Calculations of the isosteric heats of adsorption of water in LTA-4A (cf. Figure 3c,d) shows that the value of Q_{st} is about 56 kJ mol^{-1}; this value is significantly higher than the latent heat of vaporization of water, ΔH_{vap} = 42 kJ mol^{-1}. The significant departure between the values of Q_{st} and ΔH_{vap} is the primary reason for the observation in Figure 3b that the component loadings at different temperatures are not uniquely determined by (p_i/P_i^{sat}).

Figures 3c,d show that Equations (5) and (6) provide reasonable estimates of the value of Q_{st}; the differences in the predictions of using either the Polanyi or Tóth potential is not significant.

4. Data of Zhang for adsorption of water in MFI (OH^-) zeolite

Figure 4a shows the experimental data of Zhang et al. [10] for pure component isotherms for water in MFI (OH^-) zeolite at a variety of temperatures. Figure 4b shows a plot of component loadings q_i vs. (p_i/P_i^{sat}) at a variety of temperatures. We note that the data at all temperatures fall within a narrow band of data. Calculations of the isosteric heats of adsorption of water in MFI (OH^-) zeolite (cf. Figure 4c,d)

shows that the value of Q_{st} falls in the narrow range of 43.5 kJ mol^{-1}; this value is close to the latent heat of vaporization of water, ΔH_{vap} = 42 kJ mol^{-1}. The closeness of the values of Q_{st} and ΔH_{vap} is the primary reason for the observation in Figure 4b that the component loadings q_i at different temperatures appear to be uniquely determined by (p_i/P_i^{sat}).

Figures 4c,d show that Equations (5), and (6) provide good estimates of the values of Q_{st}.

5. Data of Giaya and Thompson for adsorption of water in MFI zeolite

Figure 5a shows the experimental data of Giaya and Thompson [11] for pure component isotherms for water in MFI zeolite at a variety of temperatures. Figure 5b shows a plot of component loadings q_i vs. (p_i/P_i^{sat}) at a variety of temperatures. We note that the data at all temperatures fall within a narrow band of data. Calculations of the isosteric heats of adsorption of water in MFI zeolite (cf. Figure 5c,d) shows that the value of Q_{st} is 42 kJ mol^{-1}; this value equal to the latent heat of vaporization of water, ΔH_{vap} = 42 kJ mol^{-1}. The agreement between the values of Q_{st} and ΔH_{vap} is the primary reason for the observation in Figure 5b that the component loadings q_i at different temperatures appear to be uniquely determined by (p_i/P_i^{sat}), albeit as an approximation.

Figures 5c,d show that Equations (5), and (6) provide good estimates of the values of Q_{st}.

6. Data of Llano-Restrepo for adsorption of water in LTA-3A zeolite

Figure 6a shows the experimental data of Llano-Restrepo and Mosqueera[12] for pure component isotherms for water in LTA-3A zeolite at a variety of temperatures. Figure 6b shows a plot of component loadings q_i vs. (p_i/P_i^{sat}) at a variety of temperatures. We note that the data at all temperatures do *not* overlap and we must therefore conclude that there is no unique relationship between the loadings q_i and (p_i/P_i^{sat}). Calculations of the isosteric heats of adsorption of water in LTA-3A (cf. Figure 6c,d) shows that the value of Q_{st} falls in the range 56 – 58 kJ mol^{-1}; this value is significantly higher than the latent heat of vaporization of water, ΔH_{vap} = 42 kJ mol^{-1}. The significant departure between the values of Q_{st} and ΔH_{vap} is the primary reason for the observation in Figure 6b that the component loadings at different temperatures are not uniquely determined by (p_i/P_i^{sat}).

Figures 6c,d show that Equations (5) and (6) provide good estimates of the values of Q_{st}. The estimates of Equation (6) is slightly superior.

7. Data for adsorption of water in DDR zeolite

Figure 7a shows the experimental data of den Exter et al. [13] for pure component isotherms for water in all-silica DDR zeolite at a variety of temperatures. Figure 7b shows a plot of component loadings q_i vs. (p_i/P_i^{sat}) at a variety of temperatures. We note that the data at all temperatures fall within a narrow band of data. Calculations of the isosteric heats of adsorption of water in DDR zeolite (cf. Figure 7c,d) shows that the value of Q_{st} is 41 kJ mol^{-1}; this value is equal to the latent heat of vaporization of water, ΔH_{vap} = 42 kJ mol^{-1}. The close agreement between the values of Q_{st} and ΔH_{vap} is the primary reason for the observation in Figure 7b that the component loadings q_i at different temperatures appear to be uniquely determined by (p_i/P_i^{sat}).

Figures 7c,d show that Equations (5) and (6) provide reasonable good estimates of the values of Q_{st}.

The closeness between the values of Q_{st} and ΔH_{vap} for water in all-silica DDR zeolite is also confirmed by Configurational-Bias Monte Carlo simulation data of Krishna and van Baten [5] for the pure component isotherms at 300 K and 360 K; see Figure 8a. Figure 8b shows a plot of component loadings q_i vs. (p_i/P_i^{sat}) at the two temperatures. We note that the data at all temperatures fall within a narrow band of data. Calculations of the isosteric heats of adsorption of water in DDR zeolite (cf. Figure 8c,d) shows that the value of Q_{st} is about 41 kJ mol^{-1}; this value is slightly lower than the latent heat of vaporization of water, ΔH_{vap} = 42 kJ mol^{-1}. The reasonably good agreement between the values of Q_{st} and ΔH_{vap} is the primary reason for the observation in Figure 8b that the component loadings q_i at different temperatures appear to be uniquely determined by (p_i/P_i^{sat}).

Figures 8c,d show that Equations (5) and (6) provide reasonable good estimates of the values of Q_{st}.

8. Data of Wang and LeVan for adsorption of water in 13X and LTA-5A zeolites

Figure 9a shows the experimental data of Wang and LeVan [14] for pure component isotherms for water in 13X zeolite at a variety of temperatures. Figure 9b shows a plot of component loadings q_i vs. (p_i/P_i^{sat}) at a variety of temperatures. We note that the data at all temperatures do *not* overlap and we must therefore conclude that there is no unique relationship between the loadings q_i and (p_i/P_i^{sat}). Calculations of the isosteric heats of adsorption of water in 13X zeolite (cf. Figure 9c,d) shows that the value of Q_{st} falls in the range 52 – 58 kJ mol^{-1}; this value is significantly higher than the latent heat of vaporization of water, ΔH_{vap} = 42 kJ mol^{-1}. The significant departure between the values of Q_{st} and ΔH_{vap} is the primary reason for the observation in Figure 9b that the component loadings at different temperatures are not uniquely determined by (p_i/P_i^{sat}).

Figures 9c,d show that Equations (5) and (6) provide good estimates of the values of Q_{st}. The estimates of Equation (6) is slightly superior.

Figure 10a shows the experimental data of Wang and LeVan [14] for pure component isotherms for water in LTA-5A zeolite at a variety of temperatures. Figure 10b shows a plot of component loadings q_i vs. (p_i/P_i^{sat}) at a variety of temperatures. We note that the data at all temperatures do *not* overlap and we must therefore conclude that there is no unique relationship between the loadings q_i and (p_i/P_i^{sat}). Calculations of the isosteric heats of adsorption of water in LTA-5A zeolite (cf. Figure 10c,d) shows that the value of Q_{st} falls in the range 48 – 56 kJ mol^{-1}; this value is significantly higher than the latent heat of vaporization of water, ΔH_{vap} = 42 kJ mol^{-1}. The significant departure between the values of Q_{st} and ΔH_{vap} is the primary reason for the observation in Figure 10b that the component loadings at different temperatures are not uniquely determined by (p_i/P_i^{sat}).

Figures 10c,d show that Equations (5) and (6) provide good estimates of the values of Q_{st}. The estimates of Equation (6) is slightly superior.

9. Data of Pera-Titus for adsorption of water and ethanol in LTA-4A zeolite

Figure 11a shows the experimental data of Pera-Titus et al. [15] for pure component isotherms for water in LTA-4A zeolite at a variety of temperatures. Figure 11b shows a plot of component loadings q_i vs. (p_i/P_i^{sat}) at a variety of temperatures. We note that the data at all temperatures fall within a narrow band of data; remarkably, this result is not in consonance with the experimental data of Gorbach et al. [9] for pure component isotherms for water in LTA-4A zeolite. Calculations of the isosteric heats of adsorption of water in LTA-4A,using the Clausius-Clapeyron equation (1), (cf. Figure 11c) shows that the value of Q_{st} falls in the narrow range of 40 - 41 kJ mol^{-1}; these values are close to the latent heat of vaporization of water, ΔH_{vap} = 42 kJ mol^{-1}. The closeness of the values of Q_{st} and ΔH_{vap} is the primary reason for the observation in Figure 11b that the component loadings q_i at different temperatures appear to be uniquely determined by (p_i/P_i^{sat}).

Figure 12a shows the experimental data of Pera-Titus et al. [15] for pure component isotherms for ethanol in LTA-4A zeolite at a variety of temperatures. Figure 12b shows a plot of component loadings q_i vs. (p_i/P_i^{sat}) at a variety of temperatures. We note that the component loadings at different temperatures do *not* overlap and there is no unique relationship between the loadings q_i and (p_i/P_i^{sat}). Calculations of the isosteric heats of adsorption of ethanol in LTA-4A (cf. Figure 12c) shows that the value of Q_{st} are approximately 23.5 kJ mol^{-1}; this value is significantly below the heat of vaporization of ethanol, ΔH_{vap} = 41 kJ mol^{-1}. The significant departure between the values of Q_{st} and ΔH_{vap} is the primary reason for the observation in Figure 12b that the component loadings at different temperatures are not uniquely determined by (p_i/P_i^{sat}).

Pera-Titus et al. [15] also published experimental data of the component loadings for water/ethanol mixtures at 2.1 kPa and 333 K as a function of mole fraction of water in the bulk vapor phase; see Figure 13. The experimental data are in reasonably good agreement with Ideal Adsorbed Solution Theory (IAST) calculations that are based on the pure component *T*-dependent isotherm fits shown in Figure 11a, and Figure 12a. Leppäjärvi et al.[16] have presented IAST calculations based on the

assumption that the component loadings at different temperatures are uniquely determined by (p_i/P_i^{sat}). Their IAST calculations are in poor agreement with the experimental data of Pera-Titus et al. [15]. The reasons for this poor agreement must logically be traced to the erroneous assumption of the unique releationship between q_i and (p_i/P_i^{sat}). Put another way, if proper unary isotherm fits are used, IAST works reasonably well for water/ethanol mixtures.

10. CBMC simulations for adsorption of methanol in FER zeolite

Figure 14a shows the experimental CBMC simulation data of Hibbe et al.[17] for pure component isotherms for methanol in all-silica FER zeolite at three different temperatures. Figure 14b shows a plot of component loadings q_i vs. (p_i/P_i^{sat}) at a variety of temperatures. We note that the data at all temperatures fall within a narrow band of data. Calculations of the isosteric heats of adsorption of methanol in FER,using the Clausius-Clapeyron equation (1), (cf. Figure 14c,d) shows that the value of Q_{st} falls in the narrow range of 38 - 46 kJ mol^{-1}; these values are close to the latent heat of vaporization of methanol, ΔH_{vap} = 37 kJ mol^{-1}. The closeness of the values of Q_{st} and ΔH_{vap} is the primary reason for the observation in Figure 14b that the component loadings q_i at different temperatures appear to be uniquely determined by (p_i/P_i^{sat}).

Figures 14c,d show that Equations (5) and (6) provide good estimates of the values of Q_{st}. The estimates of Equation (6) is slightly superior.

11. Data of Sakuth for adsorption of 1-propanol and toluene in DAY-55 zeolite

Figure 15a shows the experimental data of Sakuth et al. [18] for pure component isotherms for 1-propanol in DAY-55 (de-aluminated Y) zeolite at two different temperatures. Figure 15b shows a plot of component loadings q_i vs. (p_i/P_i^{sat}) at a variety of temperatures. We note that the data at both temperatures fall within a narrow band of data. Calculations of the isosteric heats of adsorption of 1-propanol in DAY-55 (cf. Figure 15c,d) shows that the value of Q_{st} falls in the range of 50-55 kJ mol^{-1}; this value is slightly below the latent heat of vaporization of 1-propanol, ΔH_{vap} = 44.8 kJ mol^{-1}. The

closeness of the values of Q_{st} and ΔH_{vap} is the primary reason for the observation in Figure 15b that the component loadings q_i at two different temperatures appear to be uniquely determined by (p_i/P_i^{sat}). Figures 15c,d show that Equations (5) and (6) provide good estimates of the values of Q_{st}. The estimates of Equation (6) is slightly superior.

Figure 16a shows the experimental data of Sakuth et al. [18] for pure component isotherms for toluene in DAY-55 at to different temperatures. Figure 16b shows a plot of component loadings q_i vs. (p_i/P_i^{sat}) at both temperatures. We note that the data at both temperatures do *not* overlap and we must therefore conclude that there is no unique relationship between the loadings q_i and (p_i/P_i^{sat}). Calculations of the isosteric heats of adsorption of toluene in DAY-55 (cf. Figure 16c,d) shows that the value of Q_{st} falls in the range 80 – 84 kJ mol^{-1}; this value is significantly higher than the latent heat of vaporization of toluene, ΔH_{vap} = 36.3 kJ mol^{-1}. The significant departure between the values of Q_{st} and ΔH_{vap} is the primary reason for the observation in Figure 16b that the component loadings at two different temperatures are not uniquely determined by (p_i/P_i^{sat}).

Figures 16c,d show that Equations (5) and (6) provide reasonable estimates of the values of Q_{st}. The estimates of Equation (6) is slightly superior.

12. Data for adsorption of dimethyl ether, methanol, ethanol, and n-hexane, and cyclohexane in Zn(bdc)dabco

Figure 17a shows the experimental data of Lee et al. [19] for pure component isotherms for dimethylether in Zn(bdc)dabco (= Zn(bdc)(dabco)$_{0.5}$) at a variety of temperatures. Figure 17b shows a plot of component loadings q_i vs. (p_i/P_i^{sat}) at a variety of temperatures. We note that the data at all temperatures do *not* overlap and we must therefore conclude that there is no unique relationship between the loadings q_i and (p_i/P_i^{sat}). For loadings $q_i < 2$ mol kg^{-1}, calculations of the isosteric heats of adsorption of dimethylether in Zn(bdc)dabco (cf. Figure 17c,d) shows that the value of Q_{st} is higher than the latent heat of vaporization of dimethylether, ΔH_{vap} = 41kJ mol^{-1}. The departure between the values of Q_{st} and ΔH_{vap} is the primary reason for the observation in Figure 17b that the component loadings at different temperatures are not uniquely determined by (p_i/P_i^{sat}).

Figures 17c,d show that both Equations (5) and (6) overestimate the value of Q_{st}.; the differences in the predictions of using either the Polanyi or Tóth potential are not significant.

Figure 18a shows the experimental data of Lee et al. [19] for pure component isotherms for ethanol in Zn(bdc)dabco at a variety of temperatures. Figure 18b shows a plot of component loadings q_i vs. (p_i/P_i^{sat}) at a variety of temperatures. We note that the data at all temperatures do *not* overlap precisely and we must therefore conclude that there is no unique relationship between the loadings q_i and (p_i/P_i^{sat}). For loadings $q_i < 3$ mol kg^{-1}, calculations of the isosteric heats of adsorption of ethanol in Zn(bdc)dabco (cf. Figure 18c,d) shows that the value of Q_{st} is significantly higher than the latent heat of vaporization of ethanol, $\Delta H_{vap} = 41$kJ mol^{-1}. The significant departure between the values of Q_{st} and ΔH_{vap} is the primary reason for the observation in Figure 18b that the component loadings at different temperatures are not uniquely determined by (p_i/P_i^{sat}).

Figures 18c,d show that both Equations (5) and (6) overestimate the value of Q_{st}.; the differences in the predictions of using either the Polanyi or Tóth potential are not significant.

Figure 19a shows the experimental data of Lee et al. [19] for pure component isotherms for methanol in Zn(bdc)dabco at a variety of temperatures. Figure 19b shows a plot of component loadings q_i vs. (p_i/P_i^{sat}) at a variety of temperatures. We note that the data at all temperatures do *not* overlap precisely and we must therefore conclude that there is no unique relationship between the loadings q_i and (p_i/P_i^{sat}). Calculations of the isosteric heats of adsorption of methanol in Zn(bdc)dabco (cf. Figure 19c,d) shows that the value of Q_{st} is higher than the latent heat of vaporization of methanol, $\Delta H_{vap} = 37$ kJ mol^{-1}. The significant departure between the values of Q_{st} and ΔH_{vap} is the primary reason for the observation in Figure 19b that the component loadings at different temperatures are not uniquely determined by (p_i/P_i^{sat}).

Figure 19c,d show that Equations (5) and (6) provide reasonable estimates of the values of Q_{st}. The estimates of Equation (6) is slightly superior.

Figure 20a shows the experimental data of Li[20] for pure component isotherms for cyclohexane in Zn(bdc)dabco at a variety of temperatures. Figure 20b shows a plot of component loadings q_i vs.

(p_i/P_i^{sat}) at a variety of temperatures. We note that the data at all temperatures do *not* overlap and we must therefore conclude that there is no unique relationship between the loadings q_i and (p_i/P_i^{sat}). Calculations of the isosteric heats of adsorption of cyclohexane in Zn(bdc)dabco (cf. Figure 20c,d) shows that the value of Q_{st} ranges between 49 kJ mol^{-1}and 65 kJ mol^{-1}; these values are higher than the latent heat of vaporization of cyclohexane, ΔH_{vap} = 31.6 kJ mol^{-1}. The significant departure between the values of Q_{st} and ΔH_{vap} is the primary reason for the observation in Figure 20b that the component loadings at different temperatures are not uniquely determined by (p_i/P_i^{sat}).

Figures 20c,d shows that Equations (5) and (6) provide reasonable estimates of the value of Q_{st}; the use of the Tóth potential appears to offer a slight improvement in the predictions.

Figure 21a shows the experimental data of Lee et al. [19] for pure component isotherms for n-hexane in Zn(bdc)dabco at a variety of temperatures. Figure 21b shows a plot of component loadings q_i vs. (p_i/P_i^{sat}) at a variety of temperatures. We note that the data at all temperatures do *not* overlap and we must therefore conclude that there is no unique relationship between the loadings q_i and (p_i/P_i^{sat}). Calculations of the isosteric heats of adsorption of n-hexane in Zn(bdc)dabco (cf. Figure 21c,d) shows that the value of Q_{st} is 50 kJ mol^{-1}; this values are significantly higher than the latent heat of vaporization of h-hexane, ΔH_{vap} = 30.5 kJ mol^{-1}. The significant departure between the values of Q_{st} and ΔH_{vap} is the primary reason for the observation in Figure 21b that the component loadings at different temperatures are not uniquely determined by (p_i/P_i^{sat}).

Figures 21c,d show that Equations (5) and (6) provide reasonable estimates of the value of Q_{st}; the use of the Tóth potential appears to offer an improvement in the predictions of Q_{st}.

The Configurational-Bias Monte Carlo simulation data, from the works of Dubbeldam et al.[21, 22] and Krishna and van Baten [23, 24], for adsorption of nC6 in Zn(bdc)dabco at four different temperatures are presented in Figure 22a.The CBMC simulations are in reasonably good agreement with the experimental data of Lee et al. [19] presented in Figure 21a. However, these two data sets are not in agreement with the isotherm data published in Bárcia et al.[25]. This discrepancy has been highlighted in the Supplementary Material accompanying the publication of Krishna and van Baten [24]. One possible

reason for this discrepancy is the possibility that the crystals of Zn(bdc)dabco used in the experiments of Bárcia et al.[25] had undergone structural transformations; Chen et al.[26] have demonstrated that the three-dimensional Zn(bdc)$(dabco)_{0.5}$ framework can undergo reversible transformation in the presence of air to Zn(bdc), also known as MOF-2 [27, 28].

Figure 22b shows a plot of component loadings q_i vs. (p_i/P_i^{sat}) at four different temperatures. We note that the data at all temperatures do *not* overlap and we must therefore conclude that there is no unique relationship between the loadings q_i and (p_i/P_i^{sat}). This isosteric heat of adsorption, calculated from the Clausius-Clapeyron equation are presented in Figure 22c,d; these yield Q_{st} values that are significantly higher than the latent heat of vaporization of h-hexane, ΔH_{vap} = 30.5 kJ mol^{-1}.

Figures 22c,d show that Equations (5) and (6) provide reasonable estimates of the value of Q_{st}; the use of the Tóth potential appears to offer an improvement in the predictions of Q_{st}.

13. Data of Nayak for adsorption of methanol in MFI (Si/Al=990) zeolite

Figure 23a shows the experimental data of Nayak and Moffat [29] for pure component isotherms for methanol in MFI (Si/Al=990) zeolite at a variety of temperatures. Figure 23b shows a plot of component loadings q_i vs. (p_i/P_i^{sat}) at a variety of temperatures. We note that the data at all temperatures overlap and we must therefore conclude that there is a unique relationship between the loadings q_i and (p_i/P_i^{sat}). Calculations of the isosteric heats of adsorption of methanol in MFI (Si/Al=990) (cf. Figure 23c,d) shows that the value of Q_{st} is only slightly higher than the latent heat of vaporization of methanol. The approximate agreement between the values of Q_{st} and ΔH_{vap} is the primary reason for the observation in Figure 23b that the component loadings at different temperatures are uniquely determined by (p_i/P_i^{sat}).

Figures 23c,d show that both Equations (5) and (6) provide reasonable estimates of the value of Q_{st}; the use of the Tóth potential appears to offer some improvement in the predictions of Q_{st}.

14. Data of Li and Böhme for adsorption of propene, and propane in ZIF-8

Figures 24a, and Figure 25a show the experimental data of Li et al.[30] and Böhme et al.[31] for pure isotherm data for propene, and propane, respectively, in ZIF-8 measured at a variety of temperatures. Figures 24b, and Figure 25b show plots of component loadings q_i vs. (p_i/P_i^{sat}) at a variety of temperatures for each of the two guest molecules. For each guest we note that the data at various temperatures do *not* overlap and we must therefore conclude that there is no unique relationship between the loadings q_i and (p_i/P_i^{sat}). The calculations of the isosteric heats of adsorption, Q_{st}, for the two guest molecules are shown in Figures 24c, and Figure 25c. For both guest molecules the values of Q_{st} are significantly higher than the corresponding latent heat of vaporization of the guest species, ΔH_{vap}. The departure from the values of Q_{st} and ΔH_{vap} provides the rationale that there is no unique relationship between the loadings q_i and (p_i/P_i^{sat}) for various temperatures, witnessed in Figures 24b, and 25b.

Figures 24c,d show that both Equations (5) and (6) provide reasonable estimates of the value of Q_{st}; the use of the Tóth potential appears to offer some improvement in the predictions of Q_{st}.

Figures 25c,d show that both Equations (5) and (6) provide reasonable estimates of the value of Q_{st}; the use of the Tóth potential appears to offer significant improvement in the predictions of Q_{st}.

15. Data for adsorption of ethyne, propene, and propane in FeMOF-74, and MgMOF-74

Figures 26a, 27a, and 28a show the experimental data of Bloch et al [32] for pure isotherm data for ethyne, propene, and propane, respectively, in FeMOF-74 measured at a variety of temperatures. Figures 26b, 27b, and 28b show plots of component loadings q_i vs. (p_i/P_i^{sat}) at a variety of temperatures for each of the three guest molecules. For each guest we note that the data at all temperatures do *not* overlap and we must therefore conclude that there is no unique relationship between the loadings q_i and (p_i/P_i^{sat}). The calculations of the isosteric heats of adsorption, Q_{st}, for the two guest molecules are shown in Figures 26c, 27c, and 28c. For all guest molecules the values of Q_{st} are significantly higher than the

corresponding latent heat of vaporization of the guest species, ΔH_{vap}. The departure from the values of Q_{st} and ΔH_{vap} provides the rationale that there is no unique relationship between the loadings q_i and (p_i/P_i^{sat}) for various temperatures, witnessed in Figures 26b, 27b, and 28b.

Figures 26c,d show that both Equations (5) and (6) provide reasonable estimates of the value of Q_{st} for ethyne; the use of the Tóth potential appears to offer some improvement in the predictions of .

Figures 27c,d show that both Equations (5) and (6) provide reasonable estimates of the value of Q_{st} for propene; the use of the Tóth potential appears to offer some improvement in the predictions of Q_{st}.

Figures 28c,d show that both Equations (5) and (6) provide reasonable estimates of the value of Q_{st} for propene; the use of the Tóth potential appears to offer some improvement in the predictions of Q_{st}.

For adsorption in MgMOF-74, which is the structural analog of FeMOF-74; the analysis is provided in Figures 29, 30, and 31. The results are completely analogous to that of FeMOF-74, as is to be expected.

Figures 29c,d show that both Equations (5) and (6) provide very good estimates of the value of Q_{st} for ethyne; the use of the Tóth potential appears to offer some improvement in the predictions of Q_{st}.

Figures 30c.d show that both Equations (5) and (6) provide resonable estimates of the value of Q_{st} for propene; the use of the Tóth potential appears to offer some improvement in the predictions of Q_{st}.

Figures 31c,d show that both Equations (5) and (6) provide very good estimates of the value of Q_{st} for propane; the use of the Tóth potential appears to offer some improvement in the predictions of Q_{st}.

16. Data for adsorption of propene, and propane in NaX zeolite

Figures 32a, and 33a show the experimental data of Costa et al.[33] for pure isotherm data for propene, and propane, respectively, in NaX zeolite measured at a variety of temperatures. Figures 32b, and 33b show plots of component loadings q_i vs. (p_i/P_i^{sat}) at a variety of temperatures for each of the three guest molecules. For both guest we note that the data at all temperatures do *not* overlap and we must therefore conclude that there is no unique relationship between the loadings q_i and (p_i/P_i^{sat}). The calculations of the isosteric heats of adsorption, Q_{st}, for the two guest molecules are shown in Figures 32c,d, and 33c,d. For both guest molecules the values of Q_{st} are significantly higher than the corresponding latent heat of

vaporization of the guest species, ΔH_{vap}. The departure from the values of Q_{st} and ΔH_{vap} provides the rationale that there is no unique relationship between the loadings q_i and (p_i/P_i^{sat}) for various temperatures, witnessed in Figures 32b, and 33b.

Figures 32c,d show that both Equations (5) and (6) provide reasonable estimates of the value of Q_{st} for propene.

Figures 33c,d show that both Equations (5) and (6) provide reasonable estimates of the value of Q_{st} for propane.

17. Data for adsorption of isobutene, and 1-butene in NaX zeolite

Figures 34a, and 35a show the experimental data of Granato et al.[34] for pure isotherm data for isobutene, and 1-butene, respectively, in NaX zeolite measured at a variety of temperatures. Figures 34b, and 35b show plots of component loadings q_i vs. (p_i/P_i^{sat}) at a variety of temperatures for each of the three guest molecules. For both guest we note that the data at all temperatures do *not* overlap and we must therefore conclude that there is no unique relationship between the loadings q_i and (p_i/P_i^{sat}). The calculations of the isosteric heats of adsorption, Q_{st}, for the two guest molecules are shown in Figures 34c,d, and 35c,d. For both guest molecules the values of Q_{st} are significantly higher than the corresponding latent heat of vaporization of the guest species, ΔH_{vap}. The departure from the values of Q_{st} and ΔH_{vap} provides the rationale that there is no unique relationship between the loadings q_i and (p_i/P_i^{sat}) for various temperatures, witnessed in Figures 34b, and 35b.

Figures 34c,d, and 35c,d show that both Equations (5) and (6) significantly underestimate the values of Q_{st} for iso-butane and 1-butene.

18. Data of Chiang for xylene isomers in AFI zeolite

Figures 36a, 37a, and 38a show the experimental data of Chiang et al.[35] for adsorption of o-xylene, m-xylene, and p-xylene in AFI zeolite at 303 K, 318 K, and 333 K. Figures 36b, 37b, and 38b show plots of component loadings vs. (p_i/P_i^{sat}) at the different temperatures. For every guest we note that the data at all temperatures do *not* overlap and we must therefore conclude that there is no unique relationship

between the loadings q_i and (p_i/P_i^{sat}). The calculations of the isosteric heats of adsorption, Q_{st}, for the four guest molecules are shown in Figures 36c, 37c, and 38c. For all three xylene isomers the values of Q_{st} are significantly higher than the corresponding latent heat of vaporization of the guest species, ΔH_{vap}. The departure from the values of Q_{st} and ΔH_{vap} provides the rationale that there is no unique relationship between the loadings q_i and (p_i/P_i^{sat}) for various temperatures, witnessed in Figures 36b, 37b, and 38b.

Figures 36c,d show that both Equations (5) and (6) significantly underestimate the values of Q_{st} for o-xylene. O-xylene molecules can fit snugly within the 8.4 Å grooves of AFI (see pore landscapes in Figure 39), and for this reason the value of Q_{st} is significantly higher than that of m-xylene and p-xylene; see discussions in Chiang et al.[35] regarding Figure 4 of their publication. The commensurate fit of o-xylene in the grooves is the reason that the experimental isosteric heats are significantly higher than the predicted one.

For m-xylene, and p-xylene, Figures 37c,d, and 38c,d show that both Equations (5) and (6) provide good estimates of the values of Q_{st}.

19. Data of Lee and Chiang for adsorption of aromatics in MFI zeolite

Figures 40a, 41a, 42a, and 43a show the experimental data of Lee and Chiang [36] for pure isotherm data for benzene, toluene, p-xylene, and ethylbenzene, respectively, in MFI zeolite measured at a variety of temperatures. The pure component isotherms display inflection characteristics at a loading of 0.7 mol kg^{-1}, which corresponds to 4 molecules per unit cell of MFI zeolite. The reason for this inflection is that the intersections are preferred locations of aromatic molecules; there are 4 intersection sites per unit cell of MFI zeolite. Figures 40b, 41b, 42b, and 43b show plots of component loadings q_i vs. (p_i/P_i^{sat}) at a variety of temperatures for each of the four guest molecules. For every guest we note that the data at all temperatures do *not* overlap and we must therefore conclude that there is no unique relationship between the loadings q_i and (p_i/P_i^{sat}). The calculations of the isosteric heats of adsorption, Q_{st}, for the four guest molecules are shown in Figures 40c, 41c, 42c, and 43c. In every case, there is a strong inflection in the Q_{st} vs loading data; this inflection is a direct consequence of the isotherm

inflection characteristics. For benzene, toluene, p-xylene, and ethylbenzene the values of Q_{st} are significantly higher than the corresponding latent heat of vaporization of the guest species, ΔH_{vap}. The departure from the values of Q_{st} and ΔH_{vap} provides the rationale that there is no unique relationship between the loadings q_i and (p_i/P_i^{sat}) for various temperatures, witnessed in Figures 40b, 41b, 42b, and 43b.

Figures 40c,d, 41c,d, 42c, and 43c,d show that both Equations (5) and (6) provide good estimates of the values of Q_{st}; the use of the Tóth potential appears to offer some improvement in the predictions of Q_{st}.

20. Data of Sun and Zhu for adsorption of iso-butane in MFI zeolite

Figure 44a shows the experimental data of Sun et al. [37] and Zhu et al. [38] for pure isotherm data for iso-butane in MFI zeolite measured at a variety of temperatures. Figure 44b show a plot of component loadings q_i vs. (p_i/P_i^{sat}) at a variety of temperatures. The reason for this inflection is that the intersections are preferred locations of branched alkanes [39]; there are 4 intersection sites per unit cell of MFI zeolite. We note that the data at all temperatures do *not* overlap and we must therefore conclude that there is no unique relationship between the loadings q_i and (p_i/P_i^{sat}). The calculations of the isosteric heats of adsorption, Q_{st}, for iso-butane in MFIare shown in Figure 44c. There is a perceptible inflection in the Q_{st} vs loading data; this inflection occurs at a loading of 0.7 mol kg^{-1} which corresponds to 4 molecules per unit cell of MFI zeolite. The reason for this inflection is that the intersections are preferred locations of iso-butane molecules; there are 4 intersection sites per unit cell of MFI zeolite. For iso-butane, the values of Q_{st} are significantly higher than the corresponding latent heat of vaporization, ΔH_{vap} = 21.5 kJ mol^{-1}. This departure from the values of Q_{st} and ΔH_{vap} provides the rationale that there is no unique relationship between the loadings q_i and (p_i/P_i^{sat}) for various temperatures, witnessed in Figure 44b.

'Figure 44c,d show that both Equations (5) and (6) provide good estimates of the values of Q_{st}; the use of the Tóth potential appears to offer some improvement in the predictions of Q_{st}.

CBMC simulation data for adsorption of iso-butane in MFI are presented in Figure 45. An exactly identical set of conclusions can be drawn.

Figure 45c,d show that both Equations (5) and (6) provide reasonable estimates of the values of Q_{st}; the use of the Tóth potential appears to offer some improvement in the predictions of Q_{st}.

21. Data for adsorption of n-hexane in MFI zeolite

Figure 46a shows the experimental data of Song and Rees [40] for pure isotherm data for n-hexane in MFI zeolite measured at a variety of temperatures. The pure component isotherms display slight inflection characteristics at a loading of 0.7 mol kg^{-1}, which corresponds to 4 molecules per unit cell of MFI zeolite. The reason for this inflection is that the intersections is discussed in detail Vlugt et al.[41]. Figure 46b show a plot of component loadings q_i vs. (p_i/P_i^{sat}) at a variety of temperatures. We note that the data at all temperatures do *not* overlap and we must therefore conclude that there is no unique relationship between the loadings q_i and (p_i/P_i^{sat}). The calculations of the isosteric heats of adsorption, Q_{st}, for n-hexane in MFI is shown in Figure 46c. There is a slight inflection in the Q_{st} vs loading data; this inflection occurs at a loading of 0.7 mol kg^{-1} ; this is a direct consequence of isotherm inflections. For n-hexane, the values of Q_{st} are significantly higher than the corresponding latent heat of vaporization, ΔH_{vap} = 30.5 kJ mol^{-1}. This departure from the values of Q_{st} and ΔH_{vap} provides the rationale that there is no unique relationship between the loadings q_i and (p_i/P_i^{sat}) for various temperatures, witnessed in Figure 46b.

Figure 46c,d show that both Equations (5) and (6) provide reasonable estimates of the values of Q_{st}; the use of the Tóth potential appears to offer some improvement in the predictions of Q_{st}.

Consider the CBMC simulation data of Krishna and van Baten. [23, 42] Pure component isotherms for n-hexane in MFI zeolite, determined at 300 K, 373 K, 398 K, and 433 K are shown in Figure 47. These data confirm the conclusions reached in the foregoing paragraph on the basis of the experimental data of Song and Rees.[40]

Figures 47c,d show that both Equations (5) and (6) provide good estimates of the values of Q_{st}; the use of the Tóth potential appears to offer some improvement in the predictions of Q_{st}.

22. Data for adsorption of n-hexane in MgMOF-74

Figure 46a shows the CBMC simulation data of Krishna and van Baten[23] for pure isotherm data for n-hexane in MgMOF-74. Figure 48b show a plot of component loadings q_i vs. (p_i/P_i^{sat}) at a variety of temperatures. We note that the data at all temperatures do *not* overlap and we must therefore conclude that there is no unique relationship between the loadings q_i and (p_i/P_i^{sat}). The calculations of the isosteric heats of adsorption, Q_{st}, for n-hexane in MgMOF-74 are shown in Figure 48c,d. For n-hexane, the values of Q_{st} are significantly higher than the corresponding latent heat of vaporization, ΔH_{vap} = 30.5 kJ mol^{-1}. This departure from the values of Q_{st} and ΔH_{vap} provides the rationale that there is no unique relationship between the loadings q_i and (p_i/P_i^{sat}) for various temperatures, witnessed in Figure 48b.

Figure 48c,d show that both Equations (5) and (6) provide good estimates of the values of Q_{st}; the use of the Tóth potential appears to offer some improvement in the predictions of Q_{st}.

23. CBMC simulations for adsorption of alkane isomers in CuBTC

Figure 49 presents CBMC simulation data for the isosteric heats of adsorption, Q_{st}, in CuBTC of n-butane, iso-butane, 2,2-dimethylpropane (= neo-pentane), and 2-methylbutane (2MB). For loadings Θ_i < 8 molecules per unit cell, the Q_{st} the values are significantly higher than for loadings Θ_i > 8 molecules per unit cell. We first need to rationalize this strong dependencies of Q_{st} on the loadings. CuBTC structure consists of two types of "cages" and two types of "windows" separating these cages. Large cages are inter-connected by 9 Å windows of square cross-section. The large cages are also connected to tetrahedral-shaped pockets of ca. 6 Å size through triangular-shaped windows of ca. 4.6 Å size. There are 8 tetrahedral pockets per unit cell, and these are preferred locations of molecules at low loadings. Each pocket can accommodate only one of nC4, iC4, neo-P or 2MB; this is illustrated by the snapshot in Figure 49 . For loadings Θ_i < 8 molecules per unit cell, the alkanes prefer location in the pockets. For location within the tetrahedral pockets, the guest molecules have stronger binding due to strong confinement within the pockets. For loadings Θ_i > 8 molecules per unit cell, the guest molecules begin to populate the larger cages; here the confinement is not severe. Consequently, molecule-molecule

interactions are dominant. For this reason the values of Q_{st} for loadings $\Theta_i > 8$ molecules per unit cell are of the same order of magnitude as the latent heats of vaporization; nC4: ΔH_{vap} = 22.8 kJ mol^{-1}, iC4: ΔH_{vap} = 21.5 kJ mol^{-1}, neo-pentane: ΔH_{vap} = 22.7 kJ mol^{-1}, 2MB: ΔH_{vap} = 25.6 kJ mol^{-1}.

24. Data of Herm for adsorption of hexane isomers in $Fe_2(BDP)_3$

The paper by Herm et al.[43] demonstrates the efficacy of $Fe_2(BDP)_3$ for separation of hexane isomers: n-hexane (nC6), 2-methylpentane (2MP), 3-methylpentane (3MP), 2,2 dimethylbutane (22DMB), and 2,3 dimethybutane (23DMB) in $Fe_2(BDP)_3$. The principle of separation relies on exploitation of the differences in the alignment of the isomers along the gutters of the triangular channels. The snapshots in Figure 50, obtained from molecular simulations, show the location and conformations of hexane isomers adsorbed within the triangular channels of $Fe_2(BDP)_3$. The alkane backbone aligns along the triangular gutters (vertices), which provide the maximum surface area for interactions. The number of C atoms in the backbone that can exert van der Waals interactions with the framework atoms in the vertices is of vital importance. From the observed conformations, it is evident that the number of C atoms that can effectively interact with the pore wall decreases with the degree of branching. The di-branched isomers are more compact and have the least amount of van der Waals interactions with the walls. The alignment of hexane isomers gets reflected in both the pure component isotherms (Figure 50a), and the values of Q_{st} (Figure 50b). The hierarchy of Q_{st} values is nC6 > 2MP > 3MP > 22DMB $\approx$ 23DMB. The Q_{st} values lie in the range 62 – 71 = kJ mol^{-1}; these values are significantly higher than the corresponding latent heats of vaporization of hexane isomers that have values in the range ΔH_{vap} = 26 - 30 kJ mol^{-1}.

25. Data of Motkuri for adsorption of R12 and R22 in MIL-101(Cr)

Figures 51, and 52 present the analyses of the pure component isotherms for R12 (dichlorodifluoromethane, CCl_2F_2), and R22 (chlorodifluoromethane, $CHClF_2$) in MIL-101(Cr), as reported in the paper by Motkuri et al.[44] The Q_{st} values are higher than the corresponding latent heat of vaporization, ΔH_{vap}.

Figures 51c,d, and 52c,d show that both Equations (5) and (6) provide good estimates of the values of Q_{st}; the use of the Tóth potential appears to offer some improvement in the predictions of Q_{st}.

26. Data of Peng for adsorption of CFC-115 and HFC-125 in MFI and in Vruf Activated Carbon

Peng et al.[45] discuss the need for separation of CFC-115 (1-chloro-1,1,2,2,2-pentafluoroethane) and HFC-125 (1,1,1,2,2-pentafluoroethane). The boiling points of CFC-115 (234.1 K) and HFC-125 (224.7 K) are very close, and their mixtures can be nearly azeotropic. Therefore, cryogenic extractive distillation has been the dominant technology utilized to separate these mixtures. Adsorptive separations offer energy-efficient alternatives to distillation. Towards this end, Peng et al.[45] have reported the pure component isotherm data for CFC-115 and HFC-125 in MFI zeolite; see data in Figures 53, and 54.

Due to the presence of the bulky chloro-group at the 1-position, CFC-115 locates preferentially at the intersections of MFI, that provides the necessary leg-room. The pure component isotherm of CFC-115 shows a pronounced inflection at a loading of 4 molecules per unit cell. HFC-125 can locate can locate comfortably within the channels, and the pure component isotherms do not show any pronounced inflection characteristics.

Figures 53c,d and 54c,d show that both Equations (5) and (6) underestimate the values of Q_{st} to a significant extent.

Figures 55, and 56 present the corresponding analysis of the data for adsorption of CFC-115, and HFC-125 in Vruf Activated Carbon. There are no isotherm inflections for CFC-115, and the binding energies are significantly lower than the corresponding ones in MFI. As a consequence, both Equations (5) and (6) provide somewhat improved estimates, as compared with MFI, for the values of Q_{st}; see Figures 55c,d, and 56c,d.

27. Comparison of Q_{st} of a guest in different materials

In the foregoing sections, we have analyzed each guest/host combination separately. Let us now compare the values of Q_{st} values of a chosen guest in different materials; the data used for this comparison is the same as in the foregoing.

Figure 57 presents a comparison of the values of Q_{st} for adsorption of water in seven different zeolites. For all-silica zeolites such as DDR and MFI, the values of Q_{st} fall in the narrow range of 41 – 43 kJ mol^{-1}; consequently, the assumption $Q_{st} \approx \Delta H_{vap}$ holds. However, for cation-exchanged zeolites such as LTA-3A, LTA-4A, LTA-5A, and 13X zeolites, the binding energies are substantially higher and fall in the range 50 – 60 kJ mol^{-1} because water molecules experience strong coulombic interactions with the extra-framework cations. The highest value of Q_{st} is realized with CuBTC due to strong interactions of water molecules with the unsaturated Cu(II) atoms.

The stronger the binding between the guest molecule and the host material, the larger is the departure between the values of Q_{st} and ΔH_{vap}. This is exemplified by the comparisons in Figures 58, 59, 60, and 61 for the heats of adsorption of C_2H_2, C_3H_6, C_3H_8, and n-hexane in different host materials.

The strong attachment of unsaturated ethyne and propene with the Fe (II) atoms of FeMOF-74 leads to the largest departures between Q_{st} and ΔH_{vap}; see Figures 58, and 59.

For n-hexane, the value of Q_{st} is the highest within the triangular channels of $Fe_2(BDP)_3$; the values are about 35 kJ mol^{-1} higher than that of ΔH_{vap}; see Figure 61.

Figure 62 presents a comparison of the isosteric heats of adsorption of methanol in FER and Zn(bdc)dabco. In all-silica FER, the value of Q_{st} is only slightly higher than that value of ΔH_{vap}.

28. Conclusions

The following major conclusions can be drawn on the T-dependency of the pure component adsorption isotherms.

(1) For several guest/host combinations in which the isotherms are steep, the calculation of the Tóth potential $RT\ln\left((\Gamma_i - 1)\frac{p_i}{P_i^{sat}}\right)$ in Equation (6) ,using analytic differentiation of the dual-Langmuir-Freundlich fits, the leads to numerical difficulties for a range of loadings. For this reason, we have used Equation (8), that has a simplified procedure for determination of the thermodynamic correction factor.

(2) Equations (5) and (6) can be used to estimate values of Q_{st} values from one set of isotherm q_i vs p_i data at temperature T. In our calculations reported below, we determined this by applying the dual-Langmuir-Freundlich fits, equations (3), and (4) in reverse.

(3) The component loadings in the adsorbed phase at different temperatures are uniquely determined by (p_i/P_i^{sat}) in cases where the isosteric heats of adsorption are nearly equal to the values of the corresponding latent heats of vaporization, ΔH_{vap}. In general, this occurs when the interactions of the guest molecules with the framework are rather weak; this is the case, for example, for all-silica zeolites; see data for DDR, and MFI at the bottom of Figure 57.

(4) In cases where there are large departures between the values of Q_{st} and ΔH_{vap}, there is no unique relationship between the loadings q_i and (p_i/P_i^{sat}) for various temperatures. This is exemplified by the data for water in cation-exchanged zeolites such as 13 X, LTA-3A, LTA-4A, and LTA-5A; see data near the top of Figure 57.

(5) The stronger the binding between the guest molecule and the host material, the larger is the departure between the values of Q_{st} and ΔH_{vap}. This is exemplified by the comparisons in Figures 57, 58, 59, 60, 61, 62 and for the heats of adsorption of water, C_2H_2, C_3H_6, C_3H_8, n-hexane, and methanol in different host materials. The strong attachment of unsaturated ethyne and propene with the Fe (II) atoms of FeMOF-74 leads to the largest departures between Q_{st} and ΔH_{vap}. For n-hexane, the value of Q_{st} is the highest within the triangular channels of $Fe_2(BDP)_3$; the values are about 35 kJ mol^{-1} higher than that of ΔH_{vap}.

(6) For several guest/host combinations, the use of Equations (5) and (6) provide good, or reasonably good, estimates of the values of the isosteric heats of adsorption. Also, the use to the Tóth potential, in place of the Polanyi potential, appears to offer some improvement in the predictions of Q_{st}.

(7) The estimations using Equations (5) and (6) though significantly better than the assumption $Q_{st} \approx \Delta H_{vap}$, do not predict Q_{st} values of sufficient accuracy for all guest/host combinations. The development of improved estimation procedures for Q_{st} remains a fruitful area for further research.

29. Notation

b_A	dual-Langmuir-Freundlich constant for species *i* at adsorption site A, $Pa^{-\nu_i}$
b_B	dual-Langmuir-Freundlich constant for species *i* at adsorption site B, $Pa^{-\nu_i}$
ΔH_{vap}	enthalpy of vaporization, J $kmol^{-1}$
f_i	fugacity of species *i*, Pa
p_i	pressure of species *i*, Pa
P_i^{sat}	saturation vapor pressure of species i, Pa
q_i	molar loading of species *i*, mol kg^{-1}
Q_{st}	isosteric heat of adsorption, J $kmol^{-1}$
R	gas constant, 8.314 J mol^{-1} K^{-1}
T	absolute temperature, K

Greek letters

Γ_i	thermodynamic factor, dimensionless
ν	exponent in dual-Langmuir-Freundlich isotherm, dimensionless

Subscripts

i	referring to component *i*
t	referring to total mixture

Table 1. Enthalpy of vaporization of various molecules. These values are calculated using the Clausius-Clapeyron equation (2) along with the Antoine vapor pressure constants (for the appropriate temperature ranges) as reported in the NIST webbook: http://webbook.nist.gov/chemistry/

	ΔH_{vap} kJ mol^{-1}
water	42
methanol	37
ethanol	41
dimethylether	41
1-propanol	44.8
cyclohexane	31.6
benzene	32.2
p-xylene	40.3
ethylbenzene	40
toluene	36.3
ethyne	16.6
propane	19.1
propene	17.7
n-butane	22.8
iso-butane	21.5
1-butene	22.1
2-methylbutane	25.6
neopentane	22.7
n-hexane	30.5
R12	18.9
R22	19,8

Table 2. Dual-Langmuir-Freundlich fits of the isotherms of water in CuBTC. These fits are based on the experimental data from Zhao et al.[8], obtained at 288 K, 298 K, 308 K, and 318 K. Note that the fit parameters provided in Table 2 of their paper are incorrect. We have re-fitted the scanned experimental isotherm data of Zhao et al.[8]

	Site A				Site B			
	$q_{A,sat}$ mol kg^{-1}	b_{A0} Pa$^{-\nu_i}$	E_A kJ mol^{-1}	ν_A dimensionless	$q_{B,sat}$ mol kg^{-1}	b_{B0} Pa$^{-\nu_i}$	E_B kJ mol^{-1}	ν_B dimensionless
water	20	3.18×10^{-22}	99.6	1.6	60	4.16×10^{-60}	236	5

Table 3. Dual-Langmuir-Freundlich fits of the isotherms of water in LTA-4A zeolite. The isotherm fits are based on the experimental data of Gorbach et al.[9]

	Site A				Site B			
	$q_{A,sat}$ mol kg^{-1}	b_{A0} Pa$^{-\nu_i}$	E_A kJ mol^{-1}	ν_A dimensionless	$q_{B,sat}$ mol kg^{-1}	b_{B0} Pa$^{-\nu_i}$	E_B kJ mol^{-1}	ν_B dimensionless
water	3.9	1.85×10^{-21}	111	1.94	12	2.18×10^{-4}	18	0.32

Table 4. Dual-Langmuir-Freundlich fits of the isotherms of water in MFI (OH^-) zeolite. The isotherm fits are based on the experimental data of Zhang.[10]

	Site A				Site B			
	$q_{A,sat}$ mol kg^{-1}	b_{A0} Pa$^{-\nu_i}$	E_A kJ mol^{-1}	ν_A dimensionless	$q_{B,sat}$ mol kg^{-1}	b_{B0} Pa$^{-\nu_i}$	E_B kJ mol^{-1}	ν_B dimensionless
water	6	1.4×10^{-25}	96	2.2	1	2.46×10^{-13}	18	0.32

Table 5. Dual-Langmuir-Freundlich fits of the isotherms of water in MFI zeolite. The isotherm fits are based on the experimental data of Giaya and Thompson.[11]

	Site A				Site B			
	$q_{A,sat}$ mol kg^{-1}	b_{A0} Pa$^{-\nu_i}$	E_A kJ mol^{-1}	ν_A dimensionless	$q_{B,sat}$ mol kg^{-1}	b_{B0} Pa$^{-\nu_i}$	E_B kJ mol^{-1}	ν_B dimensionless
water	42	5.11×10^{-13}	42	1	0.45	4.8×10^{-10}	42	1

Table 6. Dual-Langmuir-Freundlich fits of the isotherms of water in LTA-3A zeolite. The isotherm fits are based on the experimental data from the Grace-Davison sales brochure, digitized and reported in the paper of Llano-Restrepo.[12]

	Site A				Site B			
	$q_{A,sat}$ mol kg^{-1}	b_{A0} Pa$^{-\nu_i}$	E_A kJ mol^{-1}	ν_A dimensionless	$q_{B,sat}$ mol kg^{-1}	b_{B0} Pa$^{-\nu_i}$	E_B kJ mol^{-1}	ν_B dimensionless
water	1.7	3.53×10^{-38}	200	3.3	10.3	2.72×10^{-6}	29	0.52

Table 7. Dual-Langmuir-Freundlich fits of the isotherms of water in DDR zeolite. The isotherm fits are based on the experimental data of den Exter.[13]

	Site A				Site B			
	$q_{A,sat}$ mol kg^{-1}	b_{A0} Pa$^{-\nu_i}$	E_A kJ mol^{-1}	ν_A dimensionless	$q_{B,sat}$ mol kg^{-1}	b_{B0} Pa$^{-\nu_i}$	E_B kJ mol^{-1}	ν_B dimensionless
water	0.14	2.0×10^{-9}	41	1	49	3.53×10^{-13}	41	1

Table 8. Dual-Langmuir-Freundlich fits of the isotherms of water in DDR zeolite. The isotherm fits are based on the CBMC simulations of Krishna and van Baten.[5]

	Site A				Site B			
	$q_{A,sat}$ mol kg^{-1}	b_{A0} Pa$^{-\nu_i}$	E_A kJ mol^{-1}	ν_A dimensionless	$q_{B,sat}$ mol kg^{-1}	b_{B0} Pa$^{-\nu_i}$	E_B kJ mol^{-1}	ν_B dimensionless
water	5.1	8.68×10^{-45}	165	4	3.1	3.57×10^{-12}	38	1

Table 9. Dual-Langmuir-Freundlich fits of the isotherms of water in 13X zeolite. The isotherm fits are based on the experimental data of Wang and LeVan[14]

	Site A				Site B			
	$q_{A,sat}$ mol kg^{-1}	b_{A0} Pa$^{-\nu_i}$	E_A kJ mol^{-1}	ν_A dimensionless	$q_{B,sat}$ mol kg^{-1}	b_{B0} Pa$^{-\nu_i}$	E_B kJ mol^{-1}	ν_B dimensionless
water	20	7.43×10^{-4}	11	0.26	8	4.14×10^{-9}	46	0.72

Table 10. Dual-Langmuir-Freundlich fits of the isotherms of water in LTA-5A zeolite. The isotherm fits are based on the experimental data of Wang and LeVan[14]

	Site A				Site B			
	$q_{A,sat}$ mol kg^{-1}	b_{A0} Pa$^{-\nu_i}$	E_A kJ mol^{-1}	ν_A dimensionless	$q_{B,sat}$ mol kg^{-1}	b_{B0} Pa$^{-\nu_i}$	E_B kJ mol^{-1}	ν_B dimensionless
water	28	9.72×10^{-4}	11	0.24	4.4	2.24×10^{-12}	63	1

Table 11. Dual-Langmuir-Freundlich fits of the isotherms of water, and ethanol in LTA-4A zeolite. The isotherm fits are based on the experimental data of Pera-Titus et al.[15]

	Site A				Site B			
	$q_{A,sat}$ mol kg^{-1}	b_{A0} Pa$^{-\nu_i}$	E_A kJ mol^{-1}	ν_A dimensionless	$q_{B,sat}$ mol kg^{-1}	b_{B0} Pa$^{-\nu_i}$	E_B kJ mol^{-1}	ν_B dimensionless
water	2.1	2.1×10^{-60}	269	7.26	9.7	5.81×10^{-8}	33	0.83
ethanol	1.85	5.24×10^{-13}	43.3	1.9	1.4	2.65×10^{-10}	40	1.7

Table 12. Dual-Langmuir fits of the isotherms of methanol in all-silica FER zeolite. CBMC simulation data of Hibbe et al.[17]

	Site A				Site B			
	$q_{A,sat}$ mol kg^{-1}	b_{A0} Pa$^{-\nu_i}$	E_A kJ mol^{-1}	ν_A dimensionless	$q_{B,sat}$ mol kg^{-1}	b_{B0} Pa$^{-\nu_i}$	E_B kJ mol^{-1}	ν_B dimensionless
methanol	1.3	3.31×10^{-9}	29.4	0.63	3	4.28×10^{-14}	49.3	1.3

Table 13. Dual-Langmuir fits of the isotherms of 1-propanol and toluene in DAY-55. The isotherm fits are based on the experimental data of Sakuth.[18]

	Site A				Site B			
	$q_{A,sat}$ mol kg^{-1}	b_{A0} Pa$^{-\nu_i}$	E_A kJ mol^{-1}	ν_A dimensionless	$q_{B,sat}$ mol kg^{-1}	b_{B0} Pa$^{-\nu_i}$	E_B kJ mol^{-1}	ν_B dimensionless
1-propanol	3.6	2.04×10^{-13}	60	1				
toluene	0.72	2×10^{-6}	80	1	1.28	1.64×10^{-14}	70	1

Table 14. Dual-Langmuir-Freundlich fits of the isotherms of dimethylether, n-hexane, ethanol, and methanol in Zn(bdc)dabco (= Zn(bdc)(dabco)$_{0.5}$). The isotherm fits are based on the experimental data of Lee et al.[19] and Li et al.[20]

	Site A				Site B			
	$q_{A,sat}$ mol kg^{-1}	b_{A0} Pa$^{-\nu_i}$	E_A kJ mol^{-1}	ν_A dimensionless	$q_{B,sat}$ mol kg^{-1}	b_{B0} Pa$^{-\nu_i}$	E_B kJ mol^{-1}	ν_B dimensionless
dimethylether	5.4	6.3×10^{-17}	55	1.84	5.1	4.6×10^{-8}	31	0.48
ethanol	8	2.17×10^{-31}	120	3.3	10	2.23×10^{-11}	50	0.32
methanol	16	3.73×10^{-48}	185	4.4	12.5	6.35×10^{-19}	41	1
n-hexane	0.84	1.34×10^{-12}	50	1	4	6.28×10^{-11}	50	1
cyclohexane	1.4	9.12×10^{-25}	113	1.7	1.5	8.73×10^{-11}	52	1.07

Table 15. Dual-Langmuir-Freundlich fits of the isotherms of isotherms for n-hexane in Zn(bdc)dabc using CBMC simulations from the work of Dubbeldam et al.[21, 22] and Krishna and van Baten [23, 24].

	Site A				Site B			
	$q_{A,sat}$ mol kg^{-1}	b_{A0} Pa$^{-\nu_i}$	E_A kJ mol^{-1}	ν_A dimensionless	$q_{B,sat}$ mol kg^{-1}	b_{B0} Pa$^{-\nu_i}$	E_B kJ mol^{-1}	ν_B dimensionless
n-hexane	2.1	6.53×10^{-11}	51	0.7	3.1	1.29×10^{-15}	82	1.45

Table 16. 1-site-Langmuir fits of the isotherms of methanol in MFI. The isotherm fits are based on the experimental data of [29].

	Site A			
	$q_{A,sat}$ mol kg^{-1}	b_{A0} Pa$^{-\nu_i}$	E_A kJ mol^{-1}	ν_A dimensionless
Methanol in MFI	4.5	2.8×10^{-11}	42	1

Table 17. Langmuir-Freundlich parameters for pure component isotherms for ethene, ethane, propene and propane in ZIF-8. The *T*-dependent parameters are obtained by fitting the combined sets of pure component isotherm data of Li et al.[30] and Böhme et al.[31] determined for a variety of temperatures in the range 303 K to 393 K.

	q_{sat} mol kg^{-1}	b_0 Pa$^{-\nu}$	E kJ mol^{-1}	ν dimensionless
ethene	12	9.37×10^{-11}	21.5	1.08
ethane	12	8.55×10^{-11}	23.2	1.08
propene	5.2	4.64×10^{-11}	33.9	1
propane	5.2	1.39×10^{-10}	31.3	1

Table 18. Dual-site Langmuir-Freundlich parameters for pure ethyne, propene, and propane isotherms in Fe_2(dobdc) obtained by re-fitting the experimental isotherms of Bloch et al.[32] measured at 318 K, 333 K, and 353 K.

	Site A				Site B			
	$q_{A,sat}$ mol kg^{-1}	b_{A0} Pa$^{-\nu_i}$	E_A kJ mol^{-1}	ν_A dimensionless	$q_{B,sat}$ mol kg^{-1}	b_{B0} Pa$^{-\nu_i}$	E_B kJ mol^{-1}	ν_B dimensionless
C_2H_2	4.8	2.42×10^{-12}	51.4	1.1	3.2	2.07×10^{-10}	33.4	0.89
C_3H_6	5.3	1.42×10^{-20}	97	1.76	1.7	1.29×10^{-10}	33	1.13
C_3H_8	2.1	5.95×10^{-12}	48	0.83	4.3	6.15×10^{-15}	53	1.63

Table 19. Dual-Langmuir-Freundlich parameter fits for MgMOF-74 (= Mg_2(dobdc) = CPO-27-Mg). The fits are based on the experimental data of He et al.[46], Bao et al.[47], Dietzel et al.[48] the parameter values are obtained by fitting all *three* data sets. The experimental isotherms of Bao et al.[47] were measured at 278 K, 298 K, and 318 K.

	Site A				Site B			
	$q_{A,sat}$ mol kg^{-1}	b_{A0} Pa$^{-\nu_i}$	E_A kJ mol^{-1}	ν_A dimensionless	$q_{B,sat}$ mol kg^{-1}	b_{B0} Pa$^{-\nu_i}$	E_B kJ mol^{-1}	ν_B dimensionless
C_2H_2	6.3	4.62×10^{-11}	41	1	8.4	8.43×10^{-11}	26	1
C_2H_4	3.1	2.15×10^{-12}	28	1.3	6.4	2.11×10^{-12}	45.2	1.07
C_2H_6	8.4	3.28×10^{-12}	34.5	1.2				
CH_4	11	7.48×10^{-10}	18.2	1	5	1.64×10^{-11}	18.2	1
C_3H_6	7.1	6.32×10^{-13}	55	1.04	1.7	2.17×10^{-14}	40	1.44
C_3H_8	1.9	2.22×10^{-11}	42	0.73	5.9	7.84×10^{-13}	42	1.41

Table 20. Dual-site Langmuir-Freundlich parameters for pure propene, and propane isotherms in NaX zeolite. The experimental data of Costa et al.[33] measured at 279 K, 293 K, and 308 K.

	Site A				Site B			
	$q_{A,sat}$ mol kg^{-1}	b_{A0} Pa$^{-\nu_i}$	E_A kJ mol^{-1}	ν_A dimensionless	$q_{B,sat}$ mol kg^{-1}	b_{B0} Pa$^{-\nu_i}$	E_B kJ mol^{-1}	ν_B dimensionless
C_3H_6	0.2	9.63×10^{-13}	29	1.4	2.5	1.25×10^{-6}	27.5	0.5
C_3H_8	1.6	2.3×10^{-16}	62	1.55	0.7	1.46×10^{-10}	37	0.8

Table 21. Dual-site Langmuir parameters for pure isobutene, and 1-butene isotherms in NaX zeolite. The experimental data of Granato et al.[34] measured at 333 K, 353 K, 373 K, and 393 K.

	Site A				Site B			
	$q_{A,sat}$ mol kg^{-1}	b_{A0} Pa$^{-\nu_i}$	E_A kJ mol^{-1}	ν_A dimensionless	$q_{B,sat}$ mol kg^{-1}	b_{B0} Pa$^{-\nu_i}$	E_B kJ mol^{-1}	ν_B dimensionless
isobutane	0.56	1.12×10^{-14}	58	1	1.9	4.11×10^{-12}	56	1
1-butane	0.92	3.46×10^{-13}	60	1	1.6	1.2×10^{-22}	37	1

Table 22. Dual-Langmuir-Freundlich fits of the isotherms of o-xylene, m-xylene, and p-xylene in AFI zeolite. These fits are based on the experimental data from Chiang et al.[35], obtained at temperatures of 303 K, 318 K, and 333 K.

	Site A				Site B			
	$q_{A,sat}$ mol kg^{-1}	b_{A0} Pa$^{-\nu_i}$	E_A kJ mol^{-1}	ν_A dimensionless	$q_{B,sat}$ mol kg^{-1}	b_{B0} Pa$^{-\nu_i}$	E_B kJ mol^{-1}	ν_B dimensionless
o-xylene	0.36	7.4×10^{-21}	113	1.3	0.51	2.2×10^{-3}	6	0.62
m-xylene	0.46	7×10^{-18}	93	1.83	0.47	4.72×10^{-12}	58	0.8
p-xylene	0.6	5.35×10^{-12}	63.5	1.1	0.66	9.77×10^{-11}	48	0.65

Table 23. Dual-Langmuir-Freundlich fits of the isotherms of benzene, toluene, p-xylene, and ethylbenzene in MFI zeolite. These fits are based on the experimental data from Lee et al.[36].

	Site A				Site B			
	$q_{A,sat}$ mol kg^{-1}	b_{A0} Pa$^{-\nu_i}$	E_A kJ mol^{-1}	ν_A dimensionless	$q_{B,sat}$ mol kg^{-1}	b_{B0} Pa$^{-\nu_i}$	E_B kJ mol^{-1}	ν_B dimensionless
benzene	0.69346	2×10^{-43}	187	3.4	0.69346	3.12×10^{-14}	69	1.5
toluene	0.69346	9.1×10^{-20}	95	2.8	0.6	6.32×10^{-21}	91	1.7
p-xylene	0.69346	2.18×10^{-16}	94	1.7	0.69346	5.42×10^{-63}	330	5
Ethyl benzene	0.26	1.99×10^{-38}	178	2.7	0.79	7.79×10^{-17}	84	1.6

Table 24. Dual-Langmuir fits of the pure component isotherms for iso-butane in MFI zeolite. Experimental data at 277 K, 308 K, and 353 K from Sun et al. [37] Experimental data at 303 K are from Zhu et al.[38]

	Site A				Site B			
	$q_{A,sat}$ mol kg^{-1}	b_{A0} Pa$^{-\nu_i}$	E_A kJ mol^{-1}	ν_A dimensionless	$q_{B,sat}$ mol kg^{-1}	b_{B0} Pa$^{-\nu_i}$	E_B kJ mol^{-1}	ν_B dimensionless
iC4	0.72	2.81×10^{-11}	51	1	1	1.52×10^{-14}	53	1

Table 25. Dual-Langmuir fits of the pure component isotherms for iso-butane in MFI zeolite. CBMC simulation data at 277 K, 300 K, 308 K, and 353 K from the works of [49-51].

	Site A				Site B			
	$q_{A,sat}$ mol kg^{-1}	b_{A0} Pa$^{-\nu_i}$	E_A kJ mol^{-1}	ν_A dimensionless	$q_{B,sat}$ mol kg^{-1}	b_{B0} Pa$^{-\nu_i}$	E_B kJ mol^{-1}	ν_B dimensionless
iC4	0.72	1.08×10^{-10}	47.4	1	1.07	5.72×10^{-14}	49.3	1

Table 26. Dual-Langmuir-Freundlich fits of the isotherms of n-hexane in MFI zeolite. These fits are based on the experimental data from Song and Rees.[40]

	Site A				Site B			
	$q_{A,sat}$ mol kg^{-1}	b_{A0} Pa$^{-\nu_i}$	E_A kJ mol^{-1}	ν_A dimensionless	$q_{B,sat}$ mol kg^{-1}	b_{B0} Pa$^{-\nu_i}$	E_B kJ mol^{-1}	ν_B dimensionless
nC6	0.69346	8.4×10^{-19}	96	1.44	0.69346	1.22×10^{-14}	84	1.3

Table 27. Dual-Langmuir fits of the isotherms of n-hexane in MFI zeolite. The data are based on CBMC simulations of Krishna and van Baten[23, 42], obtained at 300 K, 373 K, 398 K, and 433 K.

	Site A				Site B			
	$q_{A,sat}$ mol kg^{-1}	b_{A0} Pa$^{-\nu_i}$	E_A kJ mol^{-1}	ν_A dimensionless	$q_{B,sat}$ mol kg^{-1}	b_{B0} Pa$^{-\nu_i}$	E_B kJ mol^{-1}	ν_B dimensionless
nC6	0.69346	2.43×10^{-15}	81	1	0.69346	6.83×10^{-12}	67	1

Table 28. Dual-Langmuir-Freundlich fits of the isotherms of n-hexane in MgMOF-74. These fits are based on CBMC simulation data of Krishna and van Baten.[23]

	Site A				Site B			
	$q_{A,sat}$ mol kg^{-1}	b_{A0} Pa$^{-\nu_i}$	E_A kJ mol^{-1}	ν_A dimensionless	$q_{B,sat}$ mol kg^{-1}	b_{B0} Pa$^{-\nu_i}$	E_B kJ mol^{-1}	ν_B dimensionless
nC6	3.6	1.92×10^{-52}	308	5	1.2	1.48×10^{-9}	47	0.68

Table 29. Dual-Langmuir-Freundlich parameter fits for $Fe_2(BDP)_3$ based on the experimental data of Herm et al.[43] for isotherms at 403 K, 433 K, and 473 K.

	Site A				Site B			
	$q_{A,sat}$ mol kg^{-1}	b_{A0} Pa$^{-\nu_i}$	E_A kJ mol^{-1}	ν_A dimensionless	$q_{B,sat}$ mol kg^{-1}	b_{B0} Pa$^{-\nu_i}$	E_B kJ mol^{-1}	ν_B dimensionless
nC6	0.28	2.74×10^{-26}	111	3	1.17	8.86×10^{-13}	73	1.02
2MP	0.78	2.13×10^{-13}	76	1.1	0.63	5.61×10^{-17}	89	1.36
3MP	0.36	4.62×10^{-13}	76	1.1	1.07	1.34×10^{-16}	89	1.36
22DMB	0.53	1.33×10^{-32}	167	2.9	0.94	1.42×10^{-12}	67	1
23DMB	0.61	9.74×10^{-33}	167	2.9	0.92	1.49×10^{-12}	67	1

Table 30. Langmuir-Freundlich parameters for pure component isotherms for R12, and R22 in MIL-101(Cr). The *T*-dependent parameters are obtained by fitting the pure component isotherm data of Motkuri et al.[44] determined at 288 K, 298 K, and 308 K.

	q_{sat} mol kg^{-1}	b_0 Pa$^{-\nu}$	E kJ mol^{-1}	ν dimensionless
R12	17	1.62×10^{-13}	36.8	1.3
R22	27	3.9×10^{-9}	23.3	0.82

Table 31. Dual-site Langmuir-Freundlich parameters for isotherms of CFC-115, and HFC-125 in MFI zeolite and Vruf Activated Carbon. Fits of the experimental isotherm data in the paper of Peng et al.[45], measured at temperatures of 273 K, 298 K, 323 K, and 348 K.

	Site A				Site B			
	$q_{A,sat}$ mol kg^{-1}	b_{A0} Pa$^{-\nu_i}$	E_A kJ mol^{-1}	ν_A dimensionless	$q_{B,sat}$ mol kg^{-1}	b_{B0} Pa$^{-\nu_i}$	E_B kJ mol^{-1}	ν_B dimensionless
CFC-115/ MFI	1	1.86×10^{-15}	57	1.1	0.69346	1.2×10^{-10}	45	1
HFC-125/ MFI	0.2	5.85×10^{-38}	173	1.88	1.8	7.56×10^{-11}	40	1
CFC-115/ Vruf AC	5.2	9.5×10^{-8}	22	0.7	0.4	1.61×10^{-9}	39	0.82
HFC-125/ Vruf AC	6.4	3×10^{-8}	21.4	0.75	0.4	7.73×10^{-10}	39	0.8

Table 32. Dual-Langmuir-Freundlich parameter fits for CoMOF-74 (= Co_2(dobdc) = CPO-27-Co). The fits are based on the experimental data of He et al.[46], [52], along with those reported in the US patent of Matzger et al.[53]; the fitted parameters reported below are obtained by all *three* data sets.

	Site A				Site B			
	$q_{A,sat}$ mol kg^{-1}	b_{A0} Pa$^{-\nu_i}$	E_A kJ mol^{-1}	ν_A dimensionless	$q_{B,sat}$ mol kg^{-1}	b_{B0} Pa$^{-\nu_i}$	E_B kJ mol^{-1}	ν_B dimensionless
C_2H_2	5.7	1.42×10^{-11}	45	1	9	2×10^{-10}	23.6	1
C_2H_4	5.2	5.23×10^{-10}	19.5	1	6.3	3.16×10^{-11}	41	1
C_2H_6	7.5	2.11×10^{-12}	37	1.2				
CH_4	7	3.74×10^{-11}	24.7	1	12.7	4.15×10^{-10}	17.8	1
C_3H_6	4.9	7.18×10^{-13}	54	1.16	2.3	3.55×10^{-13}	56	0.5
C_3H_8	1.3	3.27×10^{-14}	47	1	4.8	3.97×10^{-12}	47	1

Table 33. Dual-site Langmuir-Freundlich parameters for propene and propane isotherms in Cu_3(btc)$_2$. Fits of the experimental isotherm data in the paper of Yoon et al.[54], measured at temperatures of 303 K, 313 K, 323 K, 333 K, and 353 K.

	Site A				Site B			
	$q_{A,sat}$ mol kg^{-1}	b_{A0} Pa$^{-\nu_i}$	E_A kJ mol^{-1}	ν_A dimensionless	$q_{B,sat}$ mol kg^{-1}	b_{B0} Pa$^{-\nu_i}$	E_B kJ mol^{-1}	ν_B dimensionless
C_3H_6	5.8	1.85×10^{-10}	37.3	0.95	3.25	3.64×10^{-14}	59	1.25
C_3H_8	4.9	1.06×10^{-7}	25	0.62	4.0	1.45×10^{-22}	75	2.43

Table 34. Dual-site Langmuir parameters for propene and propane isotherms in NaX zeolite at 298 K, and 318 K. The parameter fits are based on the experimental data of Lamia et al [55].

	Site A				Site B			
	$q_{A,sat}$ mol kg^{-1}	b_{A0} $Pa^{-\nu_i}$	E_A kJ mol^{-1}	ν_A dimensionless	$q_{B,sat}$ mol kg^{-1}	b_{B0} $Pa^{-\nu_i}$	E_B kJ mol^{-1}	ν_B dimensionless
C_3H_6	7.1	6.32×10^{-13}	55	1.04	1.7	2.17×10^{-14}	40	1.44
C_3H_8	1.9	2.22×10^{-11}	42	0.73	5.9	7.84×10^{-13}	42	1.41

30. References

(1) Whittaker, P. B.; Wang, X.; Regenauer-Lieb, K.; Chua, H. T. Predicting isosteric heats for gas adsorption, *Phys. Chem. Chem. Phys.* **2013**, *15*, 473-482.

(2) Tóth, J. Gas-(Dampf-) Adsorption an Festen Oberfläschen Inhomogener Aktivität, I., *Acta Chim. Acad. Sci. Hung.* **1962**, *30*, 415-430.

(3) Krishna, R.; van Baten, J. M. Investigating cluster formation in adsorption of CO_2, CH_4, and Ar in zeolites and metal organic frameworks at sub-critical temperatures, *Langmuir* **2010**, *26*, 3981-3992.

(4) Krishna, R.; van Baten, J. M. Highlighting a variety of unusual characteristics of adsorption and diffusion in microporous materials induced by clustering of guest molecules, *Langmuir* **2010**, *26*, 8450-8463.

(5) Krishna, R.; van Baten, J. M. Hydrogen bonding effects in adsorption of water-alcohol mixtures in zeolites and the consequences for the characteristics of the Maxwell-Stefan diffusivities, *Langmuir* **2010**, *26*, 10854-10867.

(6) Krishna, R.; van Baten, J. M. Investigating the Relative Influences of Molecular Dimensions and Binding Energies on Diffusivities of Guest Species Inside Nanoporous Crystalline Materials *J. Phys. Chem. C* **2012**, *116*, 23556-23568.

(7) Krishna, R.; van Baten, J. M. Influence of Adsorption Thermodynamics on Guest Diffusivities in Nanoporous Crystalline Materials, *Phys. Chem. Chem. Phys.* **2013**, *15*, 7994-8016.

(8) Zhao, Z.; Wang, S.; Yang, Y.; Li, X.; Li, J.; Li, Z. Competitive Adsorption and Selectivity of Benzene and Water Vapor on the Microporous Metal Organic Frameworks (HKUST-1), *Chem. Eng. J.* **2015**, *259*, 79-89.

(9) Gorbach, A.; Stegmaier, M.; Eigenberger, G. Measurement and Modeling of Water Vapor Adsorption on Zeolite 4A—Equilibria and Kinetics, *Adsorption* **2004**, *10*, 29-46.

(10) Zhang, K.; Lively, R. P.; Noel, J. D.; Dose, M. E.; McCool, B. A.; Chance, R. R.; Koros, W. J. Adsorption of Water and Ethanol in MFI-Type Zeolites, *Langmuir* **2012**, *28*, 8664-8673.

(11) Giaya, A.; Thompson, R. W. Single-component gas phase adsorption and desorption studies using a tapered element oscillating microbalance, *Microporous Mesoporous Mat.* **2002**, *55*, 265-274.

(12) Llano-Restrepo, M.; Mosquera, M. A. Accurate correlation, thermochemistry, and structural interpretation of equilibrium adsorption isotherms of water vapor in zeolite 3A by means of a generalized statistical thermodynamic adsorption model, *Fluid Phase Equilib.* **2009**, *283*, 73-88.

(13) den Exter, M. J.; Jansen, J. C.; van Bekkum, H. Synthesis and characterization of the all-silica 8-ring Clathrasil DD3R comparison of adsorption properties with the hydrophilic zeolite A, *Zeolites* **1997**, *19*, 353-358.

(14) Wang, Y.; LeVan, M. D. Adsorption Equilibrium of Carbon Dioxide and Water Vapor on Zeolites 5A and 13X and Silica Gel: Pure Components, *J. Chem. Eng. Data* **2009**, *54*, 2839-2844.

(15) Pera-Titus, M.; Fité, C.; Sebastián, V.; Lorente, E.; Llorens, J.; Cunill, F. Modeling Pervaporation of Ethanol/Water Mixtures within 'Real' Zeolite NaA Membranes, *Ind. Eng. Chem. Res.* **2008**, *47*, 3213-3224.

(16) Leppäjärvi, T.; Kangas, J.; Malinen, I.; Tanskanen, J. Mixture adsorption on zeolites applying the P_i^{sat} temperature-dependency approach, *Chem. Eng. Sci.* **2013**, *89*, 89-101.

(17) Hibbe, F.; Van Baten, J. M.; Krishna, R.; Chmelik, C.; Weitkamp, J.; Kärger, J. In-Depth Study of Mass Transfer in Nanoporous Materials by Micro-Imaging, *Chem. Ing. Tech.* **2011**, *83*, 2211-2218.

(18) Sakuth, M.; Meyer, J.; Gmehling, J. Vapor Phase Adsorption Equilibria of Toluene + 1-Propanol Mixtures on Y-Zeolites with Different Silicon to Aluminum Ratios, *J. Chem. Eng. Data* **1995**, *40*, 895-899.

(19) Lee, J. Y.; Olson, D. H.; Pan, L.; Emge, T. J.; Li, J. Microporous Metal–Organic Frameworks with High Gas Sorption and Separation Capacity, *Adv. Funct. Mater.* **2007**, *17*, 1255-1262.

(20) Li, K.; Lee, J. Y.; Olson, D. H.; Enge, T. J.; Bi, W.; Eibling, M. J.; Li, J. Unique gas and hydrocarbon adsorption in a highly porous metal-organic framework made of extended aliphatic ligands, *Chem. Commun.* **2008**, 6123-6125.

(21) Dubbeldam, D.; Krishna, R.; Calero, S.; Yazaydın, A. Ö. Computer-Assisted Screening of Ordered Crystalline Nanoporous Adsorbents for Separation of Alkane Isomers, *Angew. Chem. Int. Ed.* **2012**, *51*, 11867-11871.

(22) Dubbeldam, D.; Galvin, C. J.; Walton, K. S.; Ellis, D. E.; Snurr, R. Q. Separation and Molecular-Level Segregation of Complex Alkane Mixtures in Metal-Organic Frameworks, *J. Am. Chem. Soc.* **2008**, *130*, 10884-10885.

(23) Krishna, R.; van Baten, J. M. In silico screening of metal-organic frameworks in separation applications, *Phys. Chem. Chem. Phys.* **2011**, *13*, 10593-10616.

(24) Krishna, R.; van Baten, J. M. A molecular simulation study of commensurate – incommensurate adsorption of n-alkanes in cobalt formate frameworks, *Molecular Simulation* **2009**, *35*, 1098-1104.

(25) Bárcia, P. S.; Zapata, F.; Silva, J. A. C.; Rodrigues, A. E.; Chen, B. Kinetic Separation of Hexane Isomers by Fixed-Bed Adsorption with a Microporous Metal-Organic Framework, *J. Phys. Chem. B* **2007**, *111*, 6101-6103.

(26) Chen, Z.; Xiang, S.; Zhao, D.; Chen, B. Reversible Two-Dimensional-Three Dimensional Framework Transformation within a Prototype Metal-Organic Framework, *Cryst. Growth Des.* **2009**, *9*, 5293-5296.

(27) Li, H.; Eddaoudi, M.; Groy, T. L.; Yaghi, O. Establishing Microporosity in Open Metal-Organic Frameworks: Gas Sorption Isotherms for Zn(BDC) (BDC = 1,4-Benzenedicarboxylate), *J. Am. Chem. Soc.* **1998**, *120*, 8571-8572.

(28) Eddaoudi, M.; Li, H.; Yaghi, O. Highly Porous and Stable Metal-Organic Frameworks: Structure Design and Sorption Properties, *J. Am. Chem. Soc.* **2000**, *122*, 1391-1397.

(29) Nayak, V. S.; Moffat, J. B. Sorption and Diffusion of Alcohols in Heteropoly Oxometalates and ZSM-5 Zeolite, *J. Phys. Chem.* **1988**, *92*, 7097-7102.

(30) Li, K.; Olson, D. H.; Seidel, J.; Emge, T. J.; Gong, H.; Zeng, H.; Li, J. Zeolitic Imidazolate Frameworks for Kinetic Separation of Propane and Propene, *J. Am. Chem. Soc.* **2009**, *131*, 10368-10369.

(31) Böhme, U.; Barth, B.; Paula, C.; Kuhnt, A.; Schwieger, W.; Alexander Mundstock, A.; Caro, J.; Hartmann, M. Ethene/Ethane and Propene/Propane Separation via the Olefin and Paraffin Selective Metal−Organic Framework Adsorbents CPO-27 and ZIF8, *Langmuir* **2013**, *29*, 8592-8600.

(32) Bloch, E. D.; Queen, W. L.; Krishna, R.; Zadrozny, J. M.; Brown, C. M.; Long, J. R. Hydrocarbon Separations in a Metal-Organic Framework with Open Iron(II) Coordination Sites, *Science* **2012**, *335*, 1606-1610.

(33) Costa, E.; Calleja, G.; Jimenez, A.; Pau, J. Adsorption Equilibrium of Ethylene, Propane, Propylene, Carbon Dioxide, and Their Mixtures on 13X Zeolite, *J. Chem. Eng. Data* **1991**, *36*, 218-224.

(34) Granato, M. A.; Lamia, N.; Vlugt, T. J. H.; Rodrigues, A. E. Adsorption Equilibrium of Isobutane and 1-Butene in Zeolite 13X by Molecular Simulation, *Ind. Eng. Chem. Res.* **2008**, *47*, 6166-6174.

(35) Chiang, A. S. T.; Lee, C.-K.; Chang, Z.-H. Adsorption and diffusion of aromatics in $AlPO_4$-5, *Zeolites* **1991**, 380-386.

(36) Lee, C. K.; Chiang, A. S. T. Adsorption of aromatic compounds in large MFI zeolite crystals, *J. Chem. Soc. - Faraday Trans.* **1996**, *92*, 3445-3451.

(37) Sun, M. S.; Shah, D. B.; Xu, H. H.; Talu, O. Adsorption equilibria of C_1 to C_4 alkanes, CO_2, and SF_6 on silicalite, *J. Phys. Chem. B* **1998**, *102*, 1466-1473.

(38) Zhu, W.; Kapteijn, F.; Moulijn, J. A. Adsorption of light alkanes on silicalite-1: Reconciliation of experimental data and molecular simulations, *Phys. Chem. Chem. Phys.* **2000**, *2*, 1989-1995.

(39) Titze, T.; Chmelik, C.; Kärger, J.; van Baten, J. M.; Krishna, R. Uncommon Synergy Between Adsorption and Diffusion of Hexane Isomer Mixtures in MFI Zeolite Induced by Configurational Entropy Effects *J. Phys. Chem. C* **2014**, *116*, 2660-2665.

(40) Song, L.; Rees, L. V. C. Adsorption and transport of n-hexane in siliaclite-1 by the frequency response technique, *J. Chem. Soc.-Faraday Trans.* **1997**, *93*, 649-657.

(41) Vlugt, T. J. H.; Krishna, R.; Smit, B. Molecular Simulations of Adsorption Isotherms for Linear and Branched Alkanes and Their Mixtures in Silicalite, *J. Phys. Chem. B* **1999**, *103*, 1102-1118.

(42) Krishna, R.; van Baten, J. M. Using molecular simulations for screening of zeolites for separation of CO_2/CH_4 mixtures, *Chem. Eng. J.* **2007**, *133*, 121-131.

(43) Herm, Z. R.; Wiers, B. M.; Van Baten, J. M.; Hudson, M. R.; Zajdel, P.; Brown, C. M.; Maschiocchi, N.; Krishna, R.; Long, J. R. Separation of Hexane Isomers in a Metal-Organic Framework with Triangular Channels *Science* **2013**, *340*, 960-964.

(44) Motkuri, R. K.; Annapureddy, H. V. R.; Vijaykumar, M.; Schaef, T.; Martin, P. F.; McGrail, B. P.; Dang, L. X.; Krishna, R.; Thallapally, P. K. Fluorocarbon Adsorption in Hierarchical Porous Frameworkss, *Nat. Commun.* **2014**, *5*, 4368. http://dx.doi.org/doi:10.1038/ncomms5368.

(45) Peng, Y.; Zhang, Z.; Zheng, X.; Wang, H.; Xu, C.; Xiao, Q.; Zhong, Y.; Zhu, W. Comparison Study on the Adsorption of CFC-115 and HFC-125 on Activated Carbon and Silicalite-1, *Ind. Eng. Chem. Res.* **2010**, *49*, 10009-10015.

(46) He, Y.; Krishna, R.; Chen, B. Metal-Organic Frameworks with Potential for Energy-Efficient Adsorptive Separation of Light Hydrocarbons, *Energy Environ. Sci.* **2012**, *5*, 9107-9120.

(47) Bao, Z.; Alnemrat, S.; Vasiliev, I.; Ren, Q.; Yu, L.; Lu, X.; Deng, S. Adsorption of Ethane, Ethylene, Propane and Propylene on a Magnesium-Based Metal-Organic Framework, *Langmuir* **2011**, *27*, 13554-13562.

(48) Dietzel, P. D. C.; Besikiotis, V.; Blom, R. Application of metal–organic frameworks with coordinatively unsaturated metal sites in storage and separation of methane and carbon dioxide, *J. Mater. Chem.* **2009**, *19*, 7362-7370.

(49) Krishna, R.; van Baten, J. M. Insights into diffusion of gases in zeolites gained from molecular dynamics simulations, *Microporous Mesoporous Mater.* **2008**, *109*, 91-108.

(50) Krishna, R.; van Baten, J. M. Onsager coefficients for binary mixture diffusion in nanopores, *Chem. Eng. Sci.* **2008**, *63*, 3120-3140.

(51) Chmelik, C.; Heinke, L.; Kärger, J.; Shah, D. B.; Schmidt, W.; van Baten, J. M.; Krishna, R. Inflection in the Loading Dependence of the Maxwell-Stefan Diffusivity of Iso-butane in MFI Zeolite, *Chem. Phys. Lett.* **2008**, *459*, 141-145.

(52) Bae, Y.-S.; Lee, C. Y.; Kim, K. C.; Farha, O. K.; Nickias, P.; Hupp, J. T.; Nguyen, S. T.; Snurr, R. Q. High Propene/Propane Selectivity in Isostructural Metal–Organic Frameworks with High Densities of Open Metal Sites, *Angew. Chem. Int. Ed.* **2012**, *51*, 1857-1860.

(53) Matzger, A. J.; Wong-Foy, A. G.; Caskey, G., Microporous coordination polymers as novel sorbents for gas separaration, The Regents of the University of Michigan, *U.S. Pat.*, US 2010/0258004 A1, 2010.

(54) Yoon, J. W.; Jang, I. T.; Lee, K.-Y.; Hwang, Y. K.; Chang, J.-S. Adsorptive Separation of Propylene and Propane on a Porous Metal-Organic Framework, Copper Trimesate, *Bull. Korean Chem. Soc.* **2010**, *31*, 220-223.

(55) Lamia, N.; Granato, M. A.; Gomes, P. S. A.; Grande, C. A.; Wolff, L.; Leflaive, P.; Leinekugel-le-Cocq, D.; Rodrigues, A. E. Propane/Propylene Separation by Simulated Moving Bed II. Measurement and Prediction of Binary Adsorption Equilibria of Propane, Propylene, Isobutane, and 1-Butene on 13X Zeolite, *Separ. Sci. Technol.* **2009**, *44*, 1485-1509.

(56) Chmelik, C.; Kärger, J.; Wiebcke, M.; Caro, J.; van Baten, J. M.; Krishna, R. Adsorption and Diffusion of Alkanes in CuBTC Crystals Investigated Using Infrared Microscopy and Molecular Simulations, *Microporous Mesoporous Mater.* **2009**, *117*, 22-32.

31. Captions for Figures

Figure 1. Calculations of the thermodynamic factor for water/CuBTC (isotherm data in Table 2), water/MFI(OH-) (isotherm data in Table 4), and water/DDR (isotherm data in Table 8).

Figure 2. (a) Pure component isotherms for water in CuBTC. Experimental data of Zhao et al.[8] The continuous solid lines are isotherm fits with dual-site Langmuir-Freundlich parameters provided in Table 2. (b) Plot of component loadings vs. (p_i/P_i^{sat}) at a variety of temperatures. (c, d) Comparison of Q_{st} with estimations of Q_{st} using Equations (5) and (6).

Figure 3. (a) Pure component isotherms for water in LTA-4A zeolite. Experimental data of Gorbach[9]. The continuous solid lines are isotherm fits with dual-site Langmuir-Freundlich parameters provided in Table 3. (b) Plot of component loadings vs. (p_i/P_i^{sat}) at a variety of temperatures. (c, d) Comparison of Q_{st} with estimations of Q_{st} using Equations (5) and (6).

Figure 4. (a) Pure component isotherms for water in MFI (OH^-) zeolite. Experimental data of Zhang[10]. The continuous solid lines are isotherm fits with dual-site Langmuir-Freundlich parameters provided in Table 4. (b) Plot of component loadings vs. (p_i/P_i^{sat}) at a variety of temperatures. (c, d) Comparison of Q_{st} with estimations of Q_{st} using Equations (5) and (6).

Figure 5. (a) Pure component isotherms for water in MFI zeolite. Experimental data of Giaya[11]. The continuous solid lines are isotherm fits with dual-site Langmuir-Freundlich parameters provided in Table 5. (b) Plot of component loadings vs. (p_i/P_i^{sat}) at a variety of temperatures. (c, d) Comparison of Q_{st} with estimations of Q_{st} using Equations (5) and (6).

Figure 6. (a) Pure component isotherms for water in LTA-3A zeolite. Experimental data from the Grace-Davison sales brochure, digitized and reported in the paper of Llano-Restrepo[12]. The continuous solid lines are isotherm fits with dual-site Langmuir-Freundlich parameters provided in Table 6. (b) Plot of component loadings vs. (p_i/P_i^{sat}) at a variety of temperatures. (c, d) Comparison of Q_{st} with estimations of Q_{st} using Equations (5) and (6).

Figure 7. (a) Pure component isotherms for water in DDR zeolite. Experimental data of de Exter[13]. The continuous solid lines are isotherm fits with dual-site Langmuir-Freundlich parameters provided in Table 7. (b) Plot of component loadings vs. (p_i/P_i^{sat}) at a variety of temperatures. (c, d) Comparison of Q_{st} with estimations of Q_{st} using Equations (5) and (6).

Figure 8. (a) Configurational-Bias Monte Carlo (CBMC) simulations of the pure component isotherms for water in DDR zeolite at 300 K and 360 K; these CBMC simulations are from Krishna and van Baten.[5] The continuous solid lines are isotherm fits with dual-site Langmuir-Freundlich parameters provided in Table 8. (b) Plot of component loadings vs. (p_i/P_i^{sat}) at a variety of temperatures. (c, d) Comparison of Q_{st} with estimations of Q_{st} using Equations (5) and (6).

Figure 9. (a) Pure component isotherms for water in 13X zeolite. Experimental data of Wang and LeVan.[14] The continuous solid lines are isotherm fits with dual-site Langmuir-Freundlich parameters

provided in Table 9. (b) Plot of component loadings vs. (p_i/P_i^{sat}) at a variety of temperatures. (c, d) Comparison of Q_{st} with estimations of Q_{st} using Equations (5) and (6).

Figure 10. (a) Pure component isotherms for water in LTA-5A zeolite. Experimental data of Wang and LeVan[14]. The continuous solid lines are isotherm fits with dual-site Langmuir-Freundlich parameters provided in Table 10. (b) Plot of component loadings vs. (p_i/P_i^{sat}) at a variety of temperatures. (c, d) Comparison of Q_{st} with estimations of Q_{st} using Equations (5) and (6).

Figure 11. (a) Pure component isotherms for water in LTA-4A zeolite. Experimental data of Pera-Titus[15]. The continuous solid lines are isotherm fits with dual-site Langmuir-Freundlich parameters provided in Table 11. (b) Plot of component loadings vs. (p_i/P_i^{sat}) at a variety of temperatures. (c) Comparison of Q_{st} with ΔH_{vap}.

Figure 12. (a) Pure component isotherms for ethanol in LTA-4A zeolite. Experimental data of Pera-Titus[15]. The continuous solid lines are isotherm fits with dual-site Langmuir-Freundlich parameters provided in 11. (b) Plot of component loadings vs. (p_i/P_i^{sat}) at a variety of temperatures. (c) Comparison of Q_{st} with ΔH_{vap}.

Figure 13. Comparison of the experimental loadings for water and ethanol in LTA-4A zeolite at 2.1 kPa and 333 K as a function of the mole fraciion of water in the bulk vapor phase. The continuous solid lines are the IAST calculations using the pure component isotherm fits provided in Table 11.

Figure 14. (a) Pure component isotherms for methanol in all-silica FER zeolite. CBMC simulation data of Hibbe et al.[17]. The continuous solid lines are isotherm fits with dual-site Langmuir-Freundlich parameters provided in Table 12. (b) Plot of component loadings vs. (p_i/P_i^{sat}) at a variety of temperatures. (c, d) Comparison of Q_{st} with estimations of Q_{st} using Equations (5) and (6).

Figure 15. (a) Pure component isotherms for 1-propanol in DAY-55. Experimental data from Sakuth[18]. The continuous solid lines are isotherm fits with dual-site Langmuir-Freundlich parameters provided in Table 13. (b) Plot of component loadings vs. (p_i/P_i^{sat}) at a variety of temperatures. (c, d) Comparison of Q_{st} with estimations of Q_{st} using Equations (5) and (6).

Figure 16. (a) Pure component isotherms for toluene in DAY-55. Experimental data from Sakuth[18]. The continuous solid lines are isotherm fits with dual-site Langmuir-Freundlich parameters provided in Table 13. (b) Plot of component loadings vs. (p_i/P_i^{sat}) at a variety of temperatures. (c, d) Comparison of Q_{st} with estimations of Q_{st} using Equations (5) and (6).

Figure 17. (a) Pure component isotherms for dimethylether in Zn(bdc)dabco. Experimental data from Lee[19]. The continuous solid lines are isotherm fits with dual-site Langmuir-Freundlich parameters provided in Table 14. (b) Plot of component loadings vs. (p_i/P_i^{sat}) at a variety of temperatures. (c, d) Comparison of Q_{st} with estimations of Q_{st} using Equations (5) and (6).

Figure 18. (a) Pure component isotherms for ethanol in Zn(bdc)dabco. Experimental data from Lee[19]. The continuous solid lines are isotherm fits with dual-site Langmuir-Freundlich parameters provided in Table 14. (b) Plot of component loadings vs. (p_i/P_i^{sat}) at a variety of temperatures(c, d) Comparison of Q_{st} with estimations of Q_{st} using Equations (5) and (6).

Figure 19. (a) Pure component isotherms for methanol in Zn(bdc)dabco. Experimental data from Lee [19]. The continuous solid lines are isotherm fits with dual-site Langmuir-Freundlich parameters provided in Table 14. (b) Plot of component loadings vs. (p_i/P_i^{sat}) at a variety of temperatures. (c, d) Comparison of Q_{st} with estimations of Q_{st} using Equations (5) and (6).

Figure 20. (a) Pure component isotherms for cyclohexane in Zn(bdc)dabco. Experimental data from Li[20]. The continuous solid lines are isotherm fits with dual-site Langmuir-Freundlich parameters provided in Table 14. (b) Plot of component loadings vs. (p_i/P_i^{sat}) at a variety of temperatures. (c, d) Comparison of Q_{st} with estimations of Q_{st} using Equations (5) and (6).

Figure 21. (a) Pure component isotherms for n-hexane in Zn(bdc)dabco. Experimental data from Lee [19]. The continuous solid lines are isotherm fits with dual-site Langmuir-Freundlich parameters provided in Table 14. (b) Plot of component loadings vs. (p_i/P_i^{sat}) at a variety of temperatures. (c, d) Comparison of Q_{st} with estimations of Q_{st} using Equations (5) and (6).

Figure 22. (a) Pure component isotherms for n-hexane in Zn(bdc)dabco. CBMC simulations from the work of Dubbeldam et al.[21, 22] and Krishna and van Baten [23, 24]. The continuous solid lines are isotherm

fits with dual-site Langmuir-Freundlich parameters provided in Table 15. (b) Plot of component loadings vs. (p_i/P_i^{sat}) at a variety of temperatures. (c, d) Comparison of Q_{st} with estimations of Q_{st} using Equations (5) and (6).

Figure 23. (a) Pure component isotherms for methanol in MFI (Si/Al=990). Experimental data from Nayak and Moffat. [29] The continuous solid lines are isotherm fits with dual-site Langmuir-Freundlich parameters provided in Table 16. (b) Plot of component loadings vs. (p_i/P_i^{sat}) at a variety of temperatures. (c, d) Comparison of Q_{st} with estimations of Q_{st} using Equations (5) and (6).

Figure 24. (a) Pure component isotherms for propene in ZIF-8. The experimental data are from Li et al.[30] and Böhme et al.[31] determined for a variety of temperatures in the range 303 K to 393 K. The continuous solid lines are isotherm fits with dual-site Langmuir-Freundlich parameters provided in Table 17. (b) Plot of component loadings vs. (p_i/P_i^{sat}) at a variety of temperatures. (c, d) Comparison of Q_{st} with estimations of Q_{st} using Equations (5) and (6).

Figure 25. (a) Pure component isotherms for propane in ZIF-8. The experimental data are from Li et al.[30] and Böhme et al.[31] determined for a variety of temperatures in the range 303 K to 393 K. The continuous solid lines are isotherm fits with dual-site Langmuir-Freundlich parameters provided in Table 17. (b) Plot of component loadings vs. (p_i/P_i^{sat}) at a variety of temperatures. (c, d) Comparison of Q_{st} with estimations of Q_{st} using Equations (5) and (6).

Figure 26. (a) Pure component isotherms for ethyne in FeMOF-74. The experimental data of Bloch et al.[32] measured at 318 K, 333 K, and 353 K. The continuous solid lines are isotherm fits with dual-site

Langmuir-Freundlich parameters provided in Table 18. (b) Plot of component loadings vs. (p_i/P_i^{sat}) at a variety of temperatures. (c, d) Comparison of Q_{st} with estimations of Q_{st} using Equations (5) and (6).

Figure 27. (a) Pure component isotherms for propene in FeMOF-74. The experimental data of Bloch et al.[32] measured at 318 K, 333 K, and 353 K. The continuous solid lines are isotherm fits with dual-site Langmuir-Freundlich parameters provided in Table 18. (b) Plot of component loadings vs. (p_i/P_i^{sat}) at a variety of temperatures. (c, d) Comparison of Q_{st} with estimations of Q_{st} using Equations (5) and (6).

Figure 28. (a) Pure component isotherms for propane in FeMOF-74. The experimental data of Bloch et al.[32] measured at 318 K, 333 K, and 353 K. The continuous solid lines are isotherm fits with dual-site Langmuir-Freundlich parameters provided in Table 18. (b) Plot of component loadings vs. (p_i/P_i^{sat}) at a variety of temperatures. (c, d) Comparison of Q_{st} with estimations of Q_{st} using Equations (5) and (6).

Figure 29.(a) Pure component isotherms for ethyne in MgMOF-74. The experimental data of He et al.[46] measured at 273 K, and 296 K. The continuous solid lines are isotherm fits with dual-site Langmuir-Freundlich parameters provided in Table 19. (b) Plot of component loadings vs. (p_i/P_i^{sat}) at a variety of temperatures. (c, d) Comparison of Q_{st} with estimations of Q_{st} using Equations (5) and (6).

Figure 30. (a) Pure component isotherms for propene in MgMOF-74. The experimental data of Bao et al.[47] measured at 278 K, 298 K, and 318 K. The continuous solid lines are isotherm fits with dual-site Langmuir-Freundlich parameters provided in Table 19. (b) Plot of component loadings vs. (p_i/P_i^{sat}) at a variety of temperatures. (c, d) Comparison of Q_{st} with estimations of Q_{st} using Equations (5) and (6).

Figure 31. (a) Pure component isotherms for propane in MgMOF-74. The experimental data of Bao et al.[47] measured at 278 K, 298 K, and 318 K. The continuous solid lines are isotherm fits with dual-site Langmuir-Freundlich parameters provided in Table 19. (b) Plot of component loadings vs. (p_i/P_i^{sat}) at a variety of temperatures. (c, d) Comparison of Q_{st} with estimations of Q_{st} using Equations (5) and (6).

Figure 32. (a) Pure component isotherms for propene in NaX zeolite. The experimental data of Costa et al.[33] measured at 279 K, 293 K, and 308 K. The continuous solid lines are isotherm fits with dual-site Langmuir-Freundlich parameters provided in Table 20. (b) Plot of component loadings vs. (p_i/P_i^{sat}) at a variety of temperatures. (c, d) Comparison of Q_{st} with estimations of Q_{st} using Equations (5) and (6).

Figure 33. (a) Pure component isotherms for propane in NaX zeolite. The experimental data of Costa et al.[33] measured at 279 K, 293 K, and 308 K. The continuous solid lines are isotherm fits with dual-site Langmuir-Freundlich parameters provided in Table 20. (b) Plot of component loadings vs. (p_i/P_i^{sat}) at a variety of temperatures. (c, d) Comparison of Q_{st} with estimations of Q_{st} using Equations (5) and (6).

Figure 34. (a) Pure component isotherms for isobutane in NaX zeolite. The experimental data of Granato et al.[34] measured at 333 K, 353 K, 373 K, and 393 K. The continuous solid lines are isotherm fits with dual-site Langmuir-Freundlich parameters provided in Table 21. (b) Plot of component loadings vs. (p_i/P_i^{sat}) at a variety of temperatures. (c, d) Comparison of Q_{st} with estimations of Q_{st} using Equations (5) and (6).

Figure 35.(a) Pure component isotherms for 1-butene in NaX zeolite. The experimental data of Granato et al.[34] measured at 333 K, 353 K, 373 K, and 393 K. The continuous solid lines are isotherm fits with dual-site Langmuir-Freundlich parameters provided in Table 21. (b) Plot of component loadings vs.

(p_i/P_i^{sat}) at a variety of temperatures. (c, d) Comparison of Q_{st} with estimations of Q_{st} using Equations (5) and (6).

Figure 36. (a) Pure component isotherms for o-xylene in AFI zeolite. Experimental data from Chiang et al.[35] The continuous solid lines are isotherm fits with dual-site Langmuir-Freundlich parameters provided in Table 22. (b) Plot of component loadings vs. (p_i/P_i^{sat}) at a variety of temperatures. (c, d) Comparison of Q_{st} with estimations of Q_{st} using Equations (5) and (6).

Figure 37. (a) Pure component isotherms for m-xylene in AFI zeolite. Experimental data from Chiang et al.[35] The continuous solid lines are isotherm fits with dual-site Langmuir-Freundlich parameters provided in Table 22. (b) Plot of component loadings vs. (p_i/P_i^{sat}) at a variety of temperatures. (c, d) Comparison of Q_{st} with estimations of Q_{st} using Equations (5) and (6).

Figure 38. (a) Pure component isotherms for p-xylene in AFI zeolite. Experimental data from Chiang et al.[35] The continuous solid lines are isotherm fits with dual-site Langmuir-Freundlich parameters provided in Table 22. (b) Plot of component loadings vs. (p_i/P_i^{sat}) at a variety of temperatures. (c, d) Comparison of Q_{st} with estimations of Q_{st} using Equations (5) and (6).

Figure 39. Isosteric heats of adsorption of xylene isomers in AFI zeolite. These values are calculated using the Clausius-Clapeyron equations along with the *T*-dependent isotherm fit parameters provided in Table 22.

Figure 40. (a) Pure component isotherms for benzene in MFI zeolite. Experimental data from Lee.[36] The continuous solid lines are isotherm fits with dual-site Langmuir-Freundlich parameters provided in Table 23. (b) Plot of component loadings vs. (p_i/P_i^{sat}) at a variety of temperatures. (c, d) Comparison of Q_{st} with estimations of Q_{st} using Equations (5) and (6).

Figure 41. (a) Pure component isotherms for toluene in MFI zeolite. Experimental data from Lee.[36] The continuous solid lines are isotherm fits with dual-site Langmuir-Freundlich parameters provided in Table 23. (b) Plot of component loadings vs. (p_i/P_i^{sat}) at a variety of temperatures. (c, d) Comparison of Q_{st} with estimations of Q_{st} using Equations (5) and (6).

Figure 42. (a) Pure component isotherms for p-xylene in MFI zeolite. Experimental data from Lee.[36] The continuous solid lines are isotherm fits with dual-site Langmuir-Freundlich parameters provided in Table 23. (b) Plot of component loadings vs. (p_i/P_i^{sat}) at a variety of temperatures. (c, d) Comparison of Q_{st} with estimations of Q_{st} using Equations (5) and (6).

Figure 43. (a) Pure component isotherms for ethylbenzene in MFI zeolite. Experimental data from Lee.[36] The continuous solid lines are isotherm fits with dual-site Langmuir-Freundlich parameters provided in Table 23. (b) Plot of component loadings vs. (p_i/P_i^{sat}) at a variety of temperatures. (c, d) Comparison of Q_{st} with estimations of Q_{st} using Equations (5) and (6).

Figure 44. (a) Pure component isotherms for iso-butane in MFI zeolite. Experimental data at 277 K, 308 K, and 353 K from Sun et al.[37]. Experimental data at 303 K are from Zhu et al.[38] The continuous solid lines are isotherm fits with dual-site Langmuir-Freundlich parameters provided in Table 24. (b)

Plot of component loadings vs. (p_i/P_i^{sat}) at a variety of temperatures. (c, d) Comparison of Q_{st} with estimations of Q_{st} using Equations (5) and (6).

Figure 45. (a) Pure component isotherms for iso-butane in MFI zeolite. CBMC simulations at 277 K, 300 K, 308 K, and 353 K from Krishna.[49-51] The continuous solid lines are isotherm fits with dual-site Langmuir-Freundlich parameters provided in Table 25. (b) Plot of component loadings vs. (p_i/P_i^{sat}) at a variety of temperatures. (c, d) Comparison of Q_{st} with estimations of Q_{st} using Equations (5) and (6).

Figure 46. (a) Pure component isotherms for n-hexane in MFI zeolite. Experimental data from Song and Rees.[40] The continuous solid lines are isotherm fits with dual-site Langmuir-Freundlich parameters provided in Table 26. (b) Plot of component loadings vs. (p_i/P_i^{sat}) at a variety of temperatures. (c, d) Comparison of Q_{st} with estimations of Q_{st} using Equations (5) and (6).

Figure 47. (a) Pure component isotherms for n-hexane in MFI zeolite. CBMC simulation data of Krishna and van Baten. [23, 42] The continuous solid lines are isotherm fits with dual-site Langmuir-Freundlich parameters provided in Table 27. (b) Plot of component loadings vs. (p_i/P_i^{sat}) at a variety of temperatures. (c, d) Comparison of Q_{st} with estimations of Q_{st} using Equations (5) and (6).

Figure 48. (a) Pure component isotherms for n-hexane in MgMOF-74. CBMC simulation data of Krishna and van Baten.[23] The continuous solid lines are isotherm fits with dual-site Langmuir-Freundlich parameters provided in Table 28. (b) Plot of component loadings vs. (p_i/P_i^{sat}) at a variety of temperatures. (c, d) Comparison of Q_{st} with estimations of Q_{st} using Equations (5) and (6).

Figure 49. CBMC simulation data for the isosteric heats of adsorption, Q_{st}, in CuBTC of n-butane, iso-butane, 2,2-dimethylpropane (= neo-pentane), and 2-methylbutane. These data are re-plotted using the information contained in Chmelik et al.[56], and Krishna and van Baten.[7]

Figure 50. (a) Pure component isotherm fits for hexane isomers, n-hexane (nC6), 2-methylpentane (2MP), 3-methylpentane (3MP), 2,2 dimethylbutane (22DMB), and 2,3 dimethybutane (23DMB) in $Fe_2(BDP)_3$. The experimental data are from the paper by Herm et al.[43] The dual-Langmuir-Freundlich parameter sets are provided in Table 29. (b) Calculations of Q_{st} for n-hexane (nC6), 2-methylpentane (2MP), 3-methylpentane (3MP), 2,2 dimethylbutane (22DMB), and 2,3 dimethybutane (23DMB) as function of the loadings.

Figure 51. (a) Pure component isotherms for R12 (dichlorodifluoromethane, CCl_2F_2) in MIL-101(Cr). Experimental data of Motkuri et al.[44] The continuous solid lines are isotherm fits with 1-site Langmuir-Freundlich parameters provided in Table 30. (b) Plot of component loadings vs. (p_i/P_i^{sat}) at a variety of temperatures. (c, d) Comparison of Q_{st} with estimations of Q_{st} using Equations (5) and (6).

Figure 52. (a) Pure component isotherms for R22 (Chlorodifluoromethane, $CHClF_2$) in MIL-101(Cr). Experimental data of Motkuri et al.[44] The continuous solid lines are isotherm fits with 1-site Langmuir-Freundlich parameters provided in Table 30. (b) Plot of component loadings vs. (p_i/P_i^{sat}) at a variety of temperatures. (c, d) Comparison of Q_{st} with estimations of Q_{st} using Equations (5) and (6).

Figure 53. (a) Pure component isotherms for CFC-115 in MFI. Experimental data of Peng et al.[45] The continuous solid lines are isotherm fits with 1-site Langmuir-Freundlich parameters provided in Table 31. (c, d) Comparison of Q_{st} with estimations of Q_{st} using Equations (5) and (6).

Figure 54.(a) Pure component isotherms for HFC-125 in MFI. Experimental data of Peng et al.[45] The continuous solid lines are isotherm fits with 1-site Langmuir-Freundlich parameters provided in Table 31. (c, d) Comparison of Q_{st} with estimations of Q_{st} using Equations (5) and (6).

Figure 55. (a) Pure component isotherms for CFC-115 in Vruf Activated Carbon. Experimental data of Peng et al.[45] The continuous solid lines are isotherm fits with 1-site Langmuir-Freundlich parameters provided in Table 31. (c, d) Comparison of Q_{st} with estimations of Q_{st} using Equations (5) and (6).

Figure 56.(a) Pure component isotherms for HFC-125 in Vruf Activated Carbon. Experimental data of Peng et al.[45] The continuous solid lines are isotherm fits with 1-site Langmuir-Freundlich parameters provided in Table 31. (c, d) Comparison of Q_{st} with estimations of Q_{st} using Equations (5) and (6).

Figure 57. Comparison of the isosteric heats of adsorption of water in a variety of host materials.

Figure 58. Comparison of the isosteric heats of adsorption of C_2H_2 in FeMOF-74 (isotherm data in Table 17), CoMOF-74 (isotherm data in Table **32**), MgMOF-74 (isotherm data in Table 19), CuBTC (isotherm data in Table **33**).

Figure 59. Comparison of the isosteric heats of adsorption of C_3H_6 in FeMOF-74 (isotherm data in Table 17), CoMOF-74 (isotherm data in Table **32**), MgMOF-74 (isotherm data in Table 19), CuBTC (isotherm data in Table **33**). and NaX zeolite (isotherm data in Table **34**).

Figure 60. Comparison of the isosteric heats of adsorption of C_3H_8 in FeMOF-74 (isotherm data in Table 17), CoMOF-74 (isotherm data in Table **32**), MgMOF-74 (isotherm data in Table 19), CuBTC (isotherm data in Table **33**). and NaX zeolite (isotherm data in Table **34**).

Figure 61. Comparison of the isosteric heats of adsorption of n-hexane in $Fe_2(BDP)_3$ (isotherm data in Table 29), Zn(bdc)dabco (isotherm data in Table 14), MgMOF-74 (isotherm data in Table 28), and MFI zeolite (isotherm data in Table 26).

Figure 62. Comparison of the isosteric heats of adsorption of methanol in FER (isotherm data in Table 25), MFI (Si/Al=990) (isotherm data in Table 16), and Zn(bdc)dabco (isotherm data in Table 14).

Figure 1

Thermodynamic factor

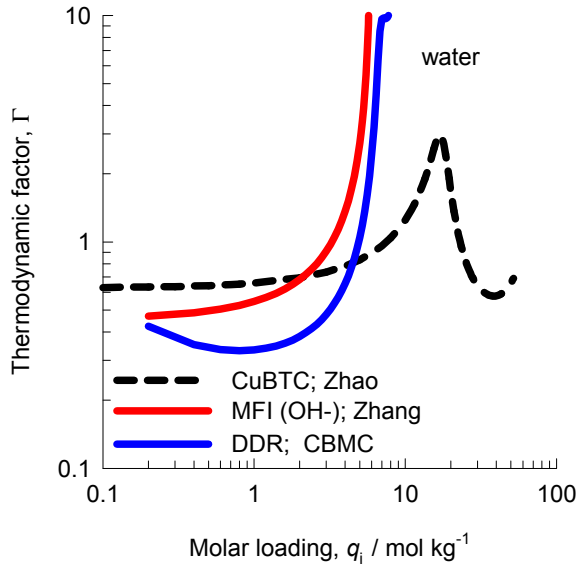

Figure 2

Water in CuBTC: Zhao experiments

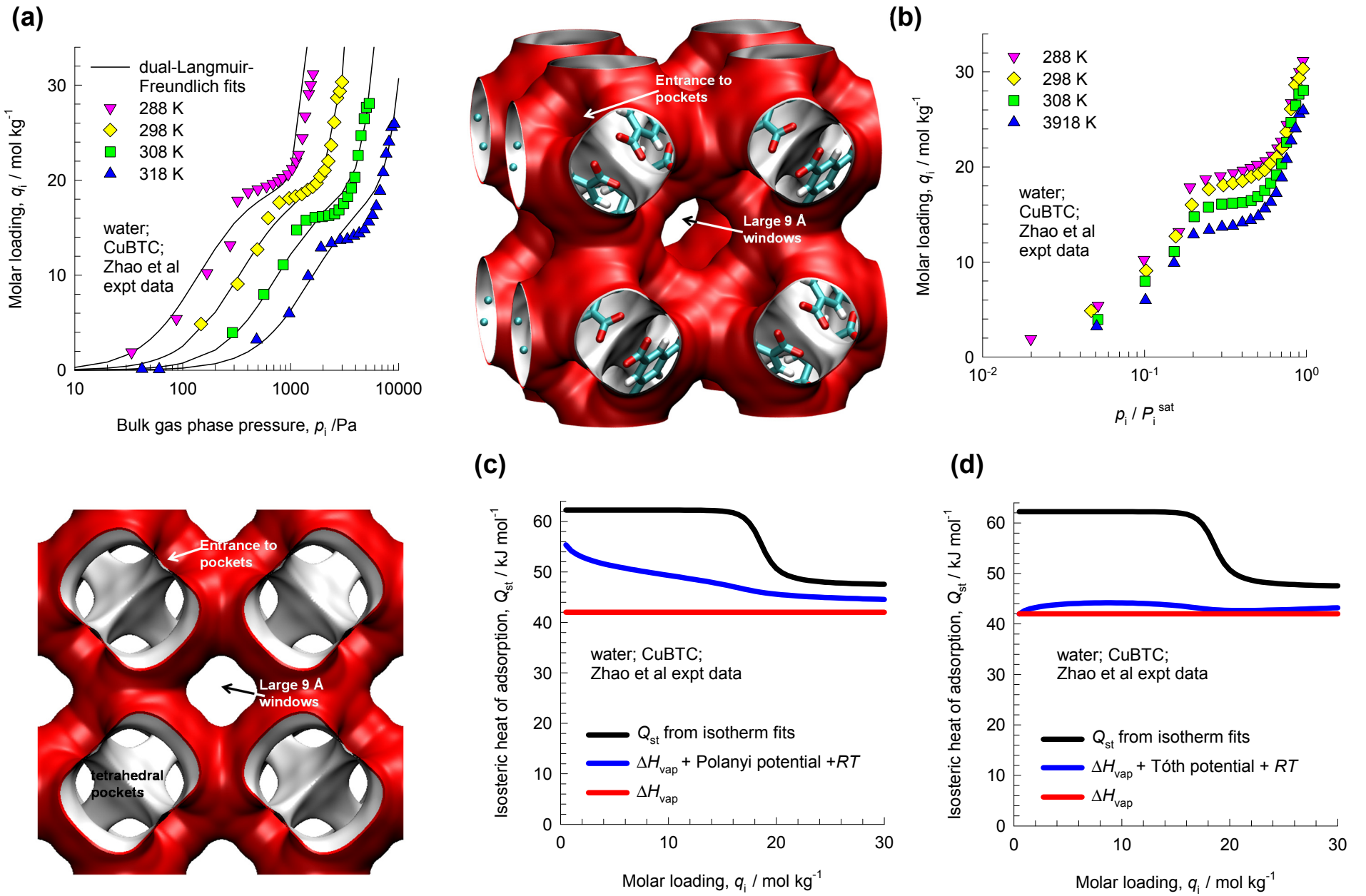

Figure 3

Water in LTA-4A: Gorbach Experiments

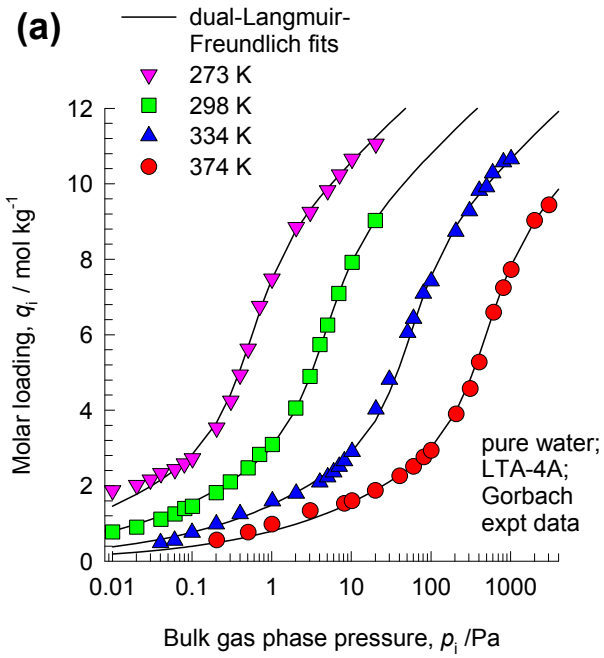

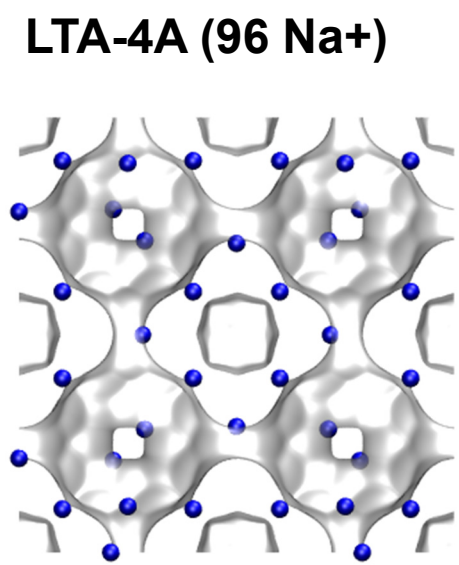

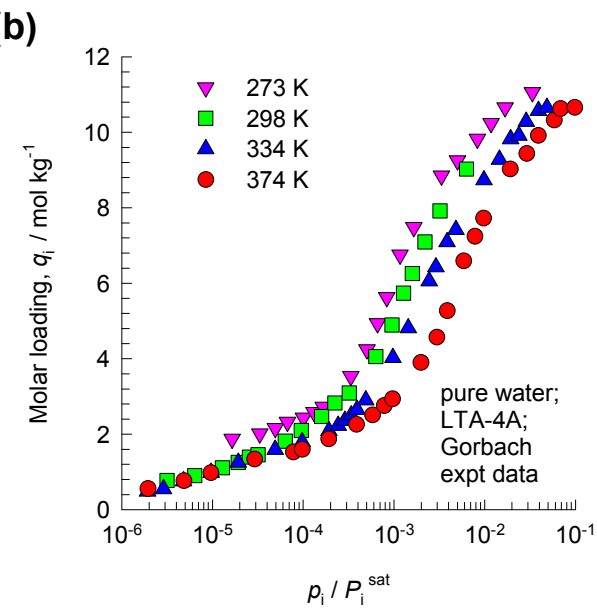

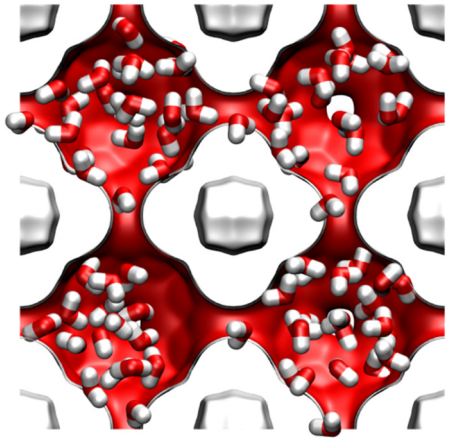

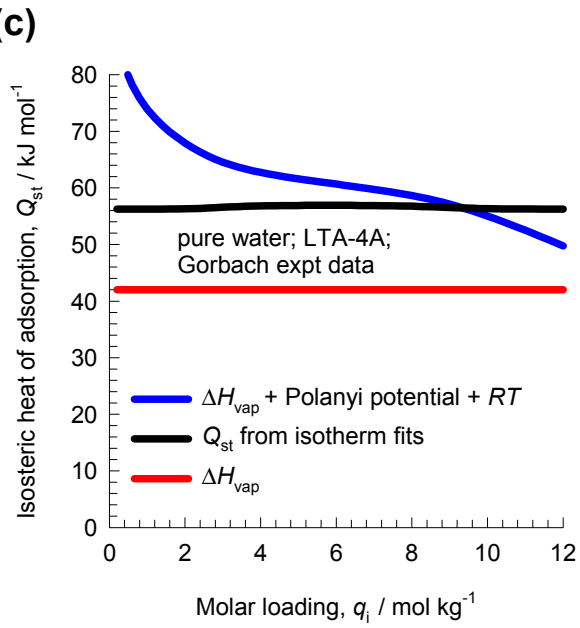

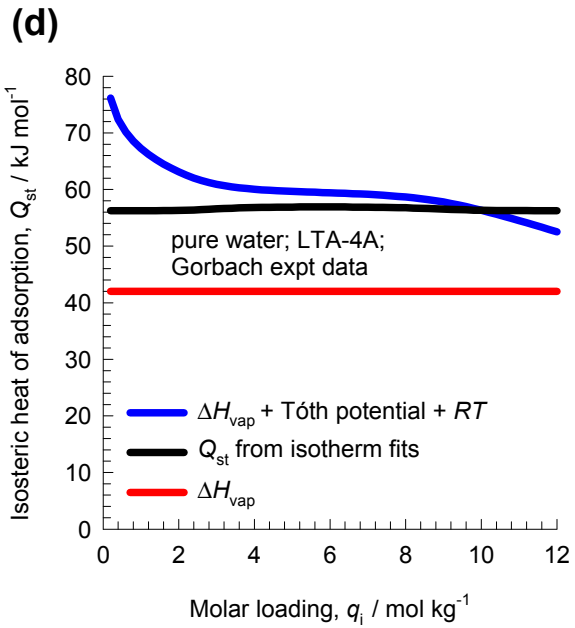

Figure 4

Water in MFI (OH-): Zhang Experiments

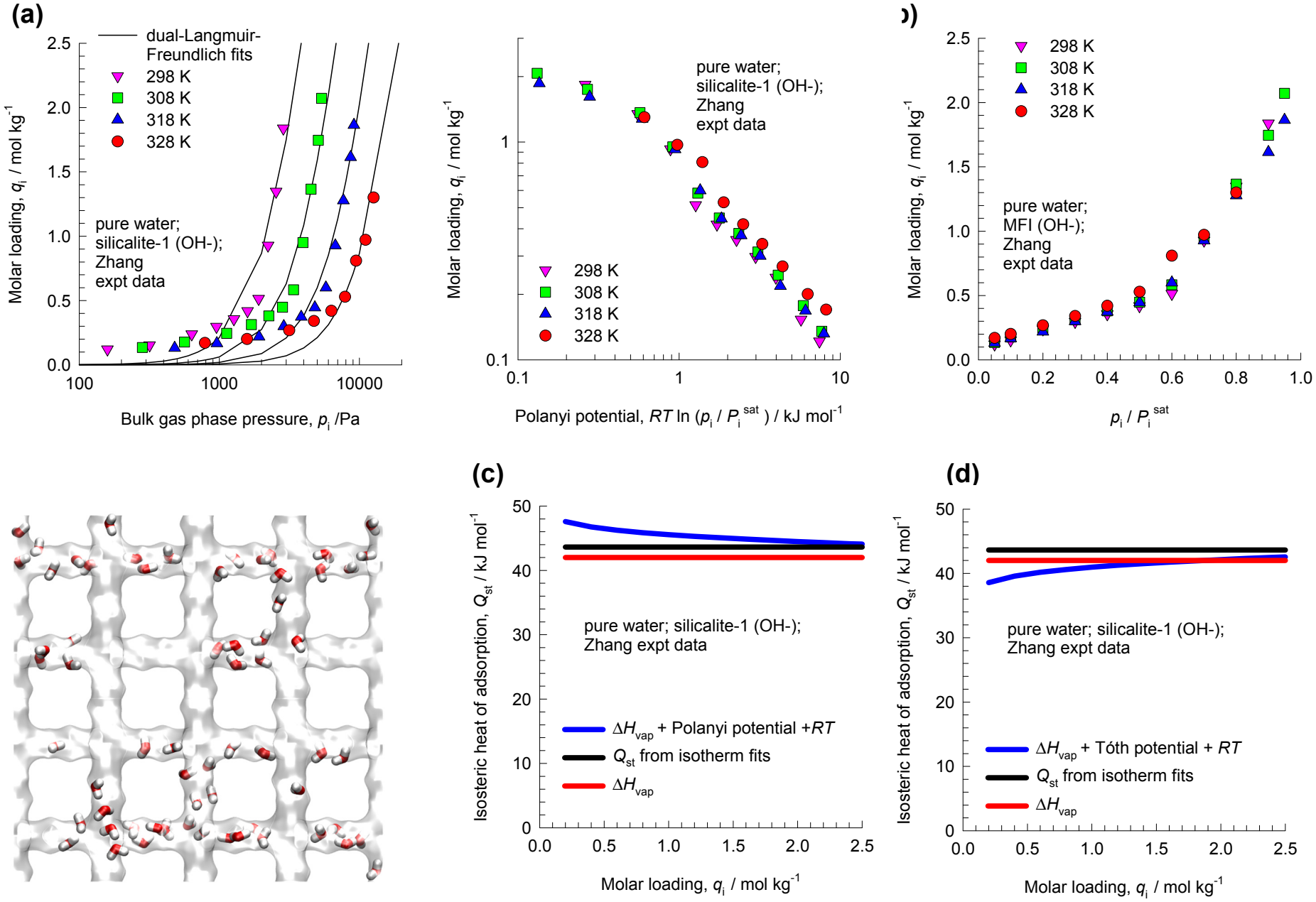

Figure 5

Water in MFI: Giaya & Thompson Experiments

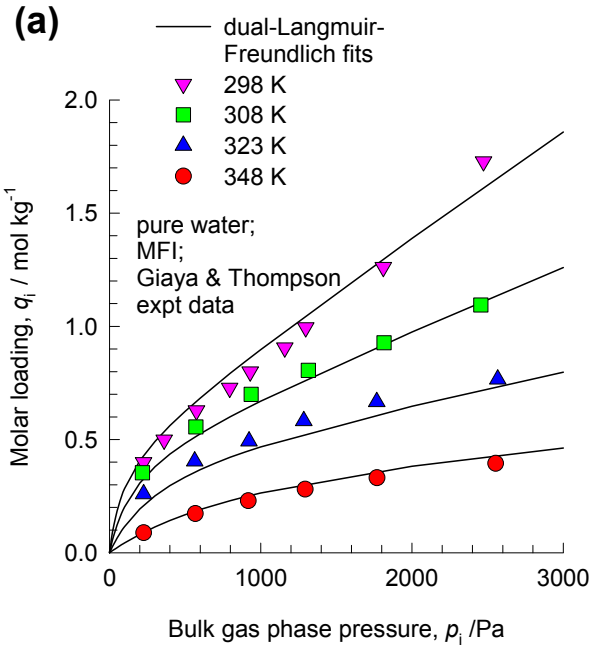

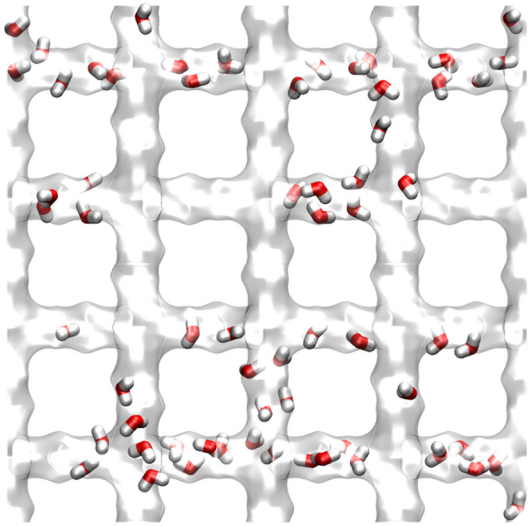

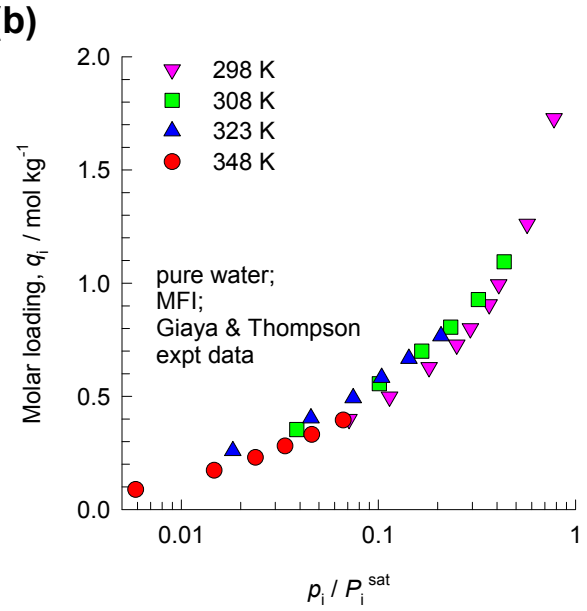

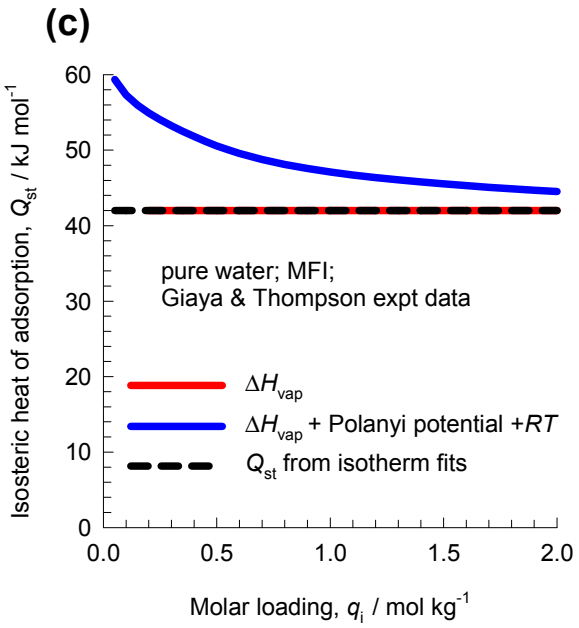

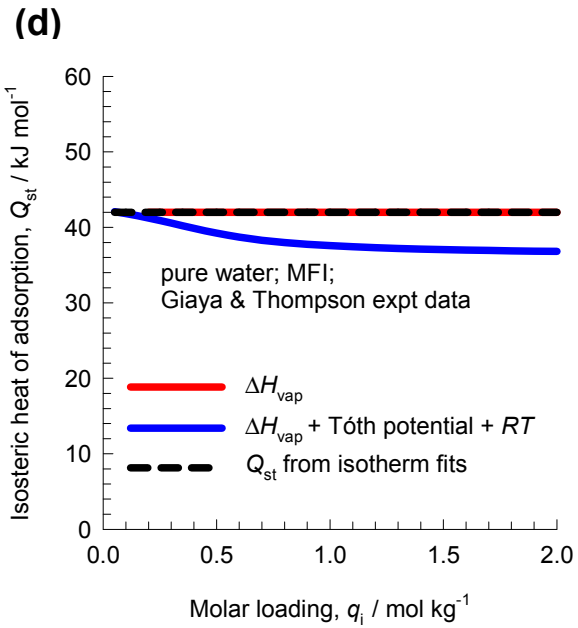

Figure 6

Water in LTA-3A: Llano-Restrepo

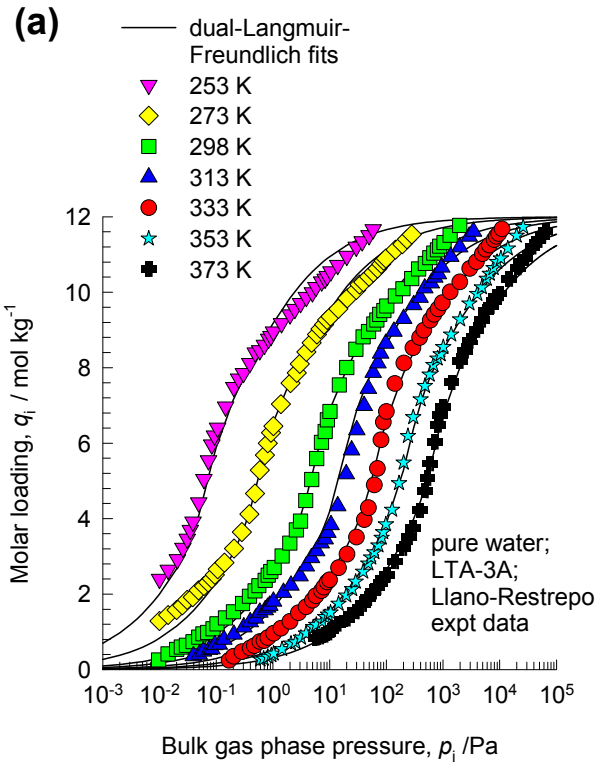

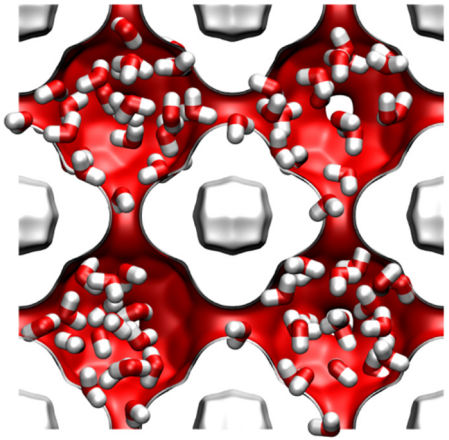

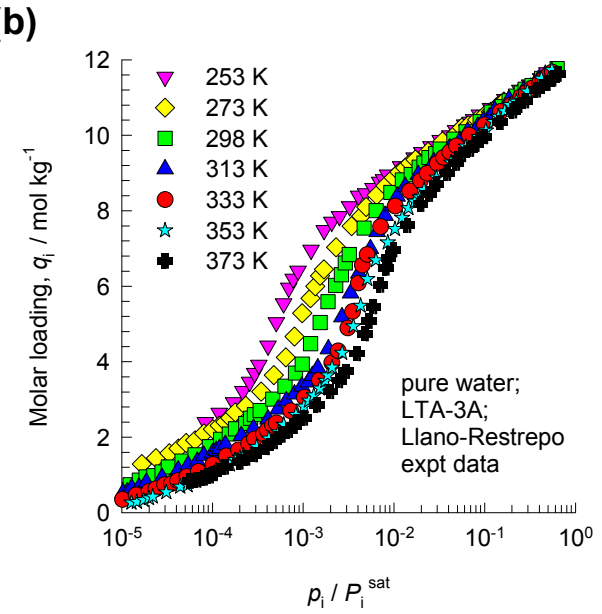

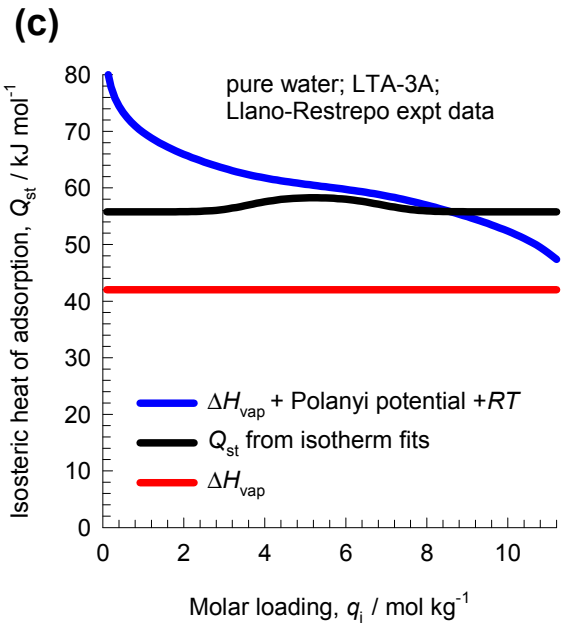

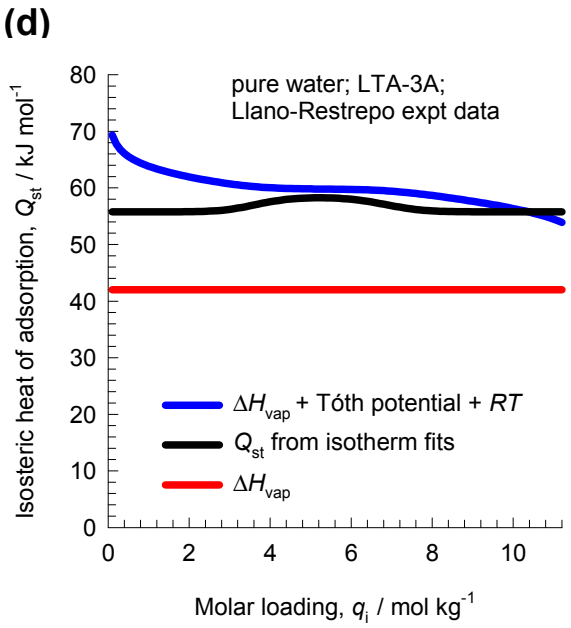

Figure 7

Water in DDR: den Exter Experiments

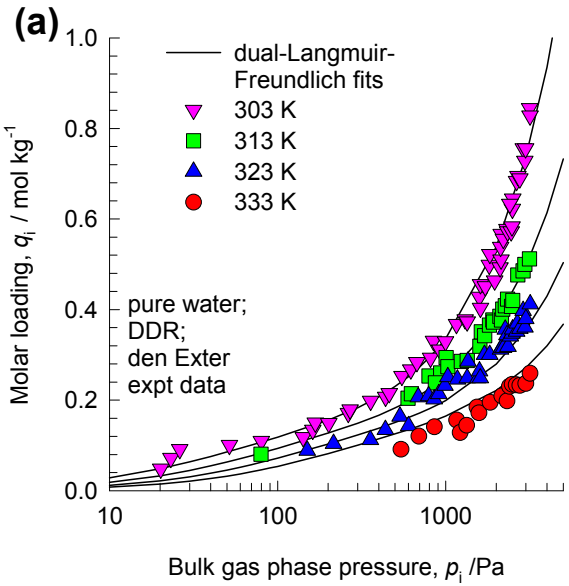

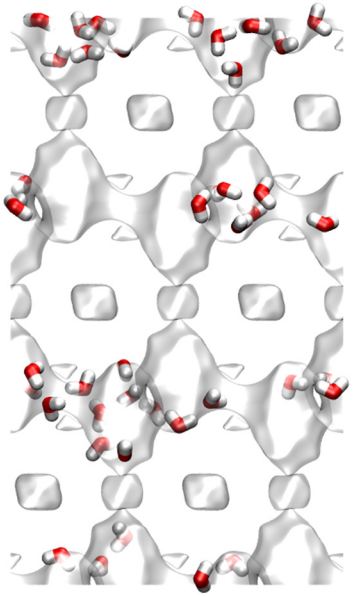

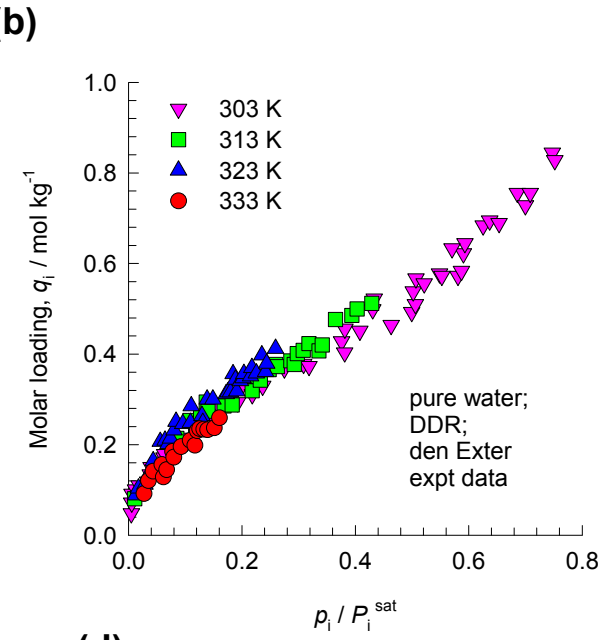

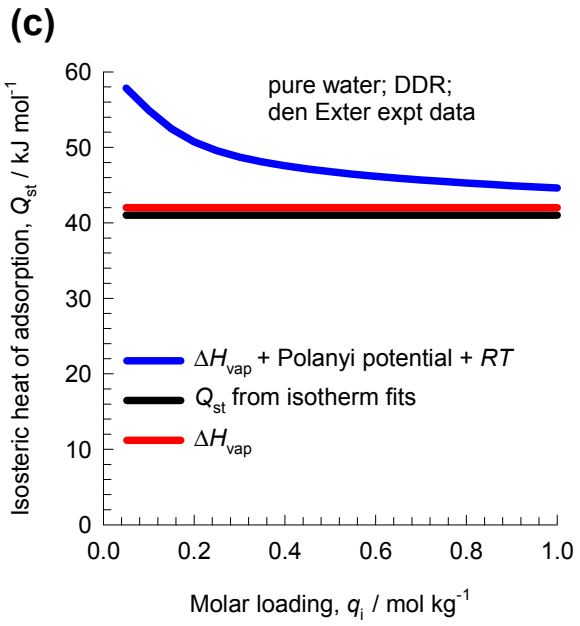

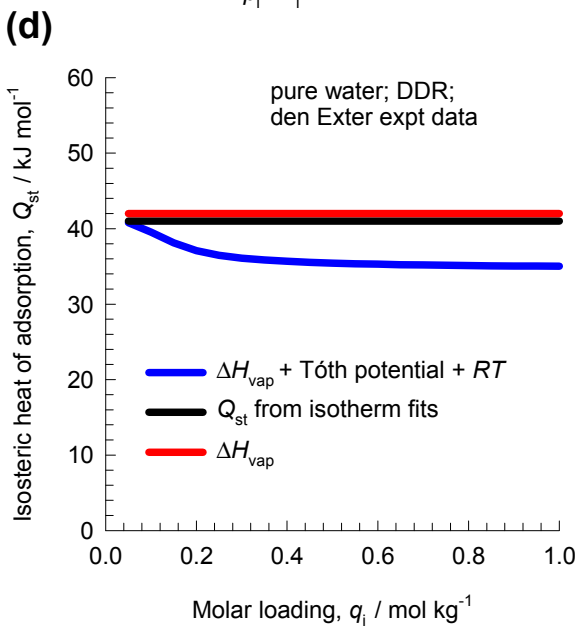

Figure 8

Water in DDR: CBMC simulations

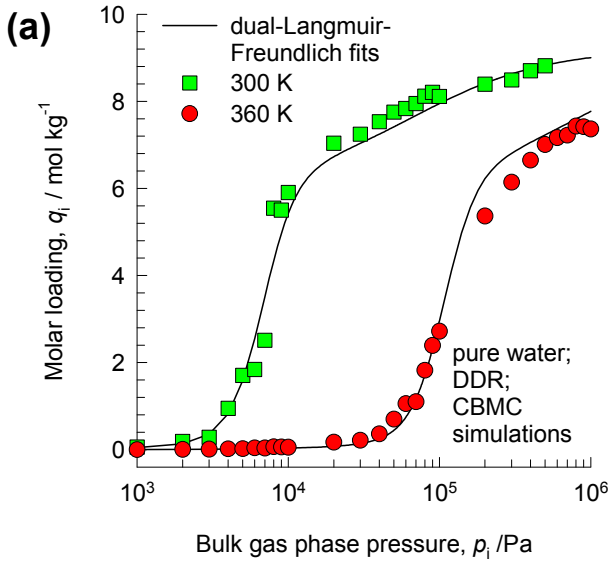

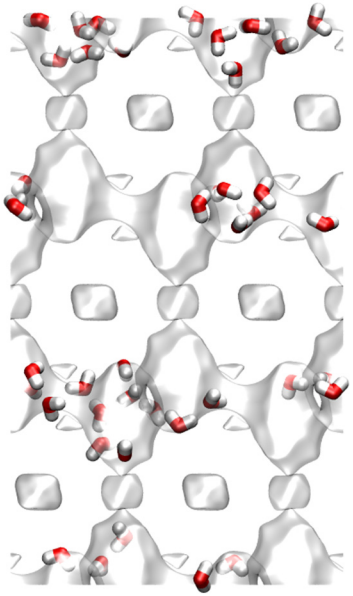

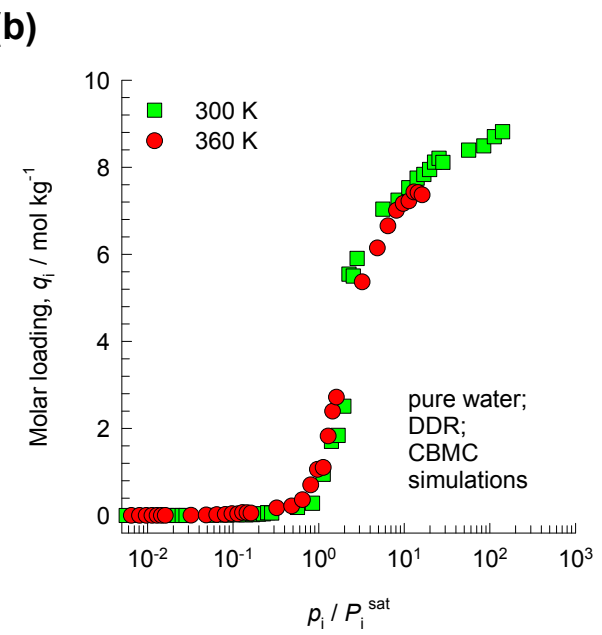

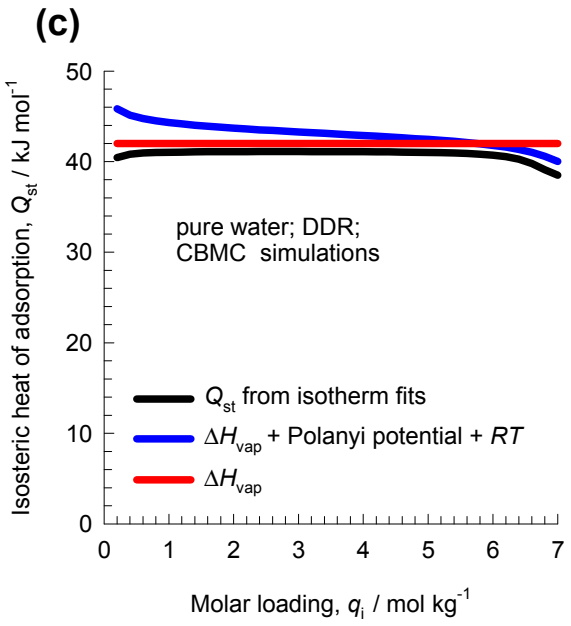

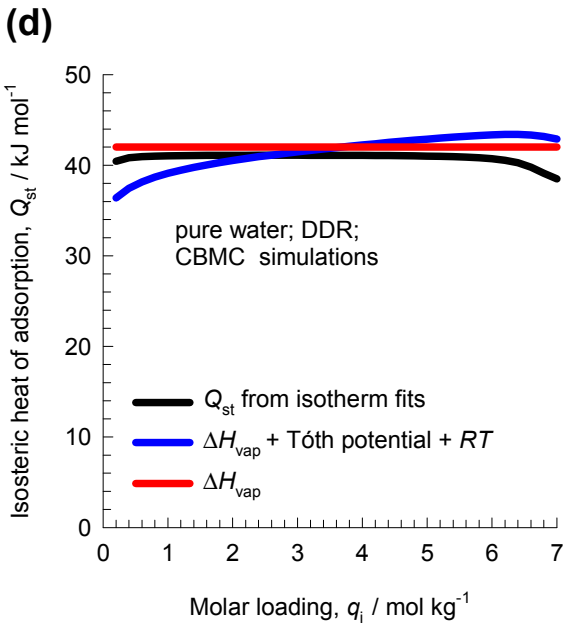

Figure 9

Water in 13X: Wang & LeVan Experiments

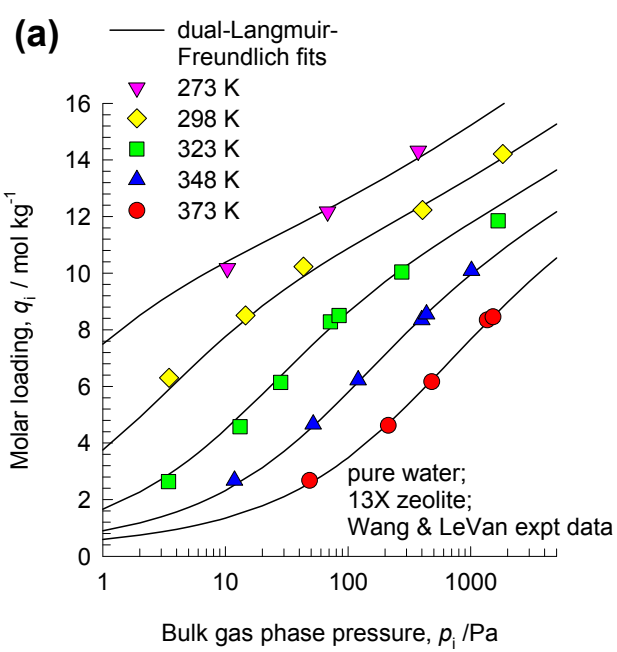

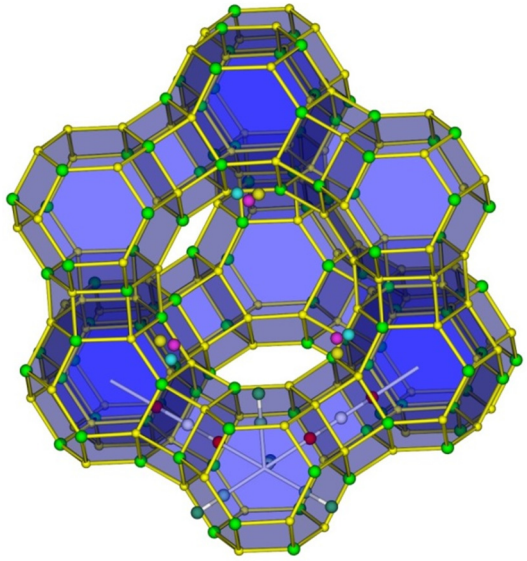

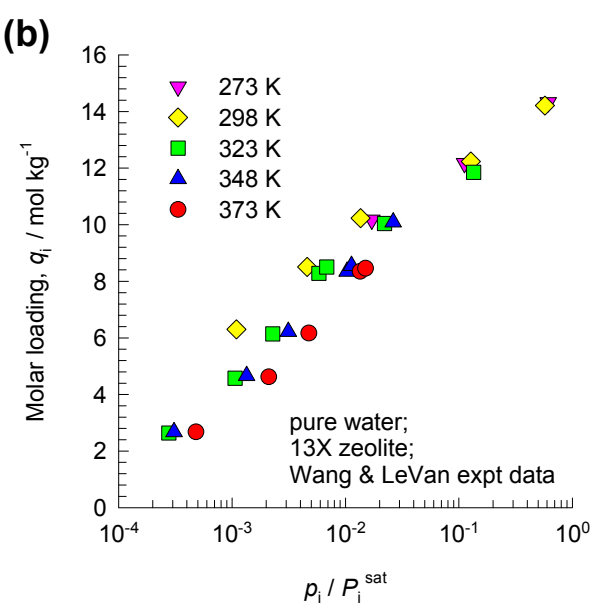

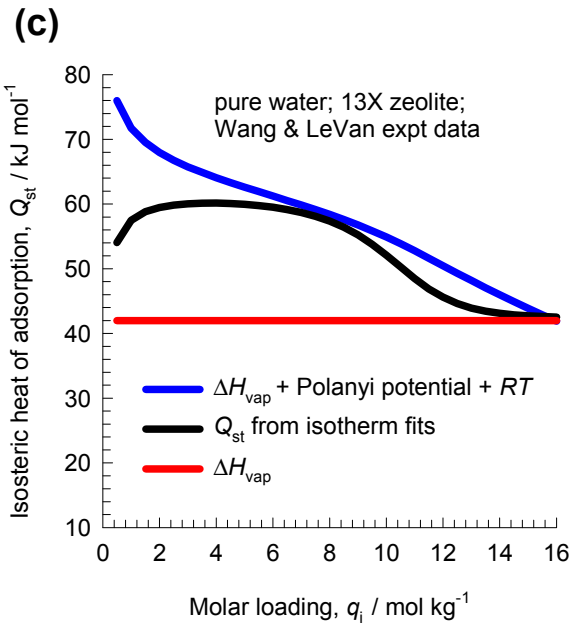

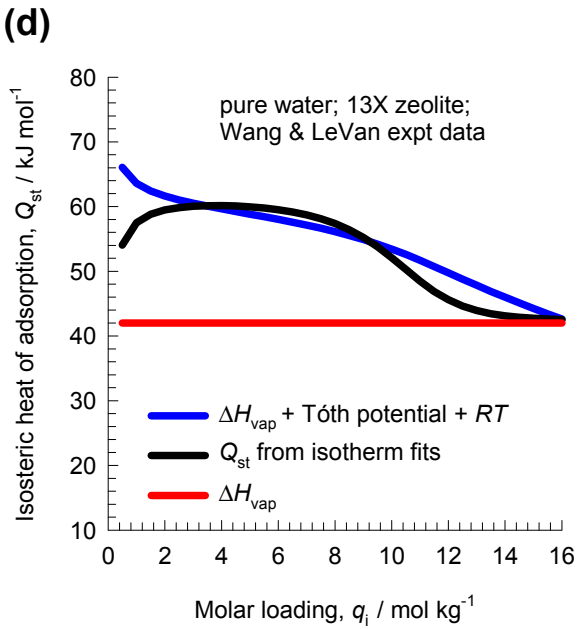

Figure 10

Water in LTA-5A: Wang & LeVan Experiments

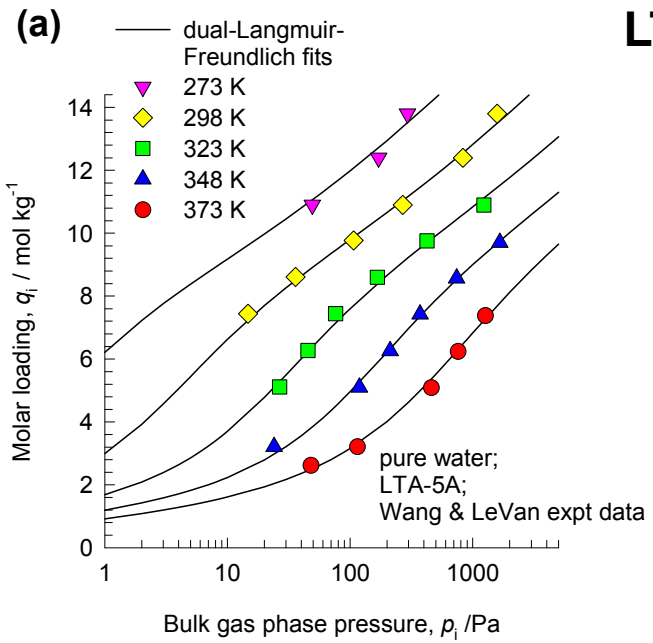

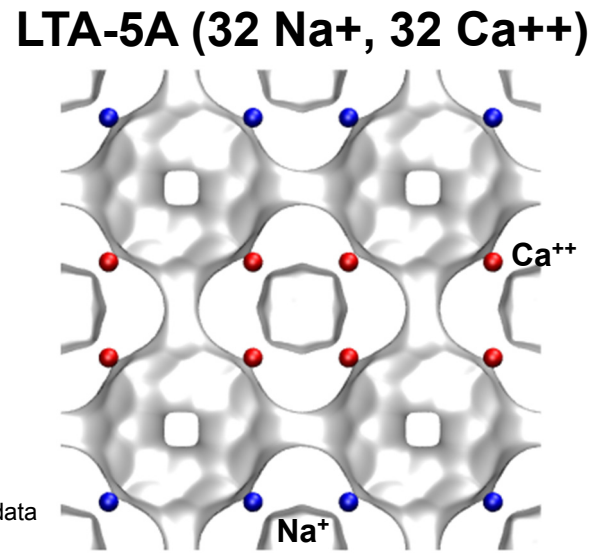

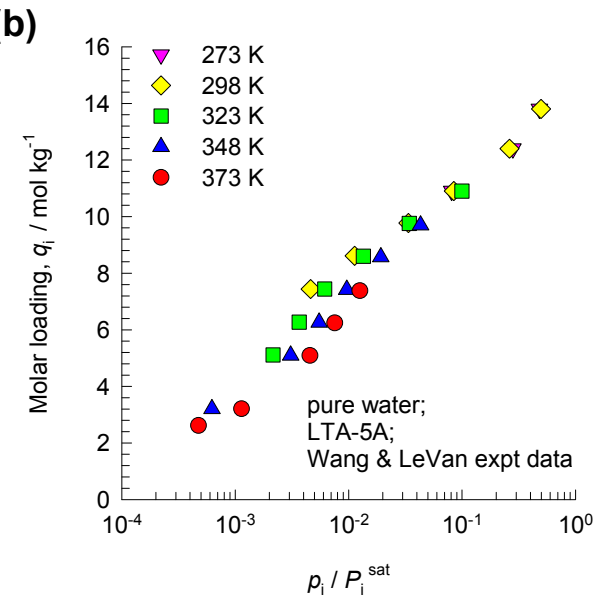

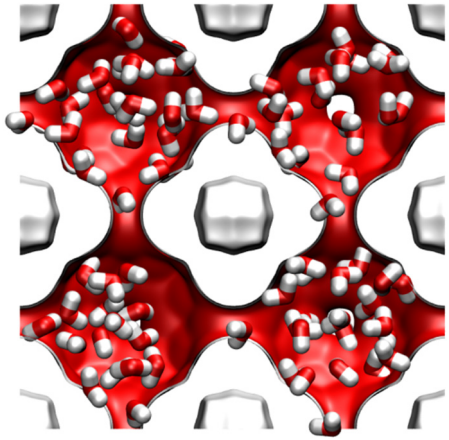

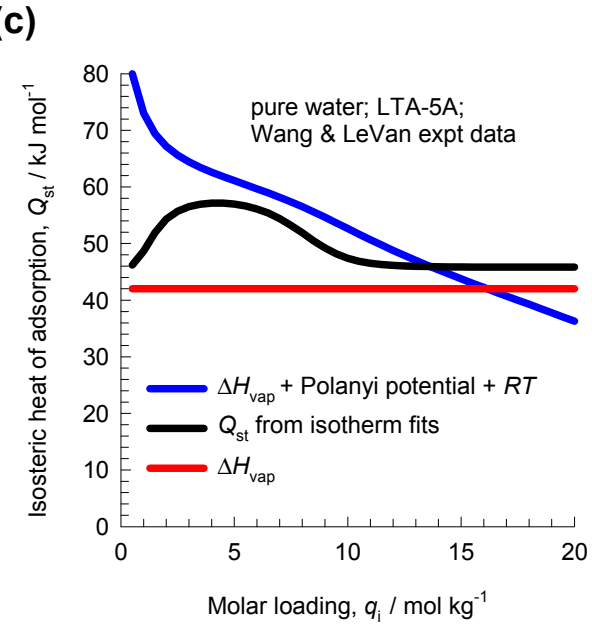

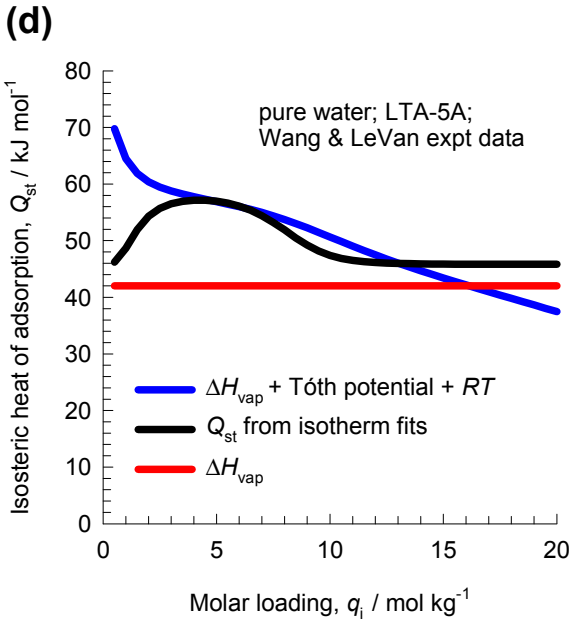

Figure 11

Water in LTA-4A: Pera-Titus Experiments

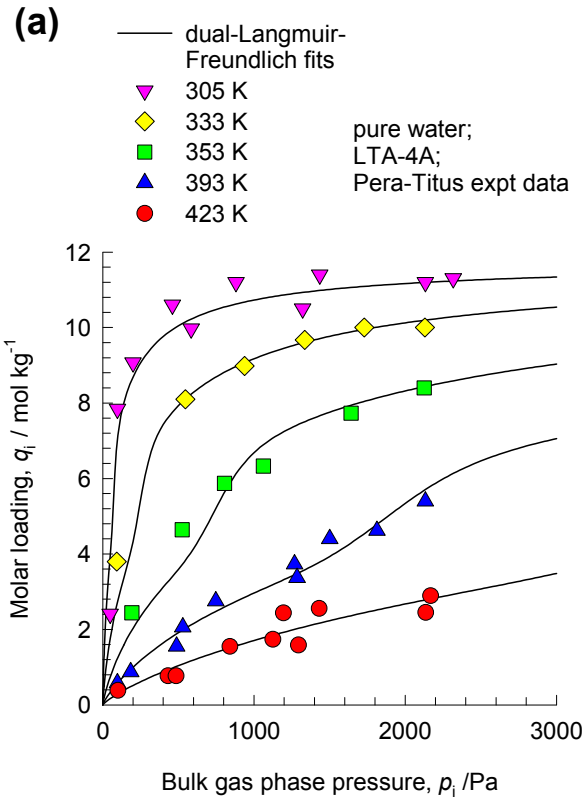

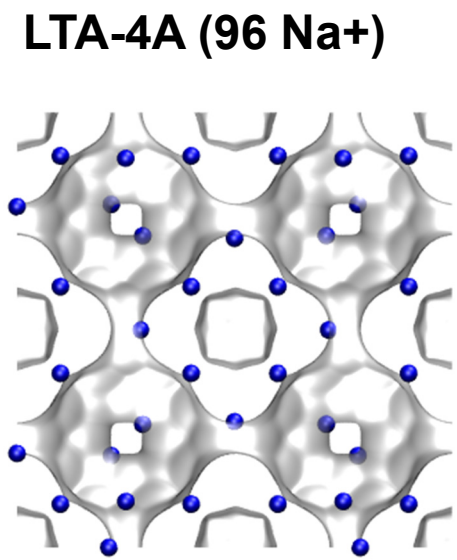

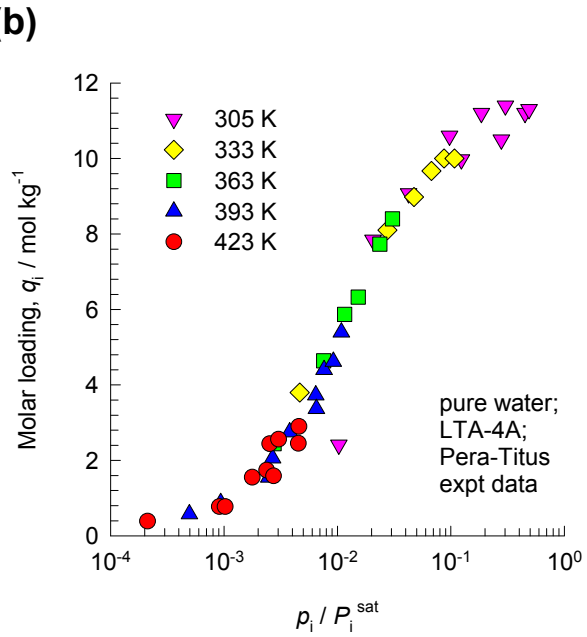

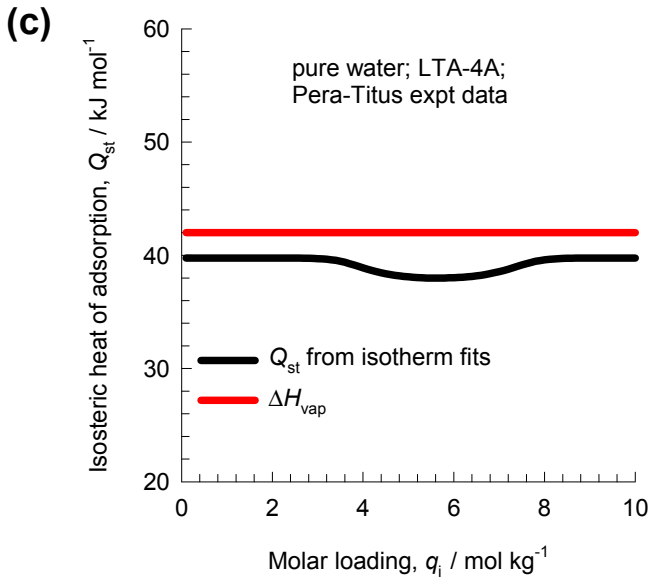

Figure 12

Ethanol in LTA-4A: Pera-Titus Experiments

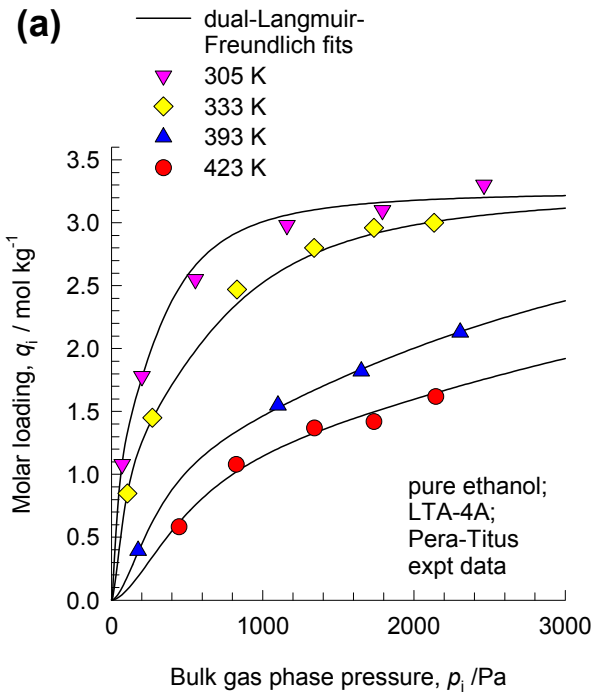

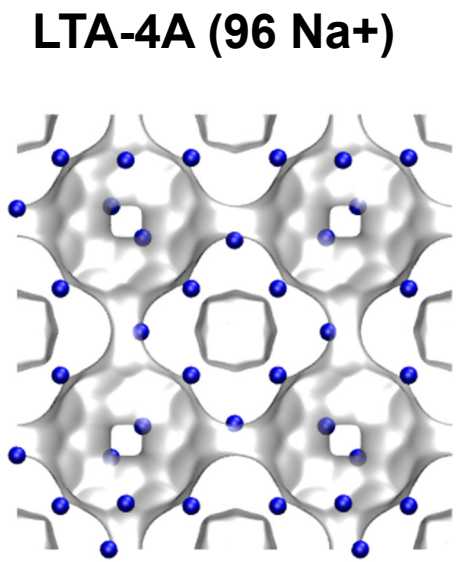

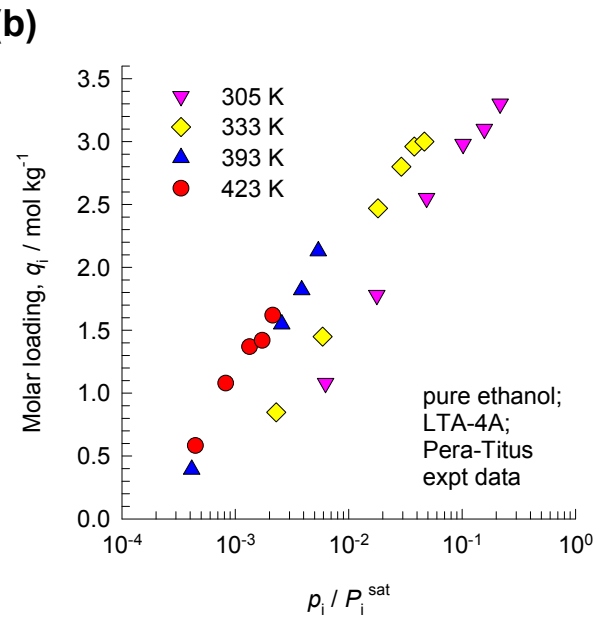

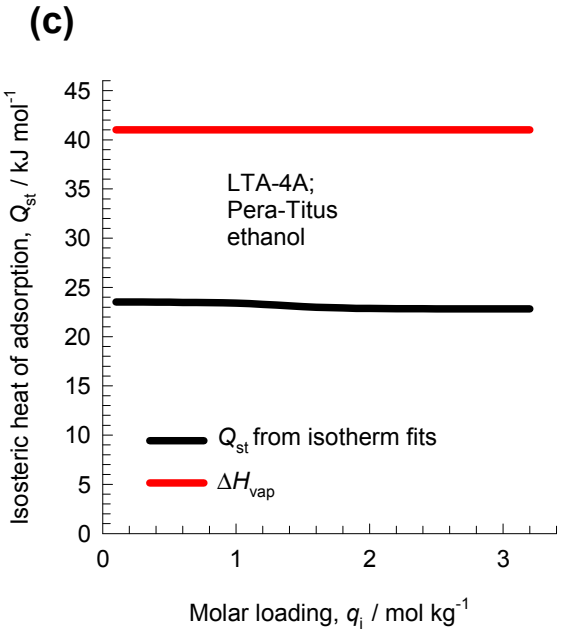

Figure 13

Water/Ethanol in LTA-4A: Pera-Titus Experiments

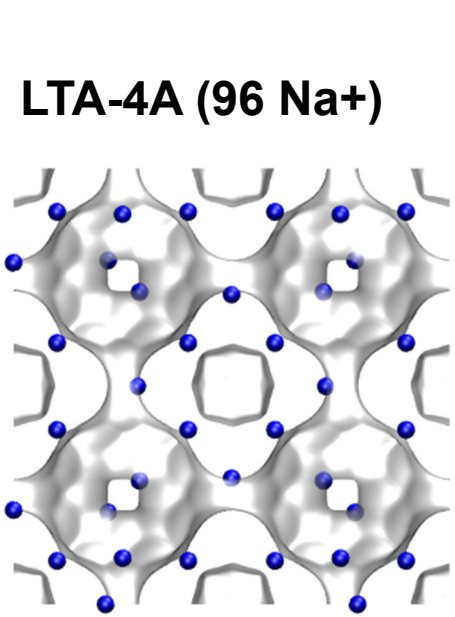

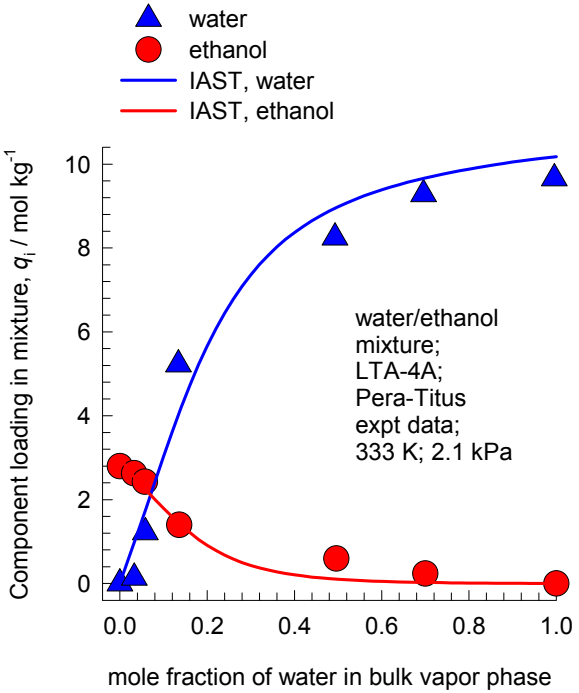

Figure 14

Methanol in FER: CBMC simulations

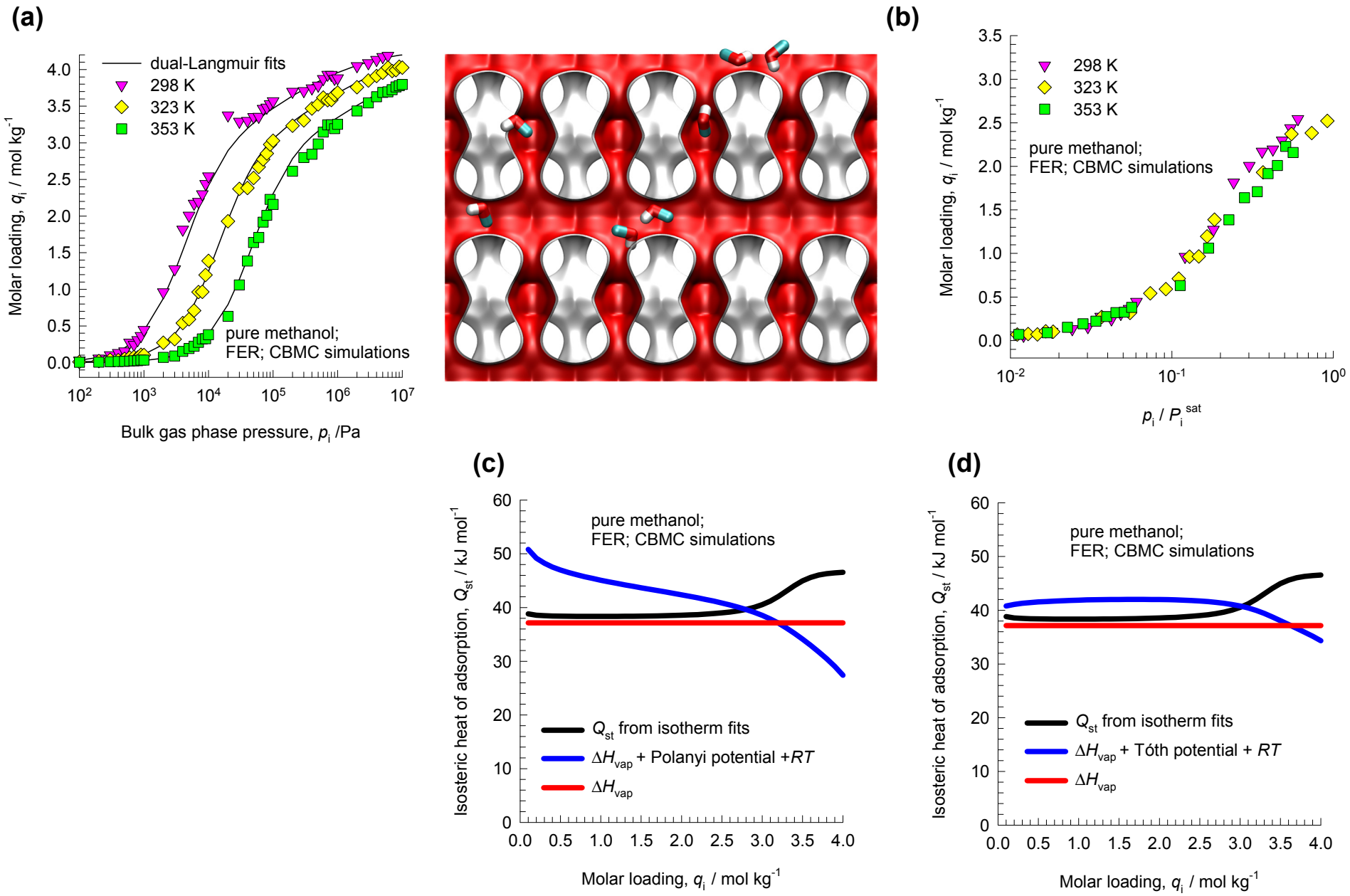

Figure 15

1-propanol in DAY-55: Sakuth Experiments

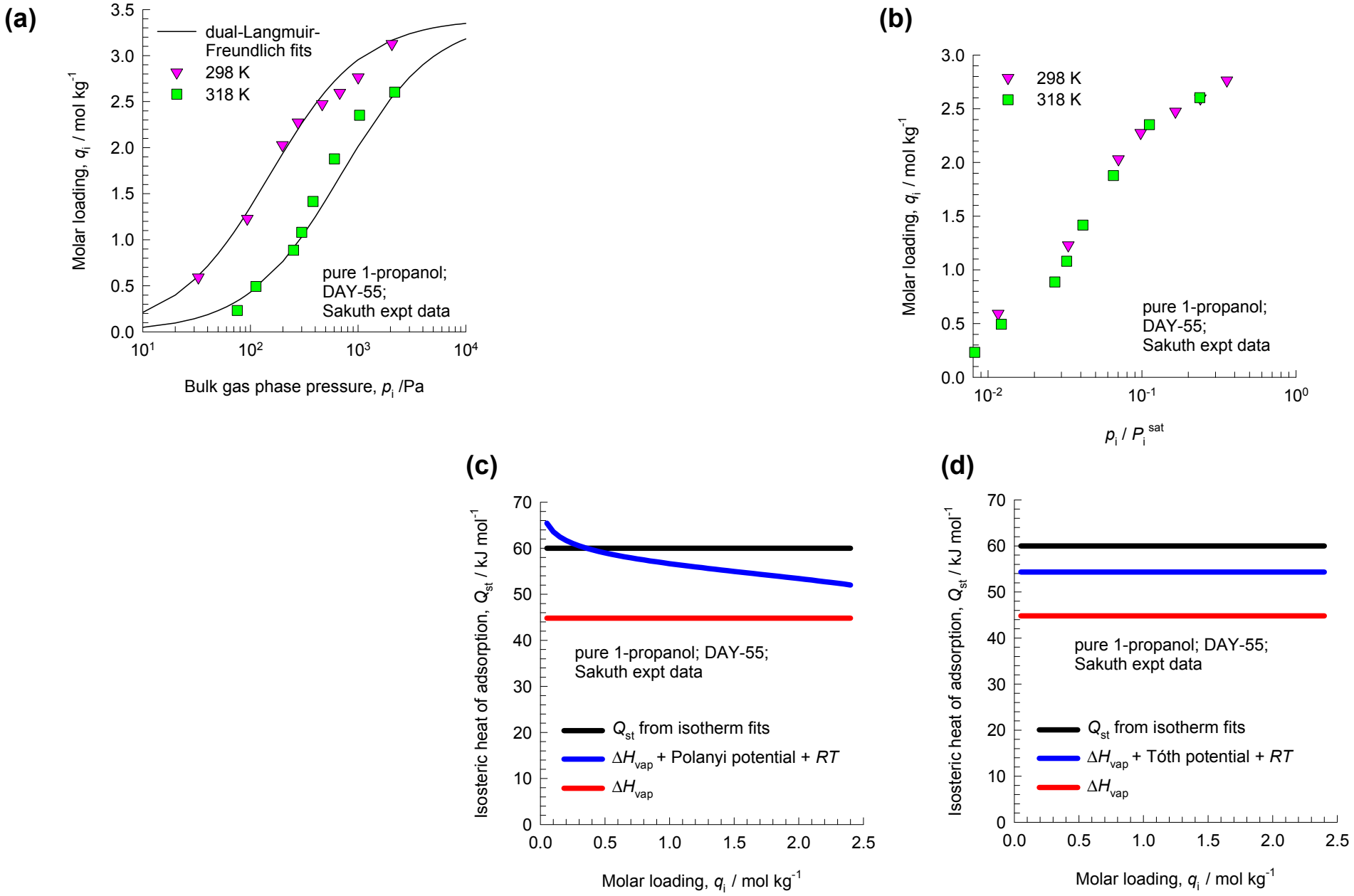

Figure 16

Toluene in DAY-55: Sakuth Experiments

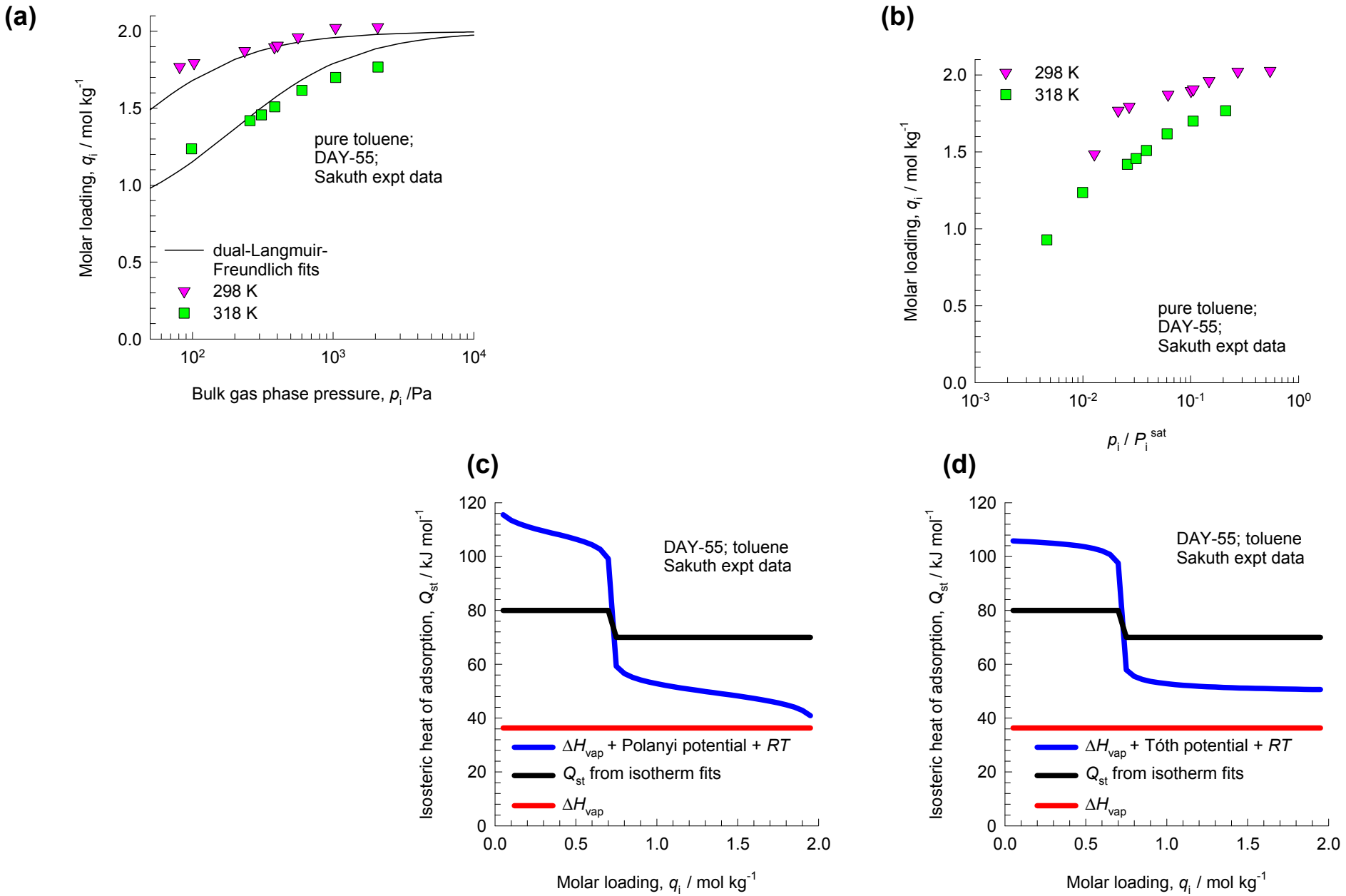

Figure 17

Dimethyl ether in Zn(bdc)dabco: Lee Experiments

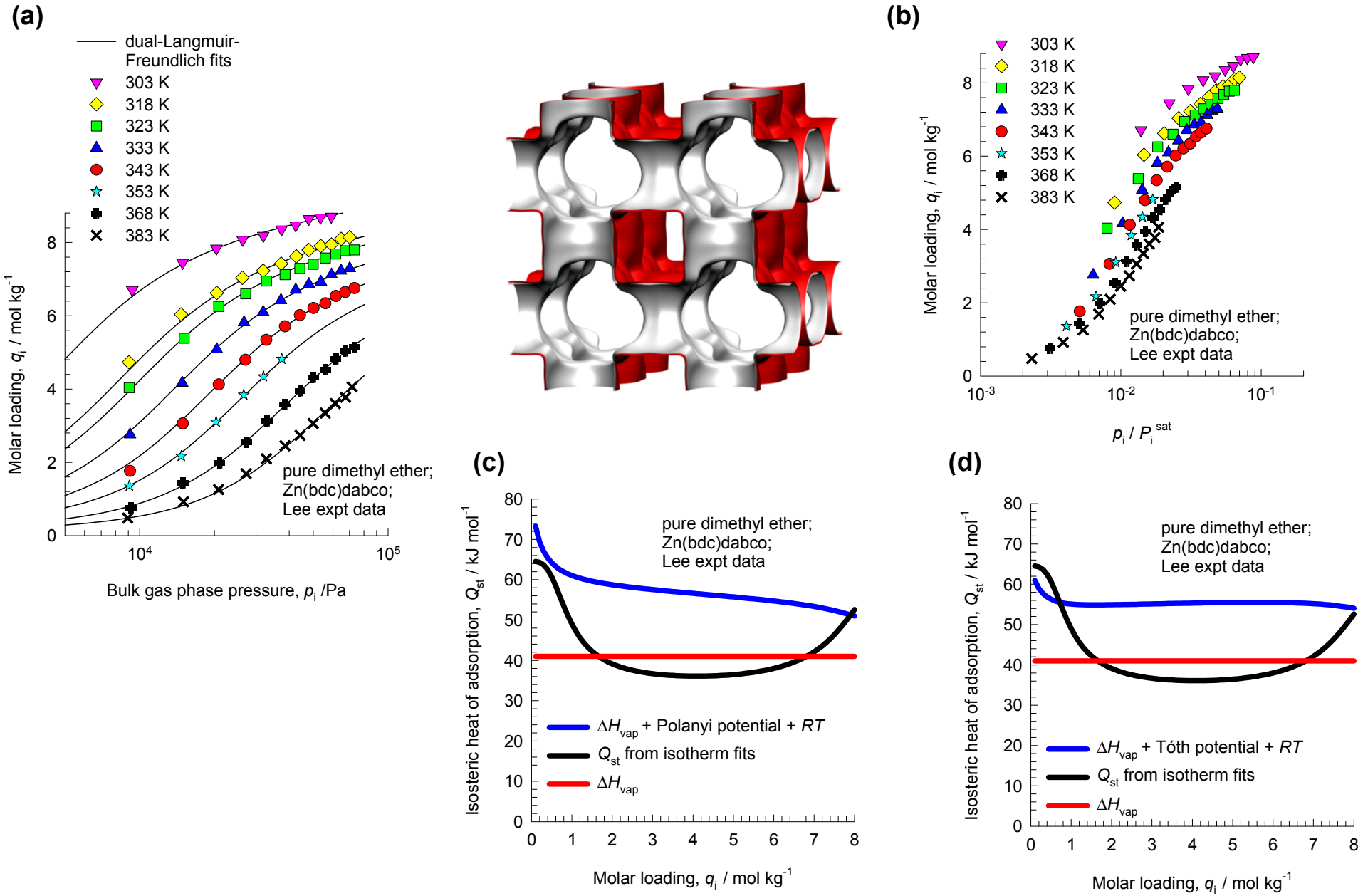

Figure 18

Ethanol in Zn(bdc)dabco: Lee Experiments

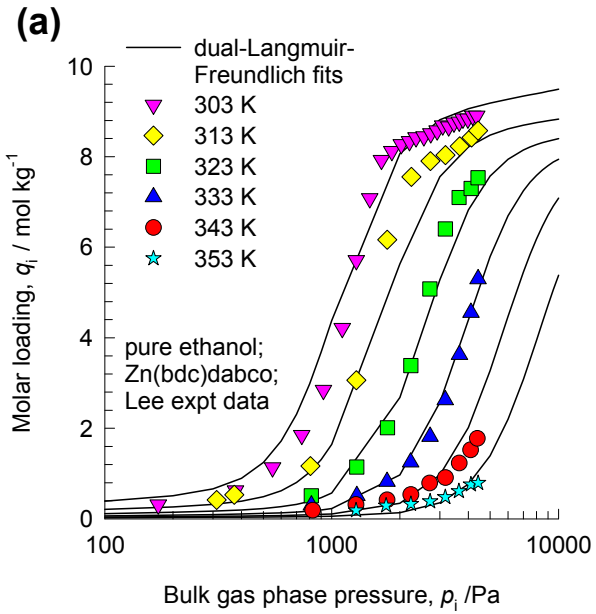

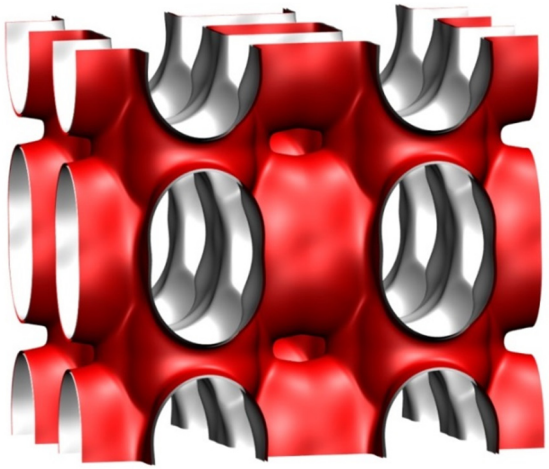

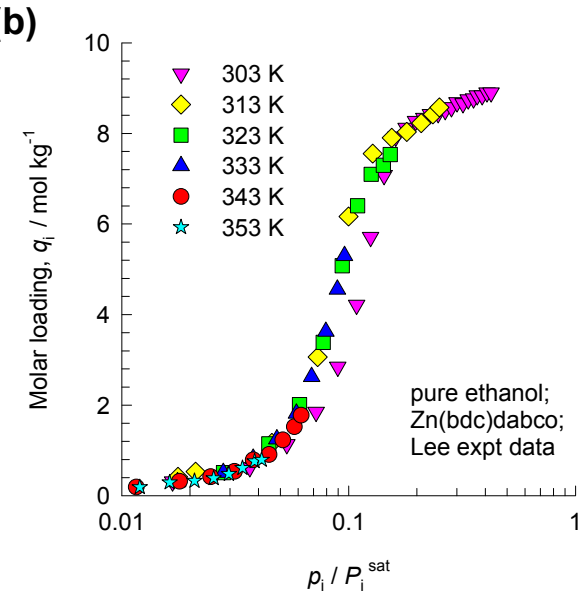

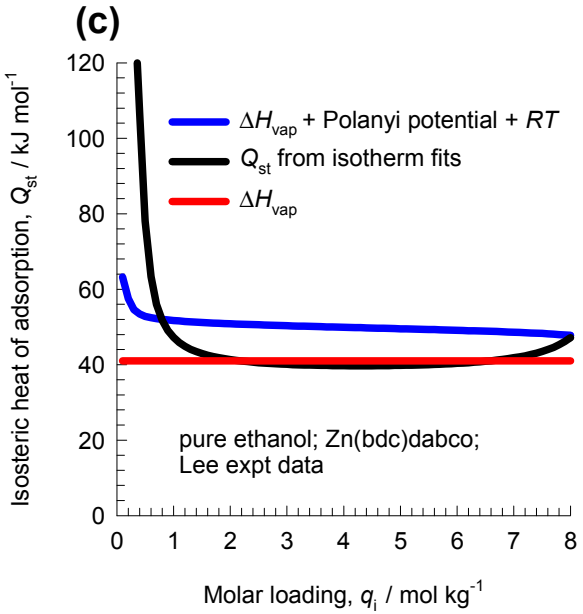

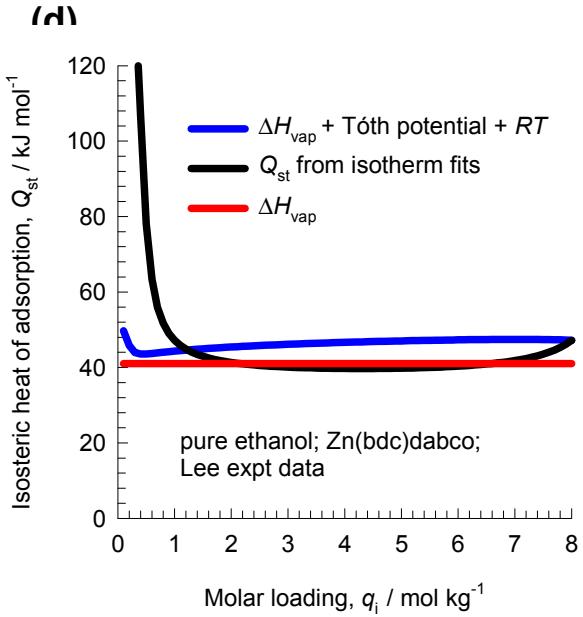

Figure 19

Methanol in Zn(bdc)dabco: Lee Experiments

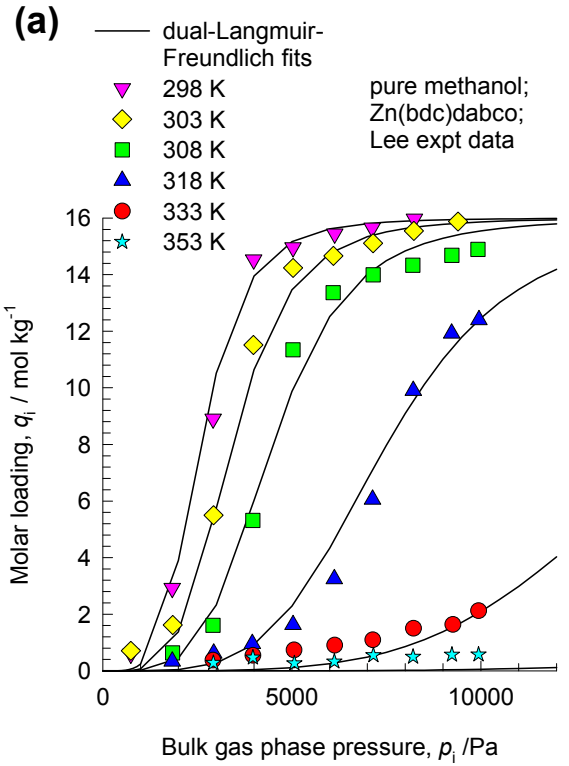

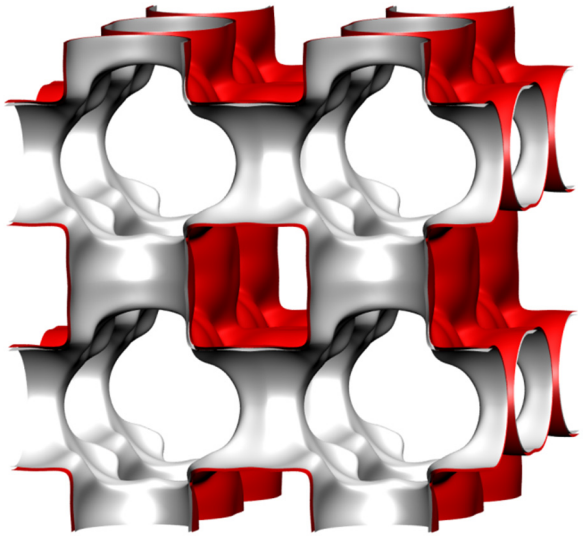

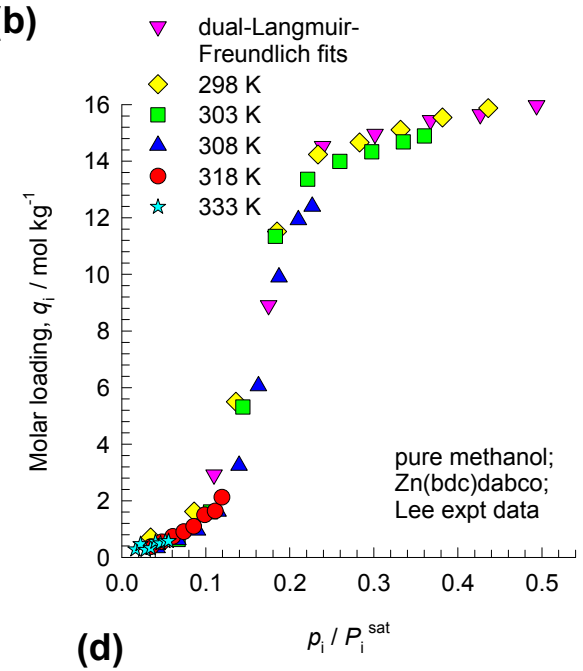

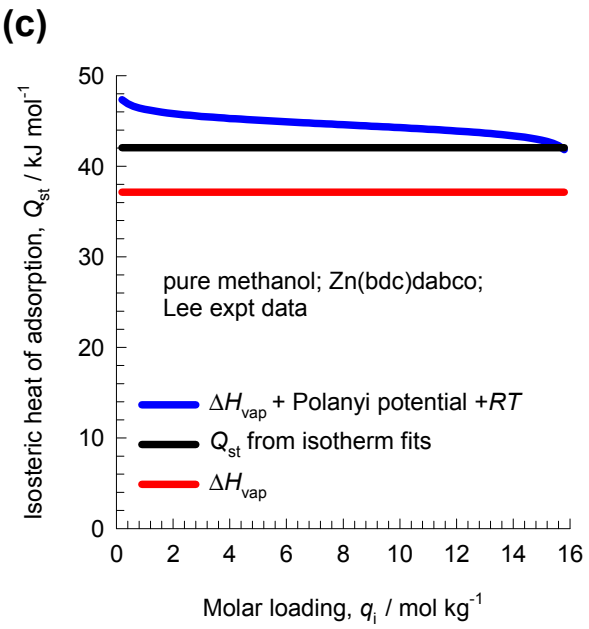

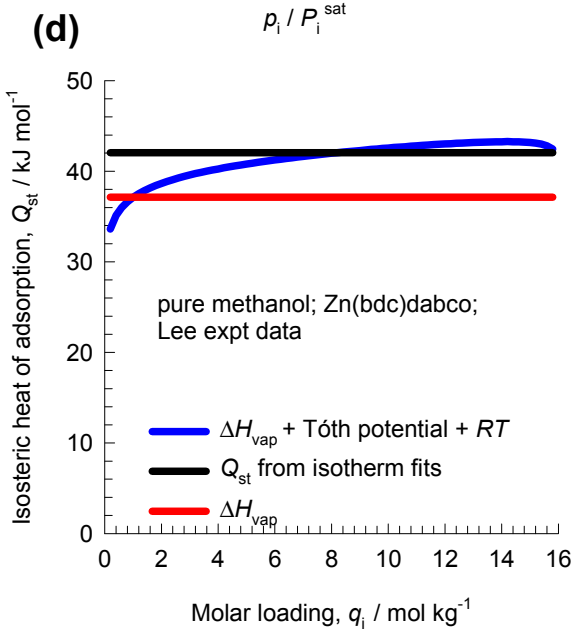

Figure 20

Cyclohexane in Zn(bdc)dabco: Li Experiments

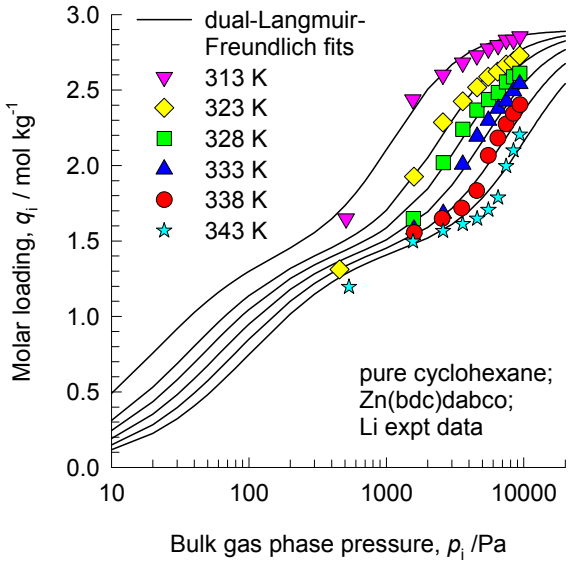

(a)

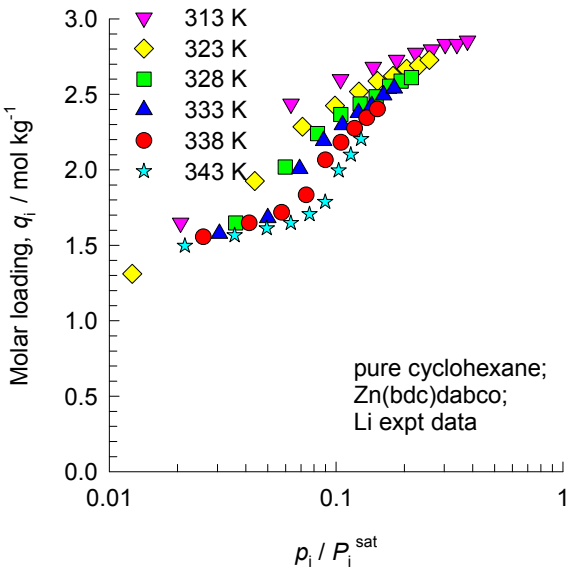

(b)

(c)

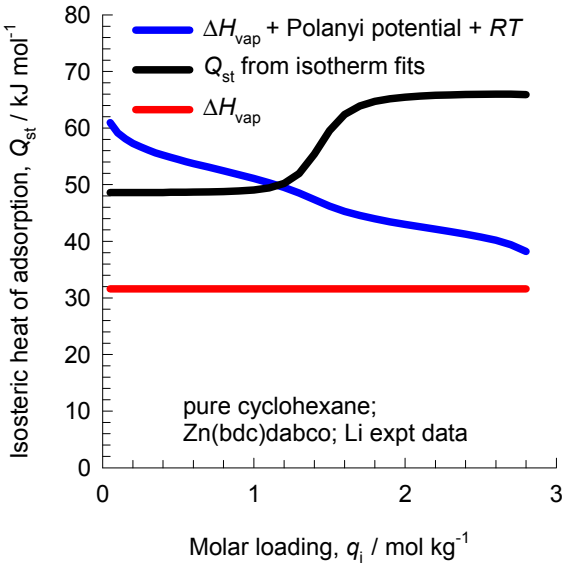

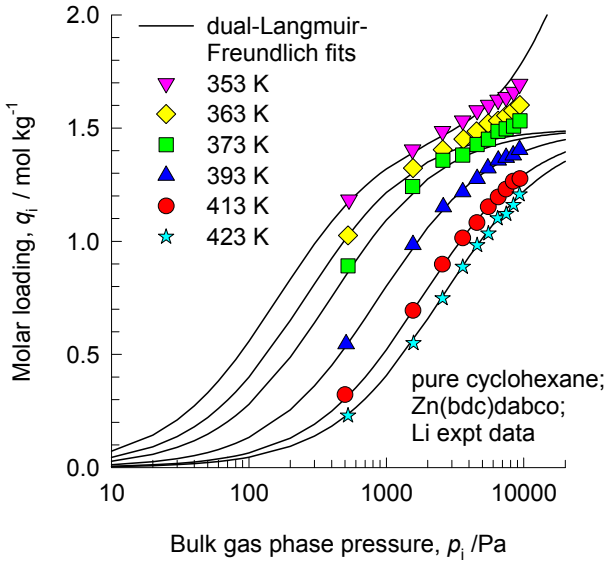

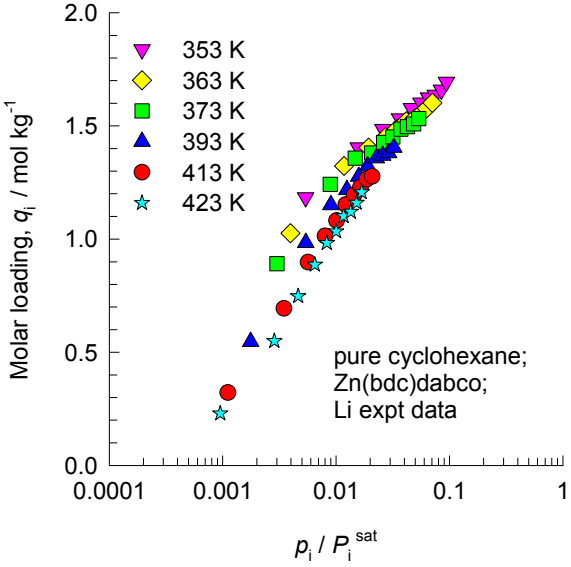

(d)

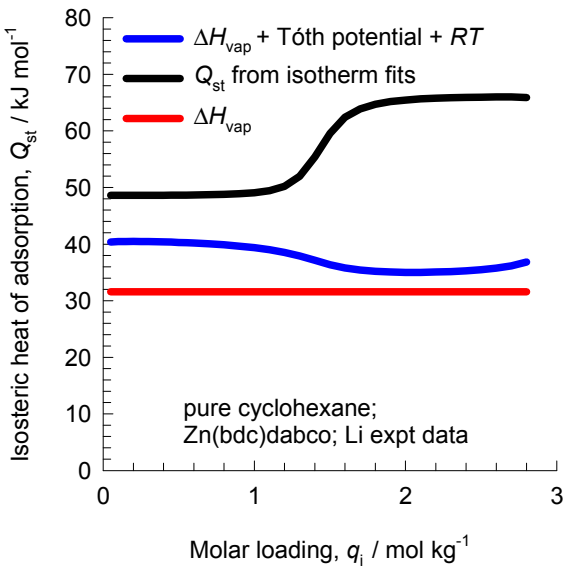

Figure 21

n-hexane in Zn(bdc)dabco: Lee Experiments

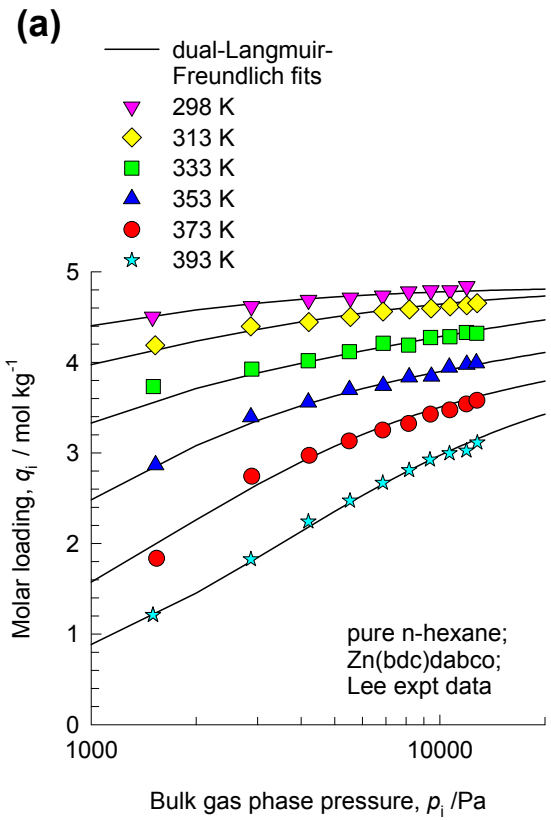

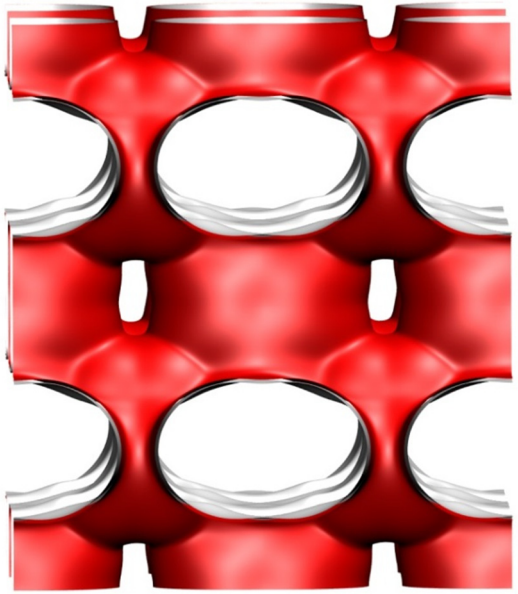

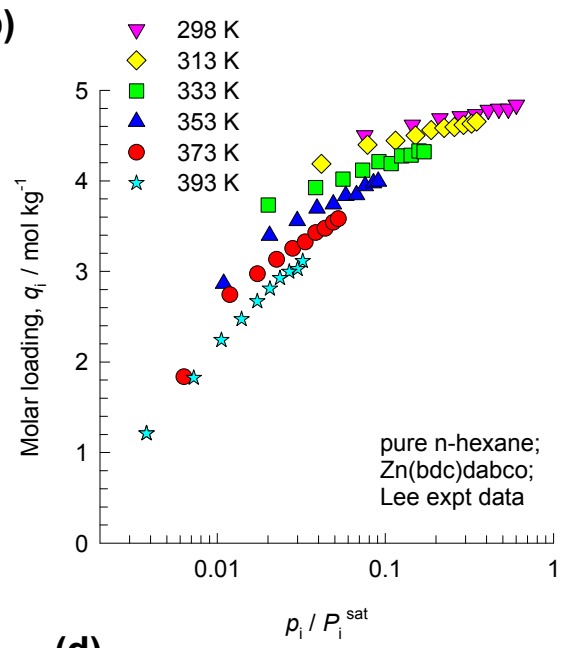

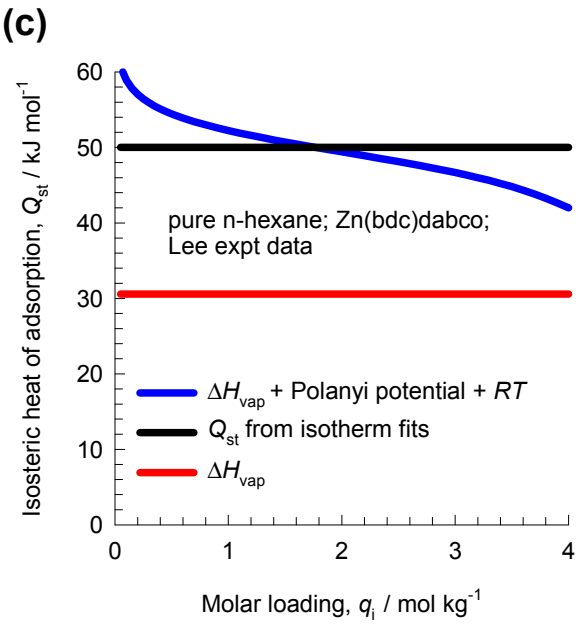

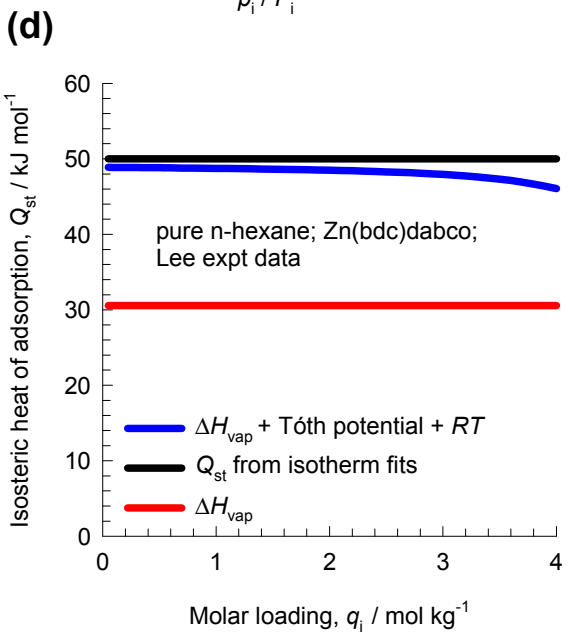

Figure 22

n-hexane in Zn(bdc)dabco: CBMC simulations

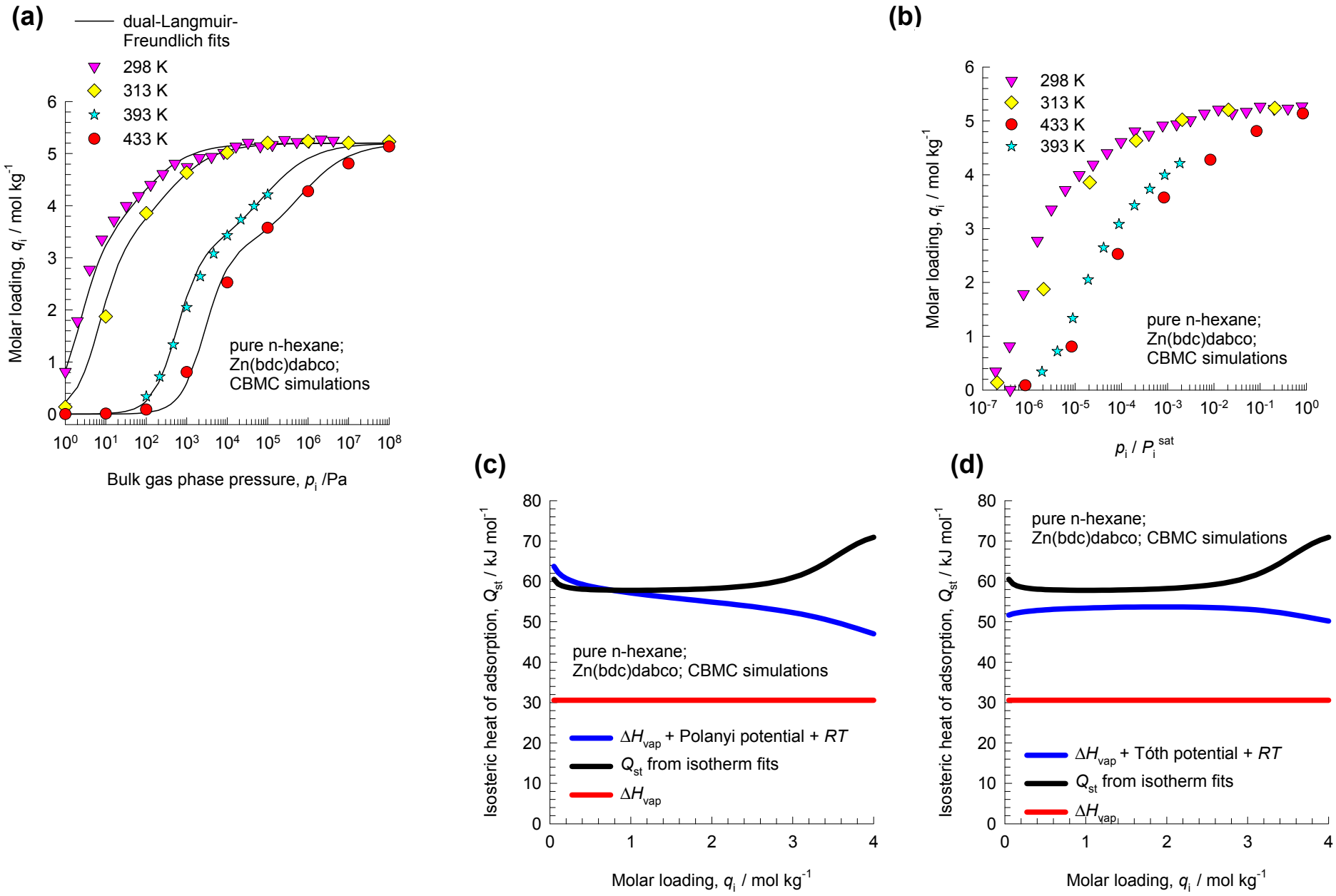

Figure 23

Methanol in MFI: Nayak Experiments

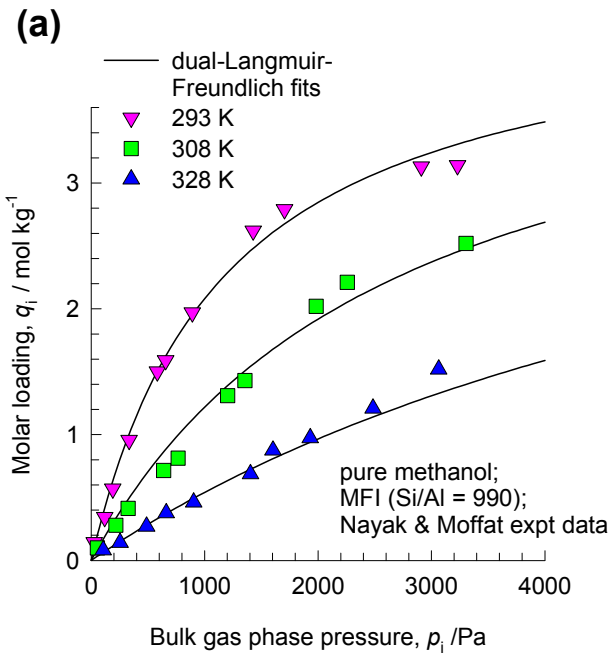

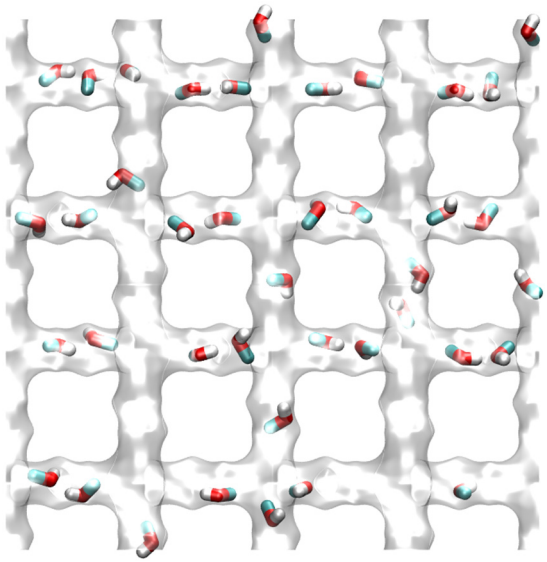

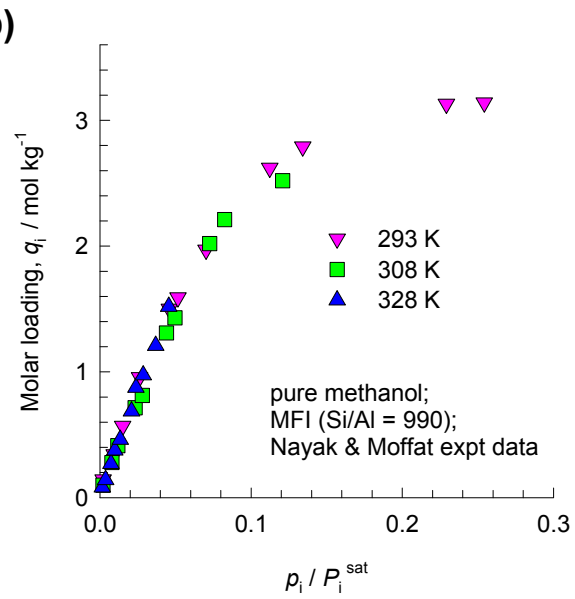

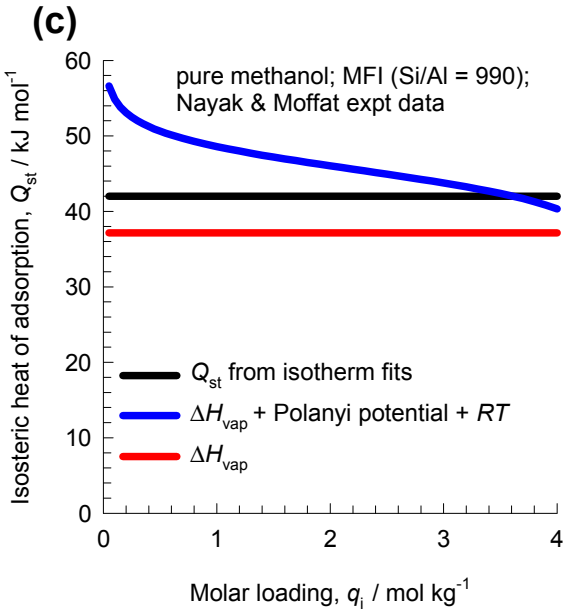

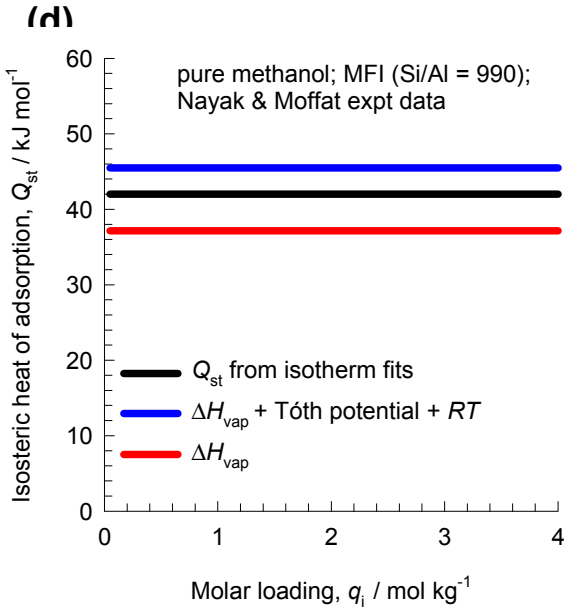

Figure 24

Propene in ZIF-8: Li & Böhme Experiments

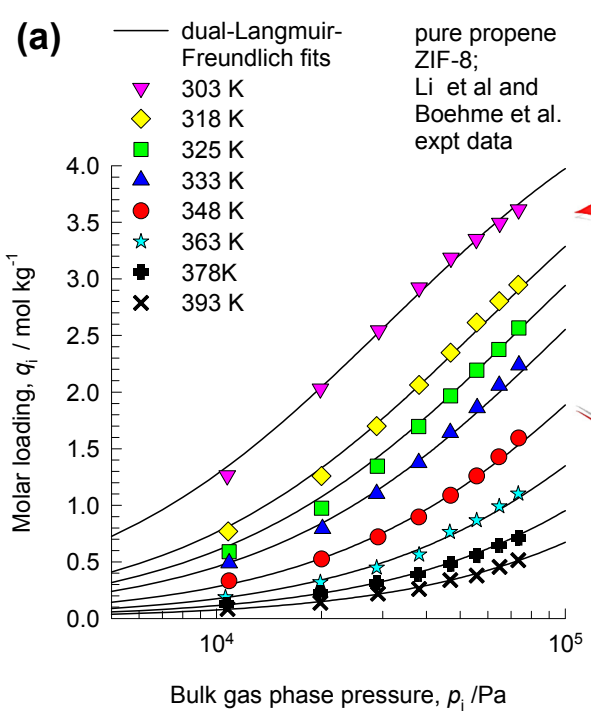

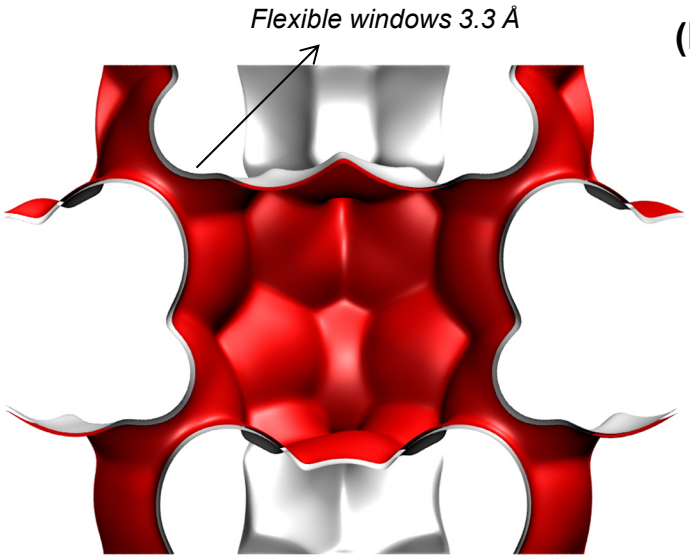

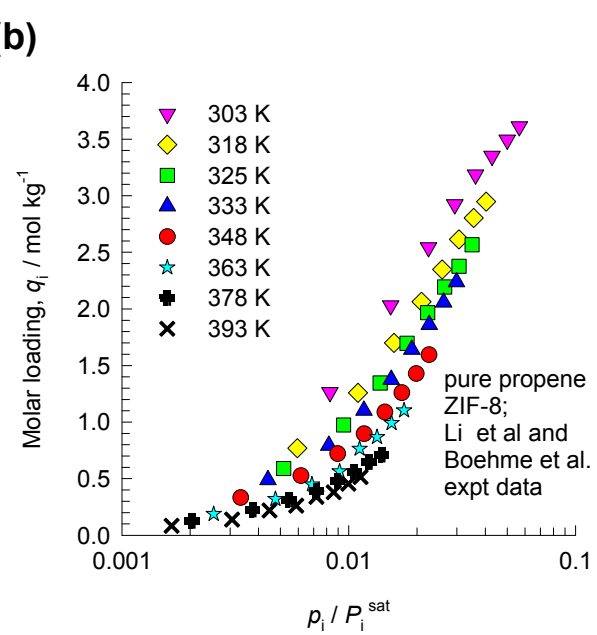

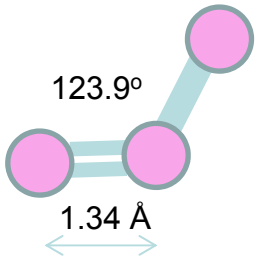

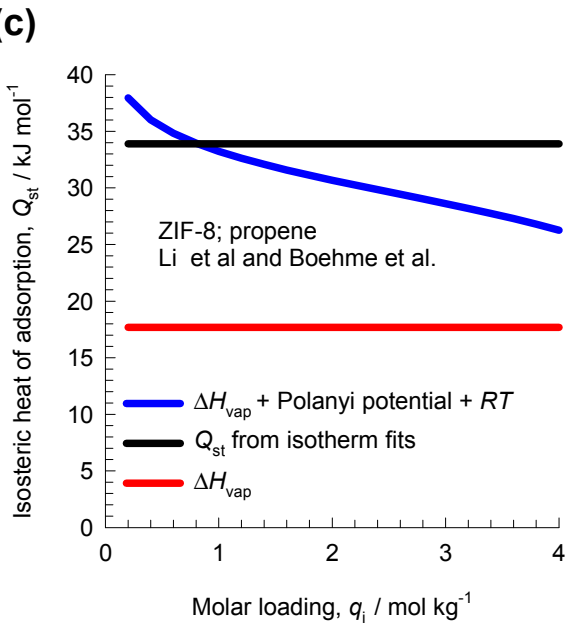

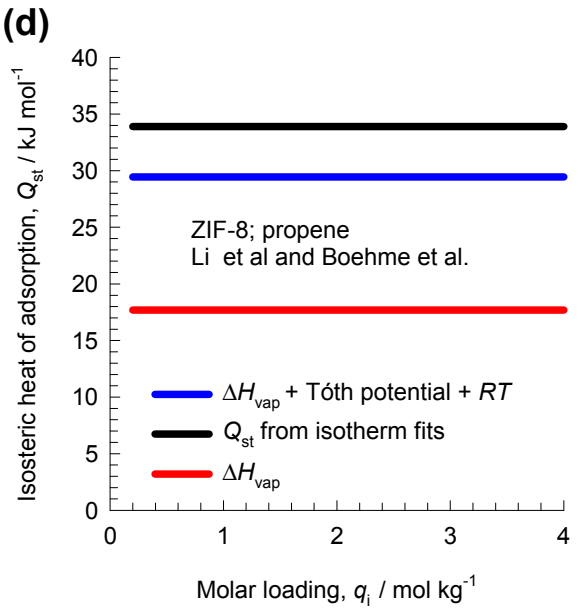

Figure 25

Propane in ZIF-8: Li & Böhme Experiments

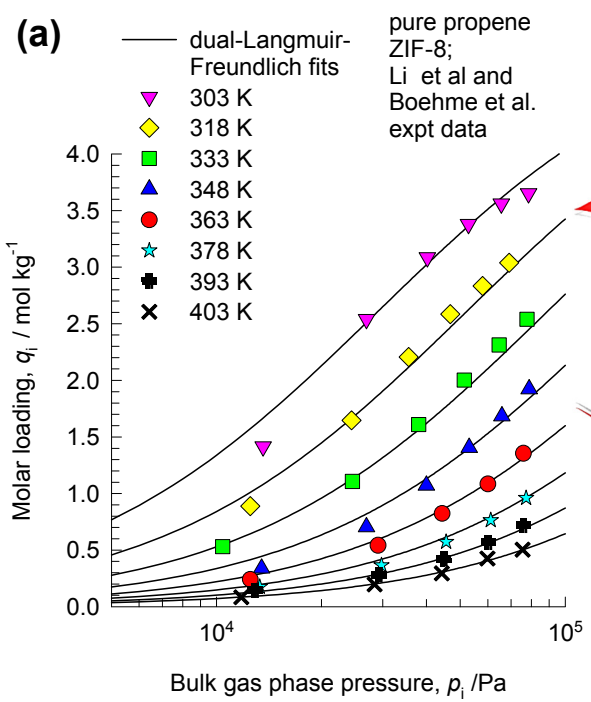

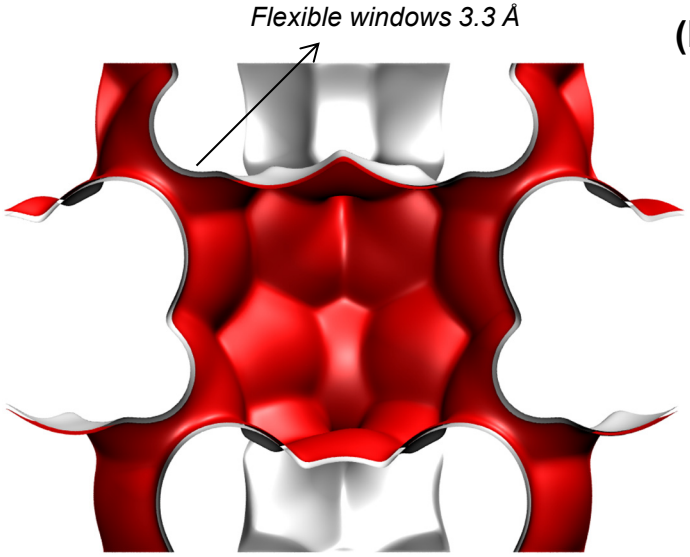

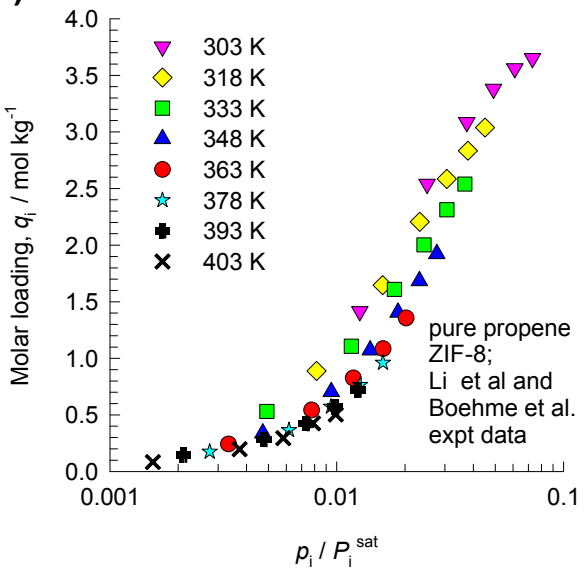

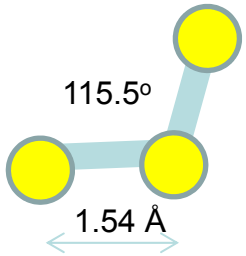

propane

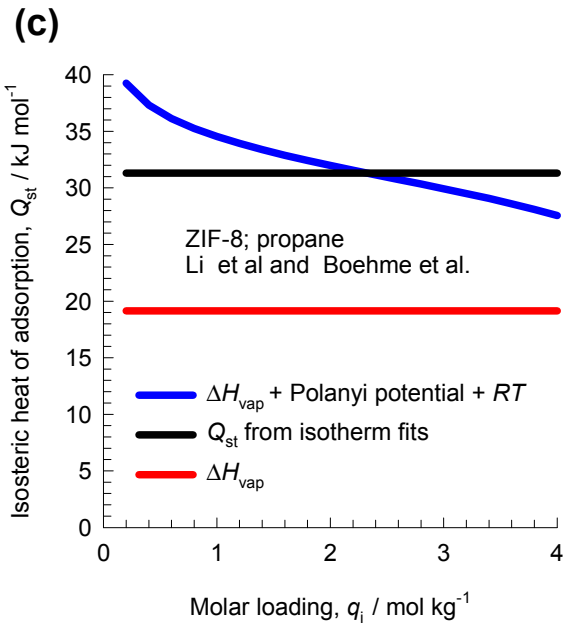

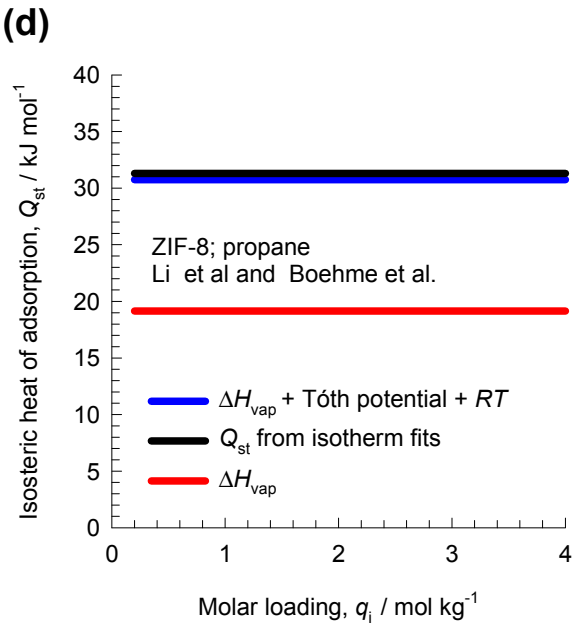

Figure 26

Ethyne in FeMOF-74: Bloch Experiments

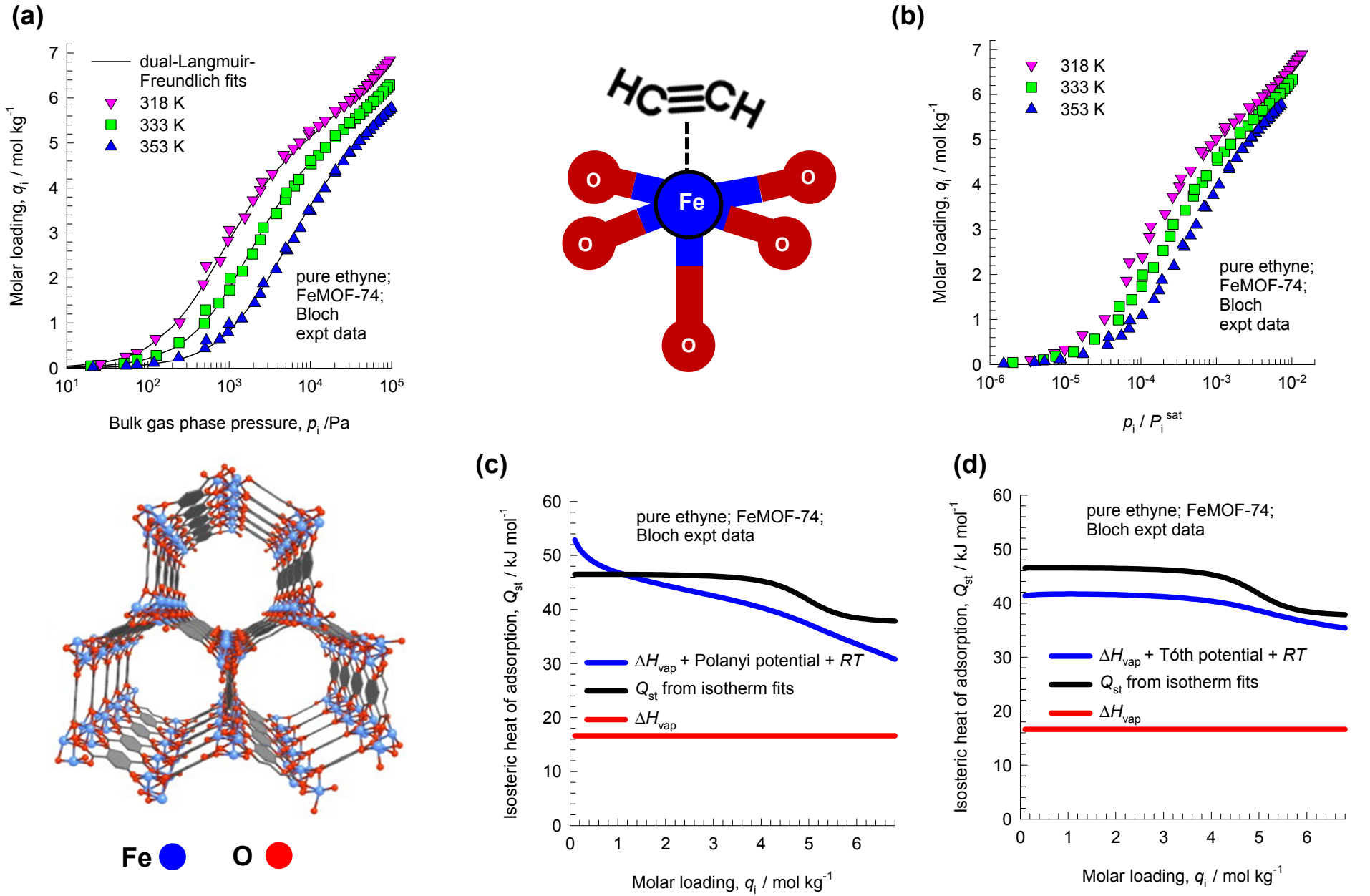

Figure 27

Propene in FeMOF-74: Bloch Experiments

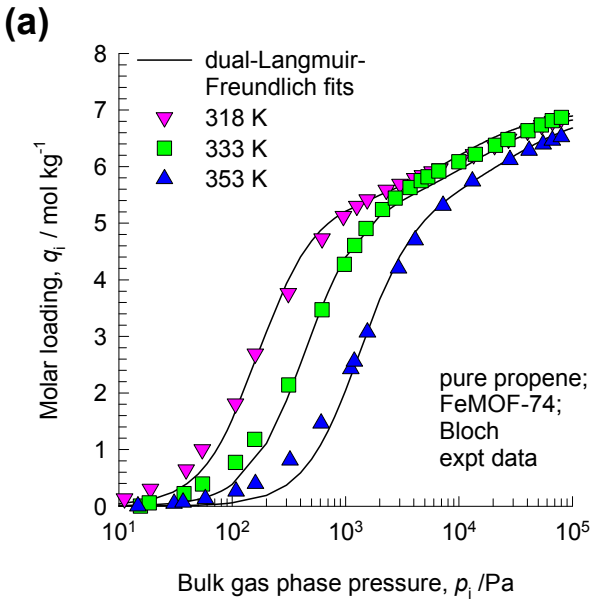

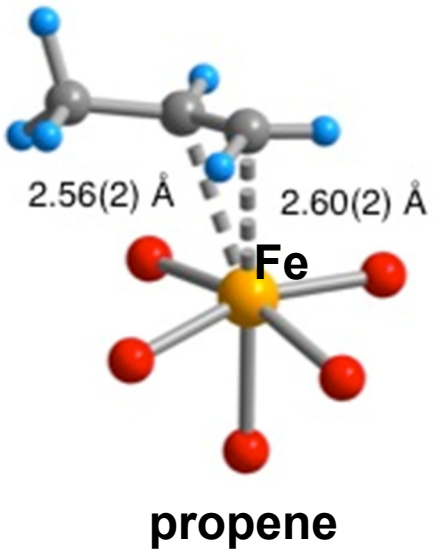

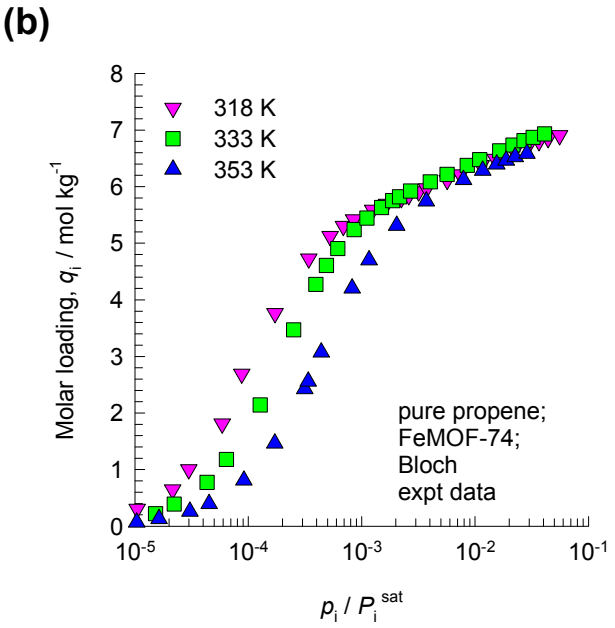

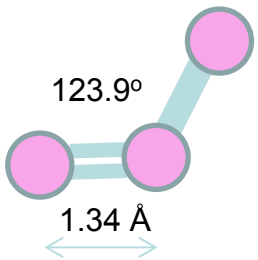

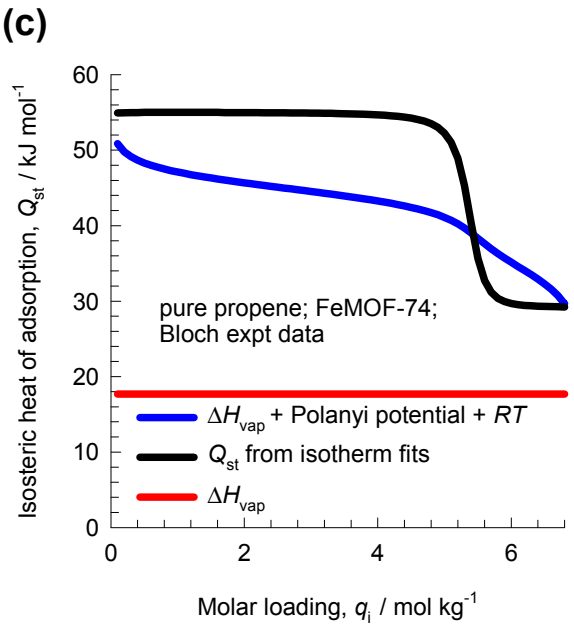

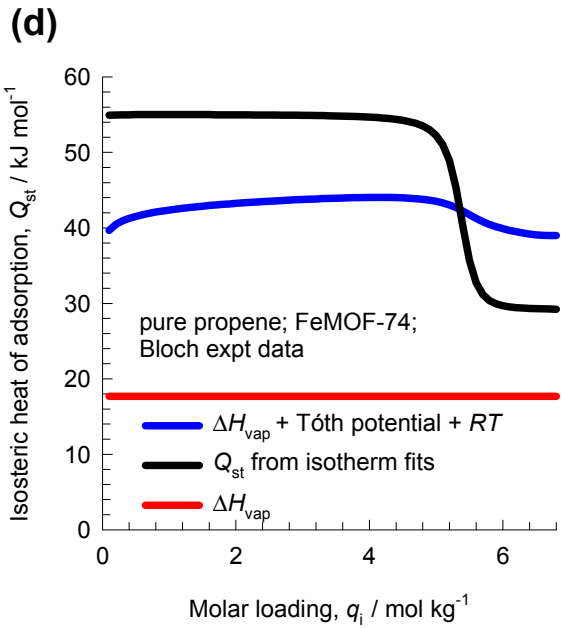

Figure 28

Propane in FeMOF-74: Bloch Experiments

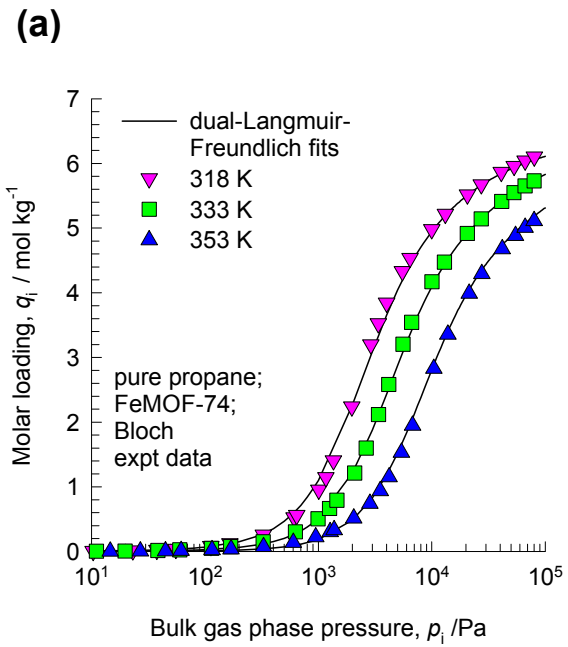

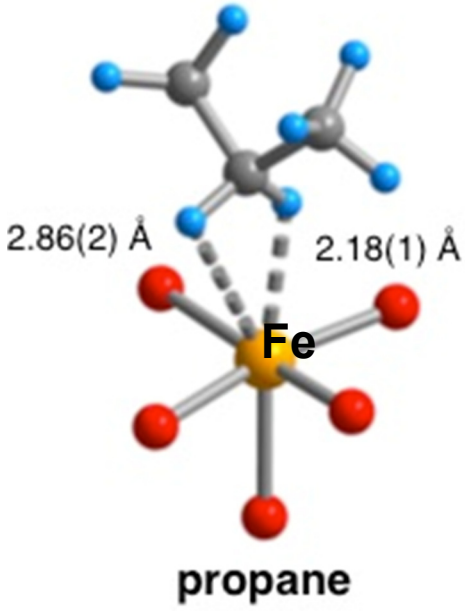

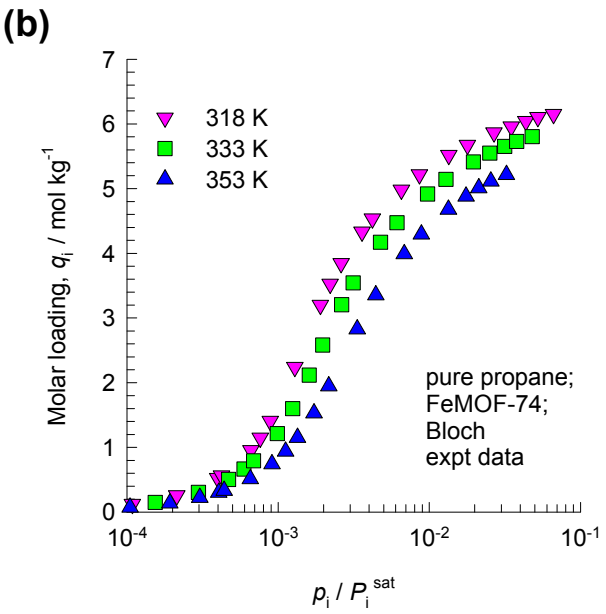

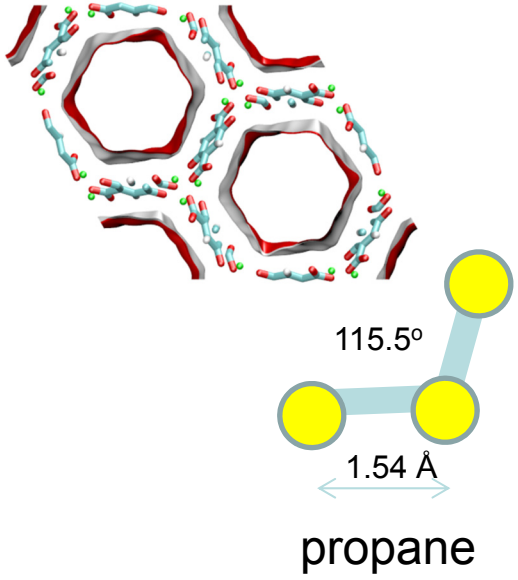

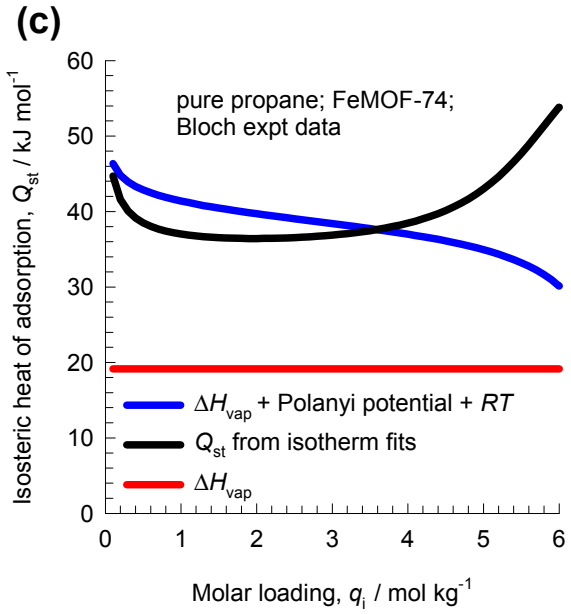

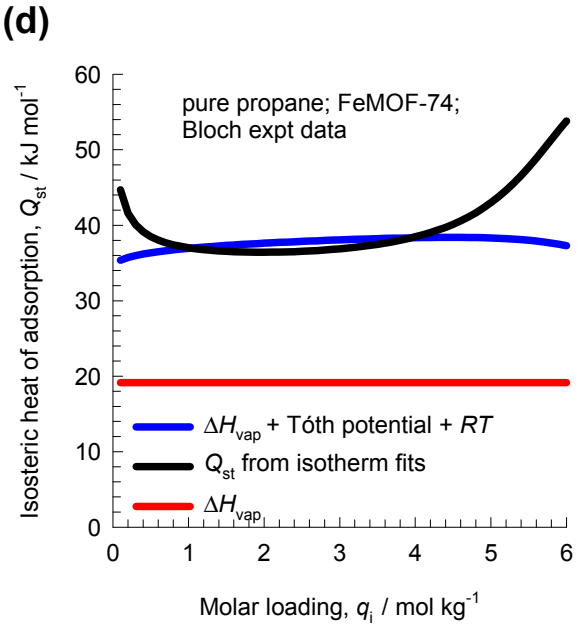

Figure 29

Ethyne in MgMOF-74: He Experiments

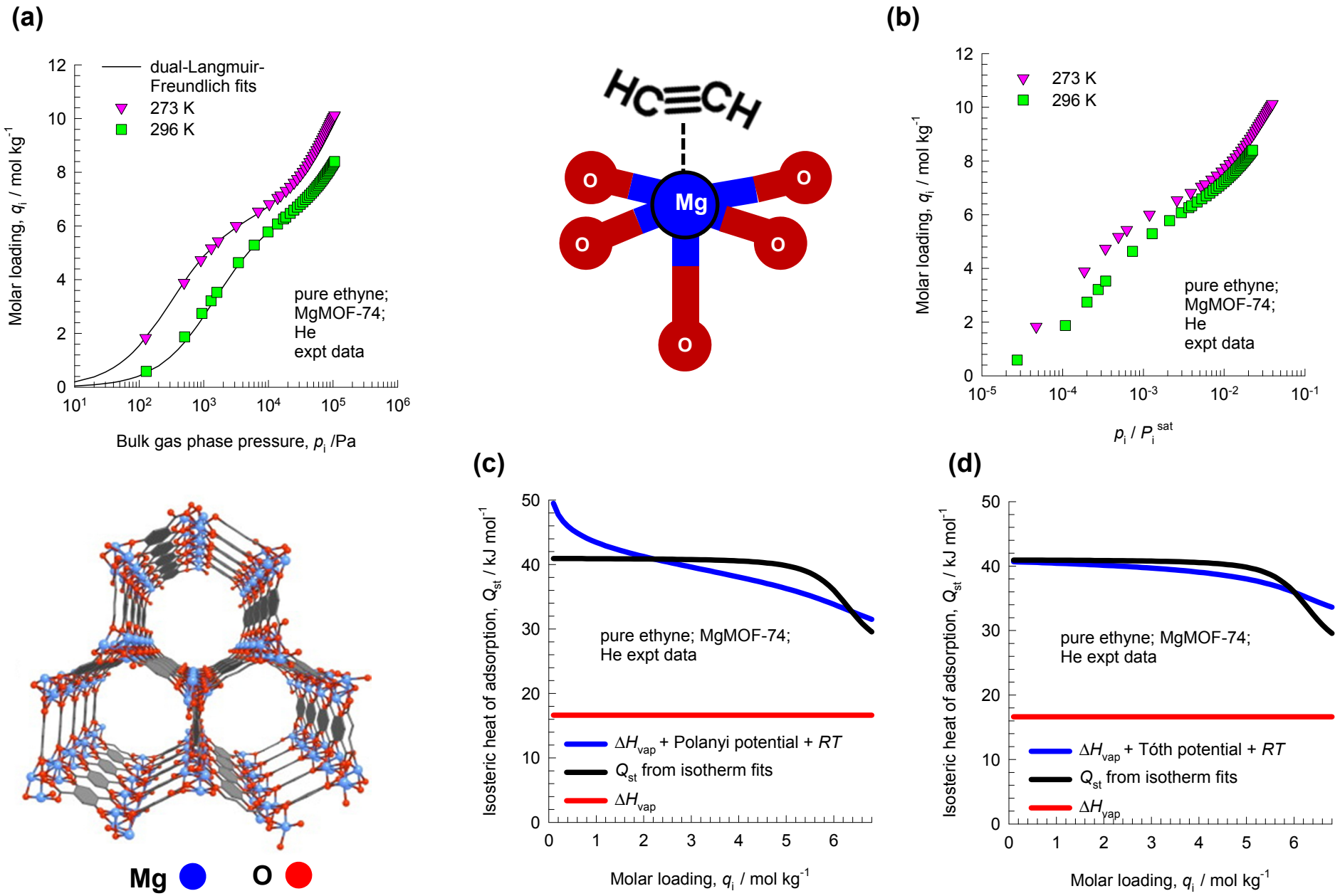

Figure 30

Propene in MgMOF-74: Bao Experiments

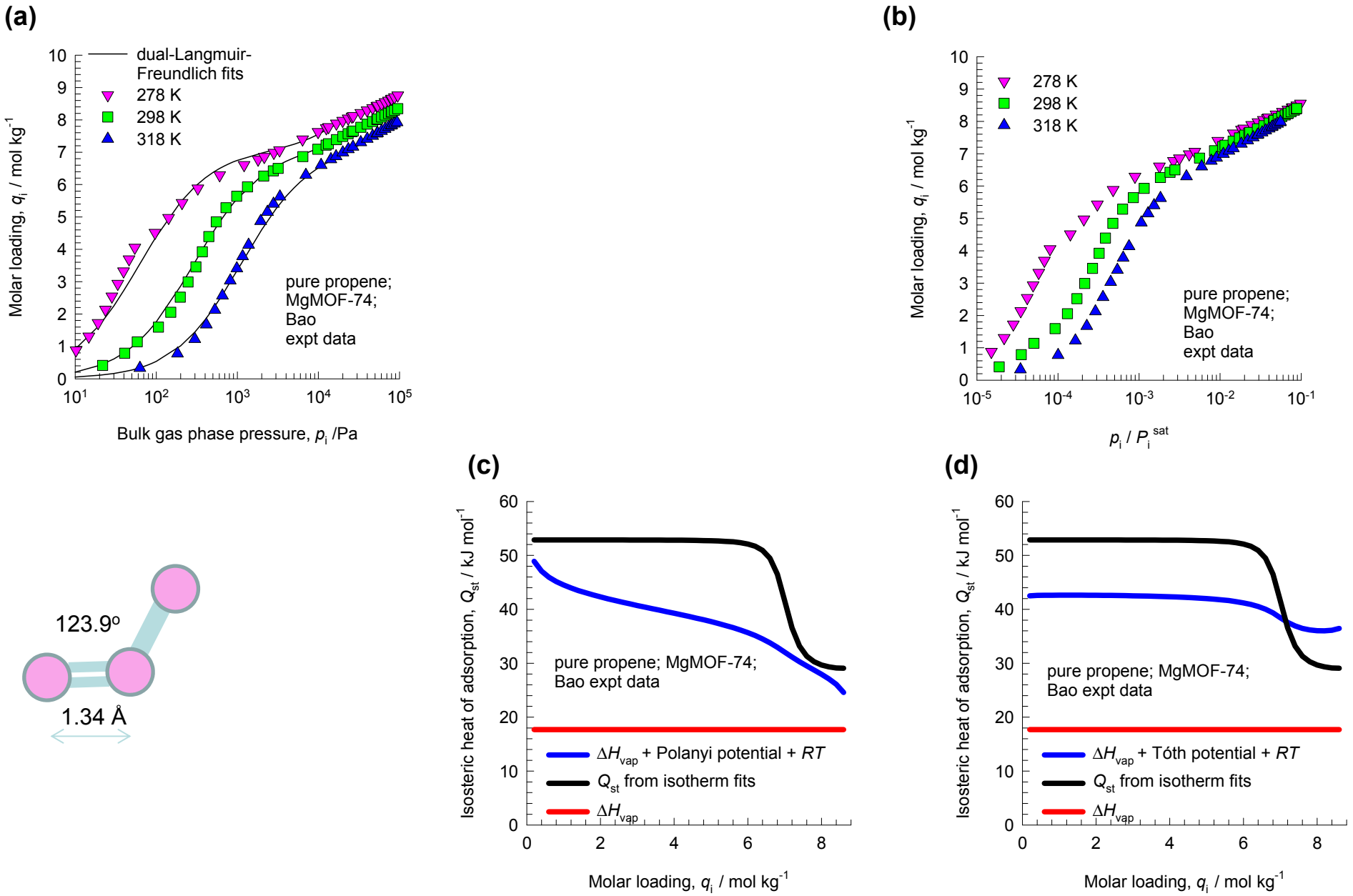

Figure 31

Propane in MgMOF-74: Bao Experiments

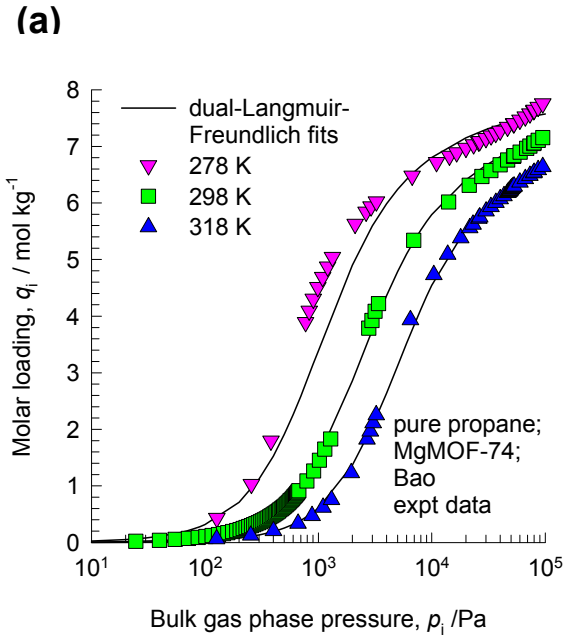

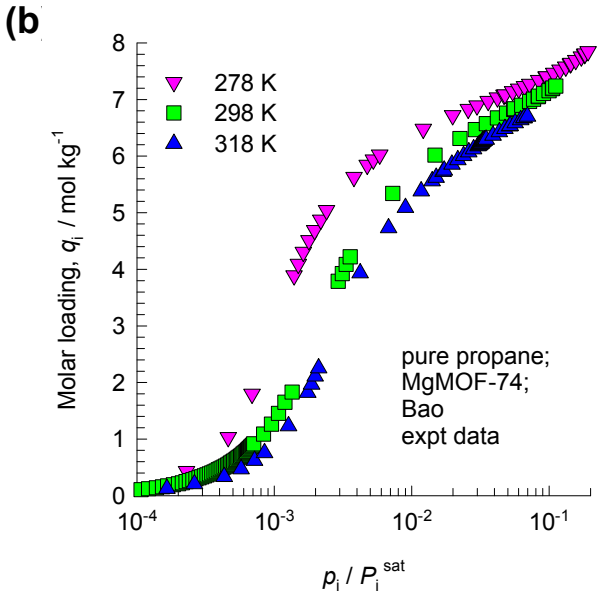

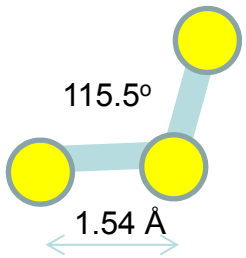

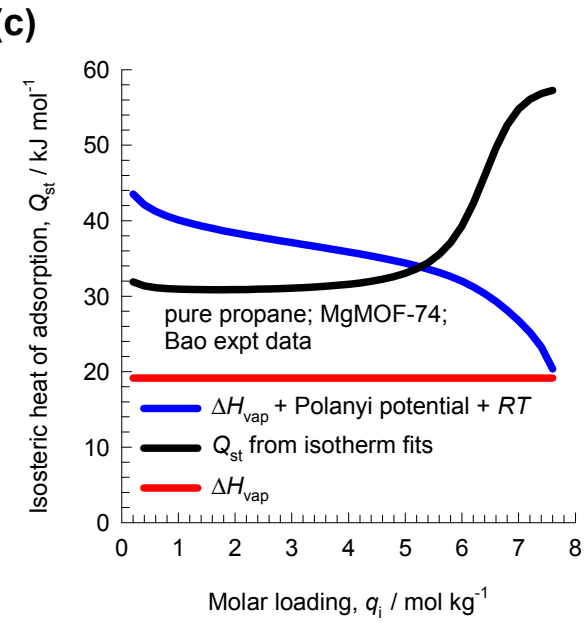

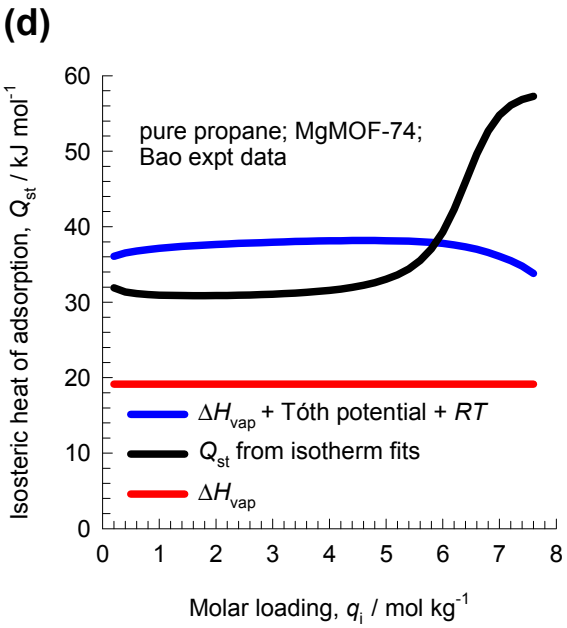

Figure 32

Propene in NaX zeolite: Costa Experiments

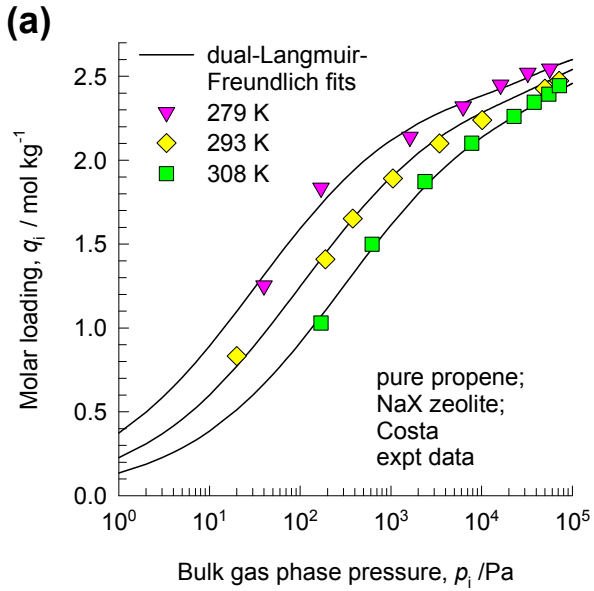

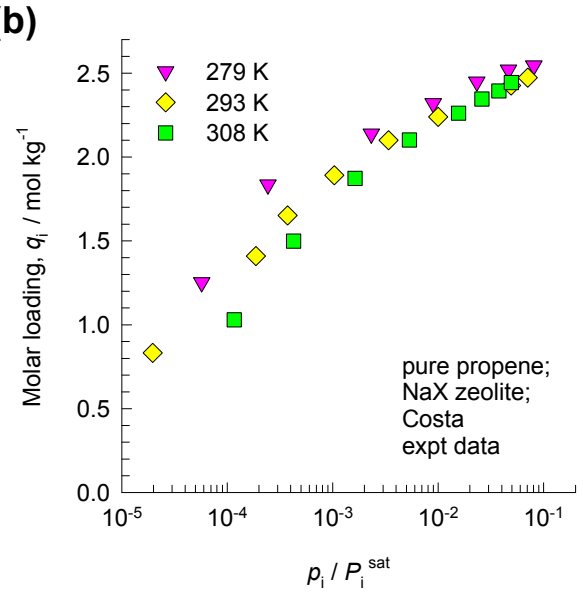

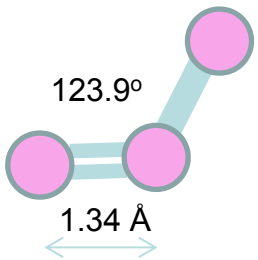

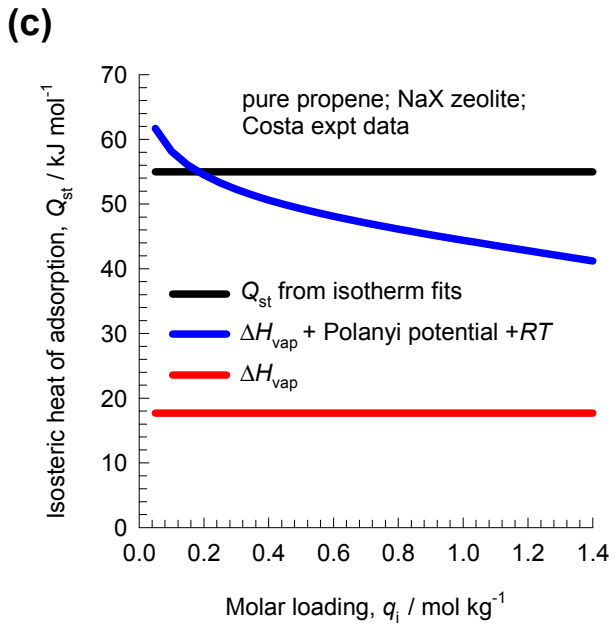

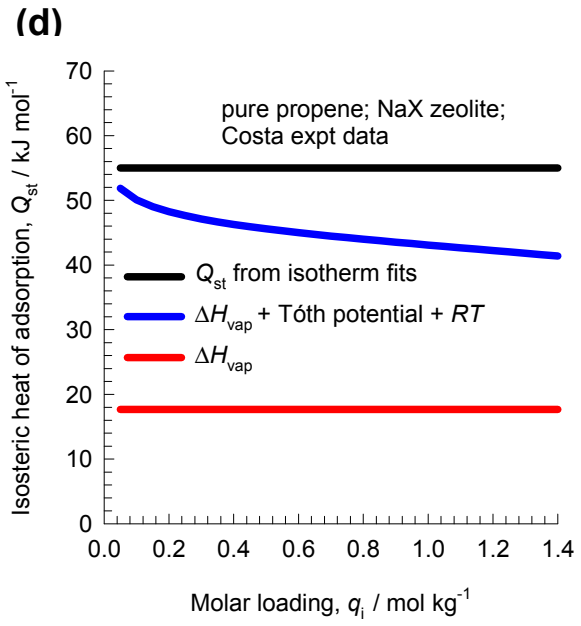

Figure 33

Propane in NaX zeolite: Costa Experiments

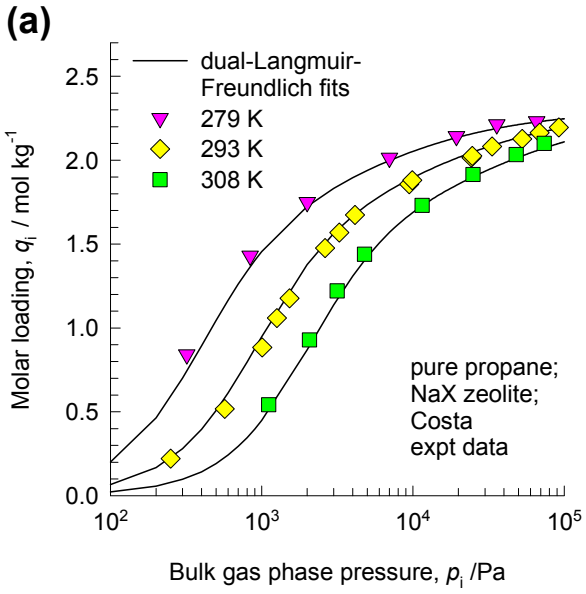

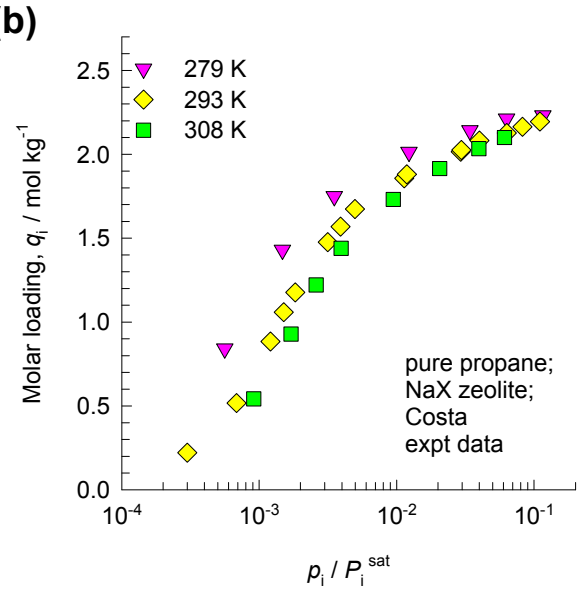

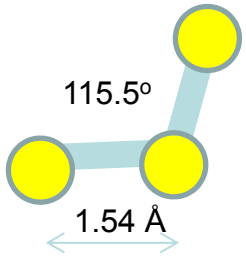

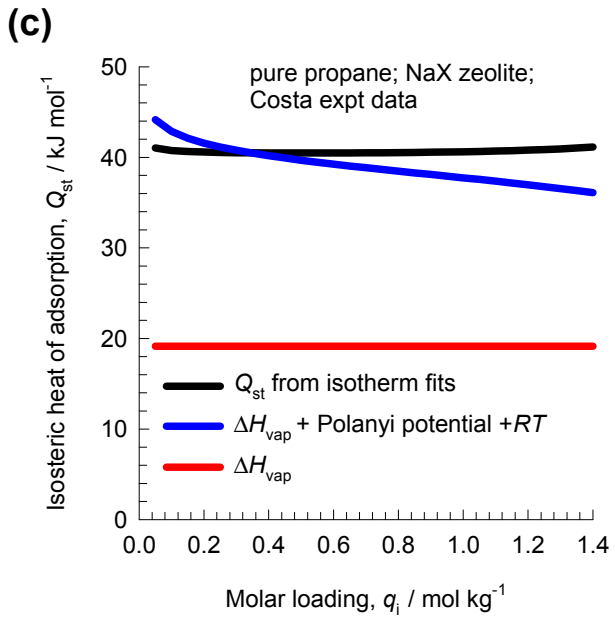

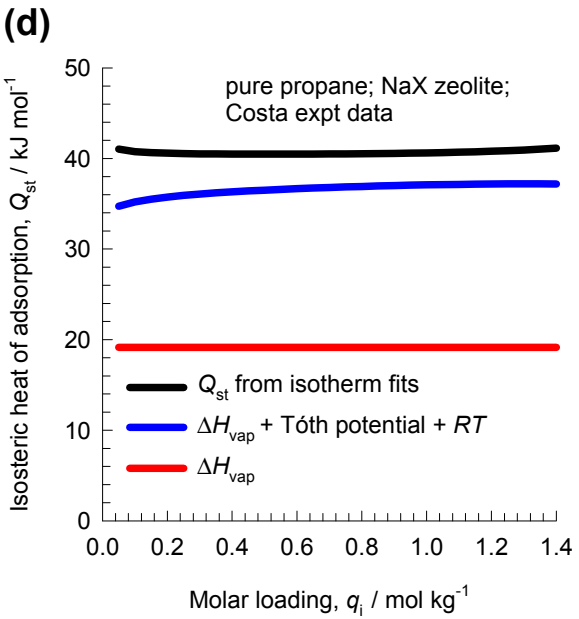

Figure 34

isobutane in NaX zeolite: Granato Experiments

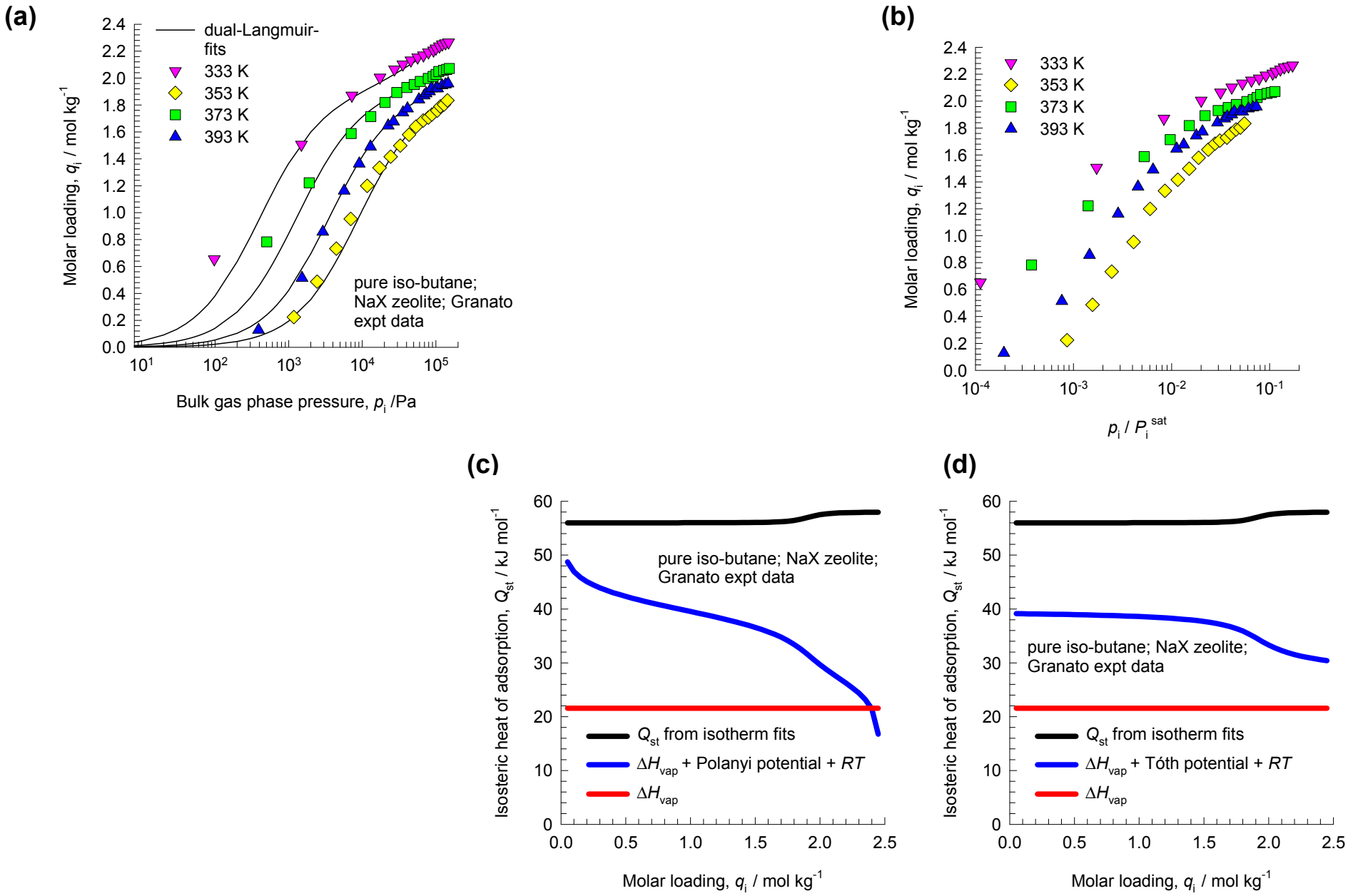

Figure 35

1-butene in NaX zeolite: Granato Experiments

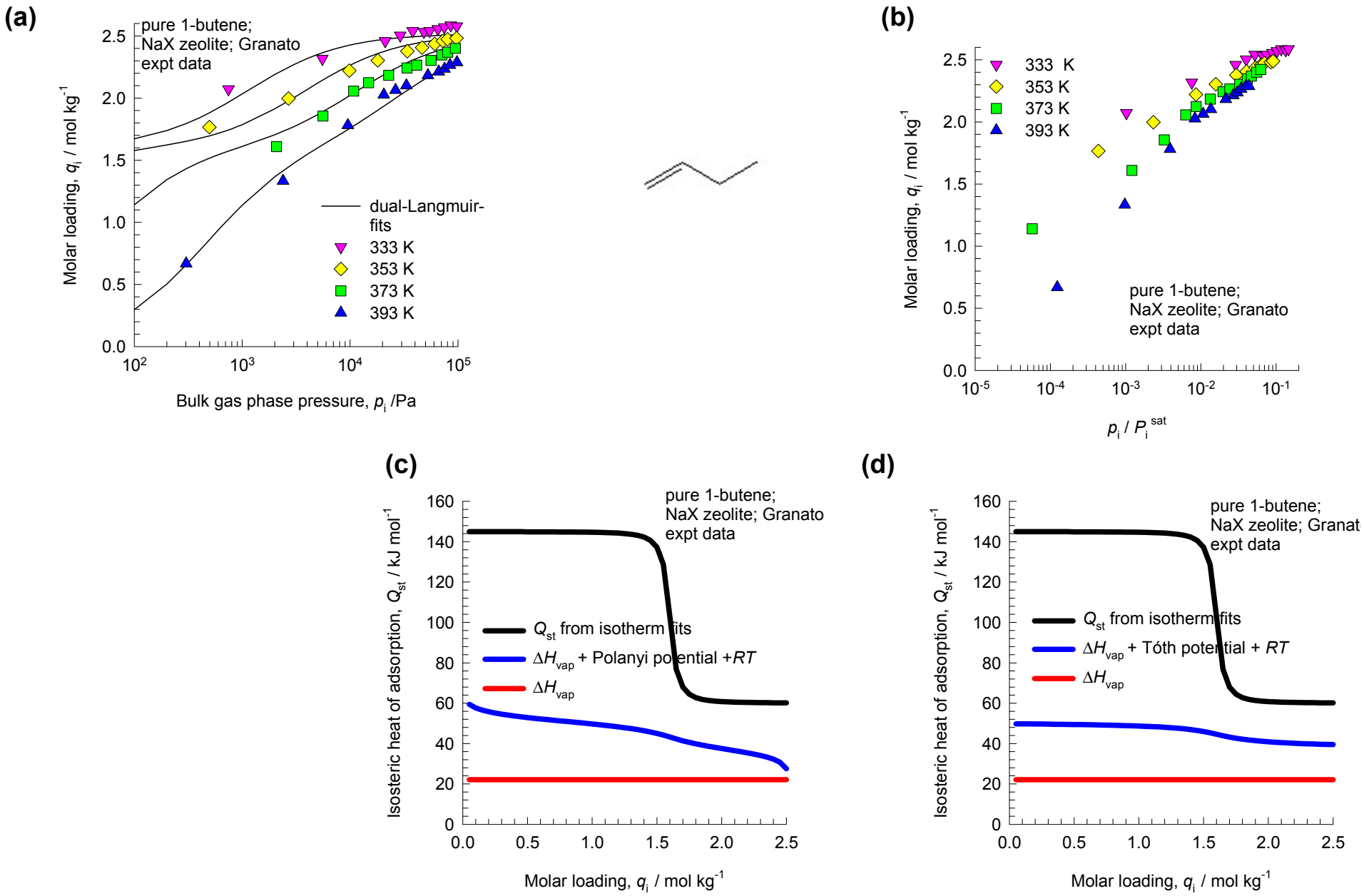

Figure 36

o-xylene in AFI zeolite: Chiang Experiments

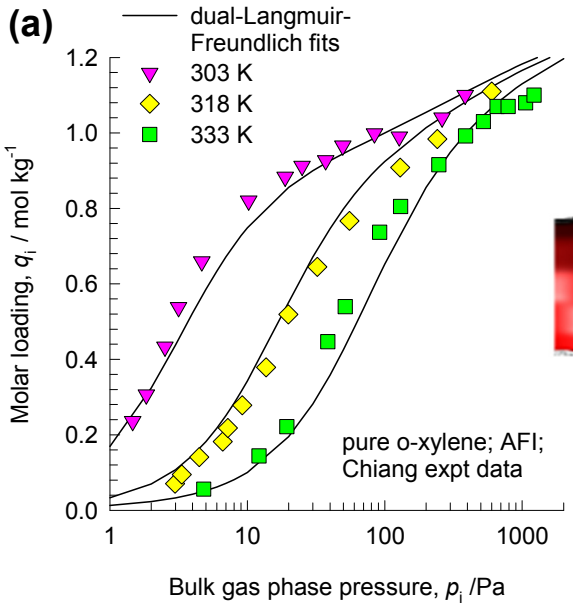

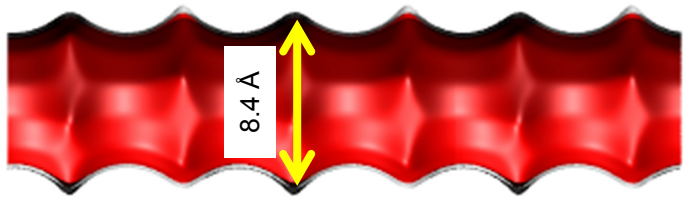

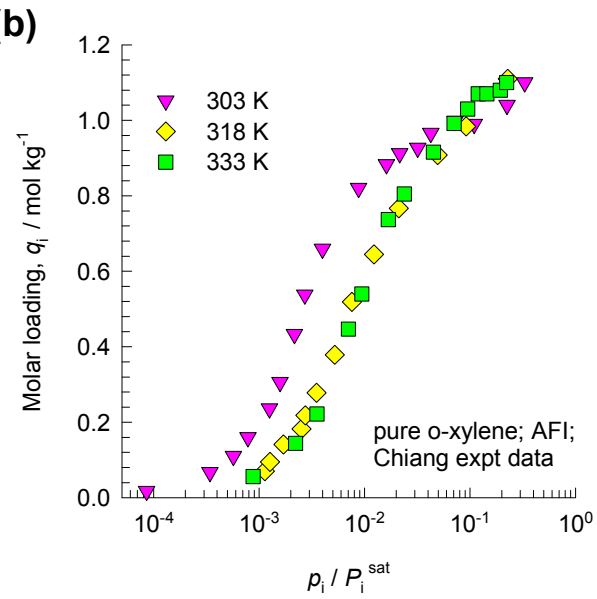

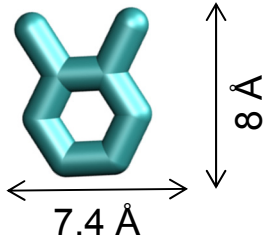

o-xylene can fit nicely within the 8.4 Å grooves of AFI

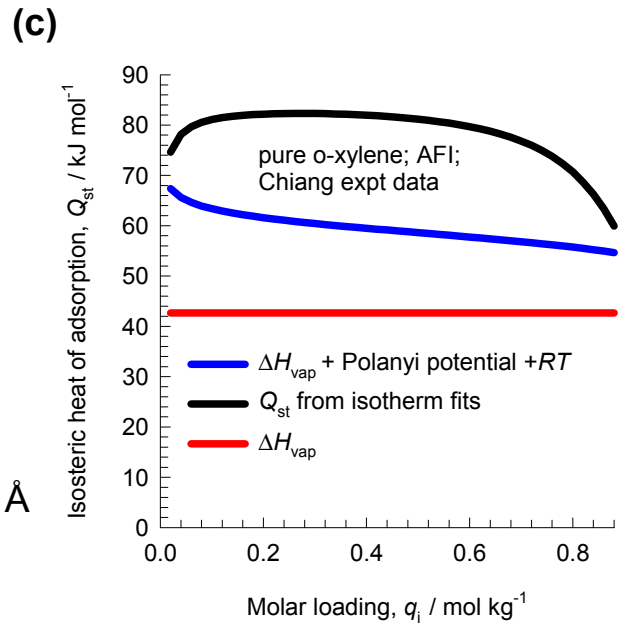

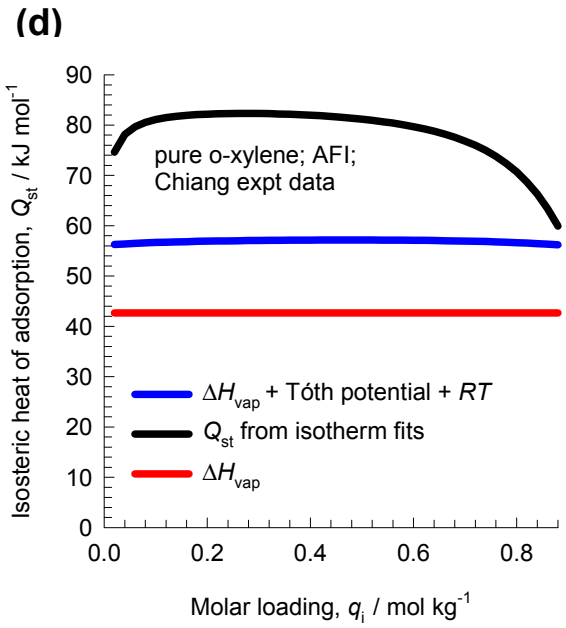

Figure 37

m-xylene in AFI zeolite: Chiang Experiments

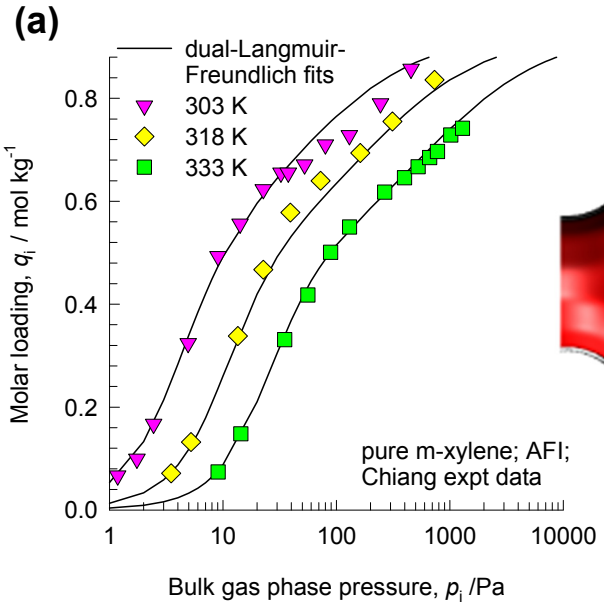

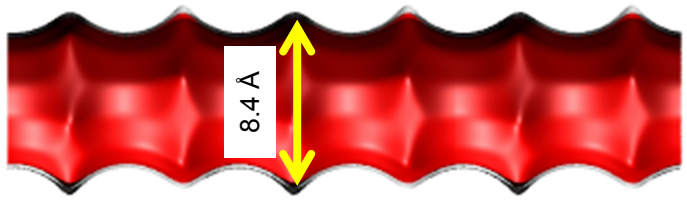

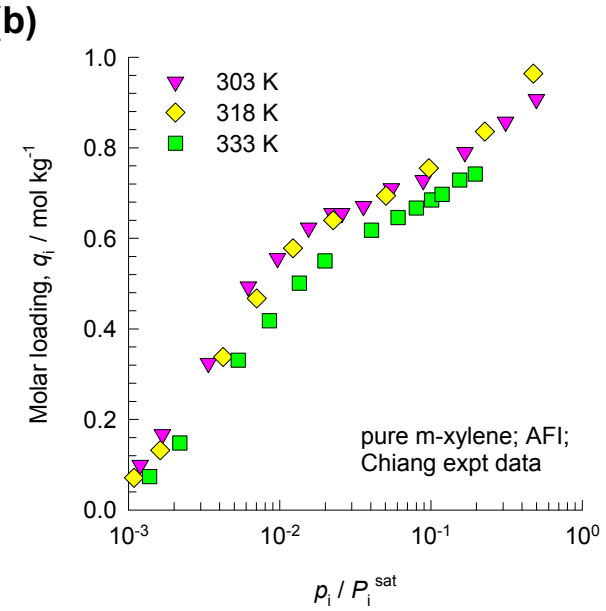

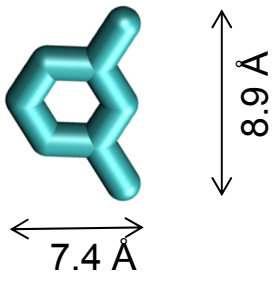

m-xylene is too "tall" to locate within the 8.4 Å grooves of AFI

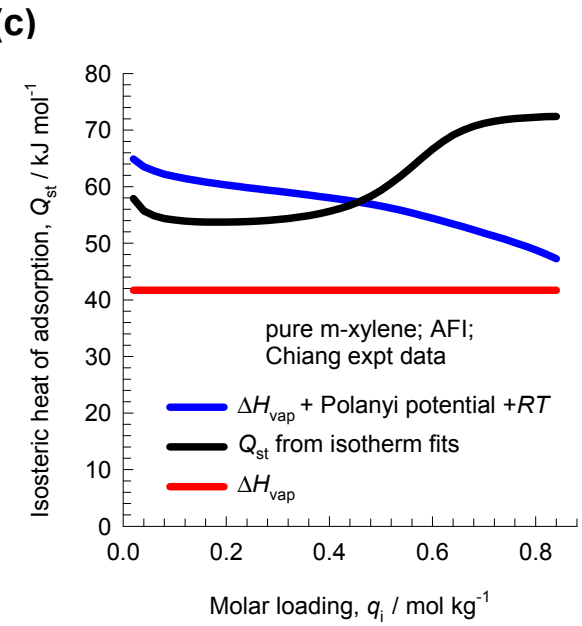

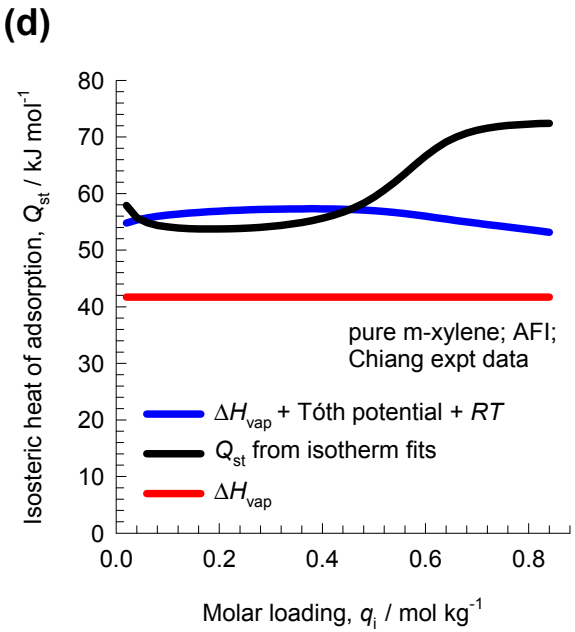

Figure 38

p-xylene in AFI zeolite: Chiang Experiments

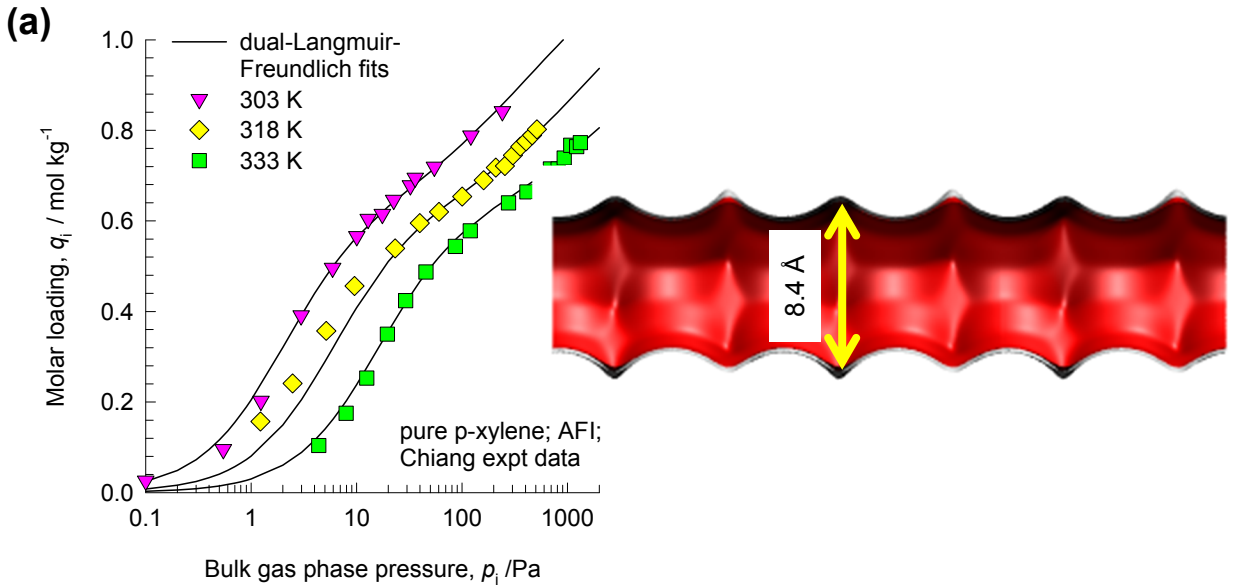

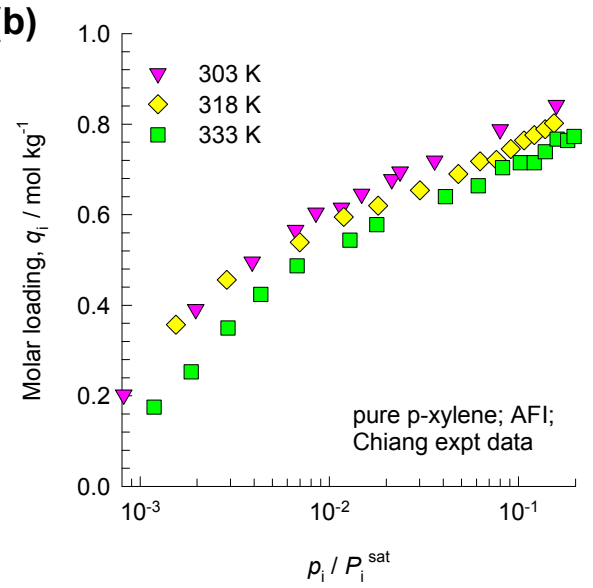

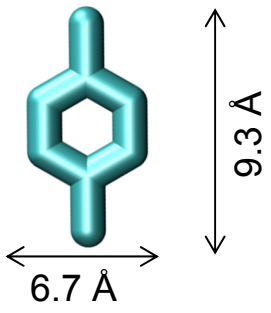

p-xylene is too "tall" to locate within the 8.4 Å grooves of AFI

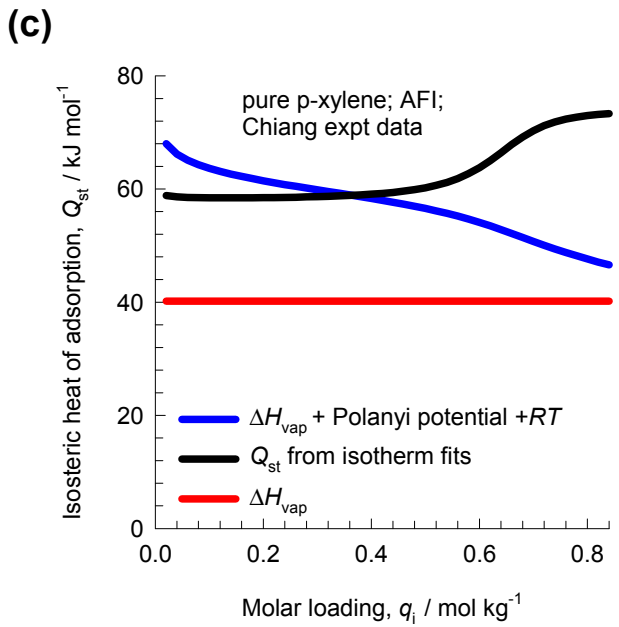

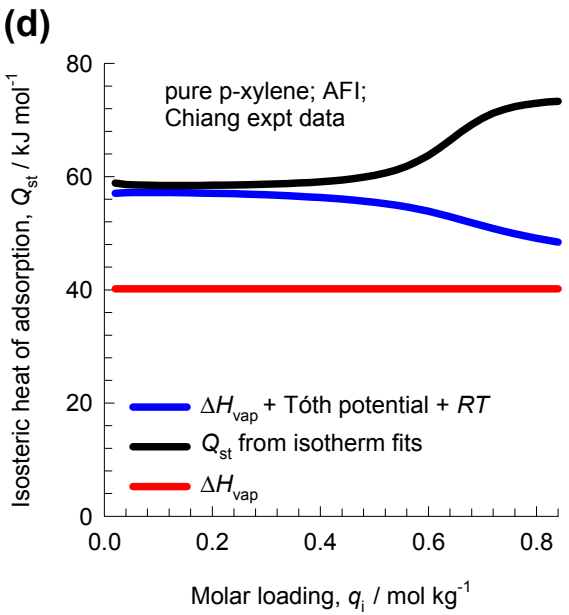

Q_{st} comparisons in AFI zeolite

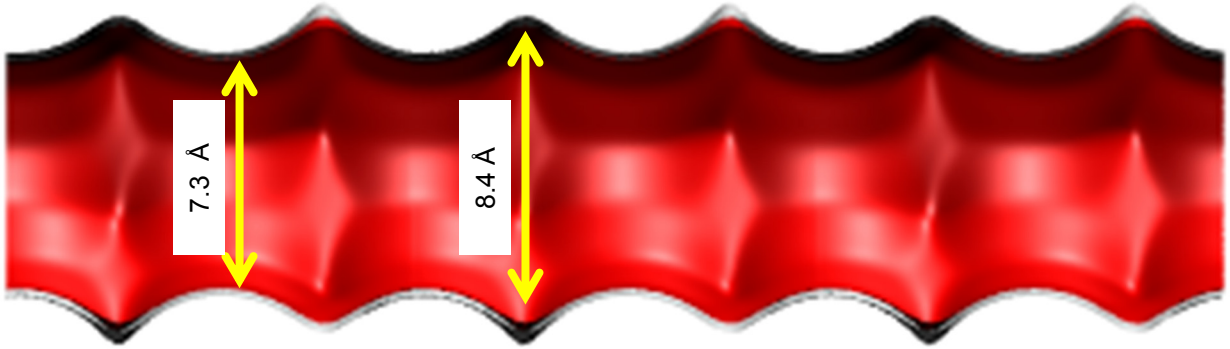

Only o-xylene can locate within the 8.4 Å grooves

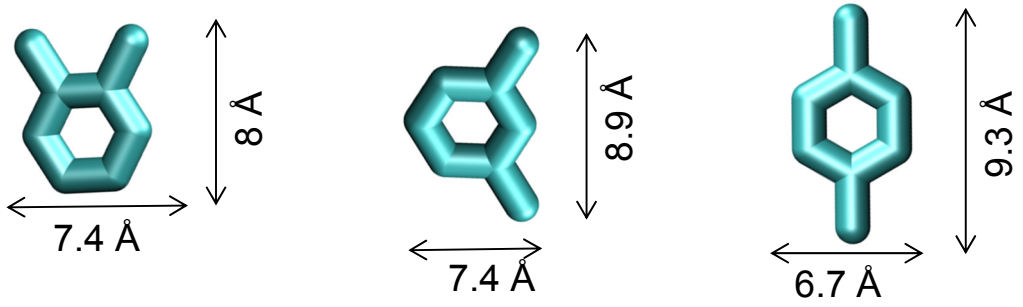

o-xylene (oX) m-xylene (mX) p-xylene (pX)

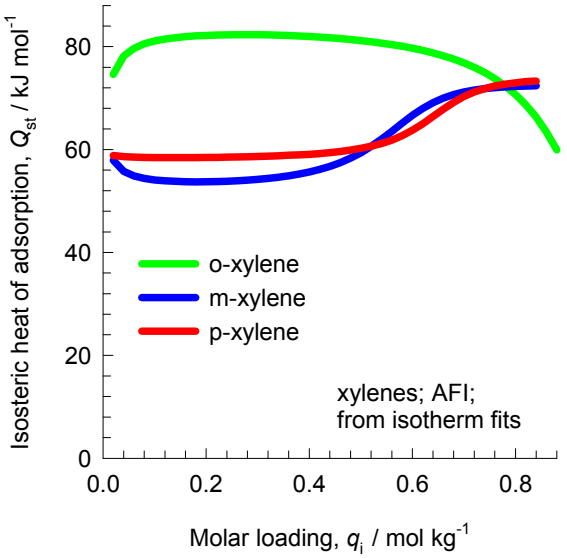

Figure 40

Benzene in MFI: Lee & Chiang Experiments

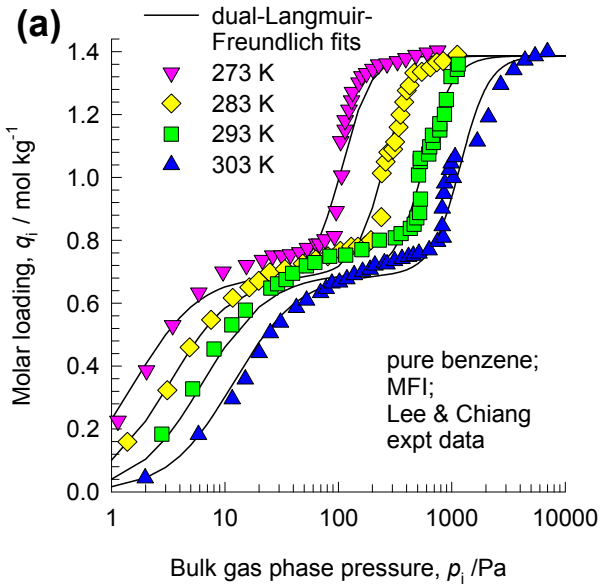

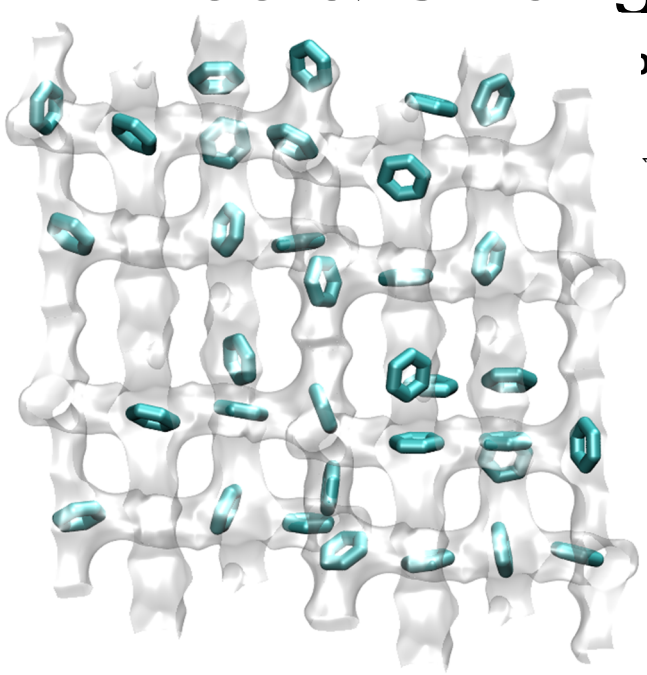

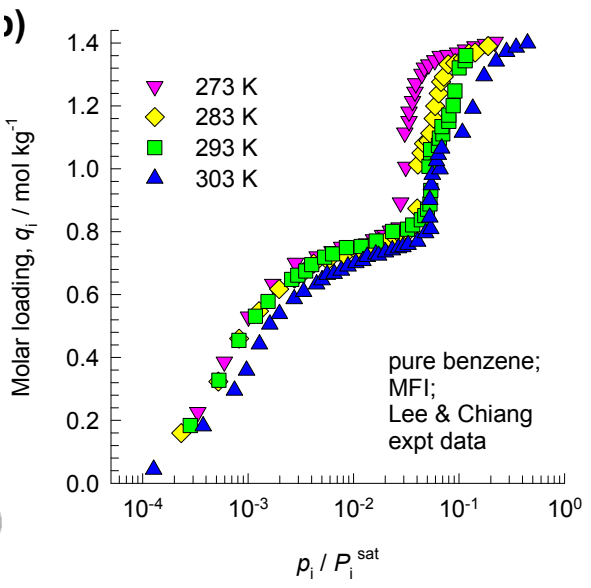

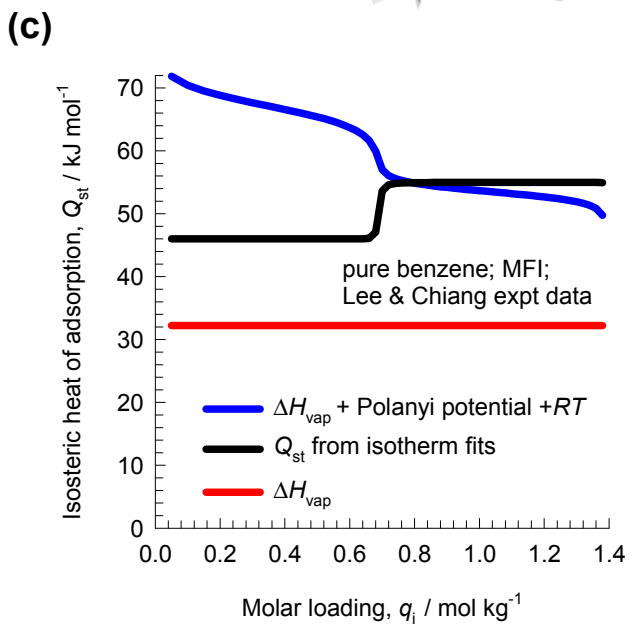

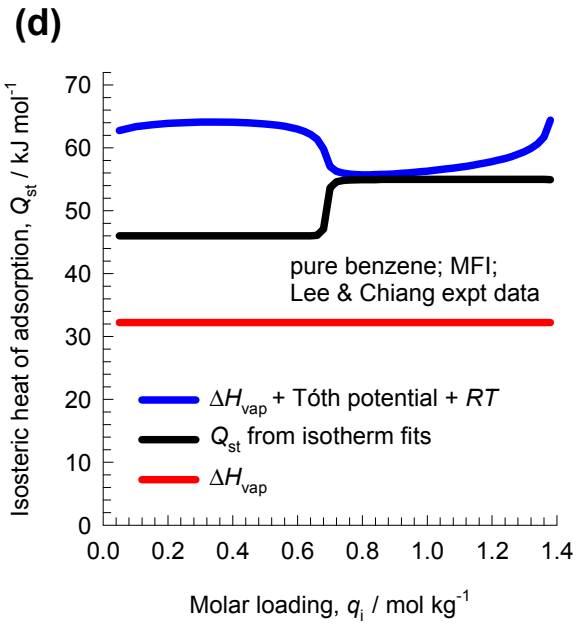

Figure 41

Toluene in MFI: Lee & Chiang Experiments

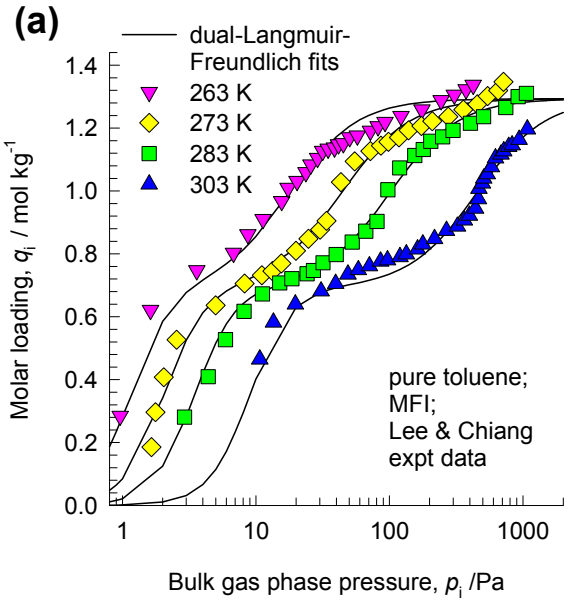

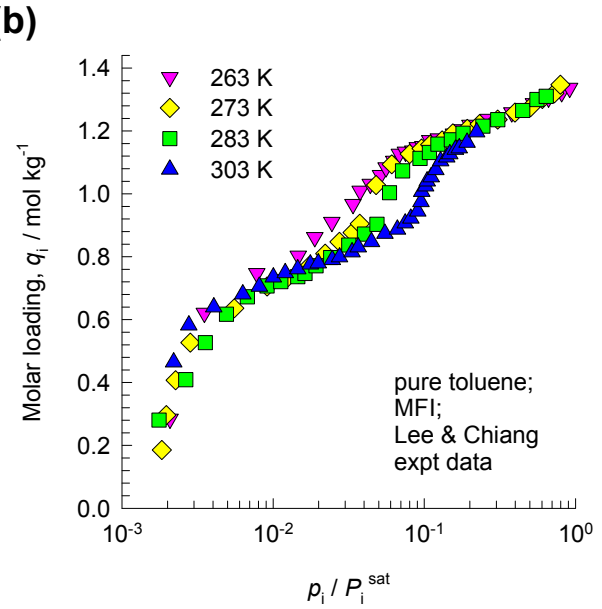

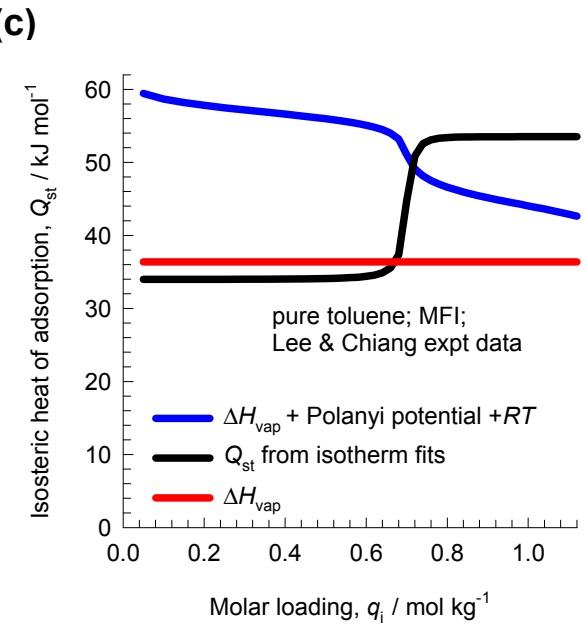

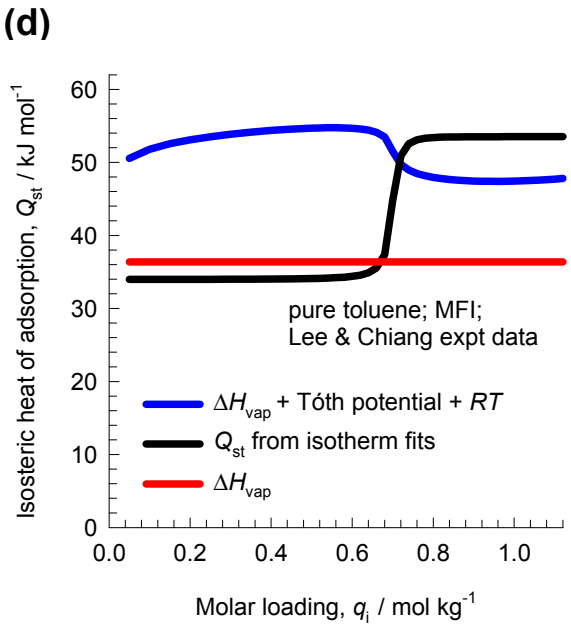

Figure 42

p-Xylene in MFI: Lee & Chiang Experiments

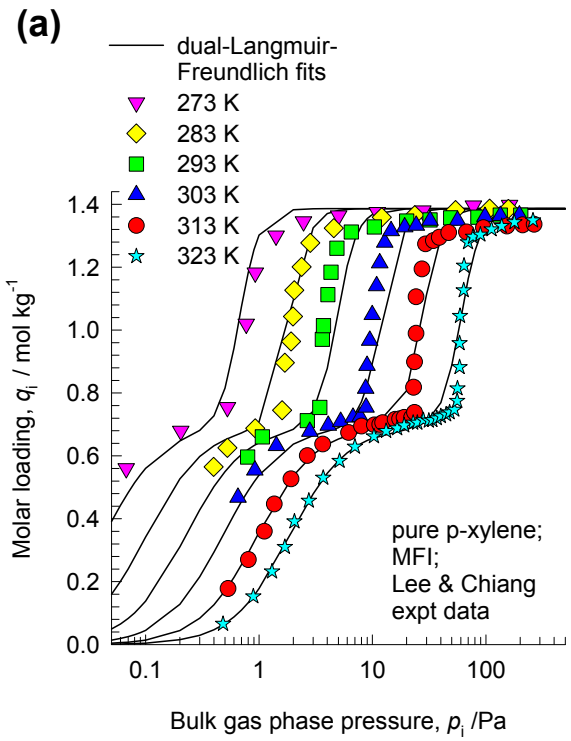

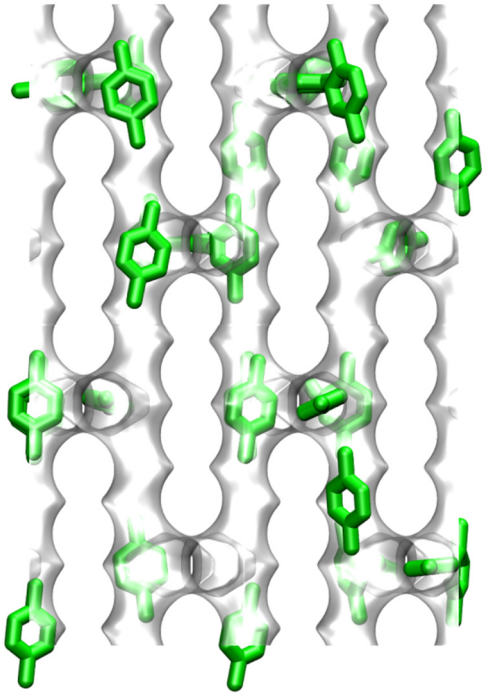

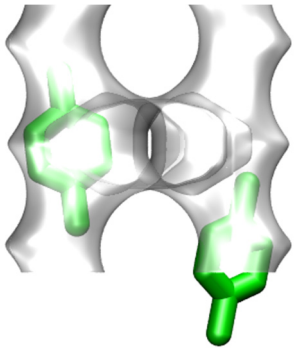

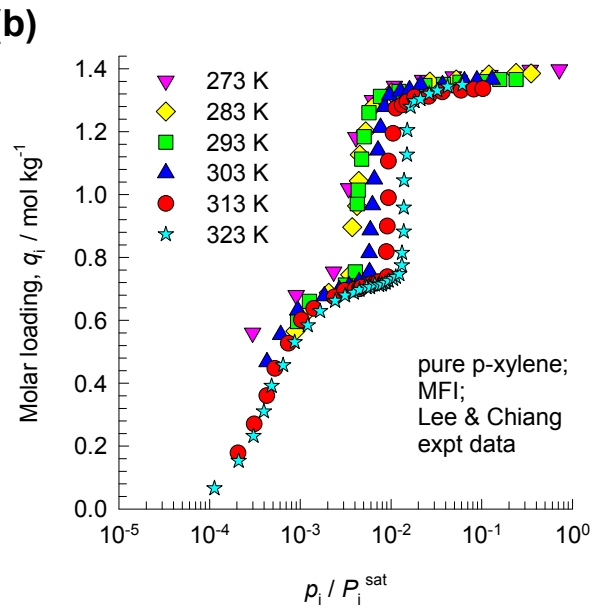

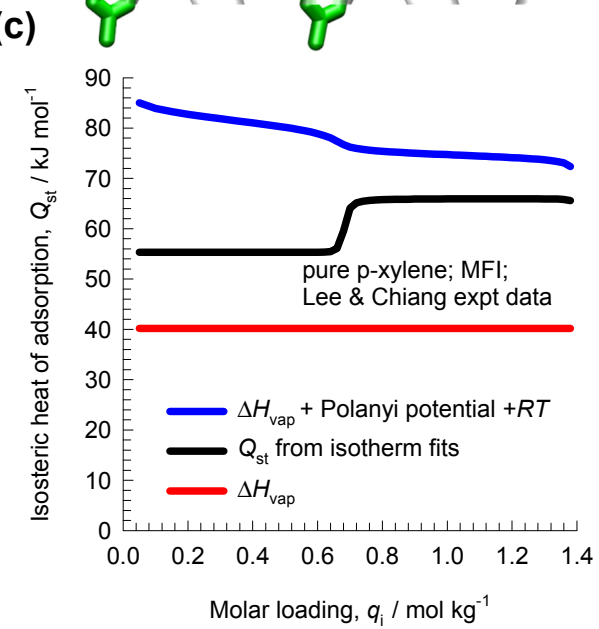

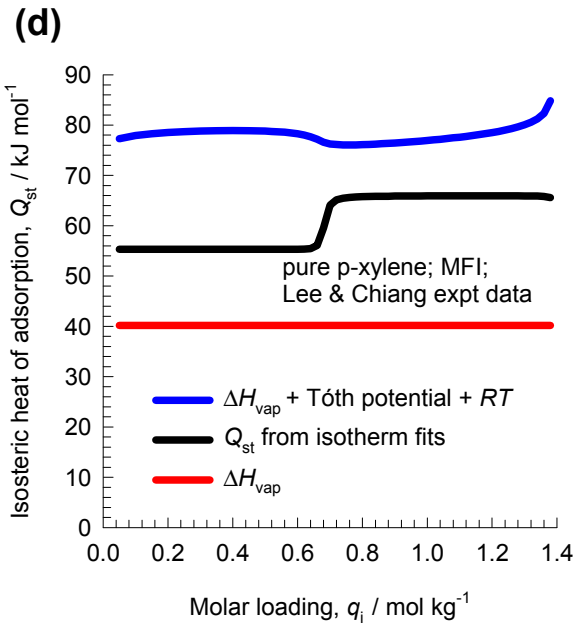

Figure 43

Ethylbenzene in MFI: Lee & Chiang Experiments

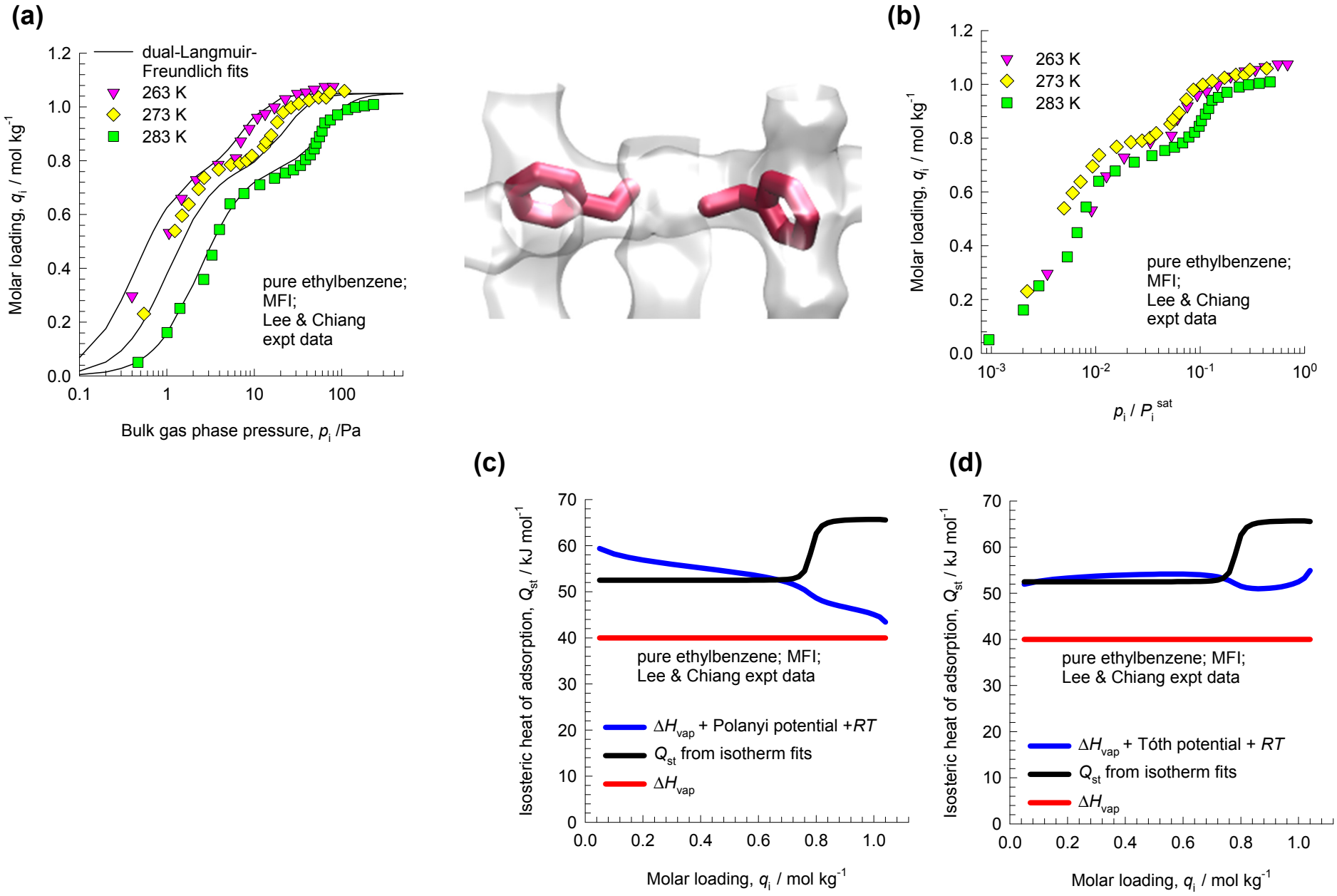

Figure 44

Iso-butane in MFI: Sun & Zhu Experiments

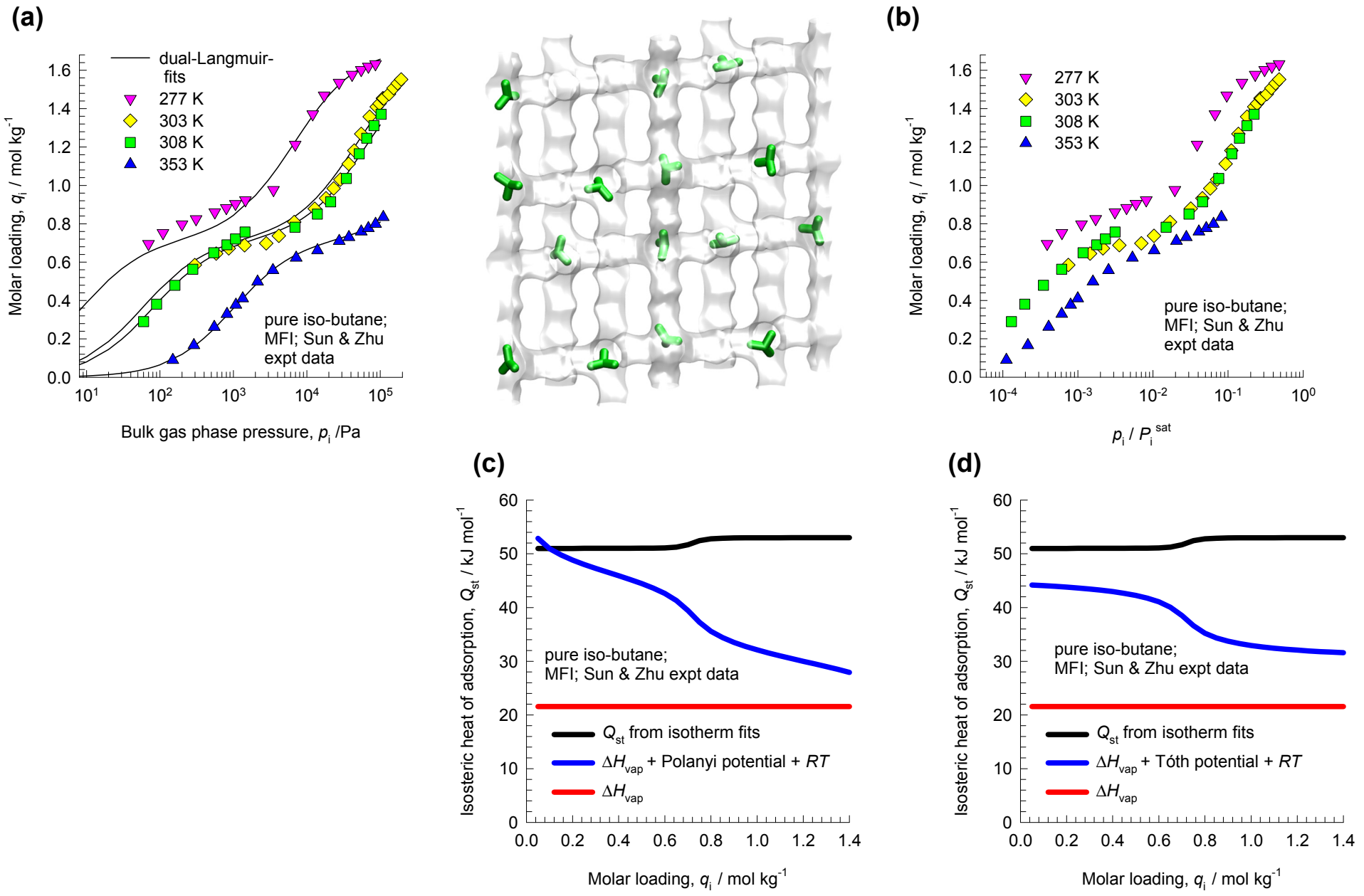

Figure 45

Iso-butane in MFI: CBMC simulations

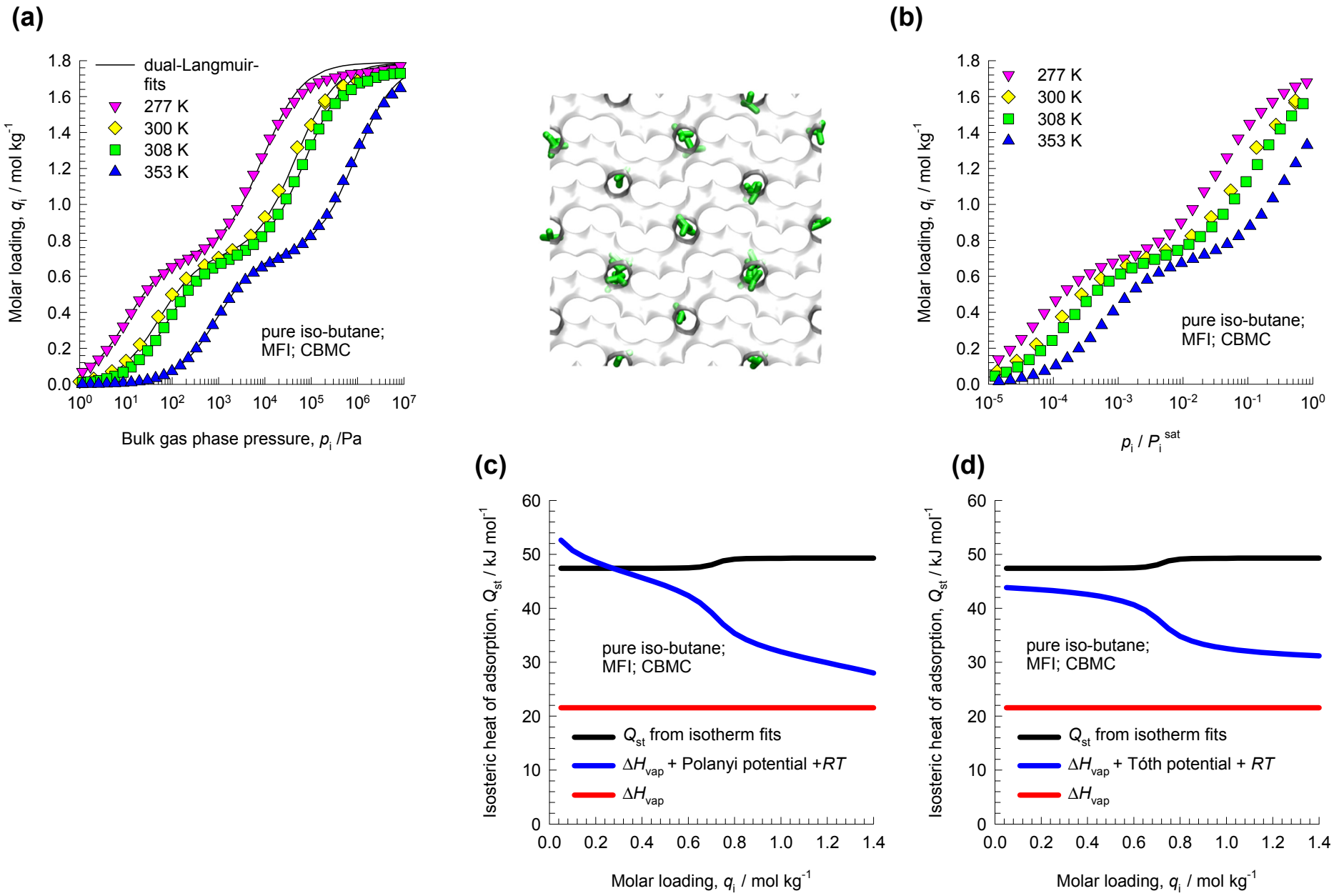

Figure 46

n-Hexane in MFI: Song & Rees Experiments

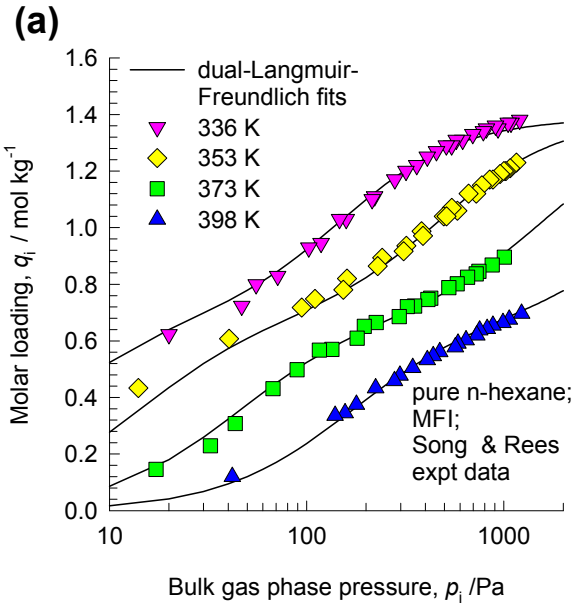

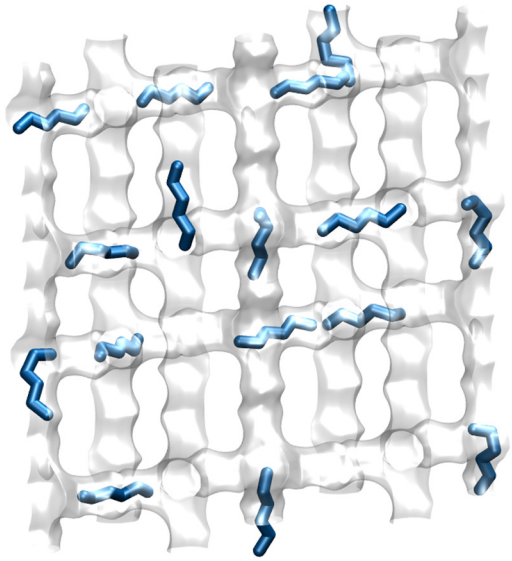

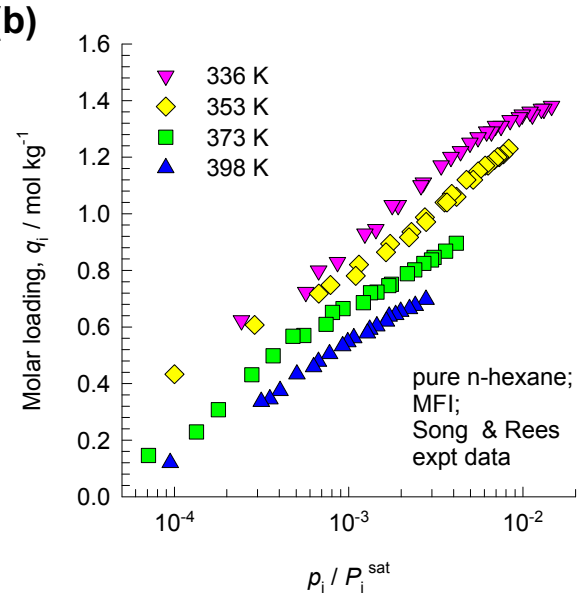

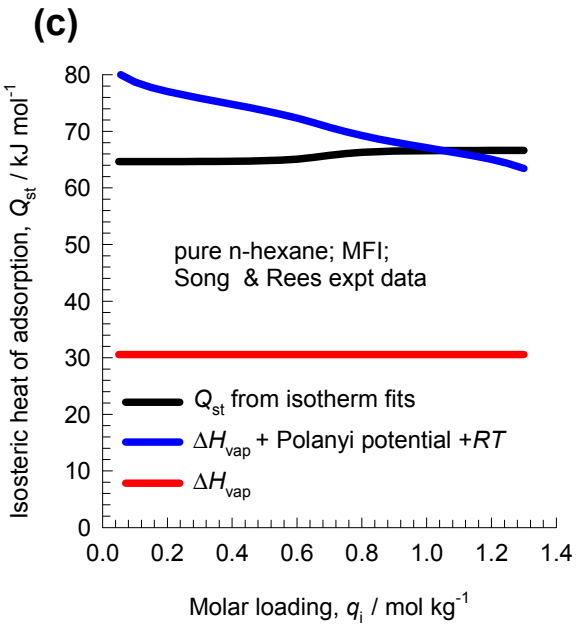

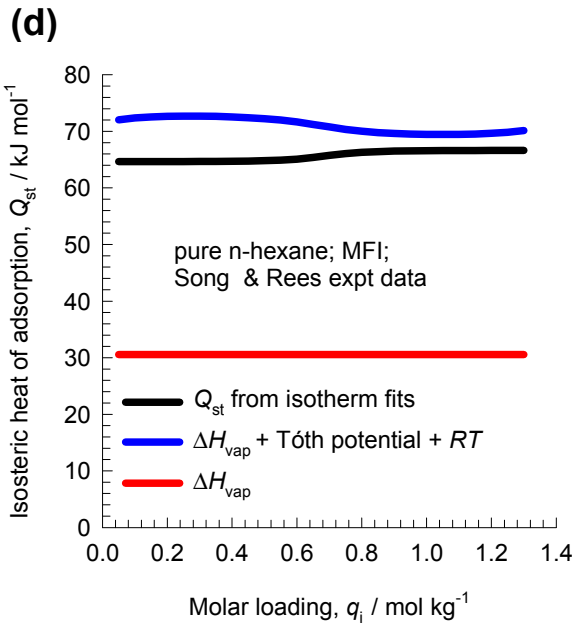

Figure 47

n-Hexane in MFI: CBMC simulations

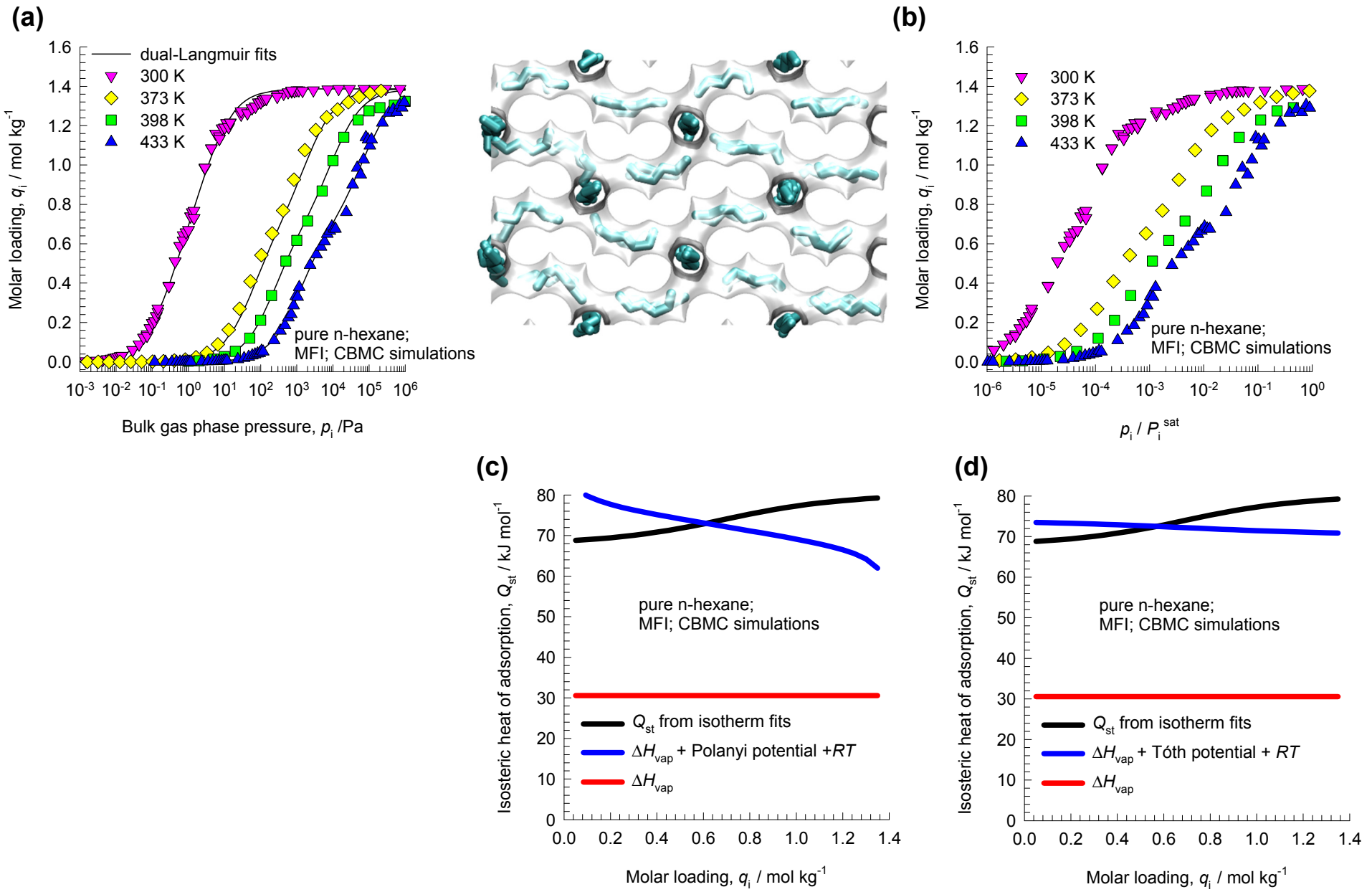

Figure 48

n-Hexane in MgMOF-74: CBMC simulations

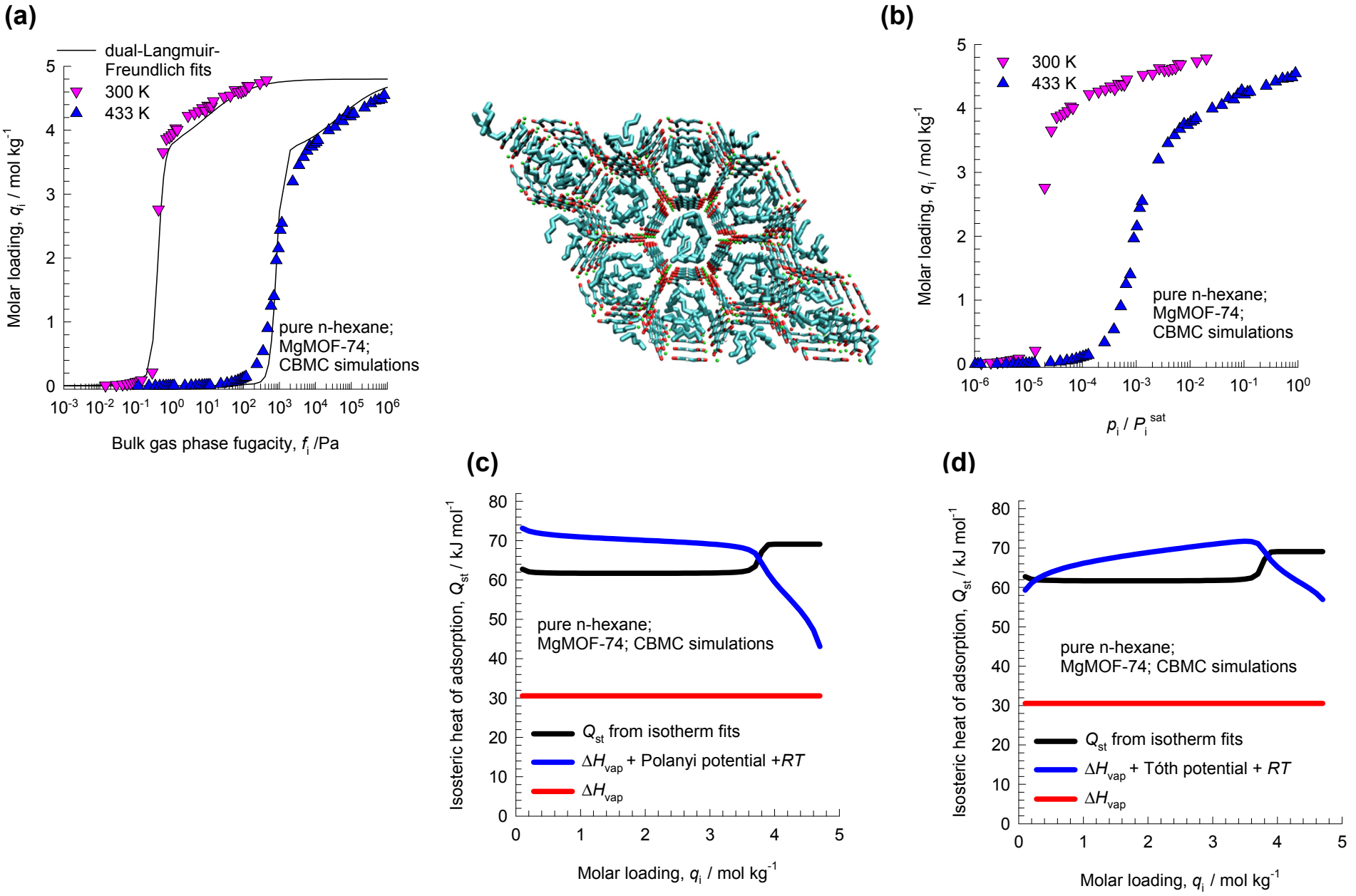

Figure 49

Alkane isomers in CuBTC: CBMC simulations

Snaps of nC_4H_{10} adsorbed in CuBTC

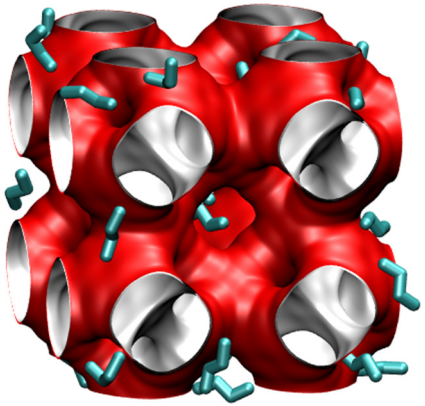

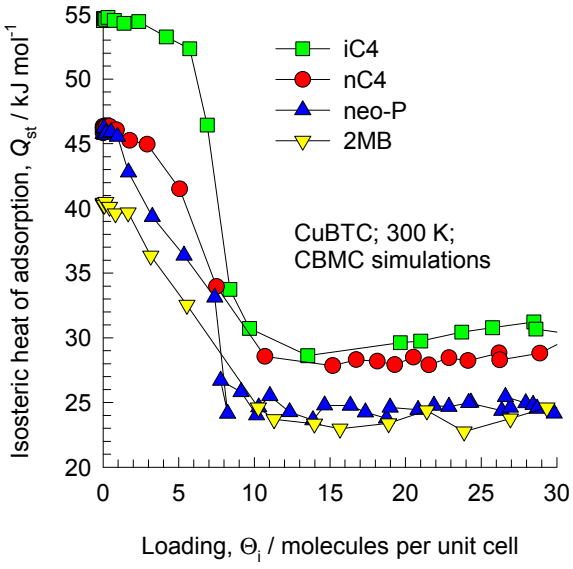

Snaps of 2MB adsorbed in CuBTC

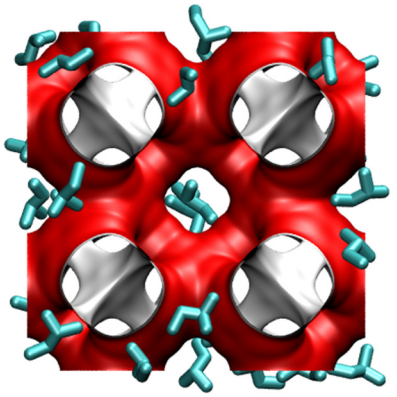

Location of nC_4H_{10} inside the tetrahedral pockets

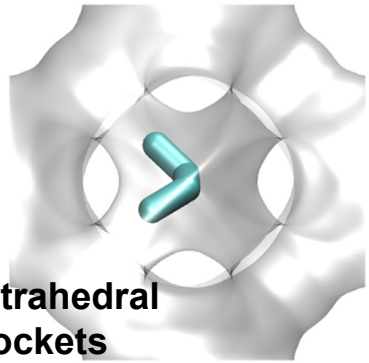

Location of iC_4H_{10} inside the tetrahedral pockets

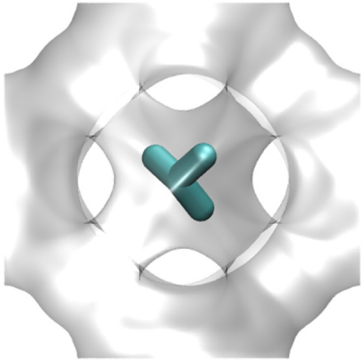

Location of neo-P inside the tetrahedral pockets

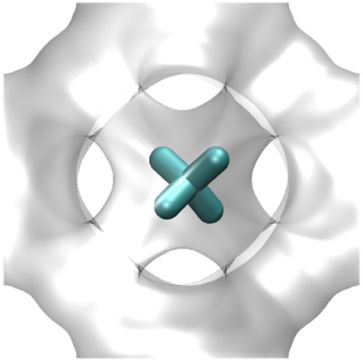

Location of 2MB inside the tetrahedral pockets

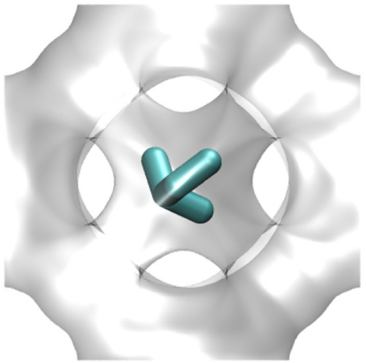

tetrahedral pockets

Figure 50

Hexane isomers in $Fe_2(BDP)_3$: Herm expt data

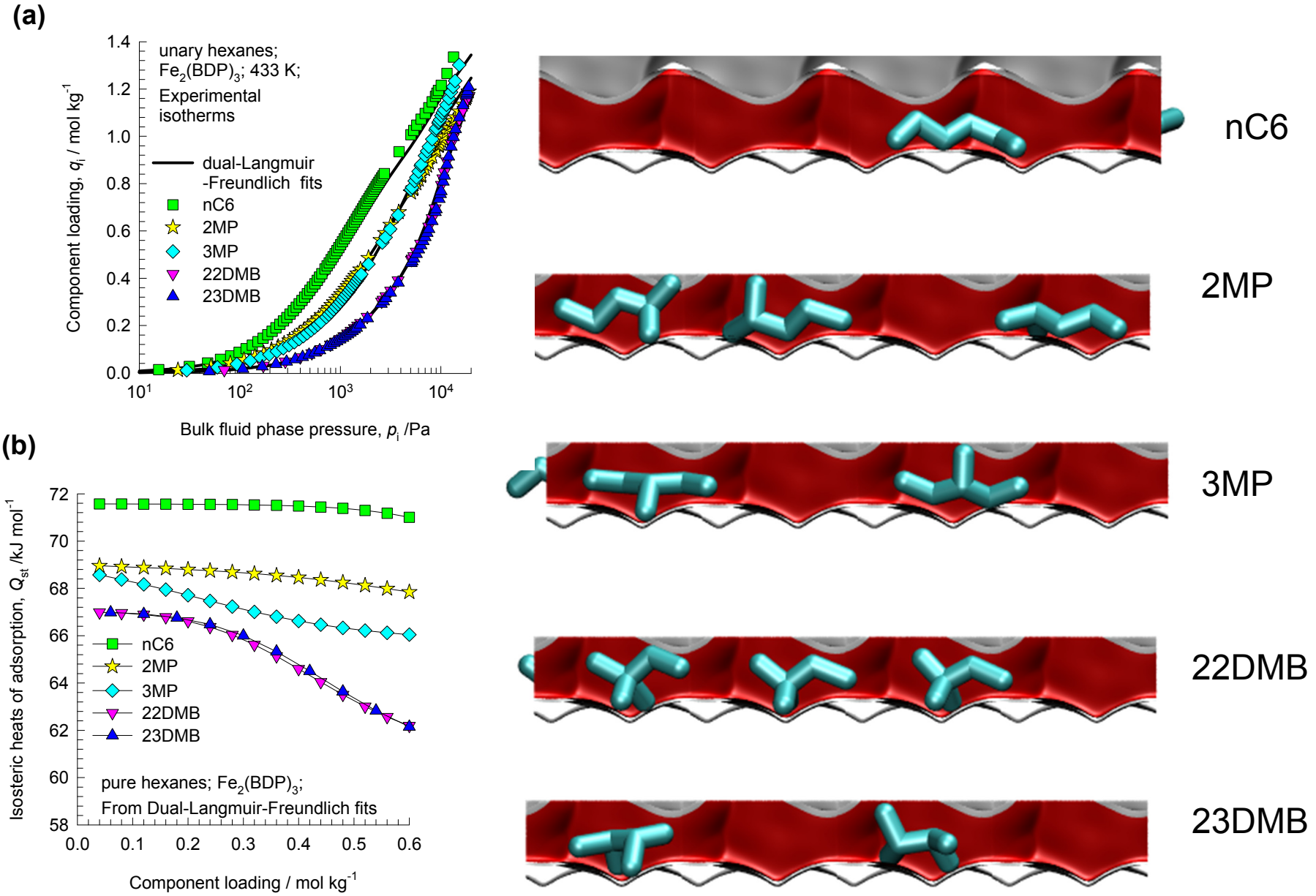

Figure 51

R12 in MIL-101(Cr): Motkuri expt data

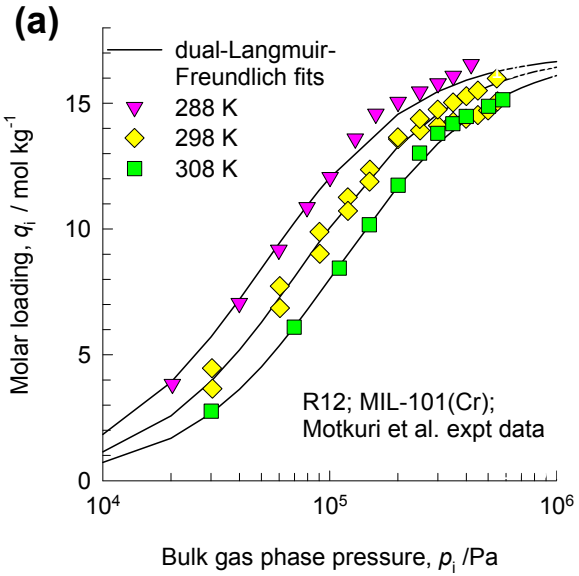

Snapshot at 50 kPa

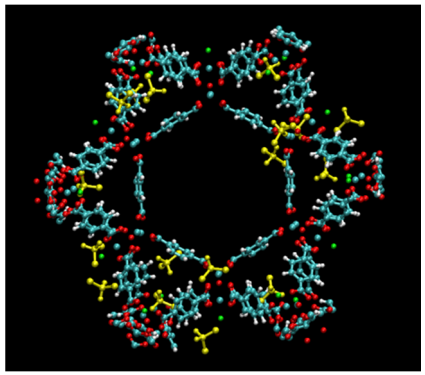

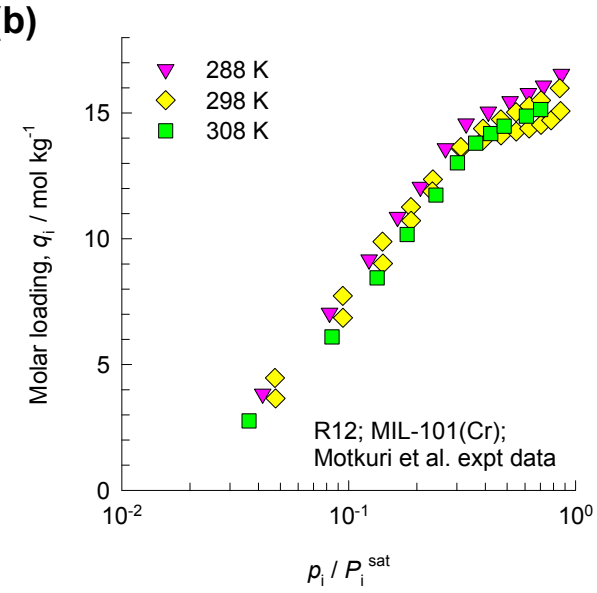

Snapshot at 200 kPa

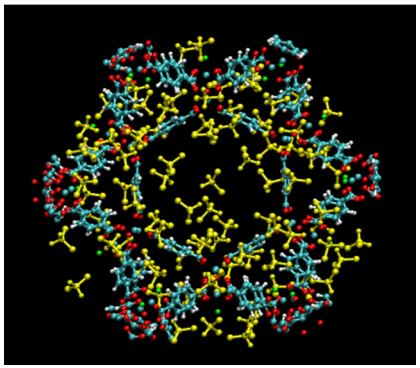

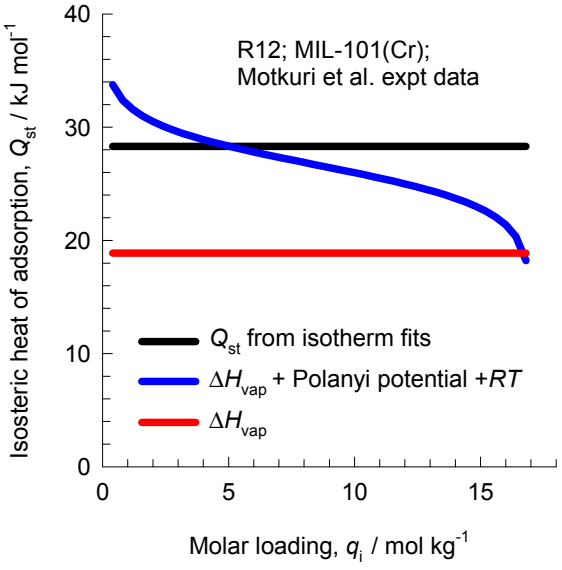

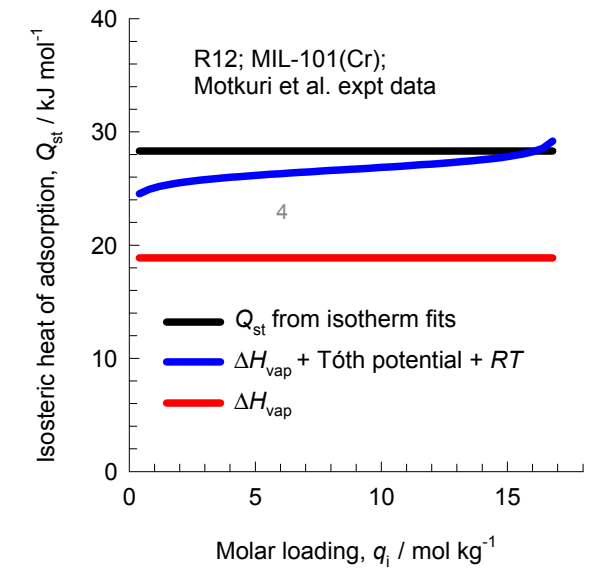

Figure 52

R22 in MIL-101(Cr): Motkuri expt data

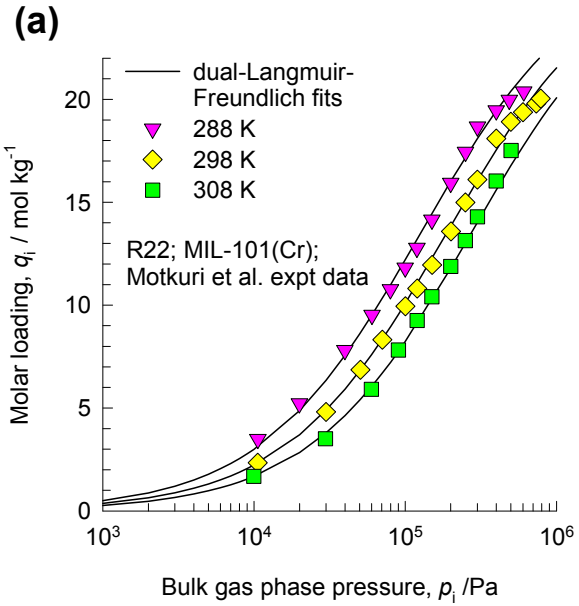

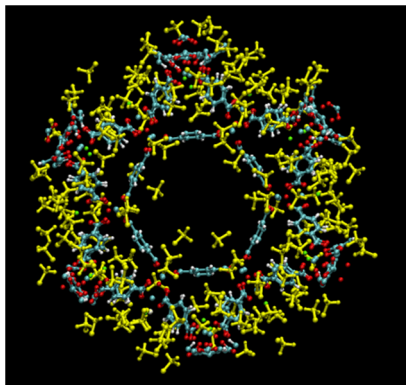

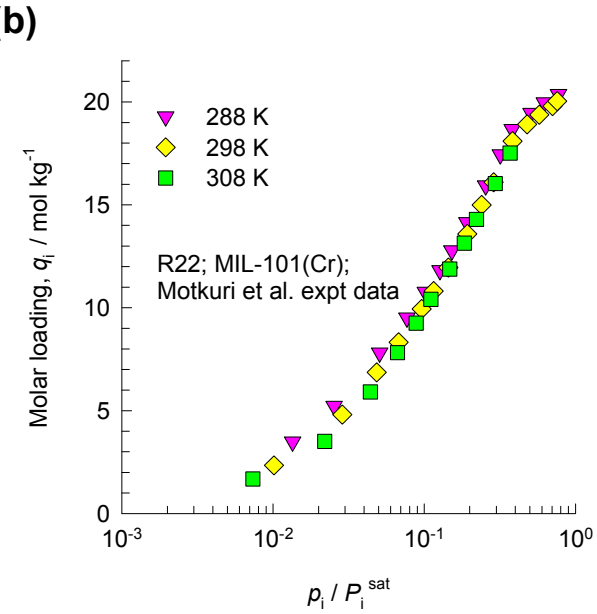

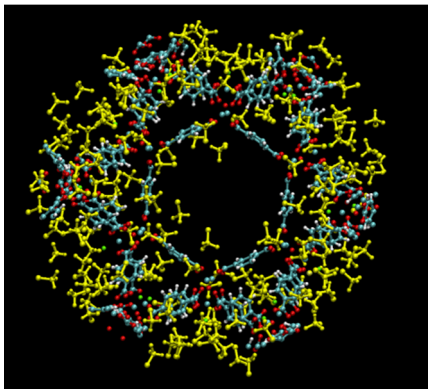

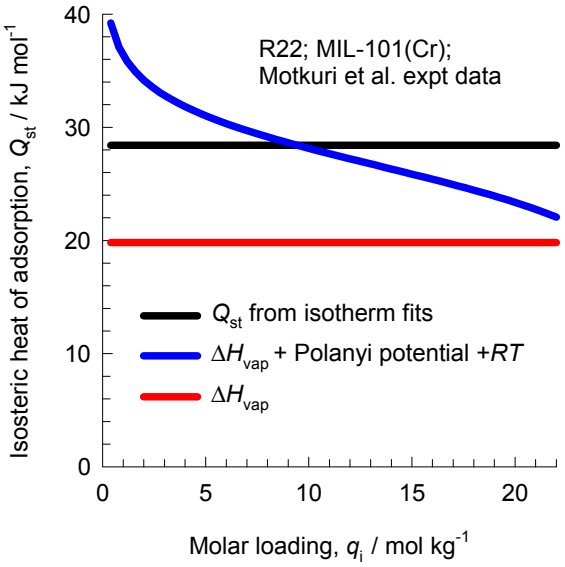

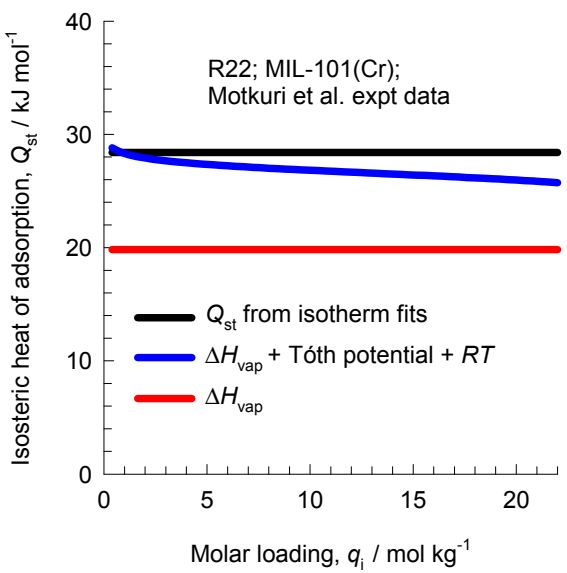

CFC-115 in MFI: Peng expt data

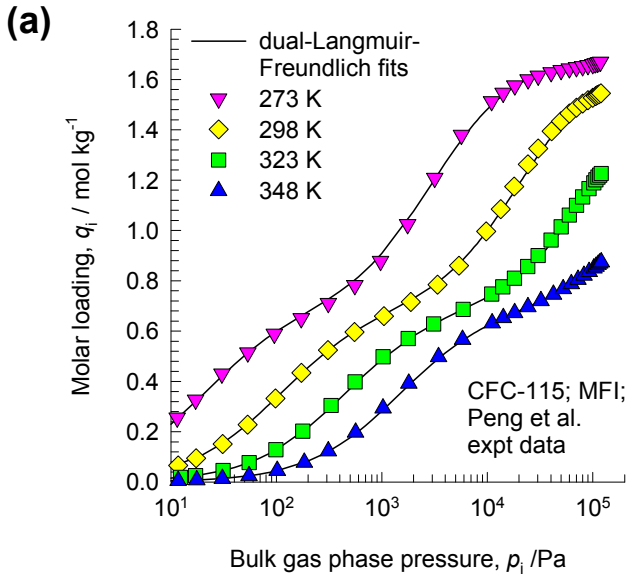

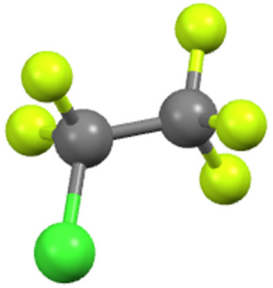

CFC-115

Antoine constants are not available

CFC-115
(1-chloro-1,1,2,2,2-pentafluoroethane)
MW = 154.47 g mol^{-1}
Boiling point = 234.1 K
Critical temperature = 353.2 K
Critical pressure = 3.229 MPa
Enthalpy of vaporization = 14.62 kJ mol^{-1}

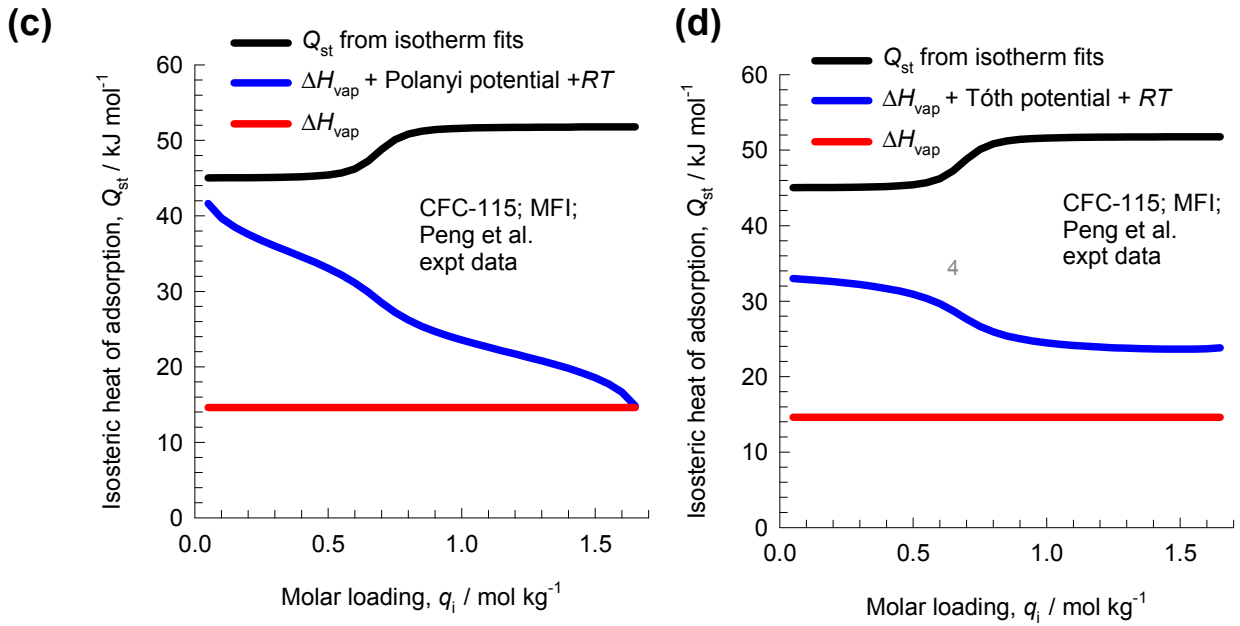

Figure 54

HFC-125 in MFI: Peng expt data

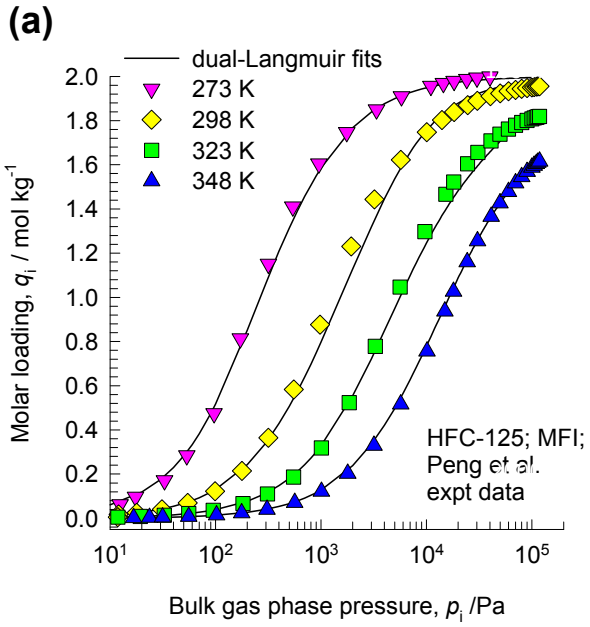

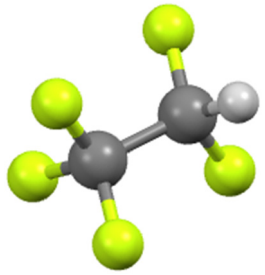

HFC-125

Antoine constants are not available

HFC-125
(1,1,1,2,2-pentafluoroethane)
MW = 120.02 g mol^{-1}
Boiling point = 224.7 K
Critical temperature = 339.2 K
Critical pressure = 3.617 MPa
Enthalpy of vaporization = 13.19 kJ mol^{-1}

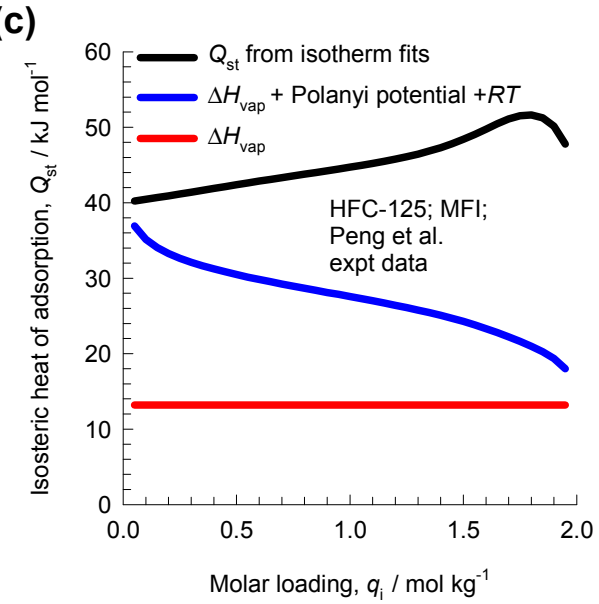

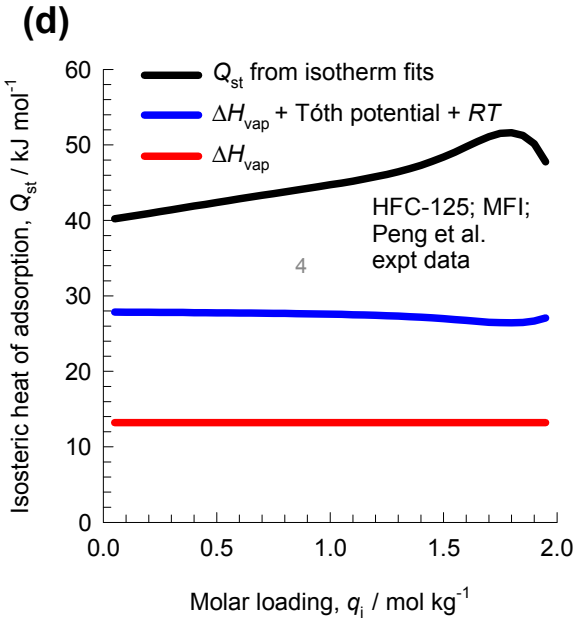

Figure 55

CFC-115 in Vruf AC: Peng expt data

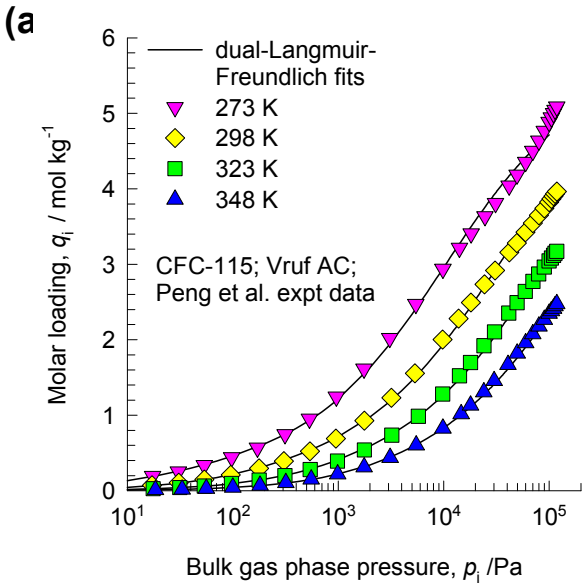

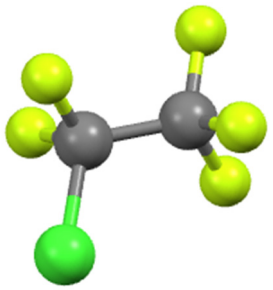

CFC-115

Antoine constants are not available

CFC-115
(1-chloro-1,1,2,2,2-pentafluoroethane)
MW = 154.47 g mol^{-1}
Boiling point = 234.1 K
Critical temperature = 353.2 K
Critical pressure = 3.229 MPa
Enthalpy of vaporization = 14.62 kJ mol^{-1}

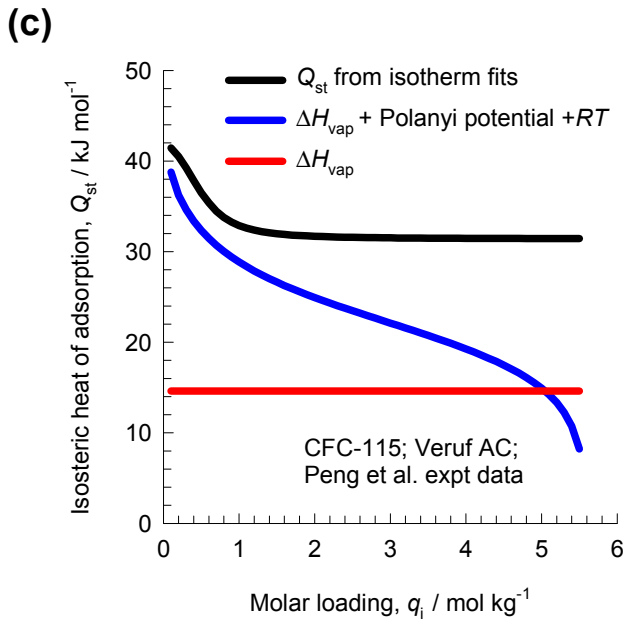

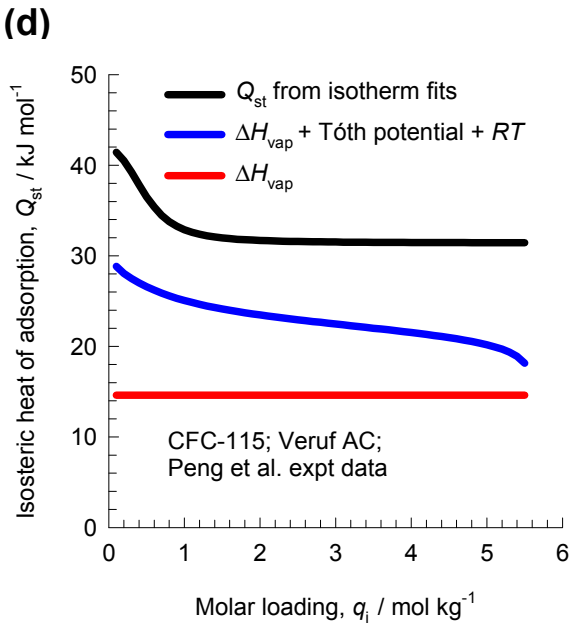

Figure 56

HFC-125 in Vruf AC: Peng expt data

(a)

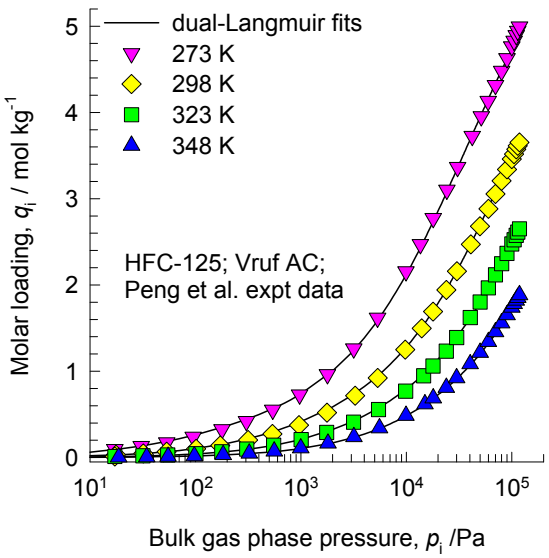

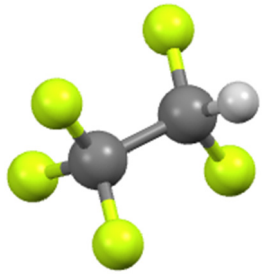

HFC-125

Antoine constants are not available

HFC-125
(1,1,1,2,2-pentafluoroethane)
MW = 120.02 g mol^{-1}
Boiling point = 224.7 K
Critical temperature = 339.2 K
Critical pressure = 3.617 MPa
Enthalpy of vaporization = 13.19 kJ mol^{-1}

(c)

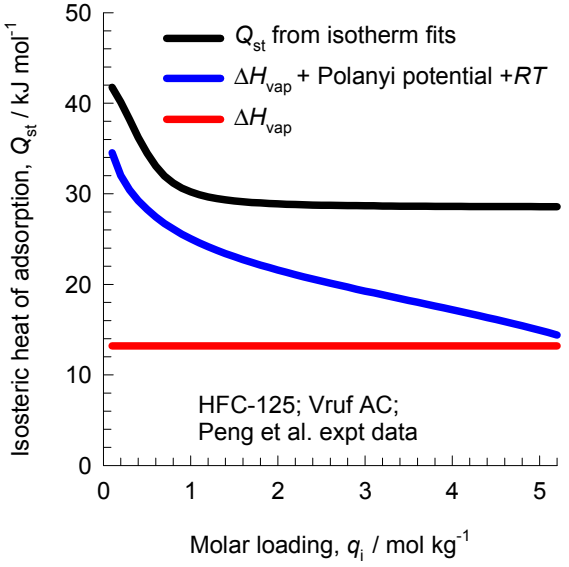

(d)

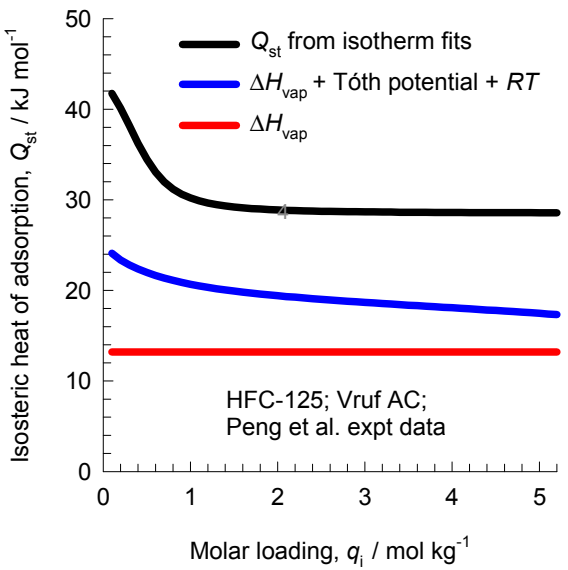

Figure 57

Comparison of Q_{st} for water in different materials

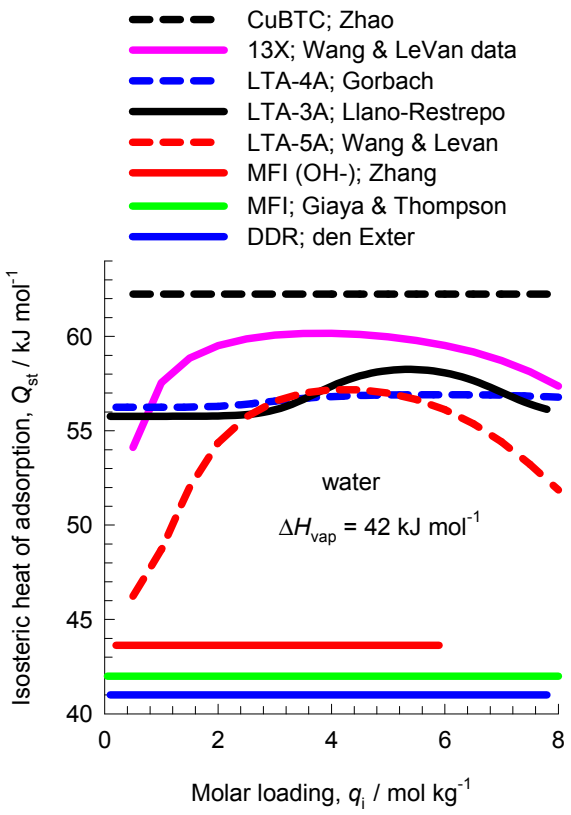

Figure 58

Comparison of Q_{st} for C_2H_2 in different materials

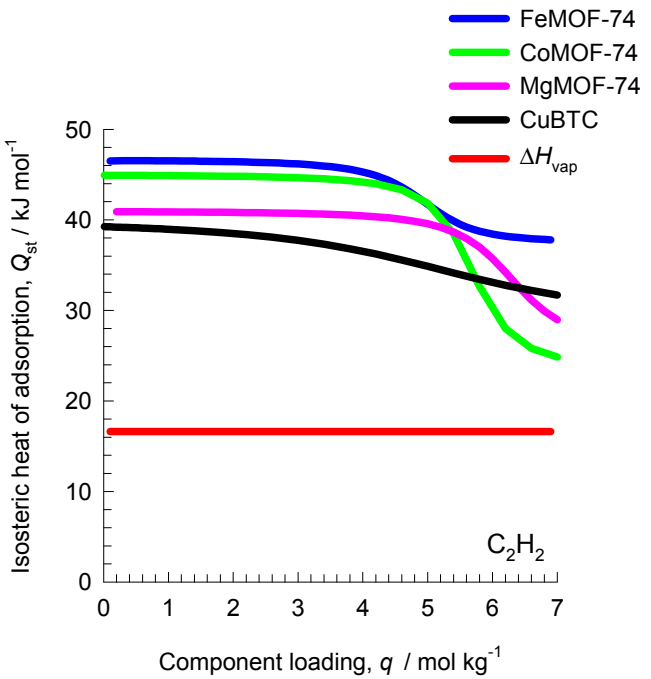

Figure 59

Comparison of Q_{st} for C_3H_6 in different materials

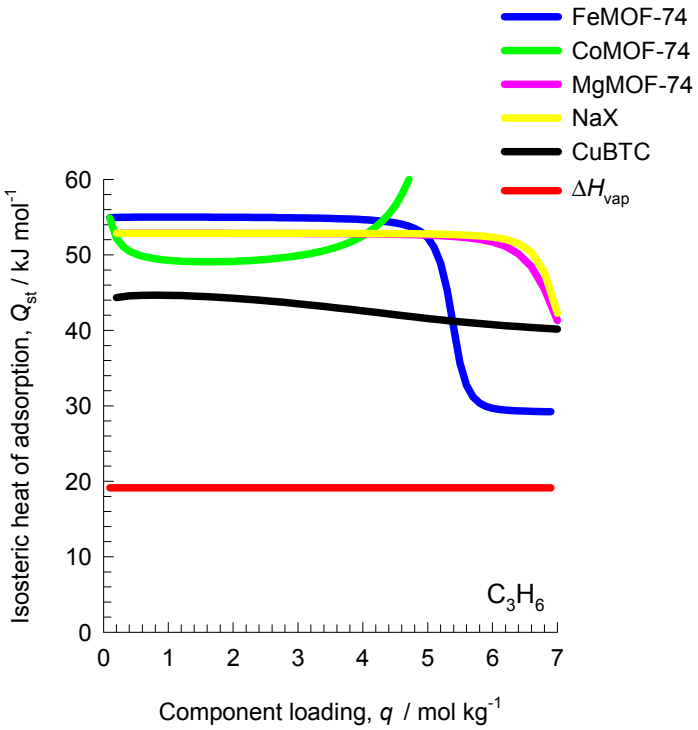

Figure 60

Comparison of Q_{st} for C_3H_8 in different materials

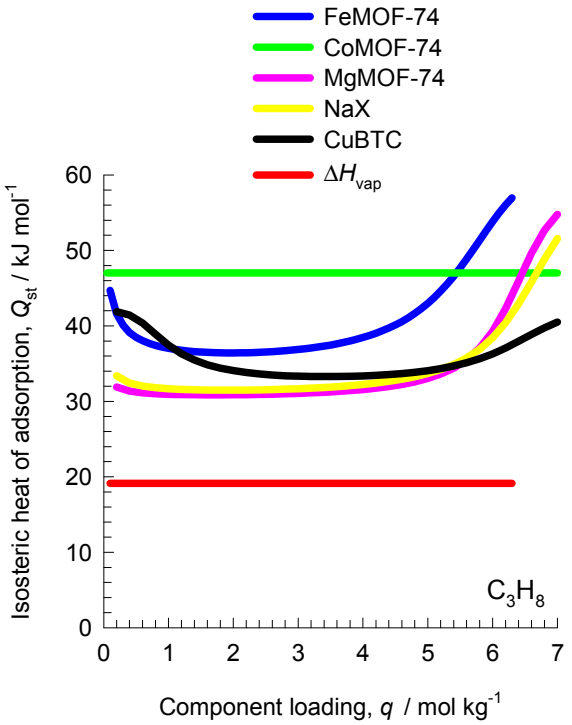

Figure 61

Comparison of Q_{st} for nC6 in different materials

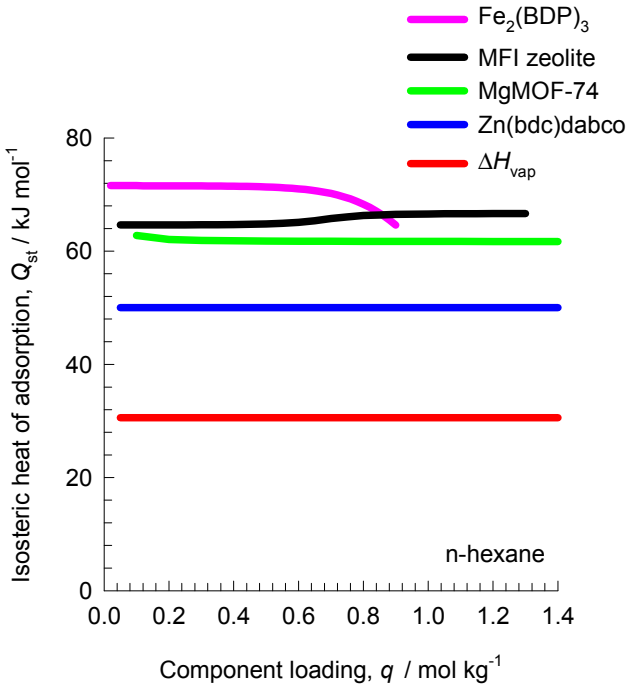

Figure 62

Comparison of Q_{st} for methanol in materials